Two-photon chromophore-polymer conjugates grafted onto gold nanoparticles as fluorescent probes for bioimaging and photodynamic therapy applications

Cristina Cepraga

N° d'ordre : 2012 ISAL 0125 Année 2012

Thèse

Two-Photon Chromophore-Polymer Conjugates Grafted onto Gold Nanoparticles as Fluorescent Probes for Bioimaging and Photodynamic Therapy Applications

Présentée devant

L'Institut National des Sciences Appliquées de Lyon

Pour obtenir

Le grade de docteur

École doctorale : École Doctorale Materiaux de Lyon (ED34)

Par

Cristina CEPRAGA

(Ingénieur ECPM Strasbourg)

Soutenue le 30 novembre 2012 devant la Commission d'Examen

Jury

ASTILEAN Simion – Professeur, Université Babes-Bolyai Cluj (Roumanie)	Rapporteur
FARINHA José Paulo Sequeira – Professeur, Instituto Superior Técnico Lisbonne (Portugal)	Rapporteur
VAN DER SANDEN Boudewijn – Chargé de Recherche CNRS, Institut des Neurosciences Grenoble	Examinateur
DUCHET Jannick – Professeur, INSA de Lyon	Examinateur
CHARREYRE Marie-Thérèse – Directeur de Recherche CNRS, INSA de Lyon	Co-Directeur de thèse
PAROLA Stéphane – Professeur, UCBL Lyon	Co-Directeur de thèse
FAVIER Arnaud – Chargé de Recherche CNRS, INSA de Lyon	Co-encadrant
LEROUGE Frédéric – Maitre de Conférence, UCBL Lyon	Co-encadrant

La photothérapie dynamique (PTD) est un traitement alternatif du cancer qui nécessite l'utilisation de chromophores (photosensibilisateurs) capables d'induire la mort cellulaire après une irradiation lumineuse. Les nanoparticles d'or (AuNP), grâce à leur phénomène de résonance plasmon localisée, peuvent exalter les propriétés photophysiques des chromophores localisés à leur surface. De plus, l'excitation biphotonique, dans le proche infrarouge, peut être utilisée pour améliorer l'action thérapeutique (PTD) ou diagnostique (imagerie de fluorescence) des chromophores en augmentant la profondeur de pénétration dans les tissus et la résolution tridimensionnelle de la zone excitée.
Lors de ce travail, l'élaboration de nouvelles nanoparticules hybrides est proposée, présentant des applications potentielles en bioimagerie (sondes brillantes) et comme photosensibilisateurs pour la PTD. Ces nanoparticules sont composées d'un cœur d'or sur lequel sont greffés des conjugués polymère-chromophores biphotoniques. La stratégie de synthèse des nano-objets a consisté en : **i)** la synthèse des conjugués polymère-chromophores biphotoniques solubles dans l'eau ; **ii)** leur greffage, *via* une extrémité de chaine, à la surface des AuNP.
Les conjugués polymère-chromophores hydrosolubles ont été synthétisés *via* le couplage efficace de chromophores hydrophobes en position latérale des copolymères P(NAM-*co*-NAS) obtenus par la technique RAFT de polymérisation radicalaire contrôlée. Cette stratégie permet le contrôle à la fois de la longueur des chaînes polymère formées (2 000 g.mol^{-1} < M_n < 37 000 g.mol^{-1}) et du nombre de chromophores couplés par chaîne (de 1 à 21). Le greffage *via* l'extrémité thiol de chaines de conjugués à la surface des AuNP a été mis en évidence (par MET, ATG et spectroscopie UV-Visible) avec des densités de greffage de ~0.5 chaîne/nm².
Un des rôles de la chaîne polymère était de contrôler la distance entre les chromophores et la surface des AuNP. La dépendance de la distance chromophores-AuNP avec la longueur, donc la masse moléculaire des conjugués a été illustrée en enregistrant une augmentation de la couronne greffée sur les AuNP (par MET), et une augmentation de l'émission de fluorescence des conjugués greffés quand la longueur de chaine augmentait.
Enfin, les propriétés biologiques des conjugués avant et après greffage sur les AuNP ont été évaluées *in cellulo*, mettant en valeur leur potentiel pour des applications thérapeutiques et diagnostiques.

Photodynamic therapy (PDT) is an alternative treatment of cancer requiring the use of chromophore molecules (photosensitizers), which can induce cell death after light excitation. Gold nanoparticles (AuNP), exhibiting localized Surface Plasmon Resonance, can enhance the photophysical response of chromophores located in their vicinity, and thus improve their therapeutic action. Moreover, the use of highly localized two-photon chromophores (photosensitizers and fluorophores), capable to undergo a localized excitation by light in the Near Infra Red region, should increase the penetration depth into tissues, thus improve the treatment efficiency (by PDT) and the imaging (by fluorescence microscopy) of cancer tissues.
In this work, we describe the elaboration of water-soluble hybrid nano-objects for PDT and fluorescence bioimaging applications, composed of two-photon chromophore-polymer conjugates grafted onto gold nanoparticles. In order to obtain these nano-objects a multistep strategy was applied: **i)** the synthesis of a well-defined water-soluble chromophore-polymer conjugates; **ii)** the end-group oriented grafting of chromophore-polymer conjugates onto 20 nm AuNP.
The coupling of hydrophobic two-photon chromophores on linear water-soluble copolymer chains (poly(*N*-acryloylmorpholine-*co*-*N*-acryloxysuccinimide)), obtained by controlled/living RAFT polymerization, resulted in well-defined water-soluble chromophore-polymer conjugates, with different polymer lengths (2 000 g.mol^{-1} < M_n < 37 000 g.mol^{-1}) and architectures (random or block), and a controlled number of chromophores *per* chain (varying between 1 and 21). Their grafting onto 20 nm AuNP in aqueous medium resulted in highly stable hybrid nano-objects (characterized by TEM, TGA and UV-Vis spectroscopy), with grafting densities ~0.5 chains/nm².
The role of the polymer chain was to tune the distance between chromophores and AuNP surface. In this context, it was evidenced that the polymer corona thickness of grafted AuNP (estimated by TEM) increased with the increasing polymer M_n, corroborating with the corresponding distance-dependent fluorescence properties of chromophores near AuNP.
Finally, the *in cellulo* biological properties of two-photon chromophore-polymer conjugates, before and after grafting onto AuNP, have been investigated, highlighting their potential for two-photon bioimaging and PDT applications.

Key Words: photodynamic therapy, photoinduced death, two-photon microscopy / bioimaging, two-photon chromophores, gold nanoparticles, surface plasmon enhanced fluorescence, fluorescence quenching, RAFT polymerization, chromophore-polymer conjugates.

Remerciements

Je tiens ici à remercier sincèrement les nombreuses personnes qui de près ou de loin ont contribué à l'aboutissement de ce projet de thèse.

J'adresse tout d'abord mes remerciements à mes deux directeurs de thèse, Marie-Thérèse Charreyre et Stéphane Parola, pour m'avoir accueilli dans leurs équipes et m'avoir donné l'opportunité de travailler sur ce sujet pluridisciplinaire.

Je tiens également à remercier mes deux co-encadrants, Arnaud Favier et Frédéric Lerouge, de m'avoir initié à leurs domaines de compétences, d'avoir su orienter mon travail et d'avoir toujours été disponibles pour me prodiguer des conseils avisés.

Mes remerciements vont également aux rapporteurs, Pr. Jose Paulo Farinha et Pr. Simion Astilean, ainsi qu'à l'ensemble des membres du jury pour l'intérêt qu'ils ont porté à ce travail et pour les remarques constructives qu'ils ont fait sur les divers aspects de ce projet de thèse.

Je souhaite remercier chaleureusement tous les collaborateurs de ce projet, sans qui cette thèse ne serait pas ce qu'elle est, pour le vrai esprit d'équipe et pour l'ambiance de travail très agréable. Notamment :

- les collègues chimistes dans l'équipe de Chantal Andraud, Thibault Gallavardin, Jean-Christophe Mulatier, Pierre-Henri Lanoë, Cyrille Monnereau et Olivier Maury, pour leurs efforts dans la synthèse des chromophores biphotoniques ;
- les collègues biologistes dans l'équipe de Jacqueline Marvel, Yann Leverrier, Sophie Marotte et Edna Ben Daoud, d'avoir évalué les propriétés biologiques des sondes fabriquées au cours de ce travail ;
- les collègues spectroscopistes, Patrice Baldeck et Mikael Lindgren ainsi qu'aux membres de leurs équipes, Jean Bernard, Kenji Kamada, Guillaume Micouin, pour leur bienveillance, leur aide et leurs conseils pertinents dans le domaine de la spectroscopie. Cette collaboration m'a permis non seulement d'enrichir connaissances dans la spectroscopie de fluorescence, mais également d'éveiller mon intérêt pour ce domaine passionnant. Je pense ici en particulier à Olivier Maury et Mikael Lindgren pour leurs encouragements et leur aide.

Je remercie également Pierre Alcouffe, Agnès Crépet, Catherine Ladavière Fernande Boisson et Cécile Chamignon du laboratoire Ingénierie de Matériaux Polymères. J'ai eu beaucoup de plaisir à travailler avec eux et d'acquérir de nouvelles connaissances.

Mes remerciements s'adressent de manière générale à tous ceux qui ont participé et contribué à la réalisation de ce travail de recherche de thèse, aussi bien par les discussions fructueuses entretenues avec eux, que par leurs suggestions et contributions : Sandrine Denis-Quanquin, Katherin Wunderlich, Rodica Chiriac, Rodrigo Pinto...

Je souhaite remercier tous mes collègues et amis thésards ainsi que les membres du Laboratoire Joliot-Curie pour leur aide, leur bonne humeur et les bons moments partagés ensemble : Salim, Sophie, Merve, Damia, Thibault, Denis, Francis, Sadhan, Zofia, Monica, Xavier, Benoit…

Enfin, une pensée toute particulière à ma famille et mes amis, ceux de loin comme ceux de près, pour leurs encouragements, leur soutien et la confiance qu'ils m'ont toujours accordée.

Résumé

(en français)

La photothérapie dynamique (PTD) est un traitement alternatif contre le cancer, qui suppose l'utilisation de photosensibilisateurs (chromophores) – molécules capables de produire des espèces cytotoxiques sous l'effet d'un rayonnement lumineux, qui peuvent s'accumuler de manière préférentielle dans les tumeurs. Comparé à d'autres types de traitements cancéreux comme la chimiothérapie, la radiothérapie ou la chirurgie, la photothérapie dynamique est considérée beaucoup moins invasive grâce à une application localisée de la lumière excitatrice, permettant le ciblage des tumeurs.

On s'intéresse dans ce projet à 2 types d'application, nécessitant l'utilisation de chromophores – molécules organiques ou complexes organométalliques capables d'absorber la lumière à certaines longueurs d'onde, la photothérapie dynamique et la bioimagerie. Les chromophores excités peuvent être utilisés pour la bioimagerie de fluorescence (fluorophores), s'ils émettent de la fluorescence, ou pour la PTD (photosensibilisateurs), si ils sont capables de réagir avec l'oxygène moléculaire présent dans le milieu biologique pour produire des espèces cytotoxiques tel que l'oxygène singulet (Figure 1).[1] Certains chromophores peuvent se désexciter à la fois en émettant de la fluorescence et en produisant de l'oxygène singulet, ce qui permet avec un seul système (une seule molécule) de traiter et de visualiser la tumeur.

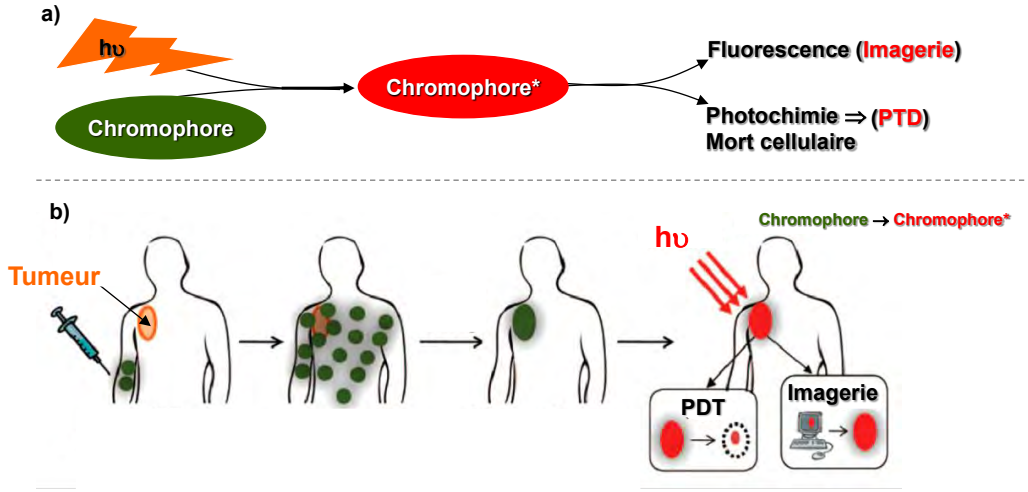

Figure 1: a) Représentation schématique d'un chromophore (fluorophore ou photosensibilisateur) après activation par la lumière (Chromophore*), qui peut servir pour la bioimagerie de fluorescence ou/et comme agent thérapeutique pour la PTD. b) Représentation schématique de la séquence d'administration intraveineuse d'un chromophore, son accumulation dans les tumeurs et son activation par la lumière.[2]

En pratique, les photosensibilisateurs utilisés en clinique sont capables, la plupart du temps, d'absorber efficacement la lumière dans la zone UV-Visible du spectre lumineux, là où l'autofluorescence et la diffusion des composantes biologiques sont non-négligeables. De plus, dans cette zone spectrale la profondeur de pénétration de la lumière dans les tissus est limitée à seulement ~1-2 mm.

Dans ce contexte, le développement des chromophores biphotoniques, capables d'être excités dans le rouge lointain et le proche InfraRouge, s'est présenté comme une solution prometteuse permettant de contourner ces désavantages et d'augmenter la profondeur de pénétration dans les tissus.[3 4]

Le phénomène optique non linéaire d'absorption à deux photons (TPA), localisé sur un volume de ~1μm^3, présente les avantages suivants :

- Permet d'exciter les chromophores dans le rouge lointain/proche InfraRouge dans la fenêtre de transparence biologique où la diffusion, l'absorption et l'autofluorescence des composantes biologiques restent négligeables.
- Permet d'augmenter la profondeur de pénétration dans les tissus, de 2-3 fois par rapport à l'excitation à un photon.
- Permet une meilleure résolution spatiale de la zone excitée.
- Diminue la photodégradation des tissus environnants grâce à l'excitation lumineuse très localisée.

Malgré les nombreux avantages énumérés ci-dessus, les chromophores biphotoniques ont des structures chimiques conjugués, présentant souvent une faible solubilité en milieu aqueux, ce qui complique leur utilisation en milieu biologique.
Pendant les dernières décennies, de nombreux efforts ont été effectués par les chimistes pour améliorer la bio-activité des principes actifs moléculaires en les associant avec des structures biocompatibles.[5] Une des stratégies largement utilisée implique les polymères hydrosolubles sous forme de micelles, d'agents dispersants (*e.g.* Pluronic®), de nanoparticules, de chaines linéaires etc. Il a été démontré que l'utilisation des polymères améliore la solubilité et la stabilité biologique des molécules hydrophobes, diminue considérablement leur toxicité, et peut également contrôler leur relargage.[6]

En parallèle, l'utilisation des nanoparticules d'or (AuNP) dans les applications biomédicales a connu une croissante importante pendant la dernière décennie grâce à leur facilité de synthèse et de fonctionnalisation, à leur biocompatibilité et faible toxicité en milieux biologique ainsi qu'à leur dispersabilité en milieu aqueux. Notamment grâce à leurs propriétés optiques uniques à l'échelle nanométrique résultant du phénomène de résonance plasmonique de surface (SPR), les AuNP sont un candidat idéal pour des nombreuses applications thérapeutiques et diagnostiques tel que l'imagerie, la détection et la libération contrôlée des principes actifs.[7]
Il est connu que le fort champ électromagnétique créé par la SPR peut influencer les propriétés photophysiques de chromophores qui se situent à la proximité des surfaces d'or : par exemple il peut y avoir quenching ou exaltation de leur fluorescence dans ces conditions. De nombreuses études théoriques et quelques études expérimentales montrent qu'en optimisant la distance entre les chromophores et les AuNP il serait possible d'améliorer de manière significative la performance photophysique des chromophores.

A notre connaissance, jusqu'à présent il n'existe pas d'exemples dans la littérature qui combinent à la fois les propriétés des AuNP avec les propriétés des chromophores biphotoniques.
Pendant la thèse des T. Gallavardin soutenue en 2010,[8] il a été démontré qu'en milieu organique le greffage directe des chromophores biphotoniques sur les AuNP résulte en un quenching total des

leurs propriétés photophysiques. A la suite de ce dernier travail, notre objectif a été d'utiliser des chaine linéaires de polymères multifonctionnels (synthétisés par la techniques de polymérisation RAFT) pour augmenter et mieux contrôler la distance entre les chromophores biphotoniques, couplés de manière covalente en positions latérales des chaines polymères, et la surface des AuNP, et ainsi de mieux comprendre les enjeux de ce phénomène

L'expertise des différentes équipes de recherches : chimistes organiciens – C. Andraud ENS Lyon, chimistes inorganiciens – S. Parola ENS Lyon, polymeristes – M.-T. Charreyre INSA Lyon, spectroscopistes – P. L. Baldeck et M. Lindgren, biologistes – J. Marvel et Y. Leverrier, physiciens – J. Lermé, a été combinée pour conduire à ce sujet de thèse réalisée dans le cadre d'un projet ANR pluridisciplinaire ANR P3N nanoPDT.

Le but final de ce travail de recherche a été d'élaborer des nano-objets hybrides (Figure 2) composés de chromophores biphotoniques, de chaines de polymère hydrosolubles et biocompatibles et de nanoparticules d'or, ainsi que d'évaluer leur potentiel pour l'imagerie de fluorescence à 2 photons et pour la photothérapie dynamique.

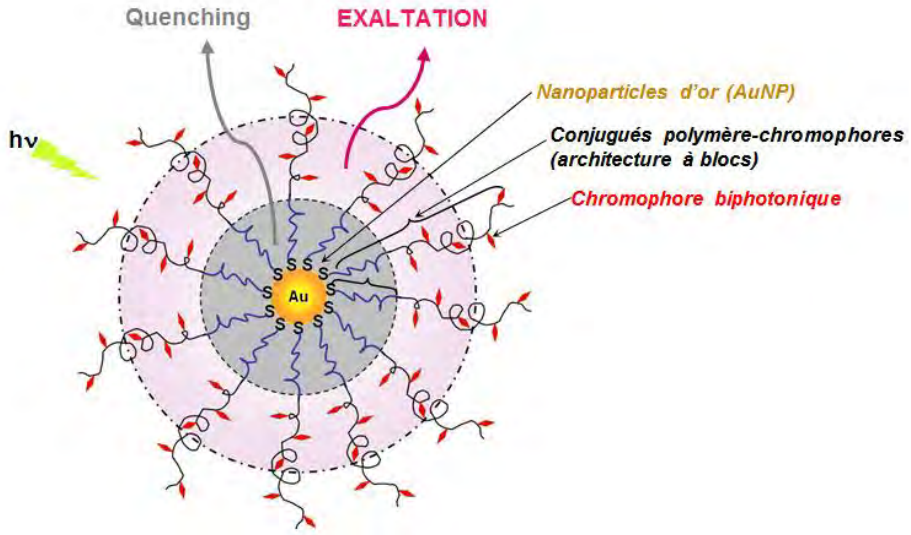

Figure 2: La structure du nano-objet hybride élaboré au cours de ce travail, se compose d'un cœur d'or nanoparticulaire greffé avec des conjugués polymère-chromophores biphotoniques. Les conjugués polymère-chromophores biphotoniques ont une architecture à blocs, avec un premier bloc espaceur sans chromophore pour augmenter la distance chromophores-AuNP.

Pour réaliser ce type de nano-objets, nous avons dans un premier temps synthétisé les conjugués polymère-chromophores, résultant du couplage covalent entre les groupements réactifs situés en position latérale des chaines de copolymères P(NAM-*co*-NAS) – composé de *N*-acryloylmorpholine (NAM) et de *N*-acryloxysuccinimide (NAS) – et des chromophores biphotoniques aminés contenant soit un cœur anthracène (Ant) très fluorescent, ou dibromobenzène (DBB), capable de produire de l'oxygène singulet. Par la suite les conjugués hydrosolubles sont greffés *via* une extrémité de chaine (fonctionnalisée avec un thiol) sur des nanoparticules d'or sphériques, choisies comme système modèle.

L'intérêt de ce type de nano-objets réside dans leur structure modulable pour obtenir la meilleure efficacité en milieu biologique, car il est possible d'optimiser la structure et la composition des objets en termes de cœurs métalliques d'or (taille, forme, propriétés SPR), et également en termes de couronne organique composé de conjugués polymère-chromophores (longueur et architecture de chaine, densité de chromophores par chaine, charge). Une synergie est attendue quand les chromophores sont situés à une distance optimale de la surface des AuNP, enduisant une exaltation de leurs propriétés photophysiques, une augmentation de fluorescence (pour la bioimagerie) ou de la phototoxicité (PDT). De plus, la forte concentration locale en chromophores dans ces cas confère aux nano-objets une brillance élevée et des propriétés photophysiques améliorées.
Etape par étape, les objectifs principaux de ces travaux ont été les suivants :

- étudier le couplage des chromophores hydrophobes le long de la chaine de polymère ;
- caractériser les propriétés des conjugués polymère-chromophore ainsi obtenus (hydrosolubilité, brillance) ;
- optimiser le greffage en milieu aqueux des polymères (conjugués) sur les AuNP ;
- étudier l'influence de la distance entre les chromophores et la surface de AuNP (chromophore-AuNP) sur les propriétés photophysiques des objets hybrides ;
- étudier le potentiel biologique des conjugués et des nanoparticules greffées en bioimagerie biphotonique de fluorescence et PDT.

Ces différentes étapes sont décrites dans les 5 chapitres de ce manuscrit qui seront résumés ci-dessous.

Le 1er chapitre introductif présente de manière large les différentes classes de nanomatériaux organiques, inorganiques ou hybrides qui sont développés pour des applications dans le domaine biomédical à but thérapeutique et/ou diagnostique.
Dans ce chapitre une attention particulière est accordée aux nanoparticules d'or (AuNP). Les propriétés uniques des AuNP à l'échelle nano sont mises en évidence ainsi que leurs nombreux avantages quant à leur utilisation dans les milieux biologiques, notamment grâce à la SPR, à leur faible toxicité et à leur biocompatibilité.

Le 2ème chapitre est centré sur la synthèse et la caractérisation des conjugués polymère-chromophores biphotoniques.
Il commence avec une présentation générale de la technique de polymérisation RAFT, ainsi que des avantages des homopolymères poly(*N*-acryloylmorpholine), PNAM (Figure 1 a)), et des copolymères poly((*N*-acryloylmorpholine)-*co*-*N*-acryloxysuccinimide)), P(NAM-*co*-NAS) (Figure 1 b)), obtenus par la polymérisation RAFT. On y trouve quelques exemples trouvés dans la littérature des conjugués polymère-chromophores pour les applications biologiques, mettant ainsi en évidence le nombre réduit de systèmes de conjugués polymère-chromophores biphotoniques.

a) b)

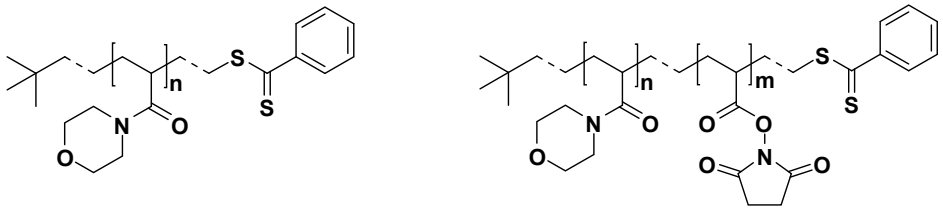

Figure 3: La structure des a) homopolymers PNAM et b) copolymères statistiques P(NAM-*co*-NAS).

La partie suivante du chapitre décrit la synthèse par la technique RAFT et la caractérisation des homopolymères PNAM, des copolymères statistiques P(NAM-*co*-NAS) avec un bon contrôle des masses molaires (M_n variant entre 2 000 g.mol^{-1} et 60 000 g.mol^{-1}) ainsi que des groupements terminaux (> 90% dithioesters), et des indices de polymolécularité faibles (PDI<1.2). De plus, l'utilisation du copolymère P(NAM-*co*-NAS) M_n=23 000 g.mol^{-1} comme macro agent de transfert (macro-CTA) permet d'obtenir des copolymère à blocs P[(NAM-*co*-NAS)-*b*-NAM)] (Figure 5) de structure et d'architecture contrôlées.

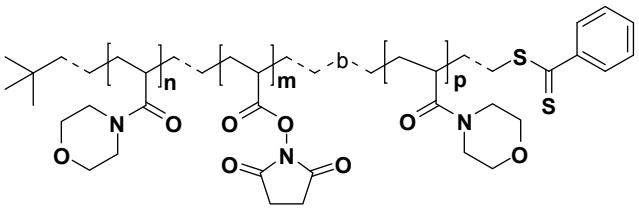

Figure 4: La structure des copolymères à blocs P[(NAM-*co*-NAS)-*b*-NAM)].

Dans une deuxième étape, les copolymères statistiques et à blocs sont utilisés pour le couplage covalent de chromophores portant une fonction amine primaire. Les chromophores utilisés dans ce travail sont : a) Lucifer Yellow Cadaverine, fluorophore commercial hydrophile utilisé comme système modèle (Figure 5 a))[9] [10] et b) chromophores biphotoniques à cœur anthracène (fluorophore) et dibromobenzène (photosensibilisateur), synthétisés dans l'équipe de C. Andraud au Laboratoire de Chimie de l'ENS Lyon (Figure 5 b)).[11]

a) b)

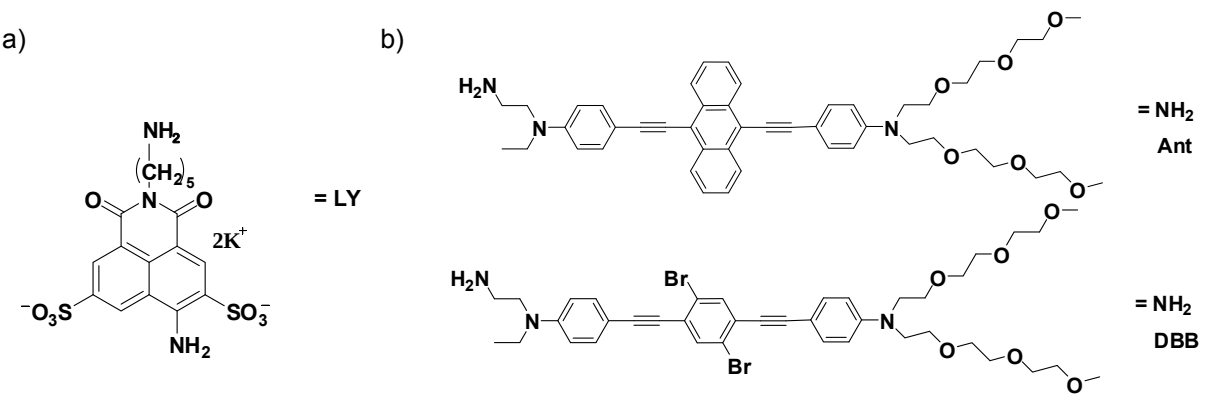

Figure 5: Les structures chimiques des chromophores aminés utilisés pour le couplage avec les copolymères : a) Lucifer Yellow Cadaverine (LY) ; b) Chromophores biphotoniques à cœur anthracène (Ant) et dibromobenzène (DBB).

Le couplage de ces différents chromophores sur les chaines de copolymère a été réalisé *via* la réaction efficace entre l'amine du chromophore et les groupements esters activés des polymères (NAS). On a pu obtenir ainsi des conjugués polymère-chromophores de différentes longueurs (2 700 $g.mol^{-1}$ < M_n < 37 700 $g.mol^{-1}$) avec un nombre variable de chromophores par chaine (Nc) entre 1 et 21 (Tableau 1). Nc a été déterminé avec précision en faisant appel à trois techniques d'analyse différentes : chromatographie d'exclusion stérique (SEC/UV), résonance magnétique nucléaire du proton (^{1}H NMR), et spectroscopie d'absorption UV-Visible. Pour désactiver le reste de groupements actifs NAS, les conjugués sont post-traités par une des deux méthodes suivantes : i) capping avec une amine primaire neutre : *4*-(*2*-aminoethylmorpholine), AEM ; ii) ou hydrolyse basique (H) conduisant à des conjugués négativement chargés.

Il a été mis en évidence dans ce chapitre que l'hydrosolubilité des conjugués polymère-chromophores biphotoniques Ant et DBB dépendait de différents facteurs (Tableau 1) : la structure chimique et l'hydrophobie du chromophore ; la densité de chromophores par chaine ; le post-traitement utilisé (AEM ou H).

En conclusion, on obtient des conjugués polymère-chromophores biphotoniques hydrosolubles qui peuvent être engagés par la suite dans le greffage en milieu aqueux sur des AuNP.[12]

Tableau 1: Résumé des propriétés physicochimiques des conjugués polymère-chromophores : nature du chromophore, M_n avant couplage, Nc, solubilité.

Chromophore	M_n du copolymère avant couplage ($g.mol^{-1}$)	Nc = nombre de chromophores par chaine (SEC/UV)	Architecture	Post-traitement	Solubilité
LY	2 200 – 34 600	1 – 5	Statistique et à blocs	AEM	H_2O et DMF
Ant	12 900	6 / 10 / 21	Statistique	AEM	$CHCl_3$ ou H_2O =f(Nc)
				H	H_2O =f(post-traitement)
DBB	12 900 / 29 400* / 35 000	4 / 10	Statistique et à blocs	AEM	$CHCl_3$ ou H_2O =f(Nc)
				H	H_2O =f(post-traitement)

Le greffage des conjugués polymère-chromophores sur les nanoparticules d'or est présenté et discuté dans le chapitre 3. Après une partie introductive sur les deux stratégies de greffage « grafting from » et « grafting to », une bibliographie détaillé des systèmes de AuNP greffés par « grafting to » avec des (co)polymères synthétisés par la polymérisation RAFT est exposée, mentionnant la facilité de greffage de ces polymères *via* leur extrémité de chaine soufrée (*e.g.* thiol, dithiocarbonate).

Dans une première partie d'optimisation, il a été montré que le greffage *in situ* des PNAM-SH sur des AuNP conduisait à des AuNP de très petite taille (2-3 nm diamètre), difficile à analyser par TEM (microscopie électronique en transmission) ou spectroscopie optique.

Une alternative, l'approche par échange de ligand a quant à elle permis d'obtenir des AuNP greffées de ~20 nm diamètre, d'optimiser la densité de greffage en jouant sur les conditions expérimentales (température, rapport molaire Au : polymère) ainsi que de caractériser les systèmes greffés par TEM (diamètre de cœur d'or et épaisseur de la couronne de polymère) et spectroscopie optiques UV-Visible (résonance des plasmons de surface localisés).

La possibilité de varier chaque élément impliqué dans le greffage par échange de ligand (taille et forme de AuNP, nature du polymère) a permis d'obtenir des AuNP greffées avec des conjugués polymère-chromophores bien définies et bien caractérisées (Figure 6).

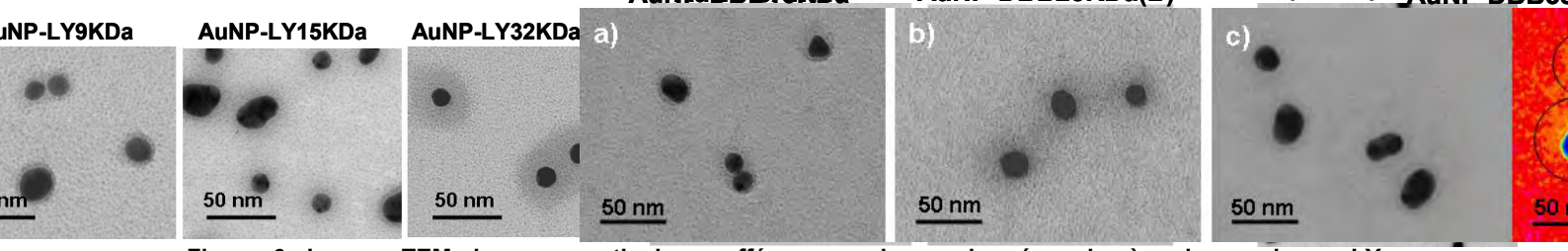

Figure 6: Images TEM des nanoparticules greffées avec des conjugués polymère-chromophores LY (gauche), des conjugués polymère-chromophores Ant (milieu), des conjugués polymère-chromophores DBB (droite). Rond noir – le cœur métallique de la AuNP ; couronne grise – le polymère greffé, visualisé grâce à l'agent de contraste RuO_4.

Les propriétés de AuNP greffées tel que l'hydrosolubilité, la densité de greffage et l'épaisseur de la couronne de polymère et la charge peuvent être contrôlés *via* la nature du chromophore, la longueur de la chaine de polymère et le choix du post-traitement. Par exemple, dans le cas du greffage des conjugués DBB, l'épaisseur de la couronne augmente de 4 nm à 13 nm quand M_n de la chaine de polymère augmente de 12 900 g.mol^{-1} à 35 000 g.mol^{-1}, tendance valide pour tous les autres conjugués greffés (Figure 7). Ce dernier résultat a prouvé qu'on pouvait contrôler la distance moyenne entre les chromophores et la surface des AuNP *via* le polymère.

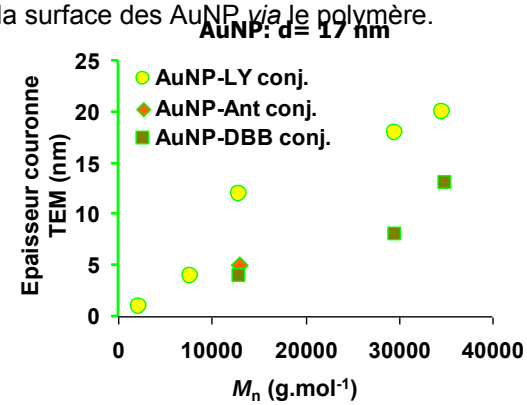

Figure 7: Influence de la longueur de la chaine de polymère et de la nature du chromophore sur l'épaisseur de la couronne mesurée par TEM.

Le chapitre 4 est centré sur les propriétés photophysiques des conjugués et des nanoparticules greffées avec ces conjugués. Deux questions importantes sont investiguées ici : l'influence de la

chaine de polymère sur les propriétés photophysiques des chromophores couplés, puis l'influence des AuNP (résonance plasmonique).

Dans un premier temps, on a montré que les spectres d'émission et d'absorption des conjugués polymère-chromophores sont similaires à ceux des chromophores libres dans le même solvant. Une diminution du rendement quantique de fluorescence des conjugués est enregistrée quand la densité de chromophores par chaine augmente et quand les interactions intrachaine entre les chromophores voisins sont plus fortes (notamment dans les cas des chromophores hydrophobes) (Tableau 2).

Tableau 2: Les propriétés photophysiques des conjugués polymère-chromophores Ant dans le chloroforme.

Chromophore *vs.* Conjugués dans le $CHCl_3$	**Section efficace TPA (GM)**	**ε ($cm^{-1}.M^{-1}$)**	**ϕ (%)**	**Brillance ($cm^{-1}.M^{-1}$)**
Chromophore libre	420	33 000	**87**	28 700
6Ant-AEM	1 930	175 000	**76**	131 000
10Ant-AEM	4 340	341 000	**65**	221 700
21Ant-AEM	5 200	608 400	**42**	255 400

Les conjugués polymère-chromophores biphotoniques hydrosolubles ont des rendements quantiques de fluorescence très faibles en milieu aqueux (ϕ<5%) par rapport au chloroforme (Tableau 3). Néanmoins, la brillance et la section efficace d'absorption à deux photons après couplage sur le polymère sont très élevées dans l'eau, justifiant par la suite leur utilisation en milieu biologique (Tableau 3).

Tableau 3: Les propriétés photophysiques des conjugués polymère-chromophores Ant dans l'eau.

Conjugués Ant dans l'eau	**Section efficace TPA (GM)**	**ϕ (%)**	**Brillance ($cm^{-1}.M^{-1}$)**
6Ant-H	760	2	1 600
6Ant-AEM	840	5	4 800
10Ant-AEM	1270	2	2 400

Concernant l'influence des AuNP sur les propriétés photophysiques des conjugués greffés, il a été mis en évidence qu'après greffage des conjugués sur les AuNP de ~20 nm, leur fluorescence est quenchée probablement par un mécanisme de transfert d'énergie à la nanoparticule. Cependant, il a été également montré que le quenching à la surface des AuNP peut être contrôlé (diminué ou même évité) en augmentant la longueur des chaines greffées, donc la distance entre les chromophores et la surface d'or. Dans le cas des conjugués polymère-chromophores LY, la fluorescence des conjugués greffés a augmenté de 10% à 90% quand la masse molaire des polymères a augmenté de ~2 000 $g.mol^{-1}$ à ~30 000 $g.mol^{-1}$ (Figure 8). Contrairement aux conjugués LY, la fluorescence des conjugués polymère-chromophores Ant biphotoniques, greffés sur les AuNP de ~20 nm, étaient entièrement quenchée dans l'eau, tandis que celle des conjugués DBB greffés était plus élevée grâce aux masses molaire plus élevées de ces conjugués.

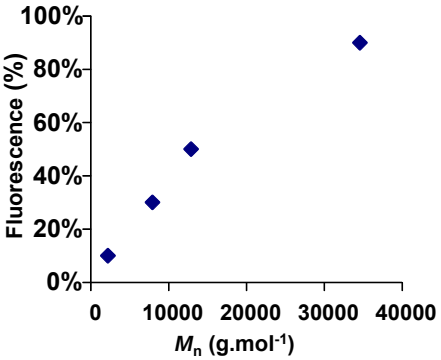

Figure 8: Influence de la longueur des chaines sur l'émission de fluorescence des conjugués polymère-chromophores LY greffés à la surface des AuNP de ~20 nm.

En outre, la capacité de produire de l'oxygène singulet a été également mise en évidence pour les conjugués DBB en quantifiant leurs rendements quantiques de génération de cette espèce cytotoxique dans le chloroforme (Φ_Δ=0.47), justifiant ainsi leur potentiel pour la PDT.
Dans ce contexte, d'autres résultats préliminaires obtenus en collaboration avec J. Navarro indiquent que les AuNP de plus grandes tailles et de différentes formes (nanobatônnets, nanobipyramides) pourraient exalter plus efficacement les propriétés photophysiques des chromophores situés dans leur proximité.

Enfin, le chapitre 5 évalue les propriétés biologiques des conjugués polymère-chromophores biphotoniques avant et après leur greffage sur les AuNP. On montre qu'après couplage sur les polymères l'internalisation des chromophores est significativement améliorée (Figure 9). De plus, les conjugués polymère Ant et DBB se sont révélés non-toxiques pour les cellules à la concentration utilisée (10^{-5} mol. L^{-1} chromophore).[12]

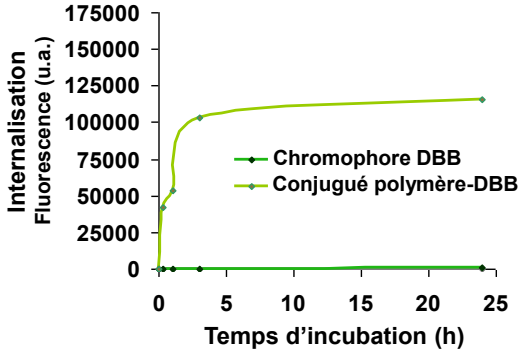

Figure 9: L'internalisation cellulaire (déterminée par cytométrie en flux) d'un conjugué polymère-DBB *vs.* l'internalisation du chromophore DBB libre solubilisé dans le DMSO (concentration=10^{-5} mol. L^{-1} chromophore).

On met en évidence dans ce chapitre que les conjugués Ant et les conjugués DBB peuvent être visualisés à l'intérieur des cellules de mélanome par microscopie de fluorescence sous excitation à un photon et à deux photons (Figure 10), prouvant ainsi leur potentiel pour les applications de bioimagerie.[12]

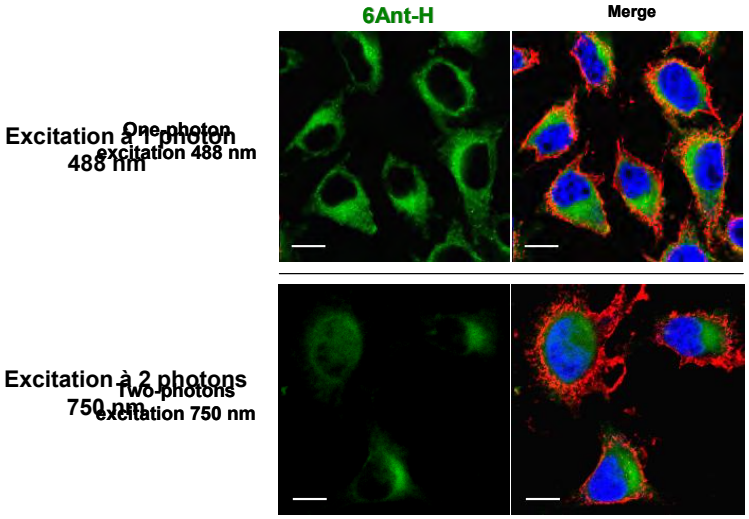

Figure 10: Imagerie de fluorescence à 1 photon (au-dessus) et à 2 photon (en dessous) du conjugué 6Ant-H. Les cellules de melanome B16-F10 ont été cultivées pendant 24 h en présence du conjugué (à 10^{-5} mol.L^{-1} chromophore). La membrane plasmique (rouge) et le noyau (bleu) ont été visualisés à 488 nm. Le conjugué (vert) est détecté à 1 photon avec une excitation à 488 nm et à 2 photons avec une excitation à 750 nm. La barre d'échelle est 10 µm.

A la fin de ce chapitre, la capacité des conjugués DBB et des nanoparticules greffés d'induire efficacement (>90%) la mort des cellules cancéreuse a été mise en évidence par des tests de phototoxicité à un photon.[12]

Ces premières études biologiques *in cellulo* représentent une preuve de concept du potentiel biologique des sondes fluorescentes synthétisées au cours de ce travail. Les expériences futures consisteront à évaluer la mort photoinduite sous excitation à 2 photons en présence des dérivés DBB et à investiguer leur potentiel *in vivo*.

Pour conclure, ce manuscrit rapporte de manière détaillée les différentes étapes qui ont amené à obtenir des nano-objets hybrides, composés d'un cœur d'or et d'une couronne de conjugués polymère-chromophores biphotoniques. Les propriétés physicochimiques, photophysiques et biologiques de ses objets sont discutées et analysées, servant à donner des éléments de réponse pour trouver la structure optimale présentant la meilleure efficacité dans les milieux biologiques.

Références

[1] **Photosensitized singlet oxygen and its applications,** M. C. DeRosa, R. J. Crutchley, *Coordin. Chem. Rev.* **2002**, *233/234*, 351-371.

[2] **Imaging and Photodynamic Therapy: Mechanisms, Monitoring, and Optimization,** J. P. Celli, B. Q. Spring, I. Rizvi, C. L. Evans, K. S. Samkoe, S. Verma, B. W. Pogue, T. Hasan, *Chem. Rev.* **2010**, *110(5)*, 2795-838.

[3] **Two-Photon Singlet Oxygen Sensitizers: Quantifying, Modeling, and Optimizing the Two-Photon Absorption Cross Section,** T. D. Poulsen, P. K. Frederiksen, M. Jùrgensen, K. V. Mikkelsen, P. R. Ogilby, *J. Phys. Chem. A* **2001**, *105*, 11488-11495.

[4] **Two-Photon Absorption and the Design of Two-Photon Dyes,** M. Pawlicki, H. A. Collins, R. G. Denning, H. L. Anderson, *Angew. Chem. Int. Ed.* **2009**, *48*, 3244-3266.

[5] a) **Multi-functional polymeric nanoparticles for tumour-targeted drug delivery,** L. E van Vlerken, M. M. Amiji, *Expert Opin. Drug Deliv.* **2006**, *3(2)*, 205-216.

b) **Nanoparticle Delivery of Cancer Drugs,** A. Z. Wang, R. Langer, O. C. Farokhzad, *Annu. Rev. Med.* **2012**, *63*, 185-198.

[6] a) **Pharmaceutical Polymeric Controlled Drug Delivery Systems,** M. N. V. Ravi Kumar, N. Kumar, A. J. Domb, M. Arora, *Adv. Polym. Sci.*, Vol. *160*, Springer-Verlag Berlin Heidelberg **2002**, 46-117.

b) **Nanonization strategies for poorly water-soluble drugs,** Huabing Chen, Chalermchai Khemtong, Xiangliang Yang, Xueling Chang, Jinming Gao, *Drug Discov. Today* **2010**, *16(7-8)*, 354-360.

[7] **Gold Nanoparticles for Biology and Medicine,** D. A. Giljohann, D. S. Seferos, W. L. Daniel, M. D. Massich, P. C. Patel, C. A. Mirkin, *Angew. Chem. Int. Ed.* **2010**, *49*, 3280-3294.

[8] **Chromophore à absorption biphotonique pour l'imagerie et la photothérapie dynamique : synthèse, vectorisation, greffage sur nanoparticules d'or et propriétés spectroscopique,** T. Gallavardin, PhD **2010**, Laboratoire de Chimie ENS de Lyon.

[9] **Lucifer dyes. Highly fluorescent dyes for biological tracing,** W. W. Stewart, *Nature* **1981**, *292*, 17–21.

[10] a) **PhD, "Water-soluble associative polymers: synthesisi and photophysical of poly(*N*,*N*-dimethylacrylamide) and poly(*N*-acryloylmorpholine)", 2006**, P. Relogio, Instituto Superior Técnico Lisboa.

b) **Fluorescent Polymers Soluble in an Aqueous Solution and a Method for the Production Thereof,** M.-T. Charreyre, B. Mandrand, J. M. G. Martinho, P. Relogio, J. P. Sequeira Farinha, Patent Application WO/2007/003781, **2006**, PCT/FR2006/001544.

[11] a) **Photodynamic therapy and two-photon bio-imaging applications of hydrophobic chromophores through amphiphilic polymer delivery,** T. Gallavardin, M. Maurin, S. Marotte, T. Simon A.-M. Gabudean, Y. Bretonnière, M. Lindgren, F. Lerouge, P. L. Baldeck, O. Stéphan, Y. Leverrier, J. Marvel, S. Parola, O. Maury, C.l Andraud, *Photochem. Photobiol. Sci.* **2011**, *10(7)*, 1216-1225.

b) **Water-soluble chromophores with star-shaped oligomeric arms: synthesis, spectroscopic studies and first results in bio-imaging and cell death induction,** C. Monnereau , S. Marotte , P.-H. Lanoë, O. Maury , P. L. Baldeck , D. Kreher , A. Favier , M.-T. Charreyre, J. Marvel, Y. Leverrier, C. Andraud, *New J. Chem.* **2012**, *36*, 2328-2333.

[12] **Biocompatible well-defined chromophore–polymer conjugates for photodynamic therapy and two-photon imaging,** C. Cepraga, T. Gallavardin, S. Marotte, P.-H. Lanoë, J.-C. Mulatier, F. Lerouge, S. Parola, M. Lindgren, P. L. Baldeck, J. Marvel, O. Maury, C. Monnereau, A. Favier, C. Andraud, Y. Leverrier, M.-T. Charreyre, *Polym. Chem*. **2013**, *4(1)*, 61-67.

Abbreviations

Ant	Anthracene
AuNP	Gold nanoparticles
CTA	Chain transfer agent
DBB	Dibromobenzene
DLS	Dynamic light scattering
^{1}H NMR	^{1}H Nuclear magnetic resonance spectroscopy
DOSY NMR	Diffusion ordered NMR
FRET	Förster (Fluorescence) resonance energy transfer
LY	Lucifer Yellow cadaverine
NAM	*N*-acryloyl morpholine
NAS	*N*-acryloxy succinimide
Nc	Number of chromophores *per* polymer chain
NearIR	Near Infra Red
NP	Nanoparticles
RAFT	Reversible Addition-Fragmentation Chain Transfer polymerization
PDT	Photodynamic therapy
P(NAM-co-NAS)	Poly[*N*(acryloyl morpholine)-*co*-*N*(acryloxy succinimide)]
SEC/UV	Size exclusion chromatography coupled with a UV-Vis detector
SPR	Surface plasmon resonance
*t*BDB	*Tert*-buthyl dithiobenzoate
TEM	Transmission electron microscopy
TGA	Thermogravimetric analysis
TP	Two-photon
TPA	Two-photon absorption
TPE	Two-photon excitation
TPEF	Two-photon excited fluorescence

Table of contents

General Introduction

During the last years, it has been extensively shown that materials at the nano-scale present many unique properties which may be useful for different kinds of applications in the biomedical sciences. This discovery offers multiple opportunities to conceive innovative complex nanodevices with promising future in therapy, diagnostic and theragnostic applications, especially for cancer treatment.[1] In this work we focus on developing new nano-systems for photodynamic therapy (PDT) and bioimaging applications.

PDT is an alternative treatment for cancer, aiming to induce death of cancer cells by using a localized light activation of drugs, called photosensitizers (PS), accumulated in tumors. Compared to other currently practiced cancer treatments as chemotherapy, radiotherapy or surgery, PDT has no long-term side effects and is considered a minimally invasive treatment, thanks to the precise localization of the light excitation, allowing spatial targeting of tumors.[2] In parallel to PDT, the development of novel bioimaging agents has been carried out to visualize and monitor the tumor treatment.

These two applications, optical imaging of tumors and treatment by PDT, require the use of chromophores – organic or organometallic molecules capable to absorb light at a certain wavelength. The excited chromophores can be used for fluorescence imaging (fluorophores) or for PDT (photosensitizers) if they are able to react with molecular oxygen in order to produce cytotoxic species (*e.g.* singlet oxygen[3]) (Figure 1). Because some chromophores can exhibit both fluorescence emission and singlet oxygen generation, they could be used as dual agents to simultaneously treat and visualize the tumor.

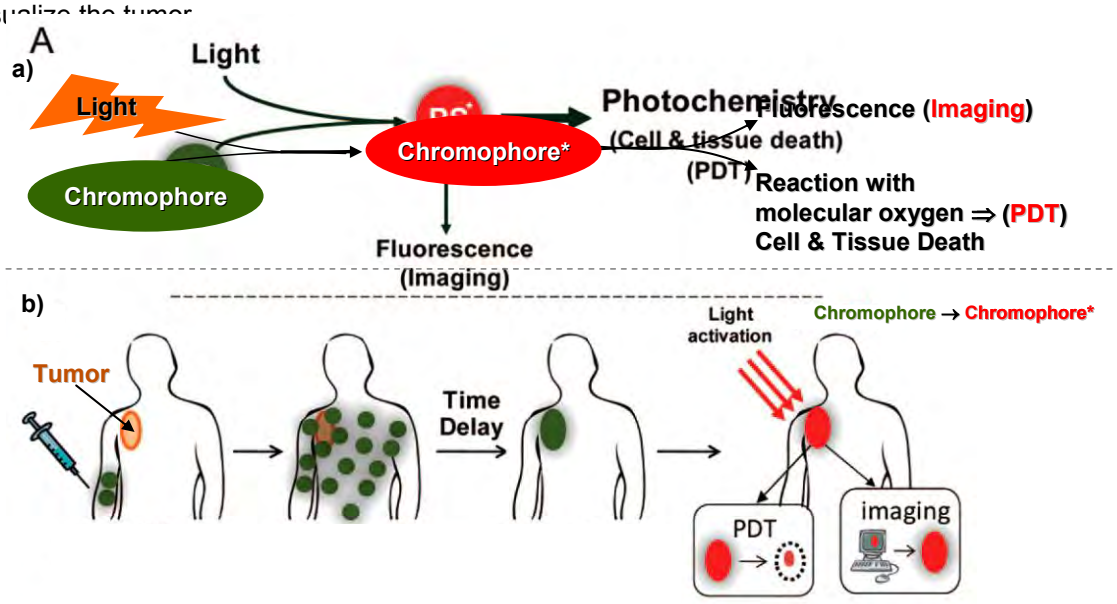

Figure 1: a) Schematic representation of a chromophore (fluorophore or photosensitizer) after light activation (Chromophore*) which can serve as a fluorescent agent (imaging) and/or a therapeutic agent (PDT); b) Schematic representation of the sequence of administration, localization, and light activation of the chromophore for PDT and fluorescence imaging.[4]

In practice, the most currently used molecular chromophores for such applications can absorb light in the UV-Vis spectral range. However, autofluorescence and scattering coming from biological tissues are high at these wavelengths. Moreover, UV-Vis light penetration into tissues is limited to only ~1-2

mm. Consequently, the development of new molecular chromophores, exhibiting non-linear two-photon absorption (TPA) properties in the NearIR region, came as a promising solution in order to increase the penetration depth into tissues and overcome the limitations mentioned above.[5 6]
TPA phenomenon, localized in ~1μm^3 excited zone, displays the following characteristics and advantages:

- excitation inside the NearIR region, which limits the scattering, the absorption and the autofluorescence of the biological tissues;
- increased penetration depth into tissues (by a factor 2-3 compared to that under one photon excitation);
- a 3D resolution of the excited area;
- decreased photo-damage due to limited out-of-focus excitation.

Despite the numerous advantages offered by two-photon (TP) chromophores (fluorophores and photosensitizers), they are generally strongly hydrophobic molecules, difficult to use in bio-relevant media. During the last couple of decades, many efforts have been done to improve the pharmacokinetics of water-insoluble molecular drugs, by associating them with water-soluble and biocompatible carriers.[7] Many of existing strategies include the use of polymers: polymer micelles or dispersant agents (*e.g.* Pluronic®), polymer nanoparticles, dendrimers, linear water-soluble polymers. The use of polymers has been shown to improve the biological efficacy of drugs by increasing their solubility and stability in biological media, decreasing their toxicity, along with improving the drug loading capacity and controlling the drug release.[8]

On the other hand, there is a growing importance of gold nanoparticles (AuNP) in biology, thanks to their ease of synthesis and functionalization, biocompatibility, low toxicity, ease of detection in biological media, and their capacity to be easily dispersed in aqueous media. Based on their unique optoelectronic characteristics resulting from the localized Surface Plasmon Resonance (SPR), AuNP are ideal candidates for many diagnostic and therapeutic applications: imaging, sensing, drug/gene delivery.[9]
However, due to the strong electromagnetic field created by the SPR, AuNP can alter the photophysical properties of chromophores located in close proximity to their surface: for instance, the fluorescence can either be quenched or enhanced. Many theoretical studies (and few experimental ones) show that an optimized distance between chromophores and AuNP surface can tremendously improve the performance of chromophores.
To the best of our knowledge, there is no example which successfully combines the properties of AuNP, with those of two-photon chromophores. During a previous PhD project completed by T. Gallavardin in 2010,[10] it has been demonstrated that in organic media TP chromophores can have their photophysical properties completely quenched after direct grafting onto AuNP. As a continuation to these findings, our strategy was based on using linear multifunctional polymers, with controlled architecture (synthesized by RAFT polymerization), in order to increase and control the distance between TP chromophores (bound on lateral positions along the polymer chain), and AuNP surface.

The expertise of different research teams: organic Chemistry – C. Andraud's team; inorganic Chemistry – S. Parola's team; polymer Chemistry – M.-T. Charreyre's team; Spectroscopy – P. L. Baldeck and M. Lindgren; Physics – J. Lermé, Biology – J. Marvel and Y. Leverrier, were combined and led to the implementation of this thesis, which was carried out in the framework of the ANR P3N nanoPDT project.

The goal of this project was to elaborate well-defined hybrid nano-probes (Figure 2) – composed of two-photon chromophores, water-soluble polymer chains and gold nanoparticles (AuNP) – and evaluate their potential for bioimaging and photodynamic therapy (PDT) applications.

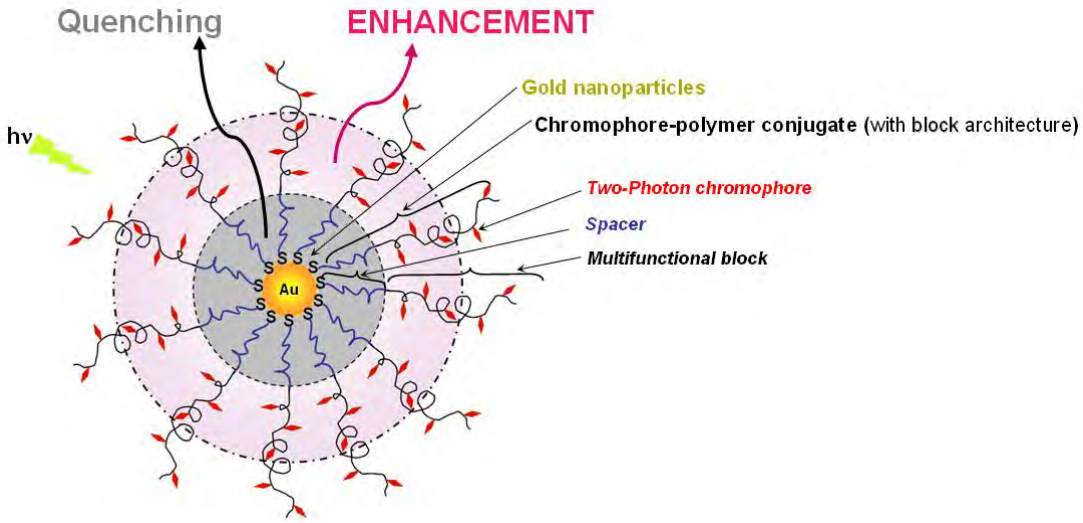

Figure 2: The hybrid nano-probes platform designed during the course of this work, composed of: gold nanoparticles, functionalized with Two-Photon chromophore-polymer conjugates. The Two-Photon chromophore-polymer conjugates have a block structure, displaying a 1st block (spacer) used to increase the distance between chromophores and AuNP surface.

In this work, we will focus, in a first step, on linear chromophore-polymer conjugates resulting from the binding onto the reactive sites of a water-soluble linear copolymer chain P(NAM-*co*-NAS) – based on *N*-acryloylmorpholine (NAM) and *N*-acryloxysuccinimide (NAS) units – of one of the following three chromophores: Lucifer Yellow Cadaverine (LY) – commercial chromophore, two-photon chromophores with an anthracene core (Ant) or a dibromobenzene core (DBB). Oriented grafting of these different conjugates on the gold surface (*via* their thiol end-group) will be investigated, using spherical AuNP as a simple model system.

This particular type of hybrid nano-particles can be optimized to obtain an efficient response in living cells by separately tuning the desired properties of the inorganic Au core (size, shape, thus SPR properties), and those of the organic chromophore-polymer shell (length and architecture of the polymer chain, chromophore density, charge). A synergy is expected when chromophores are located at an optimized distance from the AuNP surface, triggering an enhancement of their photophysical response, hence an increase of fluorescence intensity (bioimaging) or cytotoxicity (PDT).
The role of each component of the nano-probe described above is summarized in Table 1.

Table 1: The key-advantages of each element composing the hybrid nano-probes designed during this project.

Element	Role
Two-photon chromophores	○ increase the signal-to-noise ratio thanks to NearIR excitation; ○ treat and image the tumors deeper into the tissues; ○ control the treatment site *via* localized TPA process, thus decrease the photodamage.
Two-photon chromophore-polymer conjugates	○ ensure water-solubility and biocompatibility to hydrophobic molecular chromophores; ○ carry multiple chromophores, thus increase the local concentration of chromophores; ○ finely control the number of chromophores along the chain and their distance from the AuNP surface, thanks to the use of the RAFT polymerization process; ○ enable end-group oriented grafting onto AuNP.
AuNP	○ ensure biocompatibility and stability in biological media; ○ carry multiple conjugates, thus increase even more the local concentration of chromophores; ○ potentially enhance the optical properties of chromophores *via* SPR.

Stepwise, the objectives of this thesis were to:

- investigate the coupling of hydrophobic chromophores along the reactive P(NAM-*co*-NAS) copolymer chains;
- characterize the properties of the resulting chromophore-polymer conjugates (water-solubility, brightness);
- optimize the grafting of RAFT polymers (conjugates) onto AuNP;
- investigate the distance-dependent photophysical properties of chromophores (chromophore-polymer conjugates) near AuNP;
- study the biological efficacy of these nano-probes for two-photon bioimaging and PDT applications.

Based on the latter enumerated objectives, this manuscript contains five chapters. An overview of the specific literature will be given in each one these chapters.

Chapter I summarizes the main classes of nano-platforms designed for therapeutic, diagnostic and sensing purposes, and discusses their multiple advantages for biomedical applications. At the end of this chapter, a special attention is given to the class of gold nanoparticles.

Chapter II focuses on the synthesis and the physicochemical characterization of two-photon chromophore-polymer conjugates. The synthesis of copolymer chains by RAFT copolymerization is first introduced, then the covalent coupling of chromophores on these copolymer chains is described.

Chapter III discusses first the optimized grafting of RAFT (co)polymers (synthesized in Chapter II) onto AuNP. In a second part, the grafting of water-soluble two-photon chromophore-polymer conjugates (synthesized in Chapter II) onto 20nm diameter AuNP is studied.

Chapter IV reports the photophysical properties of chromophore-polymer conjugates before and after their grafting onto AuNP.

Ultimately, Chapter V presents the first *in cellulo* studies of chromophore-polymer conjugates and of AuNP functionalized with these conjugates, with respect to their potential for two-photon bioimaging and PDT.

The main conclusions and possible outlooks of this work are summarized and suggested at the end of this manuscript.

References

[1] **Engineered Nanoparticles in Cancer Therapy,** N. P. Praetorius T. K. Mandal, *Recent Pat. Drug Deliv. Formul.* **2007**, *1*, 37-51.

[2] a) **Photodynamic therapy – A strategic review,** R. Malik, A. Manocha, D. K. Suresh, *Indian J. Dent. Res.* **2010**, *21*, 285-291.

b) **Photodynamic therapy: a review of the literature and image documentation,** M. C. Almeida Issa, M. Manela-Azulay , *An. Bras. Dermatol.* **2010**, *85(4)*, 501-511.

[3] **Photosensitized singlet oxygen and its applications,** M. C. DeRosa, R. J. Crutchley, *Coordin. Chem. Rev.* **2002**, *233/234*, 351-371.

[4] **Imaging and Photodynamic Therapy: Mechanisms, Monitoring, and Optimization,** J. P. Celli, B. Q. Spring, I. Rizvi, C. L. Evans, K. S. Samkoe, S. Verma, B. W. Pogue, T. Hasan, *Chem. Rev.* **2010**, *110(5)*, 2795-838.

[5] **Two-Photon Singlet Oxygen Sensitizers: Quantifying, Modeling, and Optimizing the Two-Photon Absorption Cross Section,** T. D. Poulsen, P. K. Frederiksen, M. Jùrgensen, K. V. Mikkelsen, P. R. Ogilby, *J. Phys. Chem. A* **2001**, *105*, 11488-11495.

[6] **Two-Photon Absorption and the Design of Two-Photon Dyes,** M. Pawlicki, H. A. Collins, R. G. Denning, H. L. Anderson, *Angew. Chem. Int. Ed.* **2009**, *48*, 3244-3266.

[7] a) **Multi-functional polymeric nanoparticles for tumour-targeted drug delivery,** L. E. van Vlerken, M. M. Amiji, *Expert Opin. Drug Deliv.* **2006**, *3(2)*, 205-216.

b) **Nanoparticle Delivery of Cancer Drugs,** A. Z. Wang, R. Langer, O. C. Farokhzad, *Annu. Rev. Med.* **2012**, *63*, 185-198.

[8] a) **Pharmaceutical Polymeric Controlled Drug Delivery Systems,** M. N. V. Ravi Kumar, N. Kumar, A. J. Domb, M. Arora, *Adv. Polym. Sci.*, Springer-Verlag Berlin Heidelberg **2002**, *Vol.160*, 46-117.

b) **Nanonization strategies for poorly water-soluble drugs,** H. Chen, C. Khemtong, X. Yang, X. Chang, J. Gao, *Drug Discov. Today* **2010**, *16(7-8)*, 354-360.

[9] **Gold Nanoparticles for Biology and Medicine,** D. A. Giljohann, D. S. Seferos, W. L. Daniel, M. D. Massich, P. C. Patel, C. A. Mirkin, *Angew. Chem. Int. Ed.* **2010**, *49*, 3280-3294.

[10] **Chromophores à absorption biphotonique pour l'imagerie et la photothérapie dynamique : synthèse, vectorisation, greffage sur nanoparticules d'or et propriétés spectroscopiques,** T. Gallavardin, PhD **2010**, Laboratoire de Chimie ENS de Lyon.

Chapter I: Nanoparticles in biology and medicine

I.1. Introduction

Nanoscience is based on the fact that properties of materials change as a function of their physical dimensions.[1] The dimension at which changes in properties are observed depends on the specific material and on the considered property. However, most of those changes are usually observed at the nanoscale, generally between 1 and 100 nm, the reason why the prefix ”nano” is conventionally used. Compared to materials at the macroscopic scale, easily described and predicted by fundamental physical laws, unexpected properties of nanomaterials are governed by quantum effects and are very sensitive to structural parameters. Nanomaterials exhibit therefore unique physicochemical characteristics such as high surface area to volume ratio, high reactivity, and tunable intrinsic properties (physical, electronic, optical etc.). The development of nanoscience in the last decades, dedicated to better understand, control, and predict the properties of materials at the nanoscale, strongly contributed to the current progress in the emerging field of nanobiotechnology.[2 3]

These unique characteristics of nanomaterials are being explored in many fields of modern technology (photonics, electronics, mechanics etc.). Among them, a special interest is given to biology and medicine, since the majority of biological processes occur at the nanoscale (Figure I. 1). Nanoscience gives scientists new ideas to create nanodevices for more precise and personalized treatments, in order to overcome some limitations found in traditional biological and medical applications.[4 5 6]

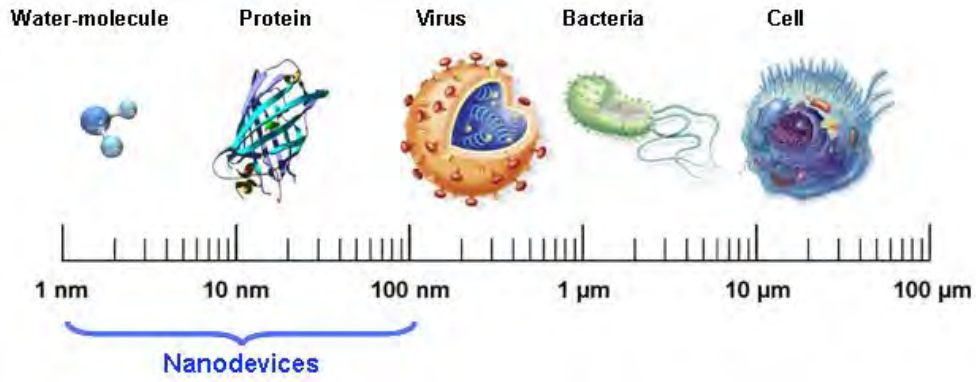

Figure I. 1: Size regime of most nanodevices compared to the size of various species encountered in biological media.

The field of nanobiotechnology has been exponentially increasing during the last decade: the number of publications in this area increased from 11 in 1991 (Web of Science) up to tens of thousands nowadays, thus becoming really difficult to exhaustively cover it all.

However, taking into account the topic of our project, is seemed important to describe the existing nano-platforms and their applications in biology and medicine (Section I.2), followed by a specific part on the class of gold nanoparticles (AuNP), as promising materials for the future of nanomedicine (Section I.3).

I.2. Diversity of nano-platforms used in biological applications

Over the last two decade, different nano-platforms were studied for their use in diagnosis and therapy, particularly in cancer treatment. Due to their increased size compared to molecular systems, nanomaterials can specifically accumulate at tumor sites *via* an enhanced permeability and retention effect (EPR).[7] Therefore, their main role is to protect the drugs from rapid metabolism and clearance, as well as nonspecific recognition and distribution.

Many of those nanomaterials are multimodal systems, allowing the combination of multiple agents (drugs, genes, biological ligands, imaging agents and/or targeting groups) in one single system and are used for targeted treatment,[8 9] drug delivery,[10] and/or imaging applications.[11] More details on the characteristics and the applications of various nano-platforms can be found in the recent reviews listed in Table I. 1. Because the most of them are usually designed for both therapy and diagnosis – the two major categories in the clinical treatment of disease, they are referred as theranostic (or theragnostic) agents. Their design and their properties combine concepts of physics, chemistry, and biology. The main classes of nano-platforms designed for therapy and/or diagnosis biomedical applications are summarized in Table I. 1.

Table I. 1: Nano-platforms and their biological applications.

Chemical nature	Type of systems	Applications	Ref.
Organic	**Liposomes**	Biocompatible carriers for molecular imaging and therapy agents	12
	Polymeric nano-platforms - polymer micelles - polymer nanoparticles - water-soluble polymer chains - dendrimers	Biocompatible carriers for molecular imaging and therapy agents Can also be biodegradable	13 14 15 16 17 18 19
Inorganic (hybrid)	**Silica-based nanoparticles**	Biocompatible carriers for molecular and inorganic imaging and therapy agents	20
	Quantum dots	Fluorescent agents for imaging and diagnosis	21
	Magnetic nanoparticles	Magnetic imaging agents Magnetic hyperthermia	22
	Noble metal nanoparticles	Imaging agents Pt: catalytic properties Ag: antimicrobial effect Au: hyperthermia	23

The designing strategies[24] for such materials at the nanoscale are ensured by the well-established chemical routes (“bottom-up” strategy), but can also be carried out by removing matter from the bulk material until obtaining the desired nanostructure (“top-down” strategy).[25] Yet, this will not be the purpose here. A brief description of organic and inorganic (hybrid) nano-platforms will be given as follows.

I.2.1. Organic nano-platforms

Organic nano-platforms[26] for therapy and diagnosis, including liposomes, polymeric nano-platforms and dendrimers, are extensively used for drug delivery, targeting, therapy and diagnosis applications, as they can encapsulate drugs with high loading efficiency and protect them from undesired effects of external conditions.

A brief overview on each one of those nano-platforms will be discussed below.

I.2.1.1. Liposomes

Liposomes are artificial, single, or multilaminar vesicles made with bilayered membrane structures, composed of natural or synthetic amphiphilic lipid molecules (Table I. 1). As drug delivery carriers, liposomes exhibit several unique properties including biocompatibility, long systemic circulation half-life, and ease of surface modification.[27]

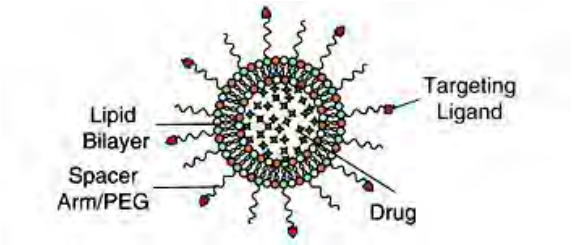

Figure I. 2: Example of liposome platforms embedding drug molecules inside the vesicles, and functionalized with poly(ethylene glycol), PEG, arms and targeting ligands. [26]

Liposomal drugs were the first nanotherapeutics to get FDA (Food and Drug Administration) approval for clinical use in 1995 with DOXIL® (doxorubicin liposomes). Since then, many other liposome based drugs have been developed for clinical use.[26]

While liposomal platforms are mainly explored for drug delivery applications, they do not readily allow for controlled release of therapeutic molecules, a significant shortcoming of this class of nano-platforms.

I.2.1.2. Polymeric nano-platforms

Polymeric nano-platforms have received great interest due to the versatility in which their structures can be modified to package and deliver the bio-active cargoes to the desired site of action, or to respond to specific physiological or external stimuli.[13]

The variety of chemistry involved in designing polymeric nano-platforms allowed them to be equipped with smart components conferring unique properties (stimuli responsiveness,[28] multivalency,[29] bio-mimicking and self-assembly[30] etc.) for more efficient *in vitro* and *in vivo* results.[31]

From the structural point of view, three classes of polymeric nano-platforms were distinguished here (Figure I. 3): polymer micelles, polymer nanoparticles (NP), water-soluble multivalent polymer chains.

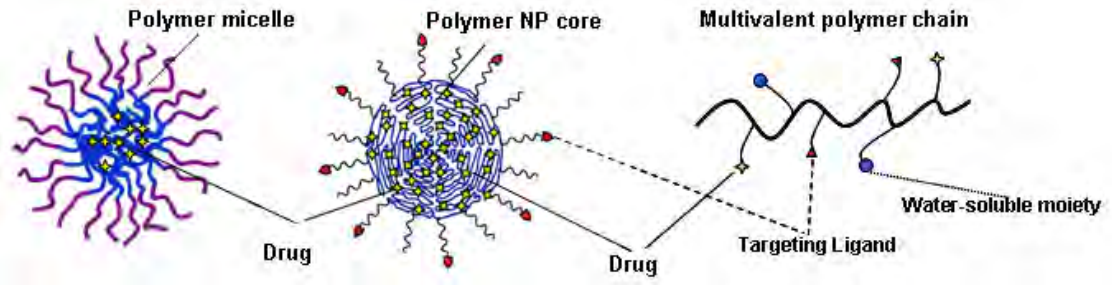

Figure I. 3: Examples of polymer nano-platforms: (left) polymer micelles loaded with hydrophilic drugs; (middle) polymer nanoparticles (NP) conjugated with drugs and targeting ligands; (right) polymer bio-conjugate composed of a multivalent polymer chain carrying drugs, targeting ligands and water-soluble moieties. [26]

Polymer micelles

Polymeric micelles are formed *via* the self-assembly of amphiphilic polymers with two or more polymer chains of different hydrophobicity. In aqueous environment, these block copolymers spontaneously self-assemble into core-shell nanostructures, with a hydrophobic core and a hydrophilic shell. Hydrophobic molecular agents (drugs, imaging and/or targeting agents) can easily be loaded inside the hydrophobic core of the micelle (Figure I. 3).[15]

Up to date, several polymeric micelles have reached different stages of clinical development, demonstrating enhanced accumulation of therapeutic agents at the target sites and reduced their adverse effects. The greatest drawback to overcome with these systems is the still immature control of drug loading and release, coming along with non-negligible risks of drug leaking in biological media.[32]

Polymer nanoparticles (NP)

Polymer NP can be obtained, for example, by crosslinking of polymer chains, self-assembly techniques, various polymerization techniques.[33] Many biocompatible polymer nanoparticles have been developed to enhance the drug loading capacity and incorporate the control over drug delivery and release, by covalently linking the drugs onto the surface of multifunctional polymer nanoparticles (Figure I. 3).

The potential benefits of such delivery devices also include controlled and long-term release rates, prolonged bioactivity, reduced side effects, and the ability to deliver to the same site at once multiple therapeutic, imaging or targeting agents.[34]

Water-soluble polymer chains

Similarly to polymer NP, water-soluble polymer chains are multifunctional platforms referring to linear or branched polymers, covalently coupled with bio-active species – a system based on the Ringsdorf model.[35]

Polymer-drug conjugates obtained using such multifunctional polymer chains have made a significant clinical impact by improving the pharmaceutical efficacy and dosing of a variety of already approved

drugs. However, compared to polymer nanoparticles, their drug loading capacity may be limited by the number of conjugation sites along the polymer chain.[36]

Dendrimers

Dendrimers are synthetic, hyperbranched macromolecules with a well-defined chemical structure (Figure I. 4) (requiring arduous and expensive synthesis), consisting of a core and multiple layers with active terminal groups.[18] Like for other organic nano-platforms, their specific molecular structure enables multiple drugs loading *via* covalent conjugation to the multivalent surfaces or *via* encapsulation in the cavities of the dendrimer core through hydrophobic interactions, hydrogen bonds, or covalent bonds.[37] High loading capacity of dendrimers makes them very attractive as drug carriers, however controlling the release kinetics of the encapsulated drug is still a challenge, depending strongly on the hydrophobicity and the size of the drug, the generation number (the size) of the dendritic carrier, the type and the extent of dendrimer surface modification.

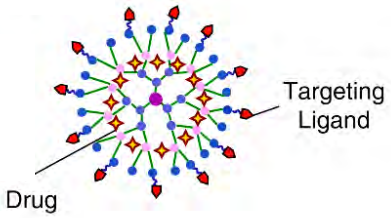

Figure I. 4: Example of dendrimer carrying molecular drugs, encapsulated inside the cavities, and targeting ligands covalently linked to the external functional groups.[26]

To conclude, the main role of organic nano-platforms is to protect and to safely deliver bio-active (molecular) agents to the desired biological sites.
While great progress has been done in precisely designing and controlling their structure, the study of their *in vitro* and *in vivo* behavior is still under active investigation.

I.2.2. Inorganic and hybrid nano-platforms

Compared to organic nanoparticles, inorganic nanoparticles exhibit more diverse and distinct physical properties depending on their size and composition, which could be used in multiple bio-related applications,[38] and more specifically in cancer therapy.[39]
Most of these nano-platforms are not purely inorganic, but hybrid inorganic-organic structures, with the organic part usually conferring complementary properties as water-solubility, bio-conjugation ability, bio-compatibility etc. The majority of such materials are multivalent nano-platforms.
Four classes could be distinguished here: silica-based nanoparticles, magnetic nanoparticles, quantum dots and Noble metal nanoparticles.

I.2.2.1. Silica-based nanoparticles

Thanks to its biocompatibility, availability to chemical or physical modification, and mechanical properties, silica has been widely used by many researchers as carriers for drug delivery purposes.[40] Recently, specific mesoporous silica NP (MSNP), also considered as gate-keepers, have been used as an attractive tool for imaging and drug delivery applications (Figure I. 5).[20 41] Their high porosity, resulting in a very large surface area, enables a high loading capacity, while protecting the 'guest molecules' from the external environment. Moreover, these systems can be modulated to regulate the local release of loaded drug molecules. The multifunctional capacity of those MSNP holds a promising future as nano-platforms for target-specific therapy and/or diagnosis.[42 43]

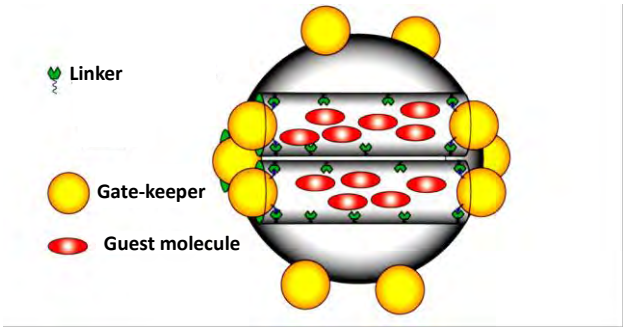

Figure I. 5: Representation of an MSNP loaded with guest molecules and end-capped with a general gate-keeper.[40]

I.2.2.2. Magnetic nanoparticles

Magnetic NP can be manipulated by a magnetic field and are used to enhance the Magnetic Resonance Imaging (MRI) signal.[44] They can also act on a molecular level as magnetic switches to control cell signaling and functions (*e.g.* angiogenesis related cellular growth), or trigger magnetic hyperthermia (*e.g.* cancer treatment).[45] The most explored magnetic NP aimed for biological applications are based on iron-oxide.[46]

Not only are these magnetic nanoparticles intrinsically functional, but can also be combined with other complementary imaging probes or drugs (*via* surface conjugation) for multimodal imaging applications and drug-delivery. An important advantage of magnetic nano-platforms relies in the lack of depth-penetration limit of the magnetic field in the human body, making them promising noninvasive devices for controlled drug release, imaging, and cell signaling applications (Figure I. 6).[22]

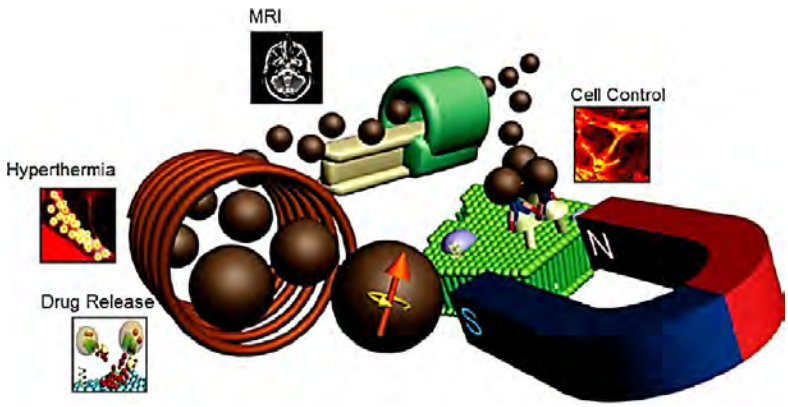

Figure I. 6: Schematic summary of biomedical applications with magnetic NP.[22a)]

I.2.2.3. Quantum dots

Quantum dots (QD) are nanocrystals composed of inorganic semiconductors which glow when stimulated by an external source of light. They are characterized by high molar extinction coefficients (~10–100 times higher than organic dyes), broad absorption spectra, narrow, symmetric and intense photoluminescence (PL) spectra in the UV-Vis/NearIR spectral range, large effective Stokes shifts, and high resistance to photobleaching with exceptional resistance to photo- and chemical degradation.[47]

Cellular labeling is where QD use has made the most progress. Compared with molecular fluorescent chromophores, QD have the unique ability to tune fluorescence emission and excitation spectra as a function of their core size. These unique properties make QD appealing as *in vivo* and *in vitro* imaging agents in investigations where traditional fluorescent labels fail to provide long-term stability and simultaneous detection of multiple signals.[48] [49]

Despite their benefits, QD may also present risks to human health and to the environment under certain conditions.[50] For example the gelatine capping on the surface of QD acts as a barrier towards the leaking of toxic ions from the core of QD.[51] In this context, the ability to make QD water-soluble, by coating them with water-soluble biocompatible ligands, has led to promising *in vivo* applications.[52] However, much work is still required to achieve reproducible surface functionalization and develop flexible bio-conjugation techniques.

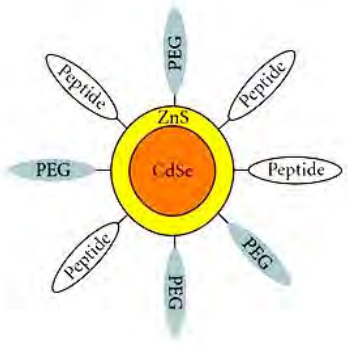

Figure I. 7: CdSe/ZnS core/shell quantum dots, functionalized with peptides and PEG moieties.

I.2.2.4. Noble metal nanoparticles

Noble metal NP, especially gold (Au), silver (Ag), are particularly interesting due to their size and shape dependent optoelectronic properties.[53] This behavior results from a strong absorption and scattering of light in the Visible/NearIR region, attributed to the phenomenon called Surface Plasmon Resonance[23] (SPR) or localized SPR, as it is confined close at the surface of the NP. SPR results from the resonant collective oscillation of surface electrons around the restoring force of the positively charged metallic lattice.

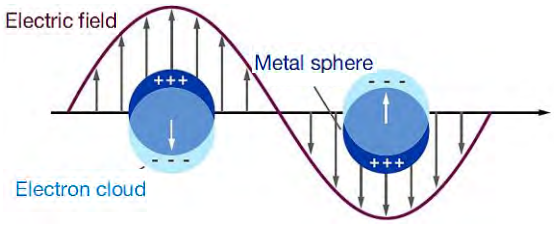

Figure I. 8: Schematic diagram of localized SPR. [54]

Colloidal solutions of those metals have been used for therapeutic purposes from ancient times.[23] Nowadays they find tremendous opportunities for sensing, imaging, manipulating and delivering biological molecules, thus provide a range of powerful tools for biological and medical studies:[55] sensing,[54] high-resolution imaging,[56] hyperthermia,[57] and as Surface Palsmon tweezers to selectively manipulate bio-specimens.[58]

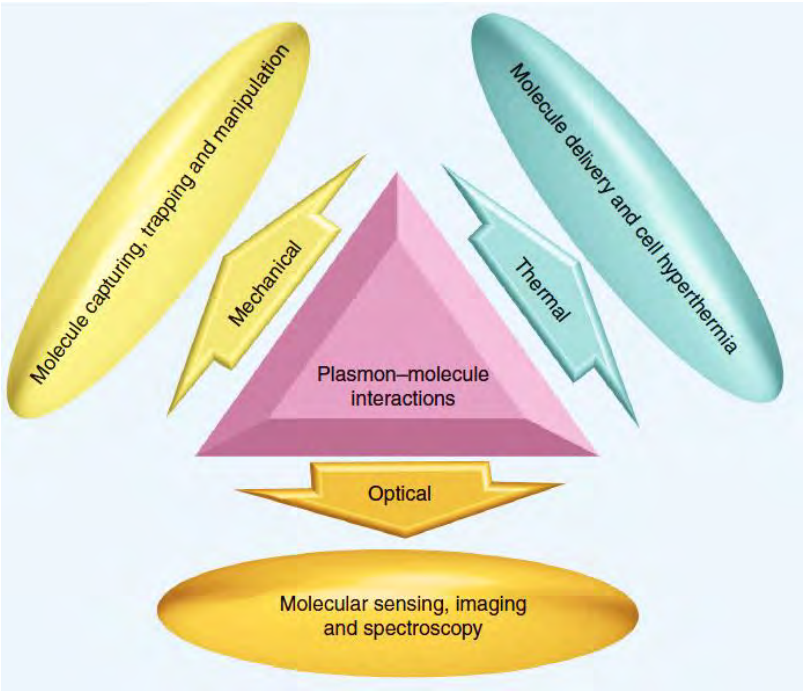

Figure I. 9: Scheme summarizing and structuring biological and nanomedical applications of SPR. Three types of molecule-plasmon interactions underpin emerging applications in biology and nanomedicine: optical, mechanical and thermal.[59]

Most of these properties will be discussed below, in the context of gold nanoparticles – the most used and studied Noble metal nanoparticles in biology.

Nanoscience and nanotechnology offers new opportunities to develop multivalent and multifunctional "smart" nanodevices. The ability to change their structural properties (size, shape), composition (organic, inorganic, hybrid), and functionality (adapted to various purposes: imaging, therapy, targeting, sensing) opens an access to a huge number of nano-platforms capable to propose customized solutions for many existing biomedical needs.[59]

I.3. Nano-platforms based on gold nanoparticles

The use of gold for medical purposes has been explored from ancient times by Chinese and Egyptians.[60] The first existing book on colloidal gold, containing information about its synthesis and applications in medicine was published in 1618 by Francisco Antonii, philosopher and doctor in medicine.[61] In spite of its old history, the use of gold nanoparticles (AuNP) in modern biomedical studies was developed during the last 40 years. Within this timeframe, researchers reached a good control and understanding over synthesis and stabilization of AuNP in terms of structure and composition. Studies over the last decade focus on providing relevant *in vitro* and *in vivo* data, as a reliable proof of the promising biomedical potential of AuNP.[62]

I.3.1. AuNP synthesis and surface functionalization

AuNP can be obtained by chemical or physical routes. During the last decades considerable efforts have been completed to achieve control over AuNP colloidal stability, size, shape, and surface functionalization.[63] [64] Numerous chemical and physical routes have been employed to synthesize AuNP: chemical reduction,[65] laser ablation,[66] UV-irradiation,[67] microwaves,[68] thermolysis,[69] digestive ripening,[70] ultrasonication[71] etc.[53]

The most known two chemical approaches for the preparation of spherical AuNP are Turkevich-Frens[72] and Brust-Schiffrin[73] methods involving the reduction of a gold salt precursor in solution (Au^{3+} → Au^0). Both methods allow to obtain AuNP ranging from ~2 nm (typical for Brust-Schiffrin method) up to 150 nm (Turkevich-Frens method). These approaches will be properly presented in Chapter III.

While most chemical and physical methods mentioned above are related to the well-known bottom-up strategy of generating nanostructured Au, several other top-down lithography techniques could also be used to obtain monodisperse AuNP with different sizes and shapes.[74]

Although, spherical AuNP are the most studied structures up to date, significant progresses have been made in synthesizing non-spherical AuNP, using seed mediated growth technique, (e.g. nanorods,

nanocubes, nanowires, nanopyramids, nanostars, nanoshells etc.)[60 75] (Figure I. 10), as they exhibit intense SPR (localized at edges), making them excellent candidates for SPR biological applications.

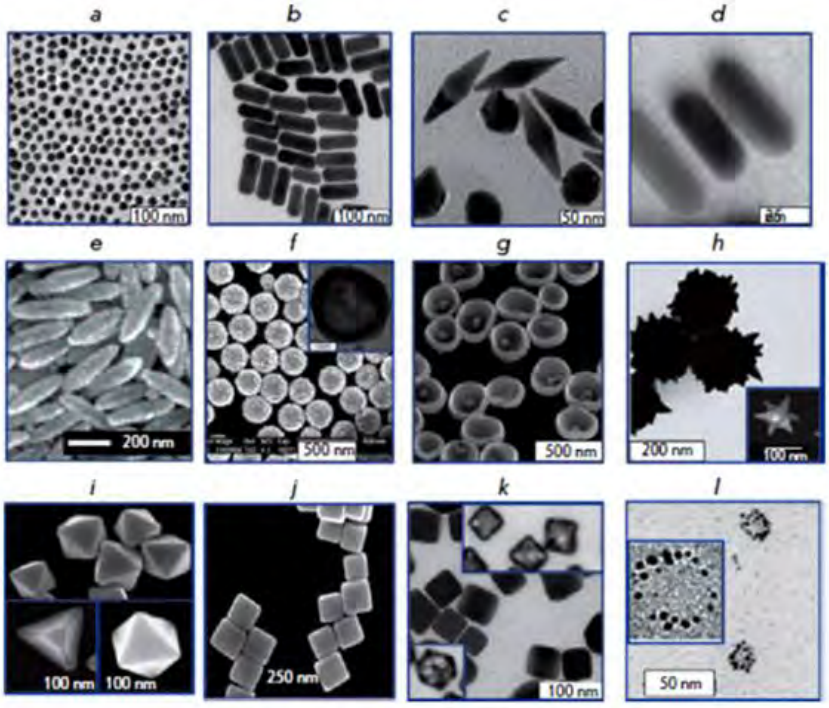

Figure I. 10: Various types of AuNP: a) 16nm spherical AuNP; b) Au nanorods; c) Au bipyramids; d) Au nanorods with silver coating; e) Nanorice – Fe_2O_3 nanorods covered by a Au nanoshell; f) Au nanoshell onto silica core; g) nanobowls, with Au seeds on the bottom; h) spiky nanoshell with SiO_2/Au shells (inset: star NP); i) polyhedral AuNP; j) Au nanocubes; h) Au-Ag nanocages; l) nanonecklaces.[60]

The stability of colloidal Au in solution is conferred by a shell of stabilizing ligands. The stabilization is ensured either by physical interactions (steric, electrostatic, adsorption), or chemisorption (usually attributed to sulfur-based ligands) on AuNP surface. The type of linkage is determined by the strength of interaction between the AuNP and the ligand. Therefore, the most used chemical groups for AuNP stabilization are phosphines, amines and sulfur-derivatives, the latter ones ensuring the strongest known interaction with Au.[76] In this context, various small molecular ligands,[76] polymers,[77] and biological entities[78] could serve to efficiently stabilize AuNP.

I.3.2. Size-dependent properties of AuNP

At the nanoscale, AuNP possess quantum size effects allowing to tailor their properties.

The most outstanding property of AuNP is the tunable Surface Plasmon Resonance (SPR), due to the light-triggered collective oscillation of surface electrons, resulting in a strong absorption band in the Visible/NearIR range and an enhancement of the local electric fields (Figure I. 11).

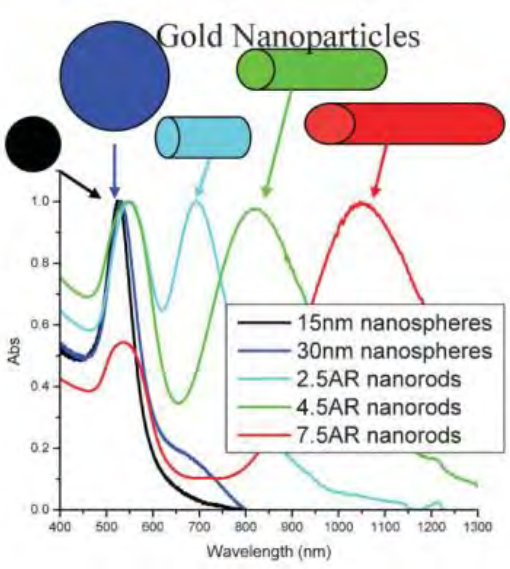

Figure I. 11: Gold nanoparticles – absorption of various sizes and shapes corresponding to the localized Surface Plasmon Resonance effect.[74]

Except the size and shape of AuNP, it has been shown using Mie theory that SPR is sensitive to the solvent and the ligand refractive indexes, as well as to the proximity of other nanoparticles. Therefore, a red-shift in the SPR band is recorded when aggregation of individual AuNP occurs, along with a sudden change in the solution color from red to purple-blue.[23a)]

The size and shape of AuNP influences not only the SPR maximum wavelength but also its intensity. AuNP are characterized by very high size-dependent extinction coefficients (ε), exceeding by several orders of magnitude those of molecular species (*e.g.* 20 nm AuNP have $\varepsilon_{525nm} \sim 10^{+9}$ $cm^{-1}.M^{-1}$).[79]

SPR can also influence the radiative processes of fluorescent chromophores placed in the vicinity of AuNP. In some cases, AuNP can act as fluorescence quenchers due to energy and/or electron transfer from the excited molecules to the AuNP surface.[23a)]

All these properties related to SPR are extensively used in many biological applications, some of them presented below.

I.3.3. Gold nanoparticles for biology

Biocompatibility, rich surface chemistry and remarkable SPR properties of AuNP place them among the most studied nanomaterials for biology and medicine. In this context, many research teams focused and still focus on understanding how and if AuNP are capable to cross the cellular barrier and whether they have a toxic effect on cells, essential properties for *in vivo* applications.

Before summarizing the biomedical applications based on the use of AuNP (*e.g.* sensing, imaging and therapy[80]), a small overview on the cell uptake and the toxicity of AuNP will be given in the next couple of pages.

Cell uptake of AuNP

Cellular uptake of AuNP with different sizes has been confirmed by many researchers using common cell lines. The parameters found to strongly influence the mechanisms of cell uptake are AuNP size, the chemical nature of surface ligands and the surface charge.[53]

Depending of the nature of ligands grafted to AuNP surfaces, the uptake can either be specific or non-specific.[78] The non-specific uptake is guaranteed by the AuNP larger size which favors AuNP accumulation inside cells compared to molecular species (EPR effect[7]). On the other hand, the specific uptake may be possible as AuNP surfaces can be easily functionalized with ligands interacting with specific receptors on the cell membranes (*e.g.* transferrin ligands which bind to membrane-linked transferrin receptors[81]). The mediated specific uptake is a huge progress in targeted cancer therapy and diagnosis. Along with cell uptake, current studies investigate also the biodistribution of AuNP, characterizing their fate in living systems.[82]

Cytotoxicity of AuNP

Due to the increased interest of AuNP in medical applications, an increase in studies concerning AuNP *in vitro* and *in vivo* cytotoxicity has been noted during the last 3-4 years. Although the existing studies show a large variety of experimental designs, including differences in analyzed AuNP size and shape, surface functionalization doses, type of cells, several general conclusions could still be deduced based mainly on *in vitro* studies:

- Influence of the size: AuNP with small sizes 1-2 nm were more toxic for cells as they could easily bind to bio-components, while AuNP with sizes larger than 15 nm showed no significant toxicity when incubated into cells.[83]
- Influence of the shape: In spite of their higher cell uptake, Au nanorods were shown to be more toxic than spherical AuNP, possibly partly due to the cationic surfactant stabilizing the rods.[84]
- Influence of the charge: Cationic AuNP exhibited a higher toxicity in cells (possibly due to the electrostatic binding with the negatively charged cell membranes), compared to no toxicity with negatively charged AuNP.[53]

A solution to decrease the toxicity of AuNP, while increasing their stability in biological medium and increasing their circulation time and accumulation capacity in tumors *vs.* healthy tissues, was to confer them “stealth” properties using highly biocompatible, water-soluble polymers as PEG (poly(ethylene glycol)).

Up to date, the few *in vivo* toxicity studies are still preliminary and rather inconsistent, requiring more investigation.

I.3.3.1. Biosensing

More than a half of biomedical applications with AuNP are related to biomedical sensing,* many of them with great potential in clinical diagnosis. In a recent article, most sensing applications with AuNP have been thoroughly reviewed and classified.[85]

The binding events with AuNP-based sensors (corresponding to changes in AuNP size, environment, and color or aggregation phenomenon) are accompanied by changes in the absorption spectrum (SPR) of AuNP solution, and can be easily detected visually, spectrophotometrically, or *via* dynamic-light scattering.

These specific properties of AuNP have been extensively used in clinical immunoassays to detect various biological molecules (antigens, antibodies, hormones, DNA, proteins etc.). The most familiar example of nanoparticles in sensing is the home pregnancy test, based on AuNP (d_{Au} < 50 nm) grafted with antibodies complementary to a pregnancy hormone. If the hormone is present in the urine, it binds to AuNP causing their aggregation, therefore resulting in a colored product, visible on the test device.[85]

Another type of sensing with AuNP worth mentioning is fluorescence sensing. Indeed, by acting as on-off fluorescence switching devices, AuNP can be used as efficient quenchers in FRET-based assays, or to selectively detect various biomolecules, since fluorescence of chromophores located in the vicinity of AuNP becomes strongly quenched.[85]

AuNP can also be tagged with Raman reporters and serve as highly sensitive sensors in Surface Enhanced Raman Spectroscopy[86] (SERS), used in molecular recognition.

I.3.3.2. Imaging

AuNP could be used as bio-probes in various imaging applications (Figure I. 12).[62]

Thanks to their high electron density, electronic microscopy (Transmission / Scanning Electron Microscopy – TEM / SEM) has historically remained the primary imaging method allowing to detect biospecific interactions with AuNP (Figure I. 12).[62]

However, based on their strong scattering, AuNP can also be used as efficient contrast agents in dark field optical microscopy (Figure I. 12) – the most popular imaging method with AuNP, allowing to detect and measure the response of electron transparent biological materials.[60 62]

Luminescence properties of Au nanorods are very weak (quantum yield ~10^{-5} – 10^{-4}). However, it has been shown that they exhibit very good resistance to photobleaching and blinking, and could be used in optical imaging showing a much higher signal intensity in cells compared to the autofluorescence emission of cells only.[74] Thanks to these properties Au nanorods could also be imaged by various

* Sensing applications require the use of two elements: an element prone to binding under certain conditions and a sensor for signaling the binding event.

optical microscopy techniques, including confocal fluorescence microscopy, resonance scattering confocal microscopy or two-photon microscopy (Figure I. 12).

Under certain conditions, AuNP can also be used to enhance the fluorescence signal of molecular chromophores placed near their surface by the so-called Surface Plasmon Enhanced Fluorescence effect.[87]

Moreover, the capacity to generate strong acoustic waves of AuNP absorbing in the in the NearIR region can improve significantly the image contrast. Therefore, Au nanorods were successfully employed to detect various molecular targets by photoacoustic tomography (Figure I. 12).

In the same context, Au nanoshells have shown great potential in improving the biomedical detection with optical coherence tomography (Figure I. 12).[62]

Another promising technique with AuNP for *in vivo* imaging is Surface Enhanced Raman Spectroscopy (SERS), allowing the imaging of several tumor markers simultaneously, by using multiple SERS AuNP exhibiting different absorption wavelengths in the NearIR region.

Therefore as multifunctional bio-probes, AuNP offer numerous opportunities for multimodal imaging.

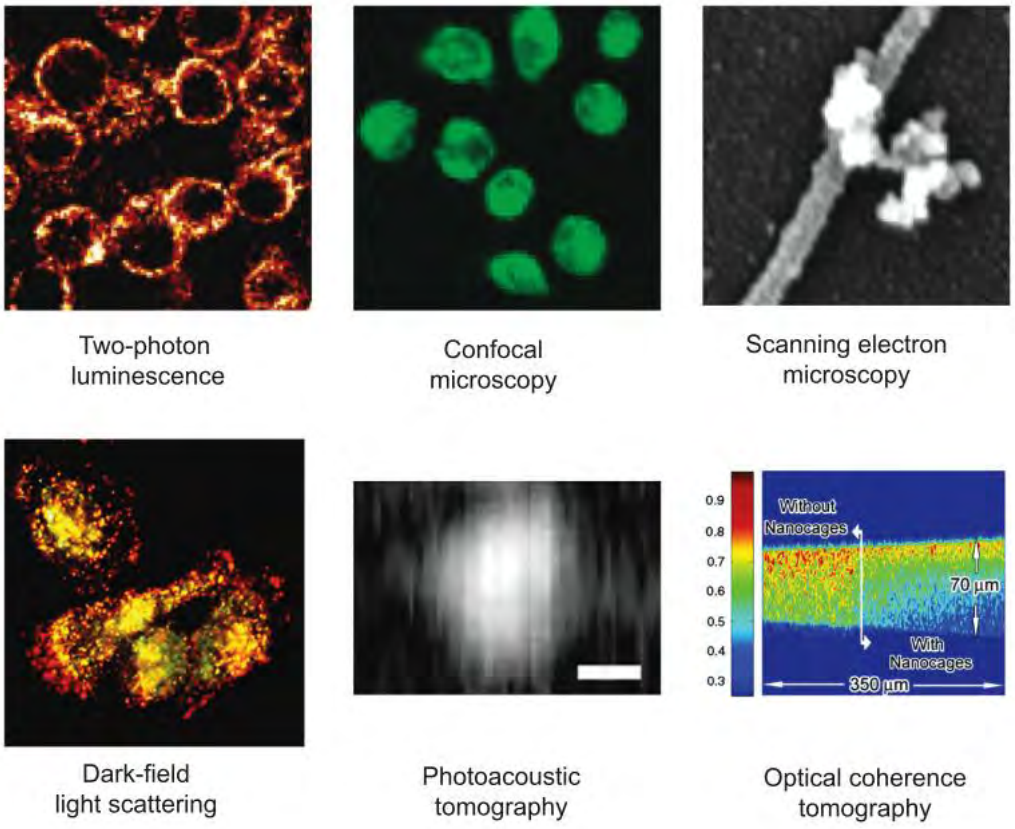

Figure I. 12: Two photon luminescence – Au nanorod-labeled cancer cells embedded in a collagen matrix; Confocal microscopy – AuNP-transferrin conjugates incubated in cancer cells; Scanning electron microscopy – AuNP-tiopronin-RGD conjugates in human fibroblast cells; Dark-field scattering – Au nanorods taken up by normal cells; Photoacoustic tomography – Au nanorod-TiO_2 in cancer cells; Optical coherence tomography – gelatin phantom embedded with gold nanocages (right portion), without nanocages (left).[62]

I.3.3.3. Therapy

Plasmonic photothermal therapy (PPTT) [88]

Thanks to the enhanced SPR absorption in the visible and the NearIR spectral range, most AuNP heat-up when excited by light at the appropriate wavelength (SPR). This property of AuNP can be used in photothermal therapy to treat cancer by hyperthermia, as tumors are selectively destroyed upon heating, due to their reduced heat tolerance compared to healthy tissues. Several nano-platforms based on AuNP have been already approved by FDA and evaluated in a number of clinical settings (*e.g.* Au nanoshells surrounding a silica core[89]).

While thermal therapy is known to be used in cancer treatment for several centuries, plasmonic photothermal therapy, PPTT, with AuNP has emerged as a minimally invasive promising treatment, along with the advances in the development of laser radiation technologies, ensuring a controlled and directed treatment of tumors. In this context, the recent research has been focused on three main issues determining the efficiency of PPTT with AuNP: 1) designing AuNP (with different sizes, shapes, and surface chemistry) with optimized absorption properties triggering an enhanced photothermal effect; 2) increasing the penetration depth of the treatment by using NearIR light excitation; 3) finding and creating new strategies for a targeted optical radiation.

Photodynamic therapy (PDT)

Photodynamic therapy (PDT) is an alternative treatment of cancer and infectious diseases, which consists in the use of photosensitizing molecules, that activated by light (usually in the Visible spectral range) can induce toxicity in tumors.

Similarly to Surface Plasmon Enhanced Fluorescence,[87] it has been demonstrated that AuNP can potentially enhance the generation of cytotoxic species produced by photosensitizers located at an optimal distance from their surface.[90]

The investigation of AuNP in PDT is still in its early stages.[91 92] Considering the great advances in the design of well-defined AuNP, as well as in the choices for lasers and light sources for PDT, upcoming expectations in this field are very promising.

Other therapeutic applications

Like almost all previously mentioned nano-platforms, AuNP can be used as vehicles for drug delivery applications. Many anti-tumor agents have shown an increase in their therapeutic efficacy when conjugated with AuNP. In a similar manner, AuNP can act as efficient carriers of genetic entities for gene therapy applications.[60]

Another use of AuNP results from their capacity to efficiently absorb X-rays, making them useful in radiation therapy of cancer. If incubated in tumors, AuNP are capable to enhance the amount of received radiation compared to the radiation received by healthy tissues.[93]

I.3.3.4. AuNP in clinical trials

Few examples exist on the use of AuNP-based nano-platforms in clinical trials (Table I. 2).[94] The first AuNP therapeutic reaching early clinical trial is CYT-6091 (Aurimune™): 27nm AuNP coated with thiolated poly(ethylene glycol) (PEG-SH) and tumor necrosis factor-α (TNF-α). CYT-6091 has been used with promising results in the treatment of solid cancers, by improving the tumor specificity and significantly reducing the TNF toxicity.

Table I. 2: Examples of the Use of Gold Nanoparticles in Clinical Practice.[84]

Type of auNP	Size (nm)	Role	Sponsor/Lab
Nanospheres	13	siRNA delivery	Mirkin
Nanorods	10 x 40	Photothermal ablation; CT contrast and thermal imaging	Bhatia
AuNP-silica Nanospleres	60/140	Raman imaging (colon cancer)	Gambhir
Nanoshells (Aurolase™)	150	Photothermal therapy (head and neck cancer)	NanoSpectra NCT00848042
Nanospheres (Aurimune™)	27	Stimulate immune response to tumor growth (solid tumors)	NCI NCT00436410

Finally, thanks to their attractive combination of chemical, physical, optical and electronic properties at the nanoscale, AuNP have shown great potential for sensing, imaging, diagnosis, therapy, and targeted drug delivery applications.

Multiple *in vitro* studies with AuNP have been completed with encouraging results in terms of AuNP bio-activity, cell uptake and cytotoxicity. Nonetheless, a number of problems especially related to AuNP toxicity, biodistribution and pharmacokinetics in living systems, still need to be elucidated.

This is the reason why an increase of *in vivo* pre-clinical and clinical investigations with AuNP is expected in the near future.

I.4. Conclusion of Chapter I

The diversity of material science and the unique and tunable properties of matter at the nanoscale enable the elaboration of several classes of efficient nano-platforms (organic, inorganic or hybrid) for various biomedical applications.
While advances in chemistry and physics enable a good control over structure-property relationships in designing well-defined nanomaterials for biology, current studies focus on better defining the interaction of such materials with living cells and organisms, therefore establishing relevant databases for predicting their behavior in bio-relevant media (uptake, toxicity, biodistribution etc.).

Unlike organic nano-platforms, which have mainly the role of carriers improving the bioavailability of molecular drugs, inorganic and hybrid nano-platforms (magnetic NP, Noble metal NP) exhibit intrinsic magnetic, optical and/or electronic properties, increasing the multifinctionality of the system and conferring new properties in biological media (higher drug loading capacity, possibility of multimodal imaging, photothermal effects etc.).
A particular attention has been drawn on gold – considered one of the most ancient Noble metal used for medical purposes. The multiple examples given in this chapter show how AuNP can efficiently act as multifunctional nano-platforms for many *in vitro* and *in vivo* biomedical applications (sensing, imaging, and therapy).

In order to take advantage of their multiple properties (biocompatibility, tunable SPR), we intend to use AuNP in this PhD project for bioimaging and photodynamic therapy applications. The new nano-platform we propose to design joins the class of hybrid nano-platforms, and is composed of chromophore-polymer conjugates grafted onto the surface of spherical AuNP. Special effects are expected when chromophores are located at an optimized distance from the AuNP surface, triggering an enhancement of their photophysical response, hence of fluorescence (bioimaging) or phototoxicity (PDT).

References

[1] **Nanoscience and technology: the next revolution in the Earth sciences,** M. F. Hochella Jr., *Earth Planet. Sci. Lett.* **2002**, *203*, 593-605.

[2] **Nanoscience, Nanotechnology, and Chemistry,** G. M. Whitesides, *Small* **2005**, *1(2)*, 172-179.

[3] **The 'right' size in nanobiotechnology.** G. M. Whitesides, *Nature Biotechnology* **2003**, *21(10)*, 1161-1165.

[4] **Nanoscience and their biological importance: human health and disease,** A. Pandey, A. Kumar Singh, S. K. Maurya, R. Raia, H.S. Shuklaa, *J. Nanomat. Biostruct.* **2008**, *3(3)*, 141-146.

[5] **Applications of Nanoparticles in Biology,** M. De, P.S. Ghosh, V. M. Rotello, *Adv. Mater.* **2008**, *20*, 4225-4241.

[6] **Applications of nanoparticles in biology and medicine,** O. V. Salata, *J. Nanobiotechnology* **2004**, *2*.

[7] **The enhanced permeability and retention (EPR) effect in tumor vasculature: the key role of tumor selective macromolecular drug targeting,** H. Maeda, *Advan. Enzyme Regul.* **2001**, *41*, 189-207.

[8] **Targeted nanoparticles for cancer therapy,** F. X. Gu, R. Karnik, A. Z. Wang, F. Alexis, E. Levy-Nissenbaum, S. Hong, R. S. Langer, O. C. Farokhzad, *Nano Today* **2007**, *2(3)*, 14-21.

[9] **Nanophotonics forMolecularDiagnostics and Therapy Applications,** J. Conde, J. Rosa, J. C. Lima, P. V. Batista, *International Journal of Photoenergy* **2012**.

[10] **Nanoparticle-based targeted drug delivery,** R. Singh, J. W. Lillard Jr., *Exp. Mol. Pathol.* **2009**, *86*, 215-223.

[11] **Synergistically Integrated Nanoparticles as Multimodal Probes for Nanobiotechnology,** J. Cheon, J.-H. Lee, *Acc. Chem. Res.* **2008**, *41(12)*, 1630-1640.

[12] **Liposomes: From a Clinically Established Drug Delivery System to a Nanoparticle Platform for Theranostic Nanomedicine,** W. T. Al-Jamal K. Kostarelos, *Acc. Chem. Res.*, 2011, *44(10)*, 1094-1104.

[13] **Emerging Technologies of Polymeric Nanoparticles in Cancer Drug Delivery,** E. Brewer, J. Coleman, A. Lowman, *J. Nanomater.* **2011**.

[14] **Nanoencapsulation I. Methods for preparation of drug-loaded polymericnanoparticles,** C. Pinto Reis, R. J. Neufeld, A. J. Ribeiro, F. Veiga*, Nanomed. Nanotechnol. Biol. Med.* **2006**, *2(1)*, 8-21.

[15] **Polymeric micelles – a new generation of colloidal drug carriers,** M.C. Jones, J.-C. Leroux, *Eur. J. Pharm. Biopharm.* **1999**, *48(2)*, 101-111.

[16] **Design of polymeric nanoparticles for biomedical delivery applications,** M. Elsabahy, K. L. Wooley, *Chem. Soc. Rev.* **2012**, *41*, 2545-2561.

[17] **Modern trends in polymer bioconjugates design,** J.-F. Lutz, H. G. Börner, *Progress in Polymer Science* **2008**, *33(1)*, 1-39.

[18] **Dendritic polymer macromolecular carriers for drug delivery,** A. K. Patri, I. J. Majoros, J. R. Baker Jr., *Curr. Opin. Chem. Biol.* **2002**, *6(4)*, 466-471.

[19] **Dendrimers as Carriers for Delivery of Chemotherapeutic Agents,** S. H. Medina, M. E. H. El-Sayed, *Chem. Rev.* **2009**, *109*, 3141-3157.

[20] **Mechanized silica nanoparticles: a new frontier in theranostic nanomedicine,** M. W. Ambrogio, C.R. Thomas, Y.-L. Zhao, J. I. Zink, J. F. Stoddart, *Acc. Chem. Res.*, **2011**, *44(10)*, 903-913.

[21] a) **Review of Quantum Dot Technologies for Cancer Detection and Treatment,** S. K. Vashist, R. Tewari, R. P. Bajpai, L. M.Bharadwaj R. Raiteri, *J. Nanotechnol.* **2006**.

b) **Quantum dot bioconjugates for imaging, labelling and sensing,** I. L. Medintz, H. T. Uyeda, E. R. Golmdman, H. Mattoussi, *Nature Materials* **2005**, *4*, 435-446.

[22] a) **Theranostic Magnetic Nanoparticles,** D. Yoo, J.-H. Lee, T.-H. Shin, J. Cheon, *Acc. Chem. Res.*, **2011**, *44(10)*, 863-874.

b) **Surface-Engineered Magnetic Nanoparticle Platforms for Cancer Imaging and Therapy,** J. Xie G. Liu, H. S. Eden, H. Ai, X. Chen, *Acc. Chem. Res.* 2011, *44(10)*, 883-892.

[23] a) **Noble Metals on the Nanoscale: Optical and Photothermal Properties and Some Applications in Imaging, Sensing, Biology, and Medicine,** P. K. Jain , X. Huang , I. H. El-Sayed M. A. El-Sayed, *Acc. Chem. Res.* **2008**, *41(12)*, 1578-1586.

b) **Synthesis, properties, and optical applications of noble metal nanoparticle-biomolecule conjugates,** J. H. Zhang, R. Huang, X. F. Zhu, L. X. Wang, C. X. Wu, *Chin Sci Bull* **2012**, *57(2-3*), 238-246.

[24] **Designing materials for biology and medicine,** R. Langer D. A. Tirrell, *Nature* **2004**, *428*, 487-492.

[25] **Strategies in the design of nanoparticles for therapeutic applications,** R. A. Petros J. M. DeSimone, *Nature reviews / Drug discovery* **2010**, *9*, 615-627.

[26] **Chapter 2: Nanoparticles for Targeted and Temporally Controlled Drug Delivery,** A. Swami, J. Shi, S. Gadde, A. R. Votruba, N. Kolishetti, O. C. Farokhzad, *Multifunctional Nanoparticles for Drug Delivery Applications: Imaging, Targeting, and Delivery, Nanostructure Science and Technology* **2012**, S. Svenson, R.K. Prud'homme (eds.).

[27] **Liposomal Drug Delivery Systems: An Update Review,** A. Samad, Y. Sultana, M. Aqil, *Current Drug Delivery* **2007**, *4*, 297-305.

[28] **Stimuli-responsive polymers and their applications in drug delivery,** P. Bawa, V. Pillay, Y. E. Choonara, L. C. du Toit, *Biomed Mater.* **2009**, *4(2)*.

[29] a) **Polymer–drug conjugates: Progress in polymeric prodrugs,** J. Khandarea, T. Minko, *Prog. Polym. Sci.* **2006**, *31*, 359-397.

b) **Polymer–drug conjugation, recent achievements and general strategies,** G. Pasut, F.M. Veronese, *Prog. Polym. Sci.* **2007**, *32*, 933-961.

[30] **Smart Nanomaterials Inspired by Biology: Dynamic Assembly of Error-Free Nanomaterials in Response to Multiple Chemical and Biological Stimuli,** Y. Lu, J. Liu, *Acc. Chem. Res.* **2007**, *40*, 315-323.

[31] **The Dawning Era of Polymer Therapeutics,** R. Duncan, *Nature Review / Drug Discovery* **2003**, *2*, 347-360.

[32] **Polymeric micelles as a new drug carrier system and their required considerations for clinical trials,** Masayuki Yokoyama, *Expert Opin. Drug Deliv.* **2010**, *7(2)*,145-158.

[33] a) **Nanoparticles – A Review,** V. J. Mohanraj, Y. Chen, *Trop. J. Pharm. Res*. **2006**, *5 (1)*, 561-573.

b) **The manufacturing techniques of drug-loaded polymeric nanoparticles from preformed polymers,** P. A. Grabnar J. Kristl*, J. Microencapsul.* **2011**, *28(4)*, 323-335.

c) **Methods for the preparation and manufacture of polymeric nanoparticles,** C. Vauthier, K. Bouchemal, *Pharm Res.* **2009**, *26(5)*,1025-1058.

[34] **Multi-functional polymeric nanoparticles for tumour-targeted drug delivery,** L. E. van Vlerken M. M. Amiji, *Expert Opin. Drug Deliv.* **2006**, *3(2)*, 205-216.

[35] **Recent advances in Drug Delivery Systems: Polymeric Prodrugs,** H. N. Joshi, *Pharm. Technol.* **1988**, *12*, 118-130.

[36] **Polymeric Conjugates for Drug Delivery,** N. Larson, H. Ghandehari, *Chem. Mater.* **2012**, *24*, 840-853.

[37] **Designing Dendrimers for Biological Applications,** C. C. Lee, J. A. MacKay, J. M. J. Fréchet F. C. Szoka, *Nature Biotech* **2005**, *23(12)*, 1517-1526.

[38] **Inorganic nanoparticles as carriers for efficient cellular delivery,** Z. P. Xu, Q. H. Zeng, G. Q. Lu, A. B. Yu, *Chem. Eng. Sci.* **2006**, *61(3)*, 1027-1040.

[39] **Inorganic nanoparticles in cancer therapy,** S. Bhattacharyya, R. A. Kudgus, R. Bhattacharya, P. Mukherjee, *Pharm Res.* **2011**, *28(2)*, 237-259.

[40] **Mesoporous silica nanoparticles as controlled release drug delivery and gene transfection carriers,** I. I. Slowing, J. L. Vivero-Escoto, C.-W. Wu, V. S.-Y. Lin, *Adv. Drug Deliv. Rev.* **2008**, *60(11)*, 1278-1288.

[41] **Mesoporous silica nanomaterial-based biotechnological and biomedical delivery systems,** S. Giri, B. G. Trewyn, V. S. Y. Lin, *Nanomedicine* **2007**, *2(1)*, 99-111.

[42] **Mesoporous Silica Nanoparticles for Intracellular Controlled Drug Delivery,** J. L. Vivero-Escoto, I. I. Slowing, B. G. Trewyn, V. S.-Y. Lin, *Small* **2010**, *6(18)*, 1952-1967.

[43] **Mesoporous silica nanoparticles in biomedical applications,** Z. Li , J. C. Barnes , A. Bosoy , J. F. Stoddart, J. I. Zink, *Chem. Soc. Rev.* **2012**, *41*, 2590-2605.

[44] **Multifunctional Magnetic Nanoparticles: Design, Synthesis, and Biomedical Applications,** J. Gao, H. Gu, B. Xu, *Acc. Chem. Res.* **2009**, *42(8)*, 1097-1107.

[45] **Applications of magnetic nanoparticles in biomedicine,** Q. A. Pankhurst, J. Connolly, S. K. Jones, J. Dobson, *J. Phys. D: Appl. Phys.* **2003**, *36*, R167-R181.

[46] **Development and use of iron oxide nanoparticles (Part 1): Synthesis of iron oxide nanoparticles for MRI,** J. Lodhia, G. Mandarano, N. J. Ferris, P. Eu, S. F. Cowell, *Biomed. Imaging Interv. J.* **2010**, *6(2)*.

[47] **Quantum dots versus organic dyes as fluorescent labels,** U. Resch-Genger, M. Grabolle, S. Cavaliere-Jaricot, R. Nitschke, Thomas Nann, *Nature Methods* **2008**, *5*, 763-775.

[48] **Quantum dot bioconjugates for imaging, labelling and sensing,** I. L. Medintz, H. T. Uyeda, E. R. Goldman, H. Mattoussi, *Nature Materials* **2005**, *4*, 435-446.

[49] **Quantum Dots: An Insight and Perspective of Their Biological Interaction and How This Relates to Their Relevance for Clinical Use,** M. J. D. Clift, V. Stone, *Theranostics* **2012**, *2(7)*, 668-680.

[50] a) **Probing the Cytotoxicity of Semiconductor Quantum Dots,** A. M. Derfus, W. C. W. Chan, S. N. Bhatia, *Nano. Lett.* **2004**, *4(1)*, 11-18.

b) **A Toxicologic Review of Quantum Dots: Toxicity Depends on Physicochemical and Environmental Factors,** R. Hardman, *Environ. Health Perspect.* **2006**, *114(2)*, 165-172.

[51] **Effects of long-term exposure of gelatinated and non-gelatinated cadmium telluride quantum dots on differentiated PC12 cells,** B. R. Prasad, G. Mullins, N. Nikolskaya, D. Connolly, T. J. Smith, V. A. Gérard, S. J. Byrne, G.-L. Davies, Y. K Gun'ko, Y. Rochev*, J. Nanobiotechnology* **2012**, *10:4*.

[52] **Quantum Dots for Live Cells, in Vivo Imaging, and Diagnostics, X. Michalet, F. F. Pinaud, L. A. Bentolila,** J. M. Tsay, S. Doose, J. J. Li, G. Sundaresan, A. M. Wu, S. S. Gambhir, S. Weiss, *Science* **2005**, *28*, 538-544.

[53] **Intrinsic therapeutic applications of noble metal nanoparticles: past, present and future,** R. R. Arvizo, S. Bhattacharyya, R. A. Kudgus, K. Giri, R. Bhattacharya, P. Mukherjee, *Chem. Soc. Rev.* **2012**, *41*, 2943-2970.

[54] a) **Localized Surface Plasmon Resonance Spectroscopy and Sensing,** K. A. Willets, R. P. Van Duyne, *Annu. Rev. Phys. Chem.* **2007**, 267-297.

b) **Towards integrated and sensitive surface plasmon resonance biosensors: A review of recent progress,** X.D. Hoa, A.G. Kirk, M. Tabrizian, *Biosensors and Bioelectronics* **2007**, *23(2)*, 151-160.

[55] **Review of Some Interesting Surface Plasmon Resonance-enhanced Properties of Noble Metal Nanoparticles and Their Applications to Biosystems,** P. K. Jain, X. Huang, I. H. El-Sayed, M. A. El-Sayed, *Plasmonics* **2007**, *2(3)*, 107-118,

[56] a) **High resolution imaging of patterned model biological membranes by localized surface plasmon microscopy,** K. Watanabe, M. Ryosuke, G. Terakado, T. Okazaki, K. Morogaki, H. Kano, *Appl. Opt.* **2010**, *49(5)*, 887-891.

b) **Seeing Molecules by Eye: Surface Plasmon Resonance Imaging at Visible Wavelengths with High Spatial Resolution and Submonolayer Sensitivity,** J. Yao, M. E. Stewart, J. Maria, T.-W. Lee, S. K. Gray, J. A. Rogers, R. G. Nuzzo, *Angew. Chem. Int. Ed.* **2008**, *47*, 5013-5017.

[57] a) **Clinical Relevance of Nanoparticle Induced Hyperthermia for Drug Delivery and Treatment of Abdominal Cancers,** N. H. Levi-Polyachenko, J. H. Stewart, *Open Nanomed. J.* **2011**, *3*, 24-37.

b) **Plasmonic photo-thermal therapy (PPTT),** X. Huang, M. A. El-Sayed, *Alexandria J. of Medicine* **2011**, *47*, 1-9.

[58] a) **On-a-chip surface plasmon tweezers,** H. M. K. Wong, M. Righini, J. C. Gates, P. G. R. Smith, V. Pruneri, R. Quidant, *Appl. Phys. Lett.* **2011**, *99*, 061107.

b) **Surface plasmon optical tweezers: tunable optical manipulation in the femtonewton range,** M. Righini, G.Volpe, C. Girard, D. Petrov, R. Quidant, *Phys. Rev. Lett.* **2008**, *100*.

[59] **Molecular plasmonics for biology and nanomedicine,** Y. Bing Zheng, B. Kiraly, P. S. Weiss, T. Jun Huang, *Nanomedicine* **2012**, *7(5)*, 751-770.

[60] **Gold Nanoparticles in Biology and Medicine: Recent Advances and Prospects,** L. A. Dykman, N.G. Khlebtsov, *Acta Naturae 2011*, *3(2)*, 34-55.

[61] **Panacea Aurea-Auro Potabile,** F. Antonii, *Bibliopolio Frobeniano* **1618**, Hamburg.

[62] **Applications of gold nanoparticles in cancer nanotechnology,** W. Cai, T. Gao, H. Hong, J. Sun, *Nanotechnology, Science and Applications* **2008**, *1*, 17-32.

[63] **Synthesis and optical properties of dyes encapsulated in gold hollow nanoshells,** A.-M. Gabudean, F. Lerouge, T. Gallavardin, M. Iosin, S. Zaiba, O. Maury, P. L. Baldeck, C. Andraud, S. Parola, *Opt. Mater.* **2011**, *33(9)*, 1377-1381.

[64] **Synthesis, electron tomography and single-particle optical response of twisted gold nano-bipyramids,** J. R. G. Navarro, D. Manchon, F. Lerouge, E. Cottancin, J. Lermé, V. Bonnet, F. Chaput, A. Mosset, M. Pellarin, S. Parola, *Nanotechnology* **2012**, *23(14)*, 145707-145715.

[65] **Shape-Controlled Synthesis of Gold and Silver Nanoparticles,** Y. Sun, Y. Xia, *Science* **2002**, *298*, 2176-2179.

[66] **Synthesis of colloidal nanoparticles during femtosecond laser ablation of gold in water,** A. V. Kabashi, M. Meunier, *J. Appl. Phys.* **2003**, *94*, 7941-7944.

[67] **Photochemical Synthesis of Gold Nanorods,** F. Kim, J. H. Song, P. Yang, *J. Am. Chem. Soc.* **2002**, *124*, 14316-14317.

[68] **Synthesis of gold nanorods and nanowires by a microwave–polyol method,** M. Tsuji, M. Hashimoto, Y. Nishizawa, T. Tsuji, *Mat. Lett.* **2004**, *58*, 2326-2330.

[69] **Synthesis and size regulation of goldnanoparticles by controlled thermolysis of ammonium gold(I) thiolate in the absence or presence of amines,** M. Nakamoto, Y. Kashiwagi, M. Yamamoto, *Inorg. Chim. Acta* **2005**, *358*, 4229-4236.

[70] **Digestive-Ripening Agents for Gold Nanoparticles: Alternatives to Thiols,** B. L. V. Prasad, Savka I. Stoeva , Christopher M. Sorensen , Kenneth J. Klabunde, *Chem. Mater.* **2003**, *15*, 935-942.

[71] **Synthesis of goldnanoparticles dispersed within pores of mesoporous silica induced by ultrasonic irradiation and its characterization,** W. Chen, W.P. Cai, C.H. Liang, L.D. Zhang, Mat. Res. Bull. **2001**, *36*, 335-342.

[72] a) **Nucleation and Growth Process in the Synthesis of Colloidal Gold.** J. Turkevitch, P. C. Stevenson, J. Hillier, *Discuss. Faraday Soc.* **1951**, *11*, 55-75.

b) **Controlled Nucleation for the Regulation of the Particle Size in Monodisperse Gold Suspensions.** G. Frens, *Nature: Phys. Sci.* **1973**, *241*, 20-22.

[73] **From Monolayers to Nanostructured Materials: An Organic Chemist's View of Self-Assembly,** D. Bethell, M. Brust, D. J. Schiffrin, C. F. J. Kiely, *Electroanal. Chem.* **1996**, *409*, 137-143.

[74] **Why gold nanoparticles are more precious than pretty gold: Noble metal surface plasmon resonance and its enhancement of the radiative and nonradiative properties of nanocrystals of different shapes,** S. Eustis, M. A. El-Sayed, *Chem. Soc. Rev.* **2006**, *35*, 209-217.

[75] a) **Gold nanocapsules synthesized using an emulsion process: towards multifunctional Au nanoshells,** F. Lux, F. Lerouge, J. Bosson, G. Lemercier, C. Andraud, G. Vitrant, P. L. Baldeck, F. Chassagneux, S. Parola, *Nanotechnology* **2009**, *20 (35)*, 355603.

b) **Synthesis and optical properties of dyes encapsulated in gold hollow nanoshells,** A.-M. Gabudean, F. Lerouge, T. Gallavardin, M. Iosin, S. Zaiba, O. Maury, P. L. Baldeck, C. Andraud, S. Parola, *Opt. Mater.* **2011**, *33(9)*, 1377-1381.

[76] **Gold Nanoparticles: Assembly, Supramolecular Chemistry, Quantum-Size-Related Properties, and Applications toward Biology, Catalysis, and Nanotechnology,** M.-C. Daniel, D. Astruc, *Chem. Rev.* **2004**, *104*, 293-346.

[77] **Recent advances in polymer protected gold nanoparticles: synthesis, properties and applications,** J. Shan H, Tenhu, *Chem. Commun.* **2007**, 4580-4598.

[78] **Gold Nanoparticles for Biology and Medicine,** D. A. Giljohann, D. S. Seferos, W. L. Daniel, M. D. Massich, P. C. Patel, C. A. Mirkin, *Angew. Chem. Int. Ed.* **2010**, *49*, 3280-3294.

[79] **Calculated Absorption and Scattering Properties of Gold Nanoparticles of Different Size, Shape, and Composition: Applications in Biological Imaging and Biomedicine**, P. K. Jain, K. Seok Lee, I. H. El-Sayed, M. A. El-Sayed, *J. Phys. Chem. B* **2006**, *110*, 7238-7248.

[80] **Theranostic Nanoshells: From Probe Design to Imaging and Treatment of Cancer,** R. Bardhan, S. Lal, A. Joshi, N. J. Halas, *Acc. Chem. Res.* **2011**, *40(10)*, 936-946.

[81] **Transferrin-Mediated Gold Nanoparticle Cellular Uptake,** P.-H. Yang, X. Sun, J.-F. Chiu, H. Sun, Q.-Y. He, *Bioconjugate Chem*, **2005**, *16(3)*, 494-496.

[82] **Elucidating the Mechanism of Cellular Uptake and Removal of Protein-Coated Gold Nanoparticles of Different Sizes and Shapes,** B. D. Chithrani, C. W. Chan, *Nano Lett.* **2007**, *7(6)*, 1542-1550.

[83] **Size-Dependent Cytotoxicity of Gold Nanoparticles,** Y. Pan, S. Neuss, A. Leifert, M. Fischler, F. Wen, U. Simon, G. Schmid, W. Brandau, W. Jahnen-Dechent, *Small* **2007**, *3(11)*, 1941-1949.

[84] **Gold Nanoparticles: A Revival in Precious Metal Administration to Patients,** A. S. Thakor, J. Jokerst, C. Zavaleta, T. F. Massoud, S. S. Gambhir, *Nano Lett.* **2011**, *11*, 4029-4036.

[85] **Gold Nanoparticles in Chemical and Biological Sensing,** K. Saha, S. S. Agasti, C. Kim, X. Li, V. M. Rotello, *Chem. Rev.* **2012**, *112*, 2739-2779.

[86] a) **Probing the enhancement mechanisms of SERS with *p*-aminothiophenol molecules adsorbed on self-assembled gold colloidal nanoparticles,** M. Baia, F. Toderas, L. Baia, J. Popp, S. Astilean, *Chem. Phys. Lett* **2006**, *422*, 127-132.

b) **The synthesis of biocompatible and SERS-active gold nanoparticles using chitosan,** M. Potara, D. Maniu S. Astilean, *Nanotechnology* **2009**, *20*, 315602.

[87] **Fluorescence Manipulation by Gold Nanoparticles: From Complete Quenching to Extensive Enhancement,** K. A Kang, J. Wang, J. B. Jasinski, Achilefu, *J. of Nanobiotechnology* **2011**, *9:16*.

[88] **Plasmonic photothermal therapy (PPTT) using gold nanoparticles,** X. Huang, K. Jain, H. El-Sayed, M. A. El-Sayed, *Lasers Med. Sci.* **2008**, *23*, 217-228.

[89] a) **Near-Infrared Resonant Nanoshells for Combined Optical Imaging and Photothermal Cancer Therapy,** A. M. Gobin , M. H. Lee, N. J. Halas, W. D. James, R. A. Drezek, J. L. West, *Nano Lett.* **2007**, *7(7)*, 1929-1934.

b) **Nanoshell-Enabled Photothermal Cancer Therapy: Impending Clinical Impact,** S. Lal, S. E. Clare, N. J. Halas, *Acc. Chem. Res.* **2008**, *41(12)*, 1842-1851.

[90] **Gold nanoparticles enhance methylene blue–induced photodynamic therapy: a novel therapeutic approach to inhibit Candida albicans biofilm,** S. Khan, F. Alam, A. Azam, A. U. Khan, *Int. J. of Nanomedicine* **2012**, *2012:7*, 3245-3257.

[91] **Targeted photodynamic therapy of breast cancer cells using antibody-phthalocyanine-gold nanoparticle conjugates,** T. Stuchinskaya, M. Moreno, M.J. Cook, D. R. Edwards, D. A. Russell, *Photochem Photobiol Sci.* **2011**, *10(5)*, 822-831.

[92] **Synthesis of phthalocyanine conjugates with gold nanoparticles and liposomes for photodynamic therapy,** N. Nombona, K. Maduray, E. Antunes, A. Karsten, Te. Nyokong, *J. Photochem.Photobiol. B: Biology* **2012**, *107*, 35-44.

[93] **Radiotherapy enhancement with gold nanoparticles,** J. F. Hainfeld, F. A. Dilmanian, D. N. Slatkin, H. M. Smilowitz, *J. Pharm. Pharmacol.* **2008**, *60(8)*, 977-985.

[94] **Gold nanoparticles as novel agents for cancer therapy,** S. Jain, D. G. Hirst, J. M. O'Sullivan, *Br. J. Radiol.* **2012**, *85*, 101-113.

Chapter II: Synthesis and characterization of chromophore-polymer conjugates using RAFT polymerization

II.1. Introduction

Besides bioactivity, water-solubility and biocompatibility – properties that are essential in biological applications, well-controlled structure and accurate characterization of nanomaterials are both essential for a good comprehension of their activity and structure-property relationship in bio-relevant media.

Following the strategy mentioned in the general introduction, the first step for the elaboration of organic/inorganic nano-probes consisted in the synthesis of well-defined two-photon (TP) chromophore-polymer conjugates. These conjugates bear on the lateral position of the polymer chain, either two-photon (TP) fluorophores for bioimaging applications, or two-photon (TP) photosensitizers for photodynamic therapy (PDT) applications.

The role of the polymer should be i) to provide water-solubility and biocompatibility, ii) to control the number of chromophores along the polymer chain in order to achieve an enhanced brightness, iii) and to enable an oriented grafting of the conjugates onto AuNP surface.

The structure of chromophore-polymer conjugates is composed of a linear hydrophilic polymer chain carrying on the lateral position covalently bound chromophore molecules and a thiol end-group (-SH) for an efficient and oriented grafting of the conjugates onto AuNP.

The chosen strategy to synthesize such conjugates is based on the use of RAFT (Reversible Addition-Fragmentation Chain Transfer) polymerization. This controlled radical polymerization (CRP) technique indeed leads to well-defined polymers and is applicable to a wide range of polar and functionalized monomers. In addition, a straightforward post-modification of polymers synthesized by the RAFT process can be used to access to a thiol end-groups (Section II.2).

Conjugate synthesis is carried out in three different steps (Figure II. 1):

1. Synthesis of reactive poly(*N*-acryloylmorpholine-*co*-*N*-acryloxysuccinimide), P(NAM-*co*-NAS), copolymer by RAFT polymerization:

- *N*-acryloylmorpholine, NAM, is a monomer conferring water-solubility to the polymer chain.
- *N*-acryloxysuccinimide, NAS, is a reactive monomer bearing an activated ester group that readily reacts with amino-containing compounds.
- The chain transfer agent (CTA) used in RAFT copolymerization of NAM/NAS mixture controls:
    - the chain-end functionalities: the ω-end-group is a dithioester (DT) easily convertible into a thiol (SH);
    - the molecular weight (MW) ensuring narrow MW distribution;
    - the architecture of the chain, giving the possibility to obtain controlled random or block copolymers.

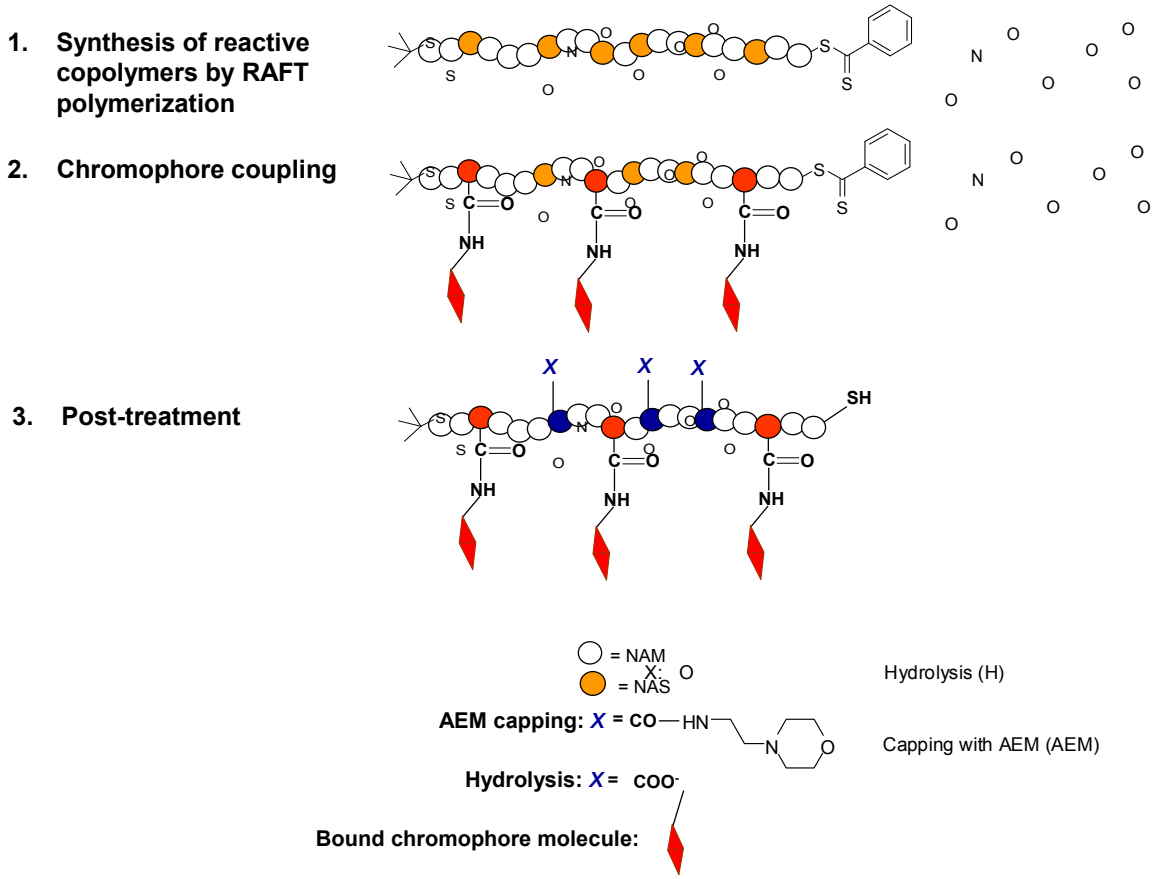

Figure II. 1 : The strategy chosen to synthesize chromophore-polymer conjugates: 1. Synthesis of reactive P(NAM-*co*-NAS) copolymers by RAFT polymerization; 2. Chromophore coupling; 3. Post-treatment of reactive NAS groups (AEM capping → neutral conjugates; Hydrolysis → negatively charges conjugates).

2. Chromophore coupling

The 2nd step consists in the efficient coupling reaction between amino-functionalized chromophores and activated esters (NAS units) located on the lateral position of the polymer chain.

3. Post-treatment of polymer-chromophore conjugates

The final step consists in modifying residual NAS reactive pendant groups, either by:

- Capping with a water-soluble primary amine, *4*-(*2*-Aminoethyl)morpholine (AEM) leading to neutral conjugates.
- Basic hydrolysis, leading to negatively charged conjugates (carboxylates).

Before presenting the synthesis of conjugates, a bibliographical part will first focus on a short introduction to RAFT polymerization (Section II.2.1), highlighting its advantages in the framework of our project, and on various chromophore-polymer conjugates developed up to date for biological applications (Section II.2.2). Then, the synthesis of well-defined PNAM homopolymers and P(NAM-*co*-NAS) copolymers by RAFT polymerization will be discussed (Section II.3).

Finally, the synthesis of well-defined chromophore-polymer conjugates, including coupling and post-treatment, will be exposed (Section II.4).

II.2. Bibliography: RAFT controlled radical polymerization and Chromophore-polymer conjugates synthesis

A short introduction on the Controlled Radical Polymerization techniques, and particularly on the Reversible Addition Fragmentation Chain Transfer Polymerization, will be presented in this Section, followed by a review about chromophore polymer conjugates (with chromophores bound on the lateral position of the polymer chain) designed for biological applications.

II.2.1. Reversible Addition Fragmentation Chain Transfer (RAFT) Polymerization

II.2.1.1. Controlled Radical Polymerization (CRP)

Today the preparation of polymer materials is mainly performed *via* conventional free-radical polymerization.[1] More than 50% of commercial synthetic polymers are obtained via this method. The main reason is that a large spectrum of monomers can be polymerized, in relatively mild conditions. However, the major drawback associated with these techniques is the rather low control over polymer MW distribution, architecture and chain-end functionality.

In this context, the discovery of living anionic[2] and cationic[3] polymerization techniques more than 50 years ago, allowed the production of well-defined polymers with low polydispersity and controlled MW. However, the high vacuum conditions (in anionic polymerization), and the required high purity of monomer and solvent (in cationic polymerization), as well as the restricted number of suitable monomers, led to the development of controlled/living radical polymerization methods (CRP)[4] more than a decade ago.

CRP techniques allowed combine the advantages of both free-radical polymerization – suitable for a large variety of monomers and tolerant over various experimental conditions, and living polymerization processes – high level of control over MW, polydispersity, end-groups, and architecture of the chain. The control of the radical polymerization is achieved by establishing a dynamic equilibrium between propagating radicals and so-called dormant species. With regards to their mechanisms, CRP processes can be divided in two categories:[5]

a) Reversible deactivation/activation of growing chains. It includes nitroxide mediated polymerization (NMP),[6] and atom transfer radical polymerization (ATRP).[7]
b) Degenerative exchange processes *via* reversible transfer of growing chains. The most known and studied degenerative polymerization technique is reversible addition-fragmentation chain-transfer (RAFT)[8] polymerization. It is probably one of the most adopted techniques among all CRP processes, tolerating many conditions, and suitable for a large variety of monomers.

II.2.1.2. RAFT polymerization

RAFT was first reported in 1998, by the Australian CSIRO group directed by Ezio Rizzardo.[9] It is a CRP technique which makes use of a chain transfer agent (CTA, Figure II. 2 a)), also referred as RAFT agent, typically having a thiocarbonylthio group (S=C-S) with substituents R and Z, allowing the control of the polymerization process, and finally accounting for the respective end-groups of the RAFT polymer (Figure II. 2 b)).

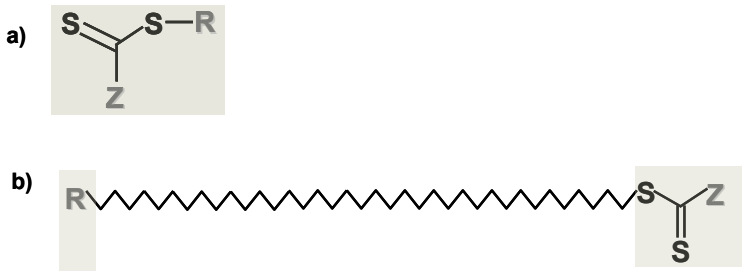

Figure II. 2: Structural features of the a) CTA (RAFT agent); b) polymer chain obtained by RAFT polymerization.

The control over MW and low polydispersities are achieved mainly by controlling the molar ratios between CTA and monomer, and between CTA and initiator. CTA amount, used in large access compared to the initiator, controls and determines the number of polymer chains formed during RAFT polymerization. A few more details about the role of the CTA and the mechanism of RAFT polymerization are given in Appendix II.1. The theoretical formulae allowing to predict the molecular weights of RAFT polymers are also given and explained in Appendix II.1.

Advantages of RAFT polymerization

Among all CRP methods, RAFT can be considered the most versatile one:

- Able to control polymerization of most monomers polymerizable by radical polymerization ((meth)acrylates, (meth)acrylamides, acrylonitrile, styrenes, dienes and vinyl monomers).
- Able to control the end-group functionalities which can be tuned to give polymers with telechelic functionality for further binding events.
- Tolerant over unprotected functionality of monomers and solvents (*e.g.*, OH, NR_2, COOH, $CONR_2$, SO_3H.
- Compatible with many reaction conditions (*e.g.*, bulk, organic or aqueous solution, emulsion, mini-emulsion, suspension).
- Requires no special equipment or vacuum glassware, rather easy to implement and inexpensive relative to competitive technologies.
- Able to produce polymers and copolymers with different compositions (*e.g.* random, gradient, graft) and architectures (*e.g.* linear, star, comb).
- RAFT does not use any cytotoxic heavy metal components (unlike ATRP), thus polymers obtained by RAFT are more appropriate for biological applications.

To conclude, RAFT is a robust and versatile technique, applicable to the majority of monomers used in radical polymerization, allowing to obtain well-defined polymers with the desired composition, architecture and functionality.

II.2.1.3. Synthesis of PNAM and P(NAM-co-NAS) (co)polymers by RAFT polymerization

In this project, RAFT technique was used to synthesize *N*-acryloylmorpholine (NAM) homopolymers and copolymers with random and block architectures using a co-monomer, *N*-acryloxysuccinimide (NAS) (see above).[10]

N-acryloylmorpholine (NAM, Figure II. 3 a)) is a bi-substituted acrylamide derivative exhibiting several attractive properties for bio-related applications. It polymerizes easily in a broad range of conditions, leading to high MW polymers, soluble in both aqueous and polar organic media. PNAM polymers display stealth properties and have been proposed as a suitable alternative to poly(ethylene glycol)(PEG)[11] polymers for the elaboration of bio-active conjugates.[12 13]

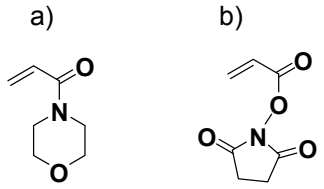

Figure II. 3: Molecular structure of a) NAM; b) NAS.

N-acryloxysuccinimide (NAS, Figure II. 3 b)) has a succinimide activated ester pendant group often used as acylating agent for coupling with amino-derived compounds, resulting in stable amide groups.[14 15 16]

In our group, PNAM (Figure II. 4 a)) has been synthesized by RAFT technique in the presence of *t*BDB as CTA (Figure II. 4 b)), leading to an excellent control over molecular weights and their distributions.[10]

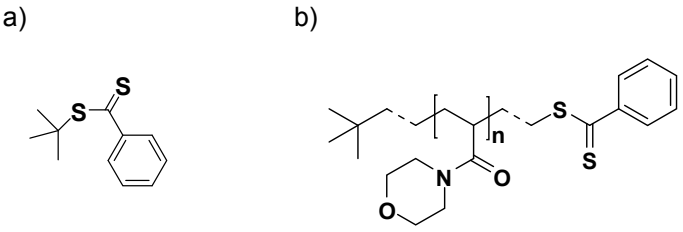

Figure II. 4: a) Molecular structure of tBDB; b) Structure of PNAM synthesized by RAFT using tBDB as CTA.

RAFT polymerization of NAM has been extensively studied regarding the control over MW (using SEC/LS*),[17] the influence of the CTA (both Z[18] and R[17] groups), the influence of the temperature, monomer concentration, CTA/initiator and CTA/monomer molar ratios on polymerization kinetics[10] and the end-group functionality (using MALDI-TOF† spectroscopy).[19]
NAM has been successfully copolymerized by RAFT with several functional monomers: galactose derivative,[20] *N*-acryloylpiperidine and *N*-acryloylazocane,[21] *N*-acryloxysuccinimide (NAS).[22]

Our previous studies on the RAFT copolymerization of NAM/NAS monomer pair resulted in an excellent control over P(NAM-*co*-NAS) MW, narrow MW distribution, but also controlled composition and homogeneous microstructure.[22] [23] It has been shown that NAM/NAS pair copolymerizes in a statistical way with a very low compositional drift.[24] In addition, an azeotropic composition, ensuring the same rate of polymerization for both monomers was found for NAM/NAS molar ratio of 60/40, leading to a regular distribution of NAS monomers in the final copolymer chain (Figure II. 5), thus allowing a regular substitution of these reactive groups with chromophore molecules (Section II.4).

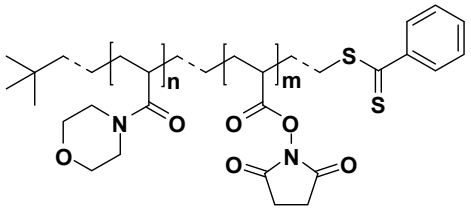

Figure II. 5: Structure of P(NAM-*co*-NAS) random copolymer.

Moreover, in order to prove the living character of RAFT P(NAM-*co*-NAS) copolymers, they have been used as macro-CTA to polymerize NAM and produce well-defined block copolymers with PNAM as a 2nd block (Figure II. 6).

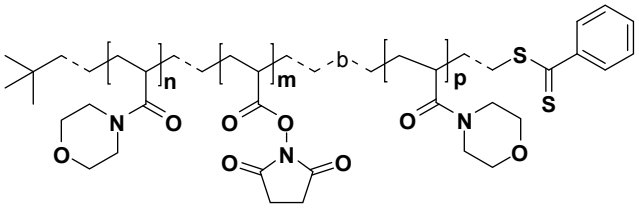

Figure II. 6: Structure of poly[(NMA-*co*-NAS)-b-NAM] block copolymer.

Taking into account the previous progress in studying RAFT polymerization of NAM/NAS monomer pair, P(NAM-*co*-NAS) copolymers exhibit many advantages[25] for the elaboration of chromophore-polymer conjugates aimed for biological applications:

- water-solubility and biocompatibility;
- reactivity *via* NAS units – binding sites for amino-derived chromophores;
- possibility to control the number and the density of chromophores *per* chain, thanks to the homogeneity of chain composition and the high reactivity of activated ester functions (NAS units);

* SEC/LS – Size Exclusion Chromatography coupled with a Multi-Angle Light scattering detector.

† MALDI-TOF – Matrix Assisted Laser Desorption/Ionisation-Time Of Flight.

- 'living character' and capacity to be used as macro-CTA in the synthesis of block copolymers (use this architecture to later tune the distance between polymer-bound chromophores and AuNP surface);
- dithioester end-groups (relative to the RAFT technique), enabling the oriented grafting onto AuNP.

The versatility of these polymers towards the controlled synthesis of chromophore-polymer conjugates will be presented in Section II.4.

II.2.2. Chromophore-polymer conjugates in biological applications

Polymer conjugates in biology

Polymer conjugates raise increasing interest in many biomedical fields.[26] [27] [28] They are usually obtained by the association of bio-active species (drugs, biological entities, targeting agents etc.) with polymers (chains, nanoparticles, micelles).

Conjugation can be realized *via* covalent[26] or non-covalent[27] bonding. Non-covalent systems (e.g. polymer micelles) are beyond the scope of this work and will not be addressed here.

Depending on the bio-active species used for conjugation, several classes of polymer conjugates can be distinguished:

- Polymer-proteins / -peptides, -enzymes / -antibodies[27] [29]
- Polymer-nucleic acids / -oligonucleotides[30]
- Polymer-lipids / -liposomes[31]
- Polymer-carbohydrates / -sugars[27]
- Polymer-drugs[26]

Note: The term of "drug" will often refer (in this chapter) to any active molecular species used for therapeutic and/or diagnostic purposes (*e.g.* therapeutic, imaging or targeting agents).

PEG is undoubtedly the most used polymer for conjugation with bio-active entities.[32] The FDA tolerated its use in foods, cosmetics and pharmaceuticals. In addition, large scale synthesis of PEG is possible and many functional PEG polymers are commercially available. However, the use of PEG in bio-conjugation presents some limitations as non-biodegradability, which sometimes can result in toxic side effects for high MW PEG conjugates, and low drug loading capacity, due to conjugation at only the chain-ends.

As a solution to these problems, a significant increase in the development of new multifunctional polymers, with various structures and architectures has been noted. The diversity of available polymers presents countless opportunities for modulating the properties of conjugates, it includes natural[33] and synthetic[26] polymers, biodegradable polymers,[34] polymers with a variety of architectures

and compositions: homopolymers *vs.* copolymers, linear *vs.* branched / hyperbranched polymers,[35] polymer networks/hydrogels,[36] [37] or dendrimers,[38] as well as end-group *vs.* pendant-group functionalized polymers (Appendix II.2). Therefore, the number of existing combinations with polymers is virtually infinite and can be used to finely tune the properties of conjugates for various biological applications (recognition and targeting, imaging, therapy, drug delivery etc.).

Designing covalent polymer conjugates

One particular approach leading to the design of modern covalent polymer conjugates for biological applications is based on the concept proposed by Helmut Ringsdorf in 1975.[39] According to Ringsdorf, the ideal polymer platform would be a combination of several components (Figure II. 7): i) a biocompatible and water-soluble polymer backbone, used as a vehicle; ii) covalently fixed active molecules (drugs, contrast agents, targeting groups) on the polymer backbone; iii) a degradable linker (X), to trigger and control the drug release in biological media.

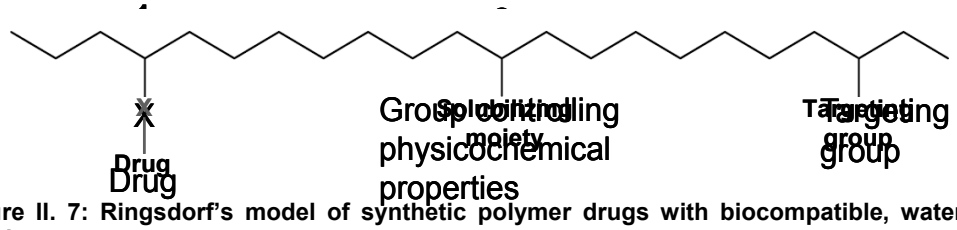

Figure II. 7: Ringsdorf's model of synthetic polymer drugs with biocompatible, water-soluble polymer backbone.

The most common strategies used to synthesize polymer conjugates, the chemistry involved in conjugation and the type of linkers used to control the dug release are briefly summarized in Appendix II.2.

Advantages of polymer conjugates in biological applications

Up to date, various polymer conjugates could be designed for diagnosis, drug delivery, sensing and recognition applications. The primary advantage of those conjugates, compared to small molecular species, comes from their capacity to preferentially accumulate in tumors *via* the enhanced permeability and retention effect or "EPR" described by Maeda and coworkers.[40]

The benefits of using polymers for biological applications are multiple and are summarized in Table II. 1.

Table II. 1: Advantages of using polymers in conjugation for bio-oriented applications.

Advantages of polymer conjugates	
Chemistry of conjugation	**Properties of polymer conjugate**
• possibility to design multi-functional platforms (Ringsdorf's model); • choice of the binding site (end-group / pendant group); • choice of the architecture (linear, branched, star, dendrimer); • control of the molecular weights, functionality, the number of binding sites can be achieved.	• biocompatibility and water-solubility; • longer retention in blood and thus capacity of passive targeting; • increased size (viral size) which minimizes their uptake by the reticuloendothelial system (RES); • conjugation with targeting groups for active targeting; • decreased immunogenicity; • can present stimuli responsive properties (pH, temperature, light); • capacity to induce triggered drug release through degradable linkers.
Critical properties	
• **limited biodegradability for many polymers;** • **bioresorbability, which depends on molecular weight and structure;** • **toxicity, depending on many factors.**	

Chromophore-polymer conjugates in biology

Chromophores are a specific class of molecules, which have their activity triggered by light at a specific wavelength (*cf.* General Introduction). According to their response to light activation, three types of chromophores could be found as potentially attractive in biology: photoresponsive,[41 42 43] fluorescent[44 45] or photosensitizing chromophores.[46 47]

The strategy used for chromophore-polymer conjugation consists mainly in the coupling of chromophore molecules on a preformed copolymer chain ("grafting to" strategy in Appendix II.2). This method is easier to implement than the polymerization of a functional monomer ("grafting through" strategy in Appendix II.2), and allows a thorough characterization of the polymer prior to chromophore coupling. Moreover, it enables to accurately choose and control the amount of coupled chromophores.
Thanks to its versatility and facility to control the polymerization process, radical polymerization is the preferred technique to synthesize such conjugates. Most of chromophore-polymer conjugates are obtained using synthetic functional polymers.
The nature of the bond linking the chromophores to the polymer backbone could be degradable or non-degradable, depending on the targeted biological application. For example, degradability was usually desired for *in vivo* therapeutic applications (PDT, imaging).

This work is focused on linear chromophore-polymer conjugates, with chromophores bound to the lateral position of the polymer chain. Many existing chromophore-polymer conjugates were obtained *via* the end-group functionalization,[48] but will not be described here. The next pages will give details on the different classes of chromophore-polymer conjugates.

Photoresponsive chromophore-polymer conjugates

The majority of photoresponsive conjugates are based on azobenzene-derived block copolymers for the development of photo-switchable polymer micelles (Table II. 2).

Table II. 2: Photoresponsive chromophore-polymer conjugates.

Polymer			***Chromophore***	***Synthesis strategy***	***Application***	**Ref.**
Polymer	**Architecture**	**Chromophore-polymer bond**				
P(tBA-*co*-AA)-*b*-PAzoMA) PAA-*b*-PAzoMA	Block copolymer (ATRP)	Non degradable upon light excitation	Azobenzene (Azo) Azobenzene	Functional monomer	Reversible light-responsive micelles	49
P(NAS-*co*-NIPAM)	Random copolymer (Free-radical chain-transfer)	Non degradable upon light excitation		Post modification of reactive copolymer	Light-responsive conjugates for light-induced precipitation	50
PEO-*b*-PMA	Block copolymer (ATRP)	Cleavable by photolysis	Pyrene (Py)	Functional monomer	Irreversible light-responsive micelles	51

Zhao and coworkers[49] have reported the synthesis of amphiphilic diblock copolymers forming micelles that can be disrupted under UV light and completely reassembled under visible light. Polyazobenzene hydrophobic block of this system is polymerized by ATRP with poly(*tert*-butyl acrylate), used to tailor the hydrophilicity of the chain. The hydrophilic block poly(*tert*-butyl acrylate-*co*-acrylic acid) P(*t*BA-AA) is obtained by partial hydrolysis of P(*t*BuA) block. Figure II. 8 illustrates the structure and the conformational changes of such conjugates after light activation.

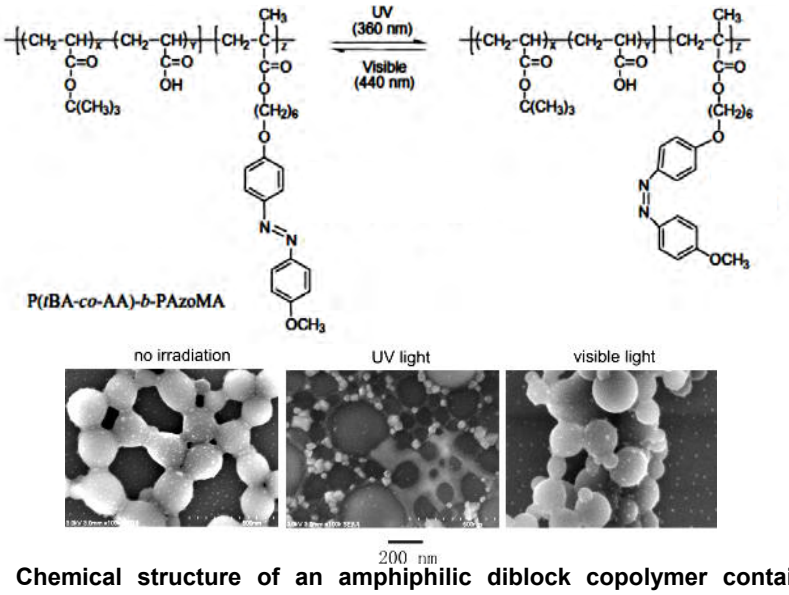

Figure II. 8: (top) Chemical structure of an amphiphilic diblock copolymer containing azobenzene chromophores. (bottom) SEM images of micelles and large micelle-like aggregates of PAzoMA-b-PAA.[49]

Zhao's group[51] used the same concept in preparing light-controlled chromophore-polymer conjugates undergoing irreversible micellar dissociation by inducing the photocleavage of pendant chromophores. The hydrophilic block in this case was PEG, and the hydrophobic block, a methacrylate monomer covalently linked with a water-insoluble pyrene. The irreversible photoinduced cleavage of pyrene moieties, triggered by one or two-photon activation, resulted in the formation of a hydrophilic copolymer backbone (Figure II. 9).

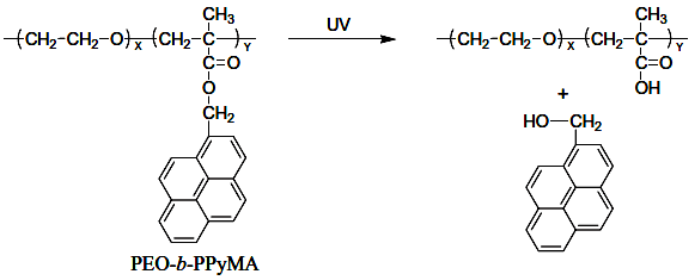

Figure II. 9: Chemical structures of two amphiphilic diblock copolymers whose hydrophobic blocks contain the pyrene moieties.[51]

In spite of their promising properties, photoresponsive conjugates rely predominantly on UV irradiation and suffer from a lack of translation to *in vivo* applications due to low tissue transparency in the UV region.

Fluorescent chromophore-polymer conjugates

The urgent need to design new bioimaging probes, with an increased sensitivity and specificity, with respect to the current molecular fluorophores, led to the development of polymer-based probes for optical imaging (Table II. 2). Thanks to the use of polymers, these new bioimaging probes exhibited prolonged plasma half-lives, enhanced stability, reduced toxicity, and improved target specificity.[52]

Table II. 3: Fluorescent chromophore-polymer conjugates.

Polymer			*Chromophore*	*Synthesis strategy*	*Application*	Ref.
Polymer	**Architecture**	**Chromophore-polymer bond**				
P(HPMA-*co*-Ma-ah-NHNH$_2$)	Random copolymer & Star copolymer (radical copolymerization)	Degradable through pH-sensitive hydrazone	DY782 & DY-66-OPB	Post modification of reactive copolymer	*In vivo*, *ex vivo* imaging of tumors	[53]

Recently P(HPMA) based random copolymer with linear and star-like architectures, was used for consecutive coupling of two different fluorescent dyes with high coupling yields (Table II. 3).[53] One fluorescent dye was coupled *via* a stable non-degradable hydrazide bond to estimate the polymer accumulation and distribution, and the other one, *via* a pH-sensitive hydrolytically cleavable hydrazone bond, to record the chromophore elimination. *In vivo* and *ex vivo* studies showed that the cleavable drug was eliminated before the polymer. Through this work, Hoffmann and coworkers demonstrated that both the polymer and the type of biodegradable spacer between polymer and chromophore play an important role in the drug-delivery process.

Photosensitizer chromophore-polymer conjugates

Various polymeric carriers have successfully been developed to overcome low solubility and nonspecific phototoxicity of hydrophobic photosensitizers (PS) (Table II. 4).[54]

Table II. 4: Photosensitizer chromophore-polymer conjugates.

Polymer			*PS*	*Synthesis strategy*	*Ref.*
Type	**Architecture**	**Chromophore-polymer bond**			
P[HPMA-*co*-(*N*-methacryloylglycylphenyl p-nitrophenyl ester)]	Random copolymer (radical precipitation)	Degradable	Mesochlorin e6 Mce$_6$	Post modification of reactive copolymer	[55]
P[HPMA-co-(*N*-methacryloyl succinimidyl ester)]	Random copolymer (radical copolymerization)	Degradable		Post modification of reactive copolymer	[56]
Glycol chitosan	Random copolymer	Degradable	Chlorine e6	Post modification of reactive copolymer	[57]

The bonding of meso-chlorine derived PS on linear N-(2-Hydroxypropyl)methacrylamide copolymers has been thoroughly investigated by Kopecek and coworkers.[55] They described the synthesis of P(HPAM) copolymer containing an amino-derived photosensitizer, meso-chlorin e6 monoethylene diamine disodium salt (Mce6), attached to the polymer backbone either *via* a degradable sequence of peptides or a non-degradable bond. Subsequently, higher cytotoxic effect was noted with the degradable conjugate. The same group synthesized later a Mec6 polymer conjugate linked *via* a disulfide (-S-S-) to P(HPMA) copolymer backbone.[56] They demonstrated that even if the disulfide is less stable in human plasma, its more efficient cleavage *in cellulo* resulted in a higher phototoxicity compared to the photosensitizer linked *via* the enzyme-sensitive peptide sequence.

Another multifunctional PS conjugate using glycol chitosan backbone (GCS, M_w = 86 000 g.mol^{-1}) for targeted cancer therapy has been recently reported (Figure II. 10).[57] As proposed by Ringersdorf's model, it contained three different pending groups: Ce6 (for phototoxicity and fluorescence monitoring of tumors), PEG (to improve the stability in serum, thus its penetration efficiency into tumor vasculature), and 3-diethylaminopropyl isothiocyanate (DEAP to improve tumor targeting).

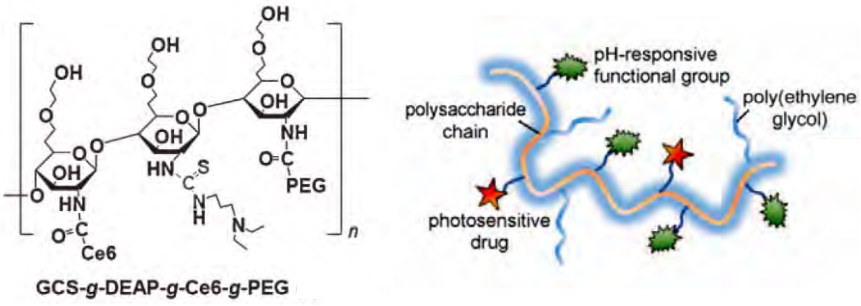

Figure II. 10: Glycol chitosan backbone grafted *via* pending amine groups with: photosensitizer Ce6, PEF and DEAP.[57]

Two-photon chromophore-polymer conjugates

The previously listed chromophores, classified with respect to their response to light excitation, can absorb generally one-photon in the UV-Vis spectral range. However, particular chromophores that can efficiently absorb two-photons of low energy (in the NearIR) are also developed (Chapter IV).

Compared to existing one-photon chromophores with relatively weak two-photon absorption properties,[58] especially-designed two-photon chromophores exhibit strong two-photon absorption cross sections.[59]

Because two-photon absorption is a key-aspect in this project, it seemed important to address it here by looking into the existing two-photon chromophore-polymer conjugates and finding very few examples (Table II. 5).

Table II. 5: Two-photon chromophore-polymer conjugates.

Polymer			***Chromophore***	***Synthesis strategy***	***Application***	***Ref.***
Type	**Architecture**	**Chromophore-polymer bond degradability**				
P(NorbornenPEG-*b*-norbornen succinimidyl ester)	Block copolymer (ROMP)	Non-degradable	Amine-terminated 2PA dyes	Post modification of reactive copolymer	Two-Photon fluorescence bioimaging	60

In a recent article,[60] new TPA chromophores have been coupled on a norbornene block copolymer (obtained by ROMP*) using post-modification of succinimidyl esters.

* ROMP = Ring-opening metathesis polymerization

This TP fluorescent polymeric probe demonstrated its high selectivity and effectiveness as carrier for two-photon microscopy and cell-specific active targeting. Its biocompatibility and targeting capacity was improved by PEG and integrin moieties attached to the polymer, ensuring longer circulatory retention time and good integrin selectivity for *in vivo* use.

To conclude, the specific class of chromophore-polymer conjugates has attracted the interest of many researchers, as they allow tuning the properties of conjugates upon light excitation. Different types of chromophores have been covalently linked to a polymer backbone for bio-oriented applications: azobenzene derived chromophores for fabrication of photoresponsive micelles; fluorophores for fluorescence bioimaging, photosensitizers for photoinduced treatment of tumors, and newly developed two-photon chromophores, that can be excited in the NearIR, for deeper *in vivo* imaging and therapy. However, to the best of our knowledge, two-photon chromophores have never been bound to polymers obtained by CRP techniques, which could improve the control over their loading and distribution along the chain.

CRP techniques present many advantages for the synthesis of well-defined polymers in a relatively easy and controlled manner, as they combine the advantages of free radical and living polymerization processes. In this context, RAFT polymerization is one of the most versatile CRP technique accessible to many functional monomers. RAFT enables a good control over molecular weights and their distribution, over end-group functionalities resulting in one thiocarbonylthio group, but also over the architecture (linear, star, comb) and the functionality along the polymer chain, for further binding events.

The successful RAFT (co)polymerization of NAM and NAS monomers has been reviewed, showing good understanding of the RAFT process by studying polymerization kinetics, experimental conditions and changes in polymer architecture (homopolymer, random and block copolymers).

Polymers can exhibit many features that make them very useful building blocks for biological applications as they can be designed or chosen to complete a number of requirements (*e.g.* water-solubility, biocompatibility, biodegradability, functionality, responsiveness to external stimuli, etc.), leading to increased therapeutic responses in biological media (bioavailability, retention, uptake, targeting etc.).

Among polymer conjugates, the specific class of chromophore-polymer has attracted the interest of many researchers, as they allow tuning the properties of conjugates upon light excitation.

In this work, the aim is to combine the advantages of functional water-soluble copolymers obtained by RAFT with those of two-photon chromophores, to obtain biocompatible two-photon chromophore-polymer conjugates with well-defined structure and composition.

II.3. Synthesis of homopolymers and reactive copolymers by RAFT polymerization

The optimized RAFT polymerization conditions of NAM and NAM/NAS monomer pair (Section II.2) were used to obtain different series of PNAM homopolymers and P(NAM-*co*-NAS) random and block copolymers with different molecular weights.

PNAM homopolymers were synthesized in order to be used in the optimization of the oriented grafting of RAFT polymer chains onto AuNP (Chapter III). Reactive P(NAM-*co*-NAS) random and block copolymers served in the last section of this chapter for the coupling of amino-derived two-photon (TP) chromophores to obtain well-defined TP chromophore-polymer conjugates.

This section will first discuss the control over the molecular weights (MW) and over chain-end functionality of the RAFT homopolymers and random copolymers. Then, the synthesis of block copolymers will be presented.

II.3.1. RAFT polymerization of NAM and NAM/NAS monomer pair

RAFT polymerization of NAM and P(NAM-*co*-NAS) was performed using the previously described experimental procedures (Experimental section II.6).[18 22] RAFT polymerization was carried out either in a Schlenk flask or in parallel reactor system (12 parallel reactors). Unlike Schlenk flasks, parallel reactors allow producing simultaneously 12 different polymers, in a relatively short time. They were used to produce homopolymers and copolymers with different molecular weights.

The key experimental parameters of RAFT homo- and copolymerization are given below ((Experimental section II.6, Figure II. 11 a)):

- Polymerization temperature was 80°C (see Experimental section II), guaranteeing a rapid polymerization and a good control over RAFT process.
- [CTA]/[AIBN]=10 was chosen to optimize the dithiobenzoate chain-end functionalization while guaranteeing a sufficiently fast polymerization rate (with azobisisobutyronitrile, AIBN, as initiator).
- Polymerization was carried out in 1,4-dioxane, a low transferring solvent.
- Initial (co)monomer concentration was set at [monomer(s)]=2 $mol.L^{-1}$, to limit the reaction medium viscosity and maintain a good control over molecular weights, while keeping a reasonable polymerization rate.

For NAM and NAS copolymerization (Figure II. 11 b)):

- [NAM]/[NAS] molar ratio was 60/40 – the azeotropic composition which leads to statistical copolymers with no compositional drift (with NAS reactive units regularly-spaced along the hydrophilic polymer backbone).
- RAFT polymerization conversion was followed by ^1H NMR spectroscopy using trioxane as an internal reference, following the procedure previously developed in the lab.[10]

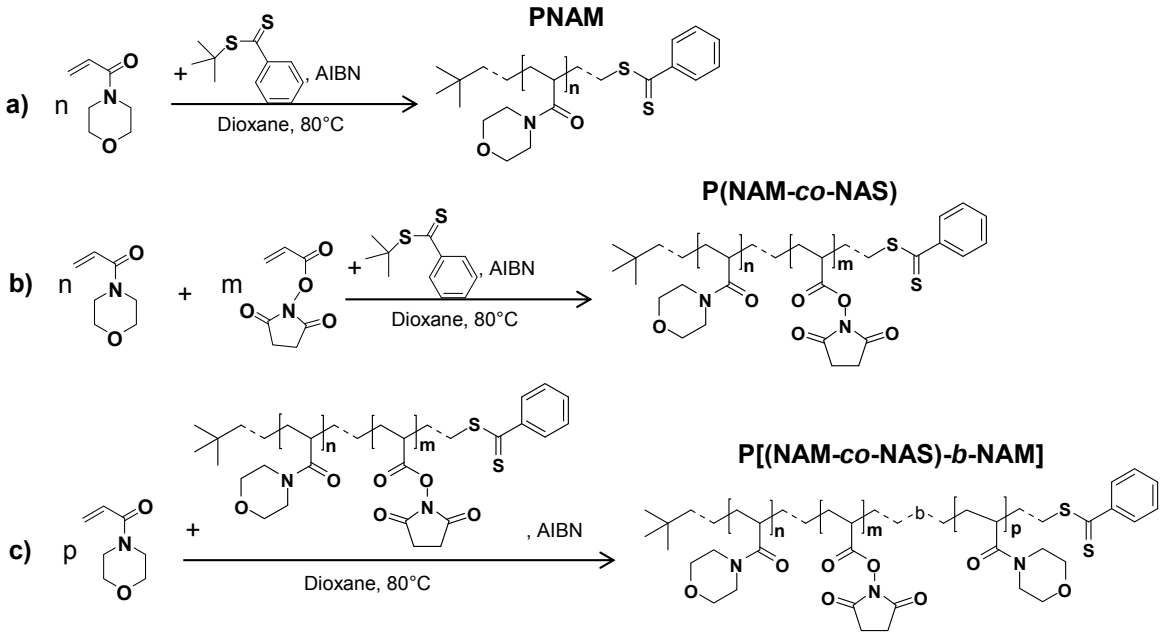

Figure II. 11: Schematic representation of RAFT polymerization reactions for: a) NAM with *t*BDB as CTA; b) NAM/NAS (co)monomer mixture (n/m=3/2) with *t*BDB as CTA; c) NAM with P(NAM-*co*-NAS) obtained by RAFT as macro-CTA.

Results of NAM homopolymerization and NAM/NAS copolymerization using the RAFT technique are recorded in Table II. 6, Table II. 7,and Table II. 8, respectively.

Absolute M_n (number average MW), M_w (weight average MW), and polydispersity indexes (PDI) values were determined experimentally both by size exclusion chromatography coupled with a refractive index detector (SEC/RI) using a PNAM calibration curve, and by size exclusion chromatography coupled with a multi-angle light scattering detector (SEC/LS), (Experimental section II.6). These values were compared to calculated and theoretical M_n values obtained from equations in Appendix II.1 (M_n(calc) and M_n(theo)).

Table II. 6: PNAM polymers obtained in Schlenk tube (polymers analyzed after aminolysis of DT groups). Molecular weights are expressed in g.mol^{-1}.

Sample	Conv. (time)	SEC/RI			SEC/LS		
		M_n	M_w	PDI	M_n	M_w	PDI
*PNAM*_P1	0.30 (30 min)	6 200	7 300	1.18	6 500	7 500	1.06
PNAM _P2	0.70 (40 min)	12 800	15 100	1.16	14 100	14 200	1.03
PNAM _P3	0.79 (1 h)	14 500	16 600	1.12	14 800	15 900	1.04

Table II. 7: Poly(NAM) polymers obtained in parallel reactor system. Molecular weights are expressed in g.mol^{-1}.

Sample	Conv. (time)	SEC/RI			SEC/LS		
		M_n	M_w	PDI	M_n	M_w	PDI
PNAM _1	0.74 (3 h)	3 500	3 980	1.13	3 300	3 100	1.01
PNAM _2	0.82 (3 h)	5 660	6 070	1.09	4 600	4 600	1.01
PNAM _3	0.85 (3 h)	10 800	11 500	1.08	8 900	9 700	1.08
PNAM _4	0.88 (3 h)	14 400	17 000	1.18	13 400	14 600	1.07
PNAM _5	0.89 (3 h)	20 700	23 000	1.13	18 000	19 500	1.08
PNAM _6	0.91 (3 h)	26 400	33 900	1.27	26 400	30 200	1.11
PNAM _7	092 (3 h)	30 600	46 130	1.42	33 200	39 700	1.14
PNAM _8	0.90 (3 h)	37 300	54 900	1.37	36 100	44 500	1.17
PNAM _9	0.91 (3 h)	38 400	65 800	1.51	39 400	53 350	1.24
PNAM _10	0.90 (3 h)	41 400	75 700	1.60	47 300	60 900	1.20
PNAM _11	0.88 (3 h)	50 300	87 800	1.53	57 800	71 700	1.12
PNAM _12	0.88 (3 h)	54 100	109 600	1.72	60 700	86 700	1.19

Table II. 8: Random P(NAM-*co*-NAS) copolymers obtained in parallel reactor system. Molecular weights are in g.mol-1.

Sample	Conv. (time)	SEC/LS		
		M_n	M_p	PDI
COPO_1	0.72 (13 h)	2 200	1 800	1.06
COPO _2	0.89 (13 h)	5 300	5 500	1.02
COPO _3	0.92 (13 h)	10 910	11 100	1.04
COPO _4	0.91 (13 h)	15 800	16 500	1.04
COPO _5	0.88 (13 h)	19 200	20 800	1.04
COPO _6	0.89 (13 h)	19 400	21 700	1.07
COPO _7	0.88 (13 h)	26 400	28 800	1.09
COPO _8	0.87 (13 h)	23 000	27 100	1.11
COPO _9	0.86 (13 h)	29 600	30 500	1.04
COPO _10	0.63 (13 h)	34 600	35 700	1.07
COPO _11	0.46 (13 h)	34 200	37 400	1.10
COPO _12	0.78 (13 h)	59 900	71 700	1.11

- Due to the good control of end-group functionality,[19] RAFT polymers can be used as macro-CTA for the elaboration of block copolymers (Figure II. 11 c)).[22] We have used one of P(NAM-*co*-NAS) random copolymers, COPO_8, as macro-CTA in the polymerization of a 2nd PNAM block.(Table II. 9).

Table II. 9: P[(NAM-*co*-NAS)-*b*-NAM] block copolymers obtained in Schlenk flask using COPO3_8 as macro-CTA for the polymerization of NAM as a 2nd block. Molecular weights are expressed in g.mol^{-1}.

Sample	Macro-CTA		Conv. (NAM)	SEC/LS		
	Sample	M_n		M_n	M_p	PDI
BLOCK_1	COPO_8	23 000	0.80 (3 h)	35 000	40 900	1.18
BLOCK_2			0.76 (3 h)	39 400	49 000	1.19

II.3.2. Control over molecular weights and molecular weight distribution

II.3.2.1. NAM homopolymerization in Schlenk flask

In Schlenk flask, PNAM with different molecular weights were obtained by extracting samples from the reaction medium, at different polymerization times, using a canula. The kinetics of NAM polymerization by RAFT was similar to the previously reported data (Appendix II.3).[10] As predicted by RAFT theory, and already reported for this CTA/monomer pair, the molecular weights increased linearly with monomer conversion (Appendix II.3). Experimental M_n values, determined either by SEC/LS or SEC/RI, were in good agreement with predicted values, and exhibited low polydispersity (PDI<1.1). At high conversion (>80%), the risks of side-reactions (*e.g.* transfer reactions) increases, leading to slightly lower experimental M_n values than values predicted by theory (*PNAM*_P3, Figure II. 12).[22]
The good control over PNAM molecular weight distributions is illustrated in Figure II. 12, showing that polydispersity indexes of all PNAM samples are < 1.1.

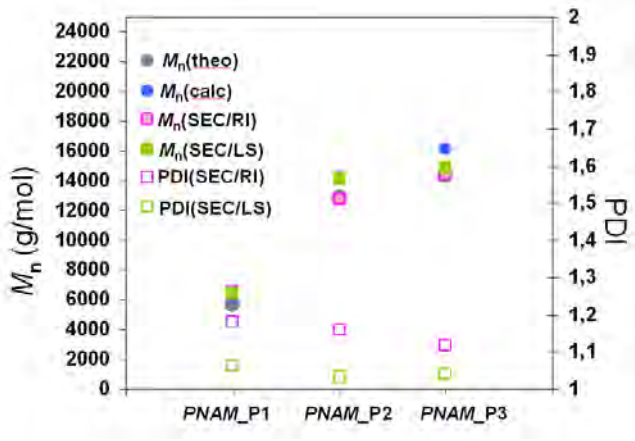

Figure II. 12 : Molecular weights (M_n) and polydispersity indexes (PDI) of PNAM polymers synthesized by RAFT in Schlenk flask. Theoretical M_n – grey circles, calculated M_n – blue circles, M_n(SEC/RI) – pink squares, M_n(SEC/LS) – green squares; PDI(SEC/RI) – open pink squares, PDI(SEC/LS) – open green squares.

II.3.2.2. NAM homopolymerization and NAM/NAS copolymerization in parallel reactors

Two sets of polymerizations were conducted in the 12-parallel reactor system: a) homopolymerization of NAM (Table II. 7); b) statistical copolymerization of NAM with NAS (60/40 azeotropic molar composition), (Table II. 8). In each case, the targeted molecular weight (MW) of the RAFT (co)polymer increased with the reactor number (Experimental section II.6).

Overall, high conversions have been attained at the end of RAFT (co)polymerization in parallel reactors (Figure II. 13).

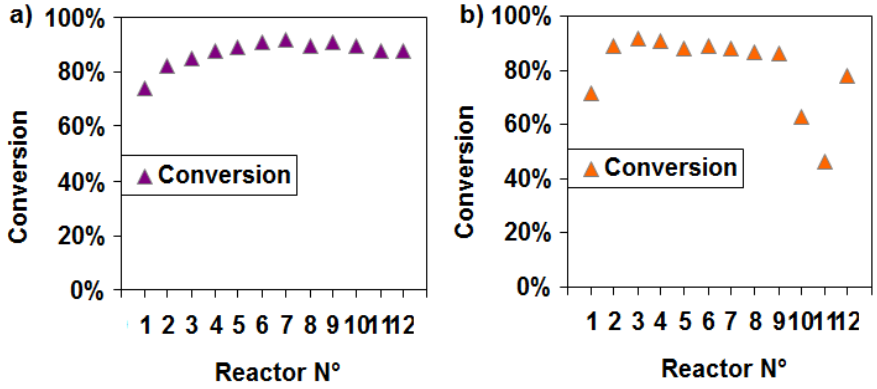

Figure II. 13 : Conversion of polymers synthesized in parallel reactors: a) PNAM_X series – PNAM polymers; b) COPO_X series – P(NAM-*co*-NAS) copolymers.

For PNAM (PNAM-X series) and P(NAM-*co*-NAS) (COPO_X series), monomer conversion was higher than 85% after 3 hours in most of the cases. However, lower conversions were observed for few samples: reactors N°1, corresponding to the lowest targeted MW, thus to the reactor with the highest CTA concentration;[61] and reactors N°10, 11 and 12 in the case of the NAM/NAS copolymerization, corresponding to high targeted MW (low AIBN concentration).

It is worth mentioning that the reproducibility of RAFT polymerization kinetics in parallel reactors could be significantly impacted by differences in terms of induction period, retardation, amount of remaining oxygen. For instance, during RAFT copolymerization, a larger induction period has been qualitatively witnessed in reactors N°10 and 11 (evidenced by a slow color change of the reaction medium[*]). This probably explains the much lower conversions obtained in these reactors.

Like in Schlenk flask, similar observations about the experimental M_n values < 40 000 g.mol^{-1}could be made in parallel reactors: M_n(SEC/RI) and M_n(SEC/LS) were in good agreement with predicted M_n (Figure II. 14), molecular weight distributions were narrow (PDI < 1.2). However, for higher targeted M_n, the difference between theoretical and experimental values increased (Figure II. 14), a

[*] Initial polymerization medium is purple due to the initial *t*BDB CTA. Final polymerization medium is orange as the chromophoric dithiobenzoate moiety is transferred to polymer chain ω-end.

phenomenon that was already evidenced for such systems,[62] suggesting that some irreversible transfer reactions (favored at high conversions and by the increased viscosity) may also occur.

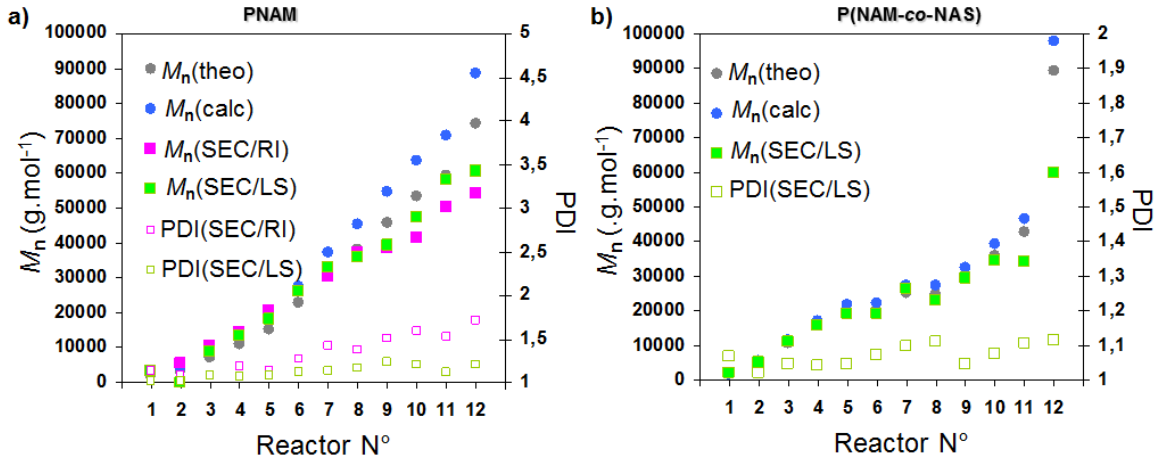

Figure II. 14: Molecular weights (M_n) and polydispersity indexes (PDI) of: a) PNAM polymers (PNAM_X) and b) P(NAM-*co*-NAS) copolymers (COPO_X) synthesized in parallel reactors. Theoretical M_n – grey circles, calculated M_n – blue circles, M_n(SEC/RI) – pink squares, M_n(SEC/LS) – green squares; PDI(SEC/RI) – open pink squares, PDI(SEC/LS) – open green squares.

Overall, SEC/LS and SEC/RI gave similar results, although, for low molecular weights (M_n < 5000 g.mol^{-1}), values determined by SEC/LS seemed less accurate due to the weak scattered intensity.

For low MW polymers and copolymers (M_n < 10 000 g.mol^{-1}), two other analytical techniques (^{1}H NMR and MALDI-TOF) were used to determine the M_n of PNAM and P(NAM-*co*-NAS) polymers.[19]

- M_n values can be determined by ^{1}H NMR if the protons corresponding to the chain-ends can be quantified (Appendix II.4). This technique tends thus to be less accurate for high molecular weights. It is also dependent on any traces of impurities (solvents, reagents).
- MALDI-TOF can also be used to determine M_n values if polymer chains can be desorbed / ionized, *i.e.* generally when M_n is < 10 000 g.mol^{-1} (Appendix II.5).[10] Comparative results of M_n determined by different methods are reported in Table II. 10.

Table II. 10 : Experimental M_n (g.mol^{-1}) determined by SEC/LS, ^{1}H NMR, MALDI-TOF *vs.* theoretical M_n values.

Polymer	M_n(calc)***	M_n(theo)***	SEC/LS		M_n ^{1}H NMR		MALDI-TOF	
			M_n	PDI	Ref1.= 2 aromatic protons at 7.9ppm**	Ref2.= 9 aliphatic protons at ~0.8ppm**	M_n	PDI
PNAM_1	2 440	2100	3 300	1.13	4 200	3 200	3 260	1.06
PNAM_2	4 300	3600	4 600	1.09	4 800	4 000	4 530	1.06
PNAM_3	8 860	7300	8 900	1.08	8 400	6 500	-	-
COPO_1	1 800	1 670	2 200	1.07	2 700	2 400	3 200*	1.09*
COPO_2	5 510	5 070	5 300	1.02	5 300	5 900	-	-
COPO_3	11 490	10 520	10 900	1.05	15 900	12 500	-	-

* Distorted baseline of MALDI-TOF chromatogram, impacting the results.

**The integral of aromatic (7.9ppm) / aliphatic (~0.8ppm) protons was taken as reference for the calculation of the rest of integrated regions on the ^{1}H NMR spectrum.

***Calculated from formulae in Appendix II.1.

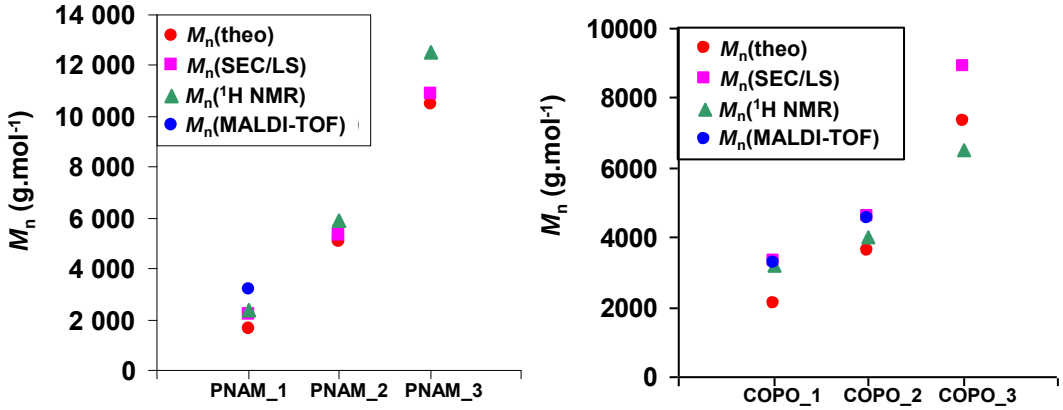

Figure II. 15: M_n values were determined by calculations M_n(theo) (red circle); by SEC/LS (spink quare); ^{1}H NMR (green triangles); MALDI-TOF (blue circles). a) PNAM series (PNAM-1,2,3); b) P(NAM-*co*-NAS) series (COPO_1,2,3).

A rather good agreement was found between the different experimental and theoretical M_n values, confirming the efficient polymerization control (Figure II. 15). Existing variations can be ascribed to experimental errors.

In conclusion, RAFT polymerization and copolymerization of NAM has been carried out using optimized conditions in Schlenk flask and in parallel reactors. In both types of reaction vessels a good control over molecular weights was achieved. The use of independent analytical techniques SEC/LS, SEC/RI, ^{1}H NMR spectroscopy and MALDI-TOF confirmed the good agreement between experimental and theoretical M_n values.

II.3.3. Control of chain-end functionalities

Besides the control of molecular weights, RAFT polymerization allows the control of chain-end functionalities *via* the use of CTA (*t*BDB) (Figure II. 2). At the end of *t*BDB-mediated polymerization, we expect that the large majority of polymer chains bear at the α-end a *tert*-butyl group and at the ω-end a dithiobenzoate (DT) group.

Control of the chain-end functionality is of particular importance in this project since the DT end-group is required to synthesize block copolymers (see below) and will be used (after conversion into thiol) for the oriented grafting of RAFT polymer chains onto the AuNP.

DT chain-end functionalization after RAFT (co)polymerization was quantified by determining the percentage of DT end-groups (DT%) (Eq. (1)) as the ratio between DT-ended chains and the total number of chains:

$$DT\% = \frac{Nb.chains\_DT}{Nb.chains\_total} \times 100\% \quad (1)$$

DT%, which is sometimes called the percentage of living chains, is usually determined by ^{1}H NMR or MALDI-TOF mass spectrometry,[19] but may also be deduced from other methods as the ratio between experimental and predicted M_n, or UV-Vis spectroscopy (Appendix II.6).

MALDI-TOF

Microstructure of MALDI-TOF spectra enables to access the molecular weight of polymer chain-ends. However, since high MW polymers (generally > 10 000 g.mol^{-1}) are poorly desorbed from the matrix, these data are only accessible for low MW polymers. A detailed MALDI-TOF study has already been conducted to quantify the DT% for PNAM produced by RAFT polymerization, leading typically to DT% values >95%.[19] The same methodology was followed to determine DT% of the low MW polymer samples synthesized either in Schlenk tube or in parallel reactors.

For our samples, the chemical nature of chain-end groups could be determined from MALDI-TOF analysis, carried out in collaboration with Catherine Ladavière (IMP, LMPB Lyon).

^{1}H NMR spectroscopy

On ^{1}H NMR spectrum of PNAM-DT obtained by RAFT, we can distinguish separately the aromatic protons corresponding to DT ω-chain-end (7 – 8 ppm), the protons corresponding to the polymer backbone (NAM: 1 – 4 ppm) and the *tert*-butyl protons of the α-chain-end (9 aliphatic protons, 0.8 – 1 ppm) (Appendix II.4).

If we approximate the integral of aromatic phenyl protons (7 – 8 ppm) with the number of DT chain-ends, and the integral of aliphatic *tert*-butyl protons (0.8 – 1 ppm) with the total number of chains, then DT% can be estimated as follows (Eq. (2)):

$$DT\% = \frac{I_{NMR\_aromaticH(7-8\,ppm)}}{I_{NMR\_aliphaticH(0-1\,ppm)}} \times 100\% \quad (2)$$

Note: The integrals should be normalized by the number of corresponding protons.

Considering this approximation and the lower accuracy of NMR broad peak integration, it has to be noted that this method may be associated with some errors. In addition, since the proportion of chain-ends decreases with the polymer MW, ^{1}H NMR method can only be applied for low MW polymers for which chain-end concentration is above NMR detection.

Even if only results obtained by MALDI-TOF and ^{1}H NMR spectroscopy are reported below, other analytical techniques may potentially be used to deduce DT% (Appendix II.6).

II.3.3.1 Analysis of chain-end functionality after RAFT (co)polymerization

Results for low M_n (co)polymers (M_n < 10 000 g.mol^{-1}), synthesized in parallel reactors, are reported in Table II. 11.

Table II. 11 : Estimation of the percentage of DT-terminated chains (DT%) after RAFT (co)polymerization of NAM and NAM/NAS in parallel reactors, by MALDI-TOF and ^{1}H NMR.

PNAM	DT%	
	MALDI-TOF	^{1}H NMR
PNAM_1	>85%	134%
PNAM_2	>85%	121%
PNAM_3	-	97%
COPO_1	>90%	87%
COPO_2	-	113%
COPO_3	-	78%

Among other techniques, ^{1}H NMR spectroscopy is very rapid and convenient to estimate the M_n via the end-group analysis, however, its accuracy decreases with the increasing MW due to the increasing difficulty to measure accurately the ratio between strong polymer backbone signals and always weaker end-group signals. It has been previously investigated and shown that the errors related to this technique can reach up to 20%.[63]

All together, we can conclude that for almost all RAFT (co)polymers the percentage of DT end-groups is very high, at least >85%, enabling to further use this polymers and copolymers as macro-CTA to obtain block copolymers by RAFT polymerization of a 2nd monomer.

II.3.4.2 Analysis of chain-end functionality after aminolysis of PNAM polymers

It has been mentioned in the previous section that DT end-groups can be quantitatively transformed into thiols by reaction with primary amines (Figure II. 16). [64] [65]

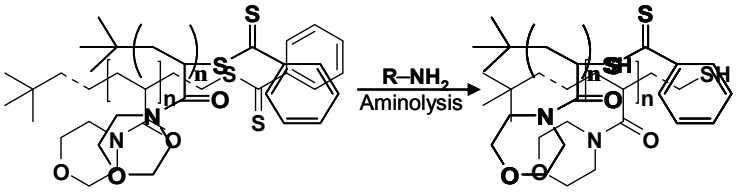

Figure II. 16: PNAM-DT aminolysis with a primary amine.

*PNAM*_PX series was treated by aminolysis after polymerization (Experimental section II.6). The MALDI-TOF chromatogram of *PNAM*_P1 polymer, illustrated in Figure II. 17, showed that the very large majority of the polymer chains in this sample are thiol-terminated chains (>99%).

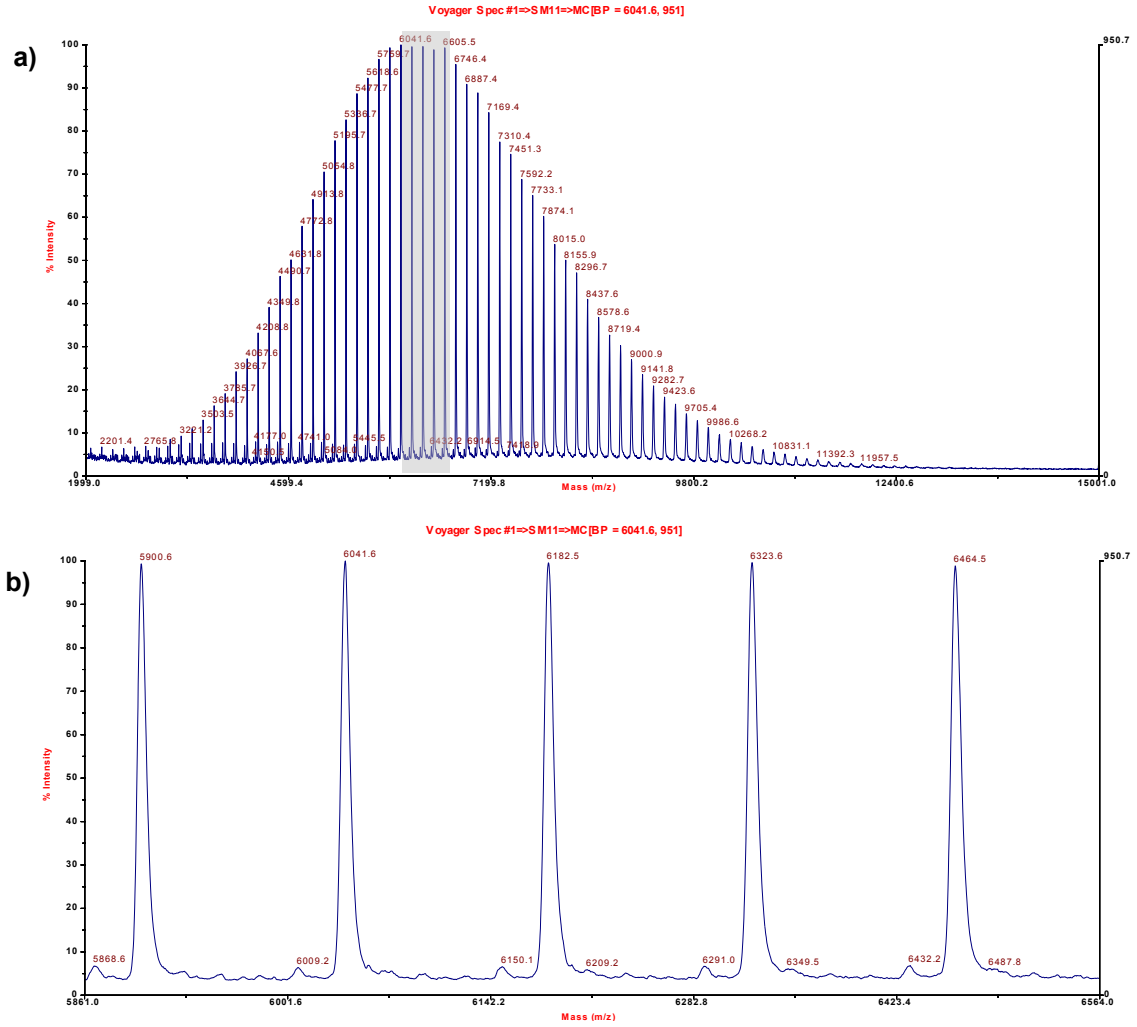

Figure II. 17: MALDI-TOF spectrogram (linear mode) of *PNAM*_P1 after aminolysis: a) MALDI-TOF chromatogram; b) zoom in on the marked zone above.

Compared to PNAM-DT before aminolysis, where the DT%~85% (Table II. 11), PNAM-SH shows a higher degree of chain-end functionalization (DT%~99%). This difference is possibly due to the fragmentation of some PNAM-DT chains in the spectrometer, leading to an underestimated DT%.[10]

II.3.4. Block copolymers

Thanks to the efficient control over chain-end functionality, RAFT (co)polymers can be used as macro-CTA to control the polymerization of a second block (Figure II. 18).

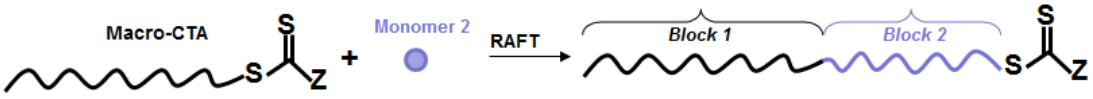

Figure II. 18: RAFT synthesis of block copolymers using a macro-CTA.

To obtain a block copolymer structure, P(NAM-*co*-NAS) copolymer (sample COPO_8) was used as macro-CTA for the polymerization of a second PNAM homopolymer block (Figure II. 11 c)).[22]

In addition to a previously synthesized sample (AF122T3), two other block copolymers with identical reactive blocks (23 000 g.mol^{-1}), but with different PNAM ones (12 000 and 16 400 g.mol^{-1}) were prepared from two polymerizations in Schlenk flask (Table II. 9).

After 3 hours of polymerization, approximately 80% conversion is reached in both cases. After purification by precipitation in diethyl ether, MW were determined by SEC/LS. Even if the initial viscosity of the reaction medium increased due to the presence of the macro-CTA, experimental MW were in very good agreement with theoretical M_n(theo) values and dispersity remained low (PDI<1.2).

These results proved the good control of the block copolymerization. Two block copolymers with PNAM blocks of 12 000 and 16 400 g.mol^{-1} respectively were obtained in gram scale. Therefore, three different block copolymers were available for further study (Table II. 12).

Table II. 12: Characteristics of P[(NAM-*co*-NAS)-*b*-NAM] block copolymers. M_n of two blocks is given in g.mol^{-1}.

Sample	Block 1 P(NAM-co-NAS) M_n	Block 2 PNAM M_n	PDI
AF122T3	21 600 (85 NAM & 56 NAS)	7 800 (54 NAM)	1.20
BLOCK_1	23 000 (90 NAM & 60 NAS)	12 0000 (83 NAM)	1.18
BLOCK_2		16 400 (114 NAM)	1.19

Using RAFT CRP technique, various polymers with controlled molecular weight and chain-end functionality were synthesized in a short time (<3 hours), either in Schlenk flask or in parallel reactors. This allowed to obtain different samples of PNAM homopolymers, P(NAM-*co*-NAS) random copolymers and P[(NAM-*co*-NAS)-*b*-NAM] block copolymers (Table II. 13).

Table II. 13: List of polymers and copolymers synthesized during the course of this work.

Sample	M_n (g.mol^{-1})	PDI
PNAM	3 000 – 61 000	< 1.2
P(NAM-*co*-NAS)	2 000 – 60 000	< 1.2
P[(NAM-*co*-NAS)-*b*-NAM]	30 000 – 50 000	~1.2

High conversions (>80%) and a good agreement between experimental and theoretical MW were obtained after RAFT polymerization of NAM and NAM/NAS (co)monomer pair. However, for high targeted MW (> 50 000 g.mol^{-1}), experimental values seemed lower than expected, which was probably due to some irreversible transfer reactions.

For (co)polymers with M_n < 10 000 g.mol^{-1} experimental MW determined by SEC/LS, ^{1}H NMR and MALDI-TOF techniques were in good agreement with theoretically predicted M_n values. These techniques were also used to quantify the percentage of DT-terminated chains (DT% >90%) of RAFT (co)polymers, confirming the good control over chain-end functionality.

Finally, block P[(NAM-*co*-NAS)-*b*-NAM] copolymers were produced by RAFT using a P(NAM-*co*-NAS) sample as macro-CTA. The polymerization of the second PNAM block was achieved with efficient control over M_n and molecular weight distribution.

Water-soluble PNAM polymers with various MW were mainly destined to optimize and study the thiol-oriented grafting onto AuNP in aqueous medium (Chapter III). Thiol-terminated PNAM samples were then prepared by aminolysis of the DT chain-ends. Quantitative conversion of DT into thiols was evidenced by MALDI-TOF.

P(NAM-*co*-NAS) random and block copolymers will be used in the next section to obtain well-defined chromophore-polymer conjugates by covalent coupling of chromophores onto the reactive lateral functions of copolymer NAS units.

II.4. Elaboration of chromophore-polymer conjugates

II.4.1. Strategy of chromophore coupling

The goal of this chapter was to synthesize well-defined two-photon (TP) chromophore-polymer conjugates completing a certain number of requirements relative to both their application in biological media and their grafting onto AuNP.

The final structure of desired conjugates is illustrated in Figure II. 19.

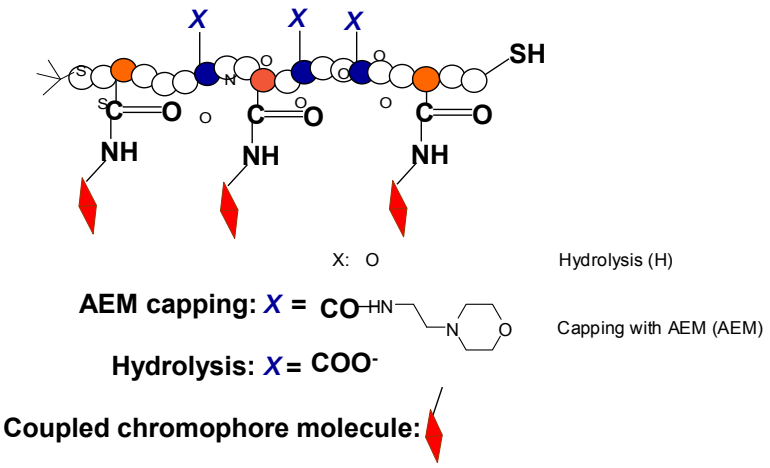

Figure II. 19 : Final structure of chromophore-polymer conjugates after coupling and post-treatment steps.

In order to obtain chromophore-polymer conjugates, the strategy proposed in the introduction of the chapter (Figure II.1) consisted in:

1. Synthesis of reactive P(NAM-*co*-NAS) copolymers by RAFT polymerization.

The synthesis and characterization of reactive random and block copolymers by RAFT polymerization was detailed above (Section II.3). RAFT technique gives functional copolymers, with random and block architectures, well-defined M_n and narrow MW distributions, and also with reactive lateral succinimide groups (on NAS units).

2. Coupling of amino-derived TP chromophores on the reactive polymer chain.

Chromophore coupling reaction allows to tune the desired number of chromophores *per* chain and study its influence on the properties of polymer conjugates, but also on the properties of grafted AuNP (Chapter III and Chapter IV).

3. Post-treatment of residual reactive groups on the TP chromophore-polymer conjugates.

Post-treatment of residual succinimide (NAS) esters was subsequently applied, whether by AEM capping or by hydrolysis, giving respectively stable and neutral conjugates or stable and negatively charged conjugates.

The steps 2 and 3 will be detailed in this section.

II.4.2. Chromophores used for coupling

Two different TP chromophores, presenting a push-pull-push structure and based on an anthracene (Ant) or a dibromobenzene (DBB) core, respectively, were used for this study. They were developed by the team of Chantal Andraud (T. Gallavardin, O. Maury, P.-H. Lanoe, J.-C. Mulatier, C. Monnereau) at the Chemistry Laboratory of ENS Lyon.[66] However, considering their high-added value, we also synthesized conjugates with a commercially-available chromophore, Lucifer Yellow Cadaverine (LY), in order to optimize the grafting of the chromophore-polymer conjugates onto the AuNP and to study more extensively the influence of various parameters (*e.g.* polymers chain length) on their properties.

II.4.2.1. Lucifer Yellow Cadaverine (LY)

Lucifer Yellow Cadaverine is a water soluble chromophore, a derivative of Lucifer Yellow family which has found a large use as fluorescent markers in cell biology,[67] allowing good detection levels in living cells without toxic effects even at high concentration.
Its structure (Figure II. 20), based on a sulfonated 4-amino-1,8-naphthalimide moiety, bears a primary aliphatic amine group (C6 linker) for efficient reaction with succinimide pendant groups (NAS units) present on the copolymer chain. Although its solubility in polar organic solvents is limited, it is characterized by good water solubility (thanks to the presence of two sulfonate groups). LY exhibits a mild fluorescence quantum yield (30 %), wide spectral separation of absorption and emission maxima (430 and 530 nm, respectively).

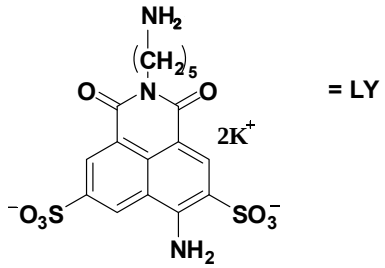

Figure II. 20: Chemical structure of Lucifer Yellow Cadaverine (LY).

LY-polymer conjugates, using P(NAM-*co*-NAS) RAFT copolymers, have been previously synthesized and characterized in our group. Extensive studies of Paula Relogio during her PhD[68] demonstrated their enhanced resistance to photobleaching and limited fluorescence quenching upon increase of the density of LY chromophores *per* polymer chain. Although, for this particular work, LY was not the best choice because of its very weak two-photon absorption capacity, LY chromophore has been chosen for several practical reasons, as availability and cost, to synthesize model chromophore-polymers conjugates for further extensive studies on grafted AuNP.

II.4.2.2. Two-Photon Anthracene (Ant) and Dibromobenzene (DBB)

Anthracene (Ant) and dibromobenzene (DBB) (Figure II. 21) are two water-insoluble chromophores that were designed and obtained through a multistep synthesis in the ENS-Lyon Chemistry Laboratory (C. Andraud's group). Both these chromophores exhibit the following characteristics:

- a quadrupolar structure with strong electro-donating end-groups and extended π-conjugated skeleton, known to exhibit a significant TPA cross-sections, while ensuring a high fluorescence quantum yield for the Ant derivative and an high singlet oxygen production for the DBB one *via* an intersystem crossing mechanism favored by the bromine atoms;[69]
- two short PEG chains to improve their hydrophilicity;
- and a primary amine group for efficient covalent coupling onto the P(NAM-*co*-NAS) copolymers.

a)

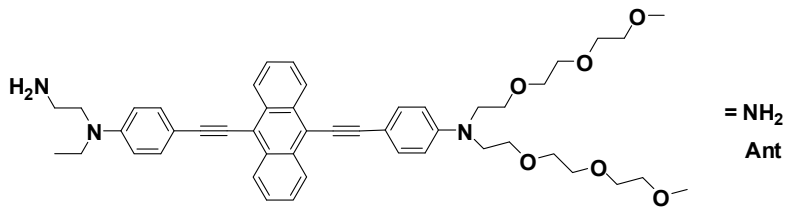

b)

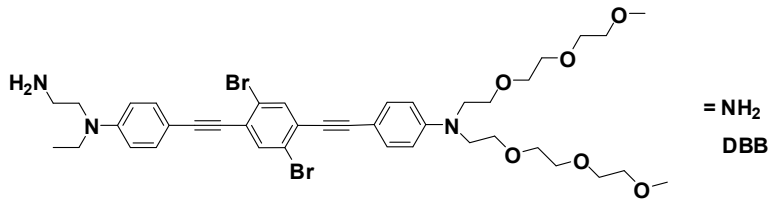

Figure II. 21: Chemical structure of a) Ant and b) DBB chromophores.

II.4.3. Experimental approach: coupling, post-treatment and purification

II.4.3.1. Coupling

The covalent coupling of amino-functionalized chromophores on the lateral position of P(NAM-*co*-NAS) copolymers (Figure II. 22) was carried out in solution, under mild conditions, *via* the reaction with the activated ester groups (of NAS units), resulting in the formation of stable amide bonds (more stable than ester bonds[70]). Reactions were conducted in homogeneous conditions, using an organic solvent where both the chromophore and polymer are soluble, to ensure an efficient coupling: dimethylformamide (DMF) for LY, and chloroform ($CHCl_3$) for Ant and DBB. The stoichiometry was adjusted depending on the targeted number of chromophores *per* chain (Nc) and assuming a final coupling yield equal to 80-90%.

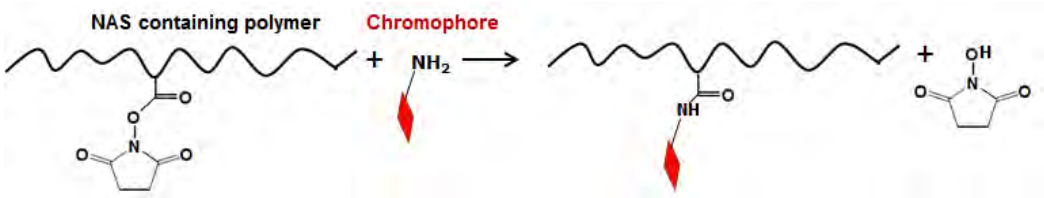

Figure II. 22: Schematic representation of the reaction between NAS pendant groups on the lateral position of the copolymer chain and the primary amine group of the chromophore. Reaction products include chromophore-polymer conjugates (coupled chromophores along the polymer chain *via* amide bonding) and the *N*-hydroxysuccinimide (NHS) as secondary product.

Several P(NAM-*co*-NAS) copolymers with different molecular weights (2 000 g.mol^{-1} < M_n < 35 000 g.mol^{-1}) and different architectures (random or block) were used for chromophore coupling. The properties of RAFT copolymers used for coupling are summarized in Table II. 14.

Table II. 14: Characteristics of P(NAM-*co*-NAS) copolymers used in chromophore coupling.

Copolymer used for coupling	Architecture	Molecular weight (g.mol-1)	PDI
COPO_1	Random	2 200 g.mol-1	1.06
AH8T2*	Random	7 900 g.mol-1	1.05
AH6T7*	Random	12 900 g.mol-1	1.05
COPO_10	Random	34 600 g.mol-1	1.07
AF122T3**	Block	Block1: P(NAM-*co*-NAS)_21 600 g/ mol Block2: PNAM_7 800 g.mol-1	1.10
BLOCK_1	Block	Block1: P(NAM/NAS)_23 000 g/ mol Block2: PNAM_12 000 g.mol-1	1.18

*Synthesized by A. Harzallah

**Synthesized by A. Favier

II.4.3.2. Post-treatment

After chromophore coupling, the residual unreacted NAS units were post-treated. Two different post-treatments were used to increase the water-solubility of the conjugates (Figure II. 23):

- Capping with a large excess of water-soluble primary amine, *4*-(*2*-aminoethylmorpholine) (AEM). The succinimidyl group of the NAS units is substituted by AEM, leading to neutral conjugates.
- Hydrolysis in a borate buffer (50mM, pH=9). Hydrolysis of succinimide esters results in carboxylate COO^- pendant groups, thus leading to negatively charged chromophore-polymer conjugates (the counter ion being mainly Na^+).

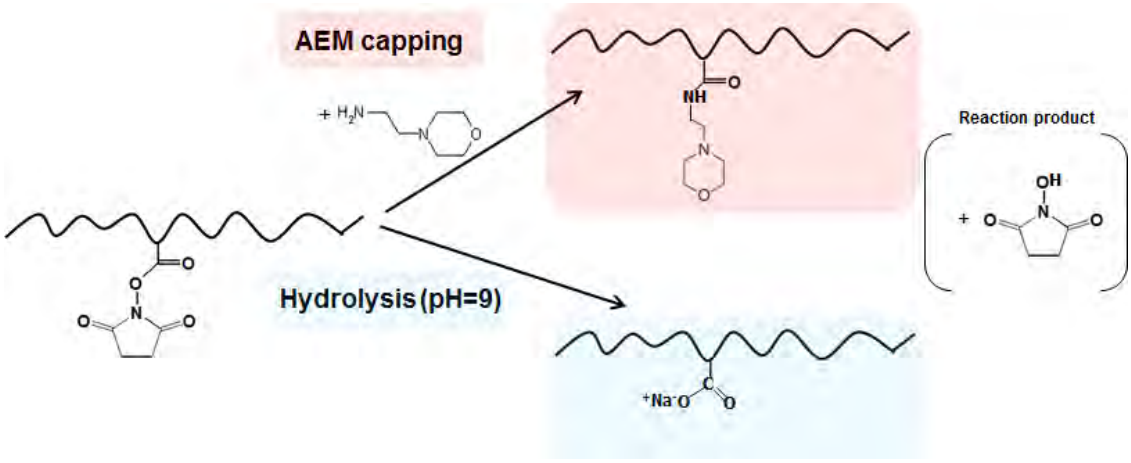

Figure II. 23: Schematic representation of the post-treatment of residual NAS units by either capping with AEM or hydrolysis.

Both post treatment techniques led to the transformation of DT end-group of the conjugates into thiol end-groups (see below).

II.4.3.3. Purification

Isolation of the chromophore-polymer conjugates from the free unreacted chromophores was an important step, especially regarding their accurate spectroscopic characterization and their use in biological media. Purification of conjugates was achieved by successive precipitations in diethyl ether, a poor solvent of the polymer and of the chromophore-polymer conjugates, but a good solvent of the free chromophores. This procedure was followed by dialysis (cellulose membrane, MWCO=2000Da) in the case of water-soluble conjugates.

The high efficiency of the purification technique was confirmed using SEC/UV analyses by comparing the chromatograms corresponding to the final coupling reaction medium (blue), the purified conjugate (pink) and the free chromophore (green) (Figure II. 24). No peak corresponding to the free chromophore (higher elution time) was evidenced in the purified sample of chromophore-polymer conjugate (21Ant-AEM, Ant-polymer conjugate, carrying 21 Ant chromophores *per* chain, post-treated by AEM capping).

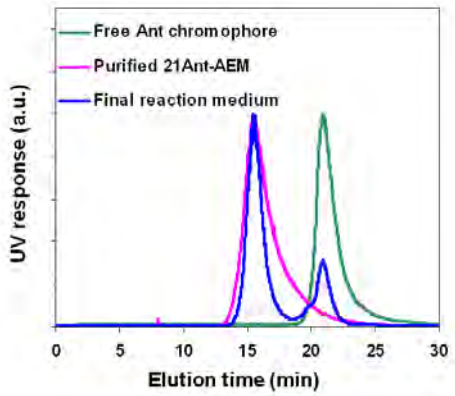

Figure II. 24: SEC/UV chromatograms recorded at 510nm corresponding to: free Ant chromophore (green), purified 21Ant-AEM conjugates (purple), and final coupling reaction mixture (blue).

II.4.4. Monitoring the chromophore coupling reaction and the number of chromophores *per* chain (Nc)

II.4.4.1. Monitoring chromophore coupling

Coupling reaction between P(NAM-*co*-NAS) and chromophores could be monitored using different techniques:

1. SEC/UV
2. ^{1}H NMR
3. UV-Vis and fluorescence spectroscopy
4. Color change of the polymer after coupling

1) SEC/UV

Coupling yields and the nu before post-treatment by SEC/UV – size ion set at the maximum absorption wavele

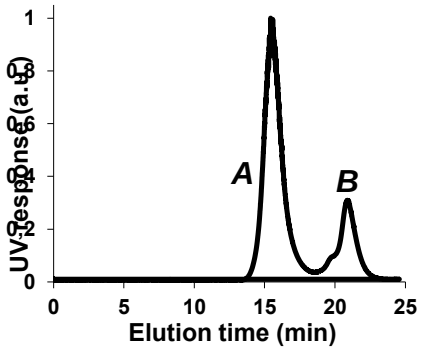

Figure II. 25: SEC/UV chromatogram of the reaction medium after the coupling of amino-derived chromophores on the P(NAM-*co*-NAS) copolymer chain.

Two different peaks could be distinguished (Figure II. 25): (*A*) chromophores bound to the copolymer chains (lower elution volume), (*B*) free unbound chromophores. *A* and *B* being the areas under each of these peaks. The coupling yield (*Y*) was determined using Eq. (3), assuming that chromophore absorption properties remained unchanged after coupling onto the copolymer. The latter assumption was validated by determination of the extinction coefficients (ε) in DMF for both the free chromophore and the chromophores bound onto the polymer: similar values of ε were obtained, within $\pm$10% error.

$$Y = \frac{A}{A+B} \quad (3)$$

$$Nc = Y \times Nc_{targeted} \quad (4)$$

Y is the coupling yield and $Nc_{targeted}$ – the expected number of chromophores *per* chain at 100% coupling yield, *i.e.* the ratio between the initial number of chromophores and the initial number of copolymer chains). The number of chromophores *per* chain (Nc) at the end of the coupling could then be deduced from Eq. (4).

2) ^{1}H NMR

^{1}H NMR analysis has been performed on purified chromophore-polymer conjugates (Appendix II.7). It allowed not only to detect the presence of chromophores in the conjugate structure, *via* the high amount of aromatic protons corresponding to coupled chromophores, but also to calculate Nc, by quantifying the amount of chromophores from the ^{1}H NMR spectra (Appendix II.7). Even if results obtained by ^{1}H NMR are in good agreement with Nc values determined by SEC/UV (see discussion below), ^{1}H NMR was strongly influenced by the choice of integrals used for calculations and by the presence of supplementary peaks corresponding to solvent trances (*e.g.* water, DMF, Et_2O) and possibly other impurities, leading to a lack of precision in the estimation of Nc.

The Nc(^{1}H NMR) of AEM capped conjugates could be determined from spectra in $CDCl_3$, a good solvent for both the TP chromophores and the polymer backbone. Nonetheless, in the case of negatively charged hydrolyzed conjugates (polyelectrolyte species insoluble in organic media) in D_2O it was difficult to detect the presence of bond chromophores on the ^{1}H NMR spectra. In order to better dissolve these conjugates (bound chromophores and polymer backbone), a mixture of deuterated solvents (methanol/water 92/8 (v/v)) was used, which enabled to calculate in the Nc(^{1}H NMR) of the 4DBB-H conjugate.

To conclude, ^{1}H NMR technique could give an idea of Nc but was highly prone to errors coming from impurities in the sample and from uncertainties related to quantitatively analyzing amphiphilic high molecular weight species.

3) UV-Vis spectroscopy

After reaction, the copolymers that initially do not exhibit any absorption above 320 nm, should absorb in the visible region thanks to the bound chromophores. UV-Vis absorption was therefore used to evidence the chromophore coupling. In addition, it enabled the quantification of Nc by comparing the total integrated absorption oscillator strength of the free chromophores and that of the corresponding conjugates (Appendix II.8).

The absorption oscillator strength is represented by the integral of the absorption peak corresponding of the chromophore (free or bound to the polymer). The ratio between the oscillator strength of the conjugate (bound chromophore) and that of free chromophore gives the number of chromophores *per* chain. It can be deduced from the last equation below Eq. (5), and depends on the M_n of the P(NAM-*co*-NAS) copolymer (M_{COPO}), on the weight of the analyzed conjugate (m_{conj}), on the molecular weights

of the chromophore and of the *N*-hydroxysuccinimide (M_{chr} and M_{NHS}), and on the ratio between the two integrated absorbance curves.

$$Nc = \frac{\frac{\int A_{conj}}{c_{conj}}}{\frac{\int A_{chr}}{c_{chr}}} = \frac{\int A_{conj}}{\int A_{chr}} \times \frac{c_{chr}}{c_{conj}}$$

$$c_{chr} = \frac{m_{chr}}{M_{chr}};\ c_{conj} = \frac{m_{conj}}{M_{conj}};\ M_{conj} = M_{COPO} + Nc \times M_{chr} - Nc \times M_{NHS}$$

$$\Rightarrow Nc = \frac{\int A_{conj}}{\int A_{chr}} \times \frac{\frac{m_{chr}}{M_{chr}}}{\frac{m_{conj}}{M_{COPO} + Nc \times (M_{chr} - M_{NHS})}} \quad (5)$$

'∫*A*' is the integrated area under the absorption peak, '*c*' the concentration, '*m*' the weight of the chromophore (*chr*) or of the conjugate (*conj*), and 'M_{COPO}' the molecular weight of the P(NAM-*co*-NAS) copolymer used to obtain the chromophore-polymer conjugates.

II.4.4.2. Results

The SEC/UV procedure, presented above, was used to monitor the coupling of the different chromophores (Section II.4.2.1.) onto various copolymers (Table II. 14) and to determine the coupling reaction yields (Table II. 15).

Table II. 15: Chromophores and polymers used in the coupling step, and the resulting coupling yields.

Chromophore	Copolymer used for coupling	Nc_targeted	Coupling time (hours)	Final coupling yields (%)
LY	COPO_1	1.2	96	~ 90 %
	AH8T2	4.3	29	76 %
	AH6T7	5.0	44	77 %
	AF122T3	5.5	48	95 %
	COPO_10	6.0	96	73 %
Ant	AH6T7	6.7	24	91 %
		13.5	72	76 %
		27.1	72	76 %
DBB	AH6T7	5.5	48	81 %
		12.1	48	80 %
	AF122T3	5.5	24	83 %
	BLOCK_1	4.2	36	95 %

At the end of coupling and post-treatment, three different types of chromophore-polymer conjugates were obtained: LY-polymer conjugates, Ant-polymer conjugates and DBB-polymer conjugates. Their chemical structures (AEM capped or hydrolyzed) are illustrated in Figure II. 26.

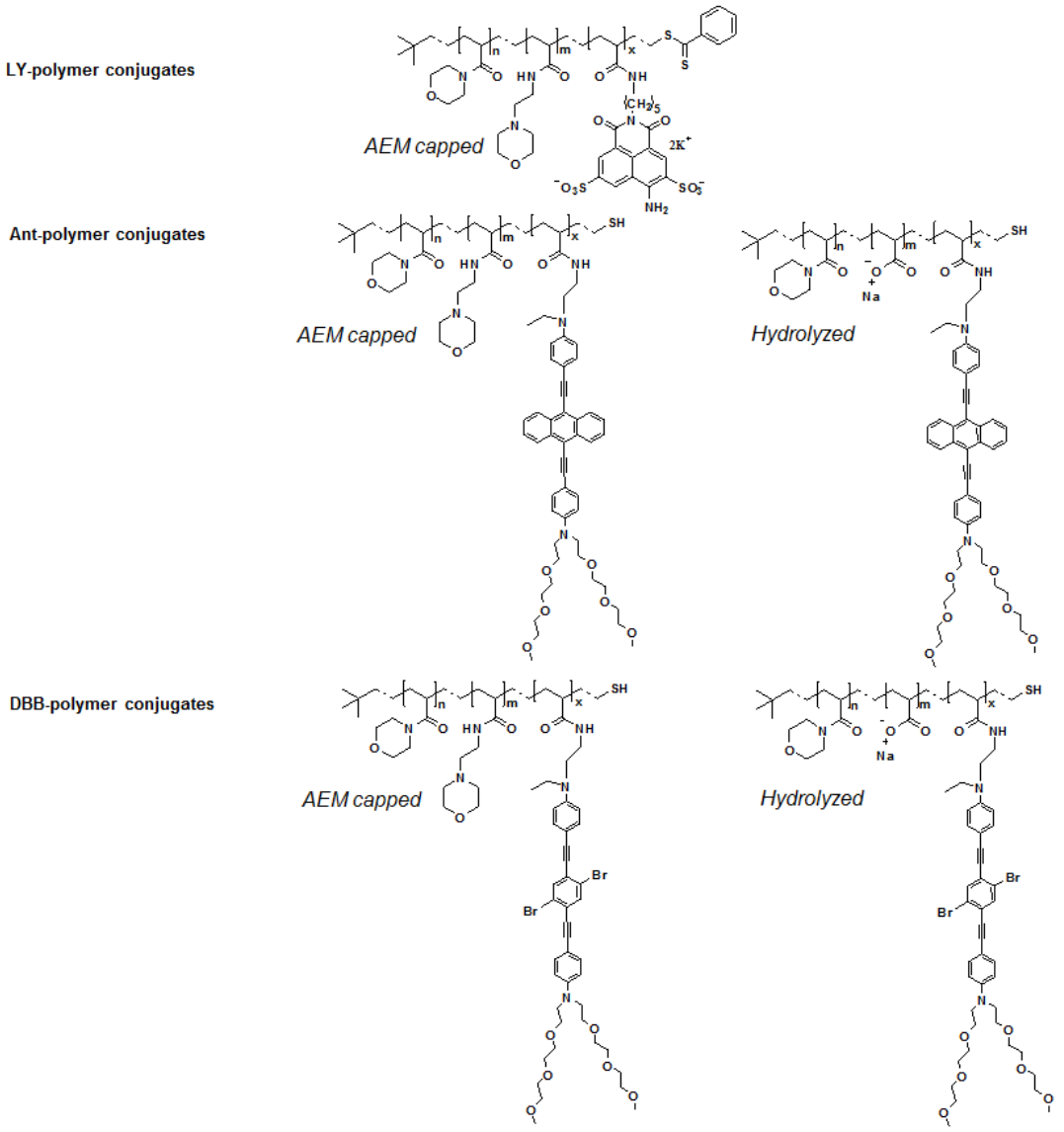

Figure II. 26: Chemical structures of the three different types of chromophore-polymer conjugates after coupling and post-treatment steps: LY-polymer conjugates (AEM capped); Ant-polymer conjugates (AEM capped or hydrolyzed); DBB-polymer conjugates (AEM capped or hydrolyzed).

II.4.4.3. Kinetics of the chromophore coupling reaction

High coupling yields (generally >75% in less than 24h) were obtained, confirming the high efficiency of the reaction between amino-functionalized chromophores (LY, Ant or DBB) and the lateral activated ester groups of the polymer backbone. The coupling reaction was very fast at the beginning of the reaction and reached a plateau after less than 24h (*e.g.* after 24h or 72h of coupling Ant chromophore, the coupling yield remained almost unchanged: 76%). This could be partly explained by the increasing steric hindrance with the number of bound chromophores.

A possible side-reaction during coupling is aminolysis of the DT chain-ends of the copolymer with the chromophore amine functions, resulting in a thioamide-modified free chromophore and a thiol-ended conjugate. The probability of this side-reaction is however limited, due to the excess of activated esters compared to the amount of chain-ends, and to slower rate of DT aminolysis compared to coupling.[71]

We supposed that coupling yields may vary with the density of chromophores *per* chains (more bound chromophores ⇒ higher steric hindrance ⇒ lower overall coupling yield), but also with the size of the chromophore (small molecule ⇒ higher coupling yield, large molecule ⇒ lower coupling yield). Nevertheless, data in Table II. 15 do not follow these trends, showing that other parameters have to be taken into account (*e.g.* the stability of the amino group of the chromophore; the variations between different batches of chromophore used for coupling).

II.4.4.4. The mean number of chromophores per chain (Nc)

Table II. 16 summarizes the properties of chromophore-polymer conjugates after coupling and post treatments steps. It contains results obtained for Nc determined by SEC/UV, ^{1}H NMR and/or UV-Vis spectroscopy. The density of chromophores *per* chain was expressed through the distance between two neighboring chromophores along the chain (in monomer units). Since the goal of this chapter was to produce well-defined water-soluble TP chromophore-polymer conjugates, their solubility properties were also reported.

In order to estimate the coupling yields by SEC/UV technique, a good separation between the conjugate peak and that of free chromophore was crucial. This requirement was fulfilled for high molecular weight conjugates (M_n > 8 000 g.mol^{-1}), but not for low MW conjugates as LY2KDa. This is why Nc for this conjugate was determined exclusively by the UV-Vis spectroscopy method discussed above.
Nc values determined by SEC/UV, ^{1}H NMR and UV-Vis spectroscopy are in a fairly good agreement, considering the experimental errors mentioned above. Nc(SEC/UV) was considered as the most accurate and will be used throughout this study.

Table II. 16: Physicochemical properties of chromophore-polymer conjugates: Nc (the average number of chromophore/chain), M_n before and after coupling, chromophores density (expressed in monomer units), solubility.

Chromophore	Conjugate	Nc after coupling*			Post-treatment	M_n before / after coupling ($g.mol^{-1}$) ***	Chromophore density (average distance between 2 chromophores in monomer units) ***	Solubility
		SEC/UV	^1H NMR	UV-Vis Abs.				
LY	LY2KDa	n.d.**	n.d.	1.1	AEM	2 200 / 2 700	-	Water & DMF
	LY9KDa	3.3	n.d.	n.d.		7 900 / 9 500	16	
	LY15KDa	3.8	n.d.	n.d.		12 900 / 15 000	22	
	LY32KDa(B)	5.2	n.d.	n.d.		29 400 / 32 400	27	
	LY37KDa	4.4	n.d.	n.d.		34 600 / 37 700	52	
Ant	6Ant-H*	6.1	n.d.	n.d.	H	12 900 / 14 800*	14	Water
	6Ant-AEM	6.1	6.3	5.5	AEM	12 900 / 17 300	14	Water & $CHCl_3$
	10Ant-AEM	10.3	7.6	n.d.	AEM	12 900 / 20 000	8	Water & $CHCl_3$
	21Ant-AEM	20.6	25.0	n.d.	AEM	12 900 / 26 600	4	$CHCl_3$
DBB	4DBB-H = DBB13KDa	4.4	4.8	n.d.	H	12 900 / 13 800*	19	Water
	4DBB-AEM	4.4	4.6	4.1	AEM	12 900 / 16 700	19	Water & $CHCl_3$
	10DBB-H*	9.8	n.d.	n.d.	H	12 900 / 18 100*	8	Water
	10DBB-AEM	9.8	9.5	n.d.	AEM	12 900 / 20 400	8	$CHCl_3$ & Poorly soluble in water
	DBB28KDa(B)*	4.6	n.d.	n.d.	H	29 400 / 28 800*	31	Water
	DBB33KDa(B)*	4.0	n.d.	n.d.	H	35 000 / 33 800*	38	Water

* M_n of hydrolyzed conjugates was calculated assuming that Na^+ was the counter ion of the COO^- groups.

** n.d.=not determined.

***Calculated using Nc(SEC/UV).

II.4.4.5. End-group modification during the post-treatment step

The post-treatment techniques, AEM capping or hydrolysis, modified not only the activated ester groups, but also the DT chain-ends.

AEM capping is carried out under a large excess of AEM, a primary amine that leads to the amidation of the activated esters and the aminolysis of DT polymer chain-ends into thiols.[64] In order to confirm that all DT groups were transformed into thiols after AEM capping, a P(NAM-*co*-NAS) random

* Due to the homogeneity of the polymer chains, the number of chromophores is considered to be Nc ±1 chromophore.

copolymers was treated with AEM, then analyzed using various techniques: (i) the colorless aspect of AEM capped copolymer endorsed the previous affirmation, indicating a virtual absence of DT groups (responsible for the pink color of the initial P(NAM-*co*-NAS) copolymer); (ii) quantitative transformation of DT groups has been monitored by UV-Vis spectroscopy, showing the absence of the characteristic DT absorption at 305 nm (Appendix II.9). Moreover, the quantitative transformation of DT end-groups during aminolysis has already been mentioned and discussed above in Section II.3.4.2.[19]

Hydrolysis of activated ester groups occurs under basic conditions (pH=9). It has been previously reported that hydrolysis of DT groups can also occur in these conditions;[72] however, this reaction is less efficient and slower than the hydrolysis of ester groups.
The quantification of DT chain-end hydrolysis was not possible by MALDI-TOF analyses due to the polyanionic nature of the resulting copolymer.
Using a similar experience as in the case of AEM capping, with a fully hydrolyzed P(NAM-*co*-NAS) random copolymer, we could however bring into light that conversion of DT units into thiols during hydrolysis seems partial: (i) the hydrolyzed P(NAM-*co*-NAS) copolymer had a pale pinkish color (sign of residual DT groups?); (ii) its UV-Vis spectrum shows a low residual absorption at 305 nm, corresponding most possibly to unreacted DT end-groups (Appendix II.9).

II.4.5. Influence of the conjugate structure on its physicochemical properties

Solubility and conformation of the chromophore-polymer conjugates in aqueous media are expected to play an important role on their final properties before and after grafting onto AuNP.

Regarding the conformation of each conjugate, we can easily imagine that it would depend on the nature of the coupled chromophore (hydrophilic/hydrophobic), its density and orientation on the polymer chain, the post-treatment, and also the polymer architecture (random or block). A specific study of these conformations (molecular modeling) would be interesting, although challenging, and was out of the scope of this work.
Solubility properties of chromophore-polymer conjugates are listed in Table II. 16. It can be noted that after coupling of hydrophobic chromophores along the polymer, thanks to the good water-solubility of the multifunctional copolymer chain, water-soluble chromophore-polymer conjugates could be obtained. For all water-soluble conjugates, no visible sign of aggregation was detected in water by DLS.

Unlike LY conjugates all soluble in water, the solubility of TP chromophore-polymer conjugates depends on 1) the density of chromophores *per* chain, 2) the nature of the chromophores and 3) on the post-treatment.

1) Influence of the density of chromophores *per* chain

Chromophore density is represented by the distance between two neighboring chromophores expressed in monomer units separating them (Table II. 16). It is related to two parameters: the number of chromophore *per* chain and the length of the polymer backbone.

Chromophore density influences the conjugate conformation and its water-solubility. For the hydrophobic TP chromophores, the increase in chromophore density tends to decrease the solubility in aqueous media. For instance, 21Ant-AEM is water-insoluble, whereas 10Ant-AEM is water-soluble, carrying respectively 21 and 10 Ant chromophores *per* chain.

2) Influence of the chromophore structure

Water solubility of conjugates also depends on the structure of the chromophore (LY conjugates *vs.* Ant and DBB conjugates).

LY conjugates (post-treated by AEM) are all water-soluble, independently on the number of chromophores *per* chain, thanks to the two negative charges directly attached to the chromophoric center. On the other hand, the solubility of Ant and DBB conjugates is impacted by the marked hydrophobicity of these TP chromophores. At similar chromophore density, 10DBB-AEM conjugate is insoluble in water, whereas 10Ant-AEM conjugate is water-soluble.

3) Influence of the post-treatment

The type of post-treatment (AEM capping of hydrolysis) influences the hydrophilic/hydrophobic balance and play an important role on the conformation (and the solubility) of the conjugates. We may suppose that AEM-capped neutral conjugates adopt a more compact, less hydrophilic, coil-like structure, whereas hydrolyzed thus negatively-charged conjugates adopt a more expanded, more hydrophilic, conformation due to the electrostatic repulsive forces coming from carboxylate lateral groups between neighboring chromophores. Indeed, AEM capped 21Ant-AEM and 10DBB-AEM conjugates (M_n(copolymer)=12 900 g.mol^{-1}), bearing each 21 and 10 chromophores *per* chain respectively, were not fully water-soluble due to the high density of hydrophobic chromophores (Table II. 16). On the other hand, all hydrolyzed conjugates were water-soluble, thanks to the negatively charged polymer backbone. However, for the same reason, they are insoluble or exhibit poor solubility in most polar organic solvents.

In the last part of this chapter amino-functionalized chromophores were successfully bound onto reactive P(NAM-*co*-NAS) random and block RAFT copolymers. Efficient coupling reaction between the NAS active ester pendant groups and the primary amine of the chromophores led to a library of chromophore-polymer conjugates by varying the nature and the number of chromophores *per* chain (Nc), the polymer MW and post-treatment.

Three different chromophores were bound on P(NAM-*co*-NAS) copolymers: LY – a fluorescent water-soluble commercially available chromophore; Ant and DBB – two hydrophobic TP chromophores, presenting high fluorescence emission (Ant) and singlet oxygen generation (DBB). Coupling yields, determined by SEC/UV, were higher than 75% (in less than 24h), regardless of the chromophore type.

Two different post-treatment methods (AEM capping or hydrolysis), were applied to transform the residual NAS activated ester groups and adjust the conformation of the conjugate, were applied after coupling.

The solubility of TP chromophore-polymer conjugates has been discussed with respect to the chosen density of chromophores along the polymer chain, the chromophore chemical nature and the post-treatment.

Additionally, both post-treatment methods led to the transformation of the conjugate DT chain-end into a thiol, which is a very important feature for the subsequent grafting of these conjugates onto AuNP (Chapter III).

II.5. Conclusion of Chapter II

Chapter II described the synthesis and characterization of two-photon chromophore-polymer conjugates.

First, the bibliographic section highlighted the advantages of the RAFT polymerization and of P(NAM-*co*-NAS) copolymers for conjugation with bio-active species. In addition, it was shown that chromophore-polymer conjugates form a class of polymer conjugates that are particularly interesting, since their activity can be triggered by light at a specific wavelength. Chromophore-polymer conjugates are used in various biological applications. However, the development of well-defined conjugates with two-photon chromophores (which can be excited in the NearIR), is at the beginning of its development and particularly desirable for bioimaging and PDT applications.

RAFT polymerization was used to synthesize well-defined PNAM and P(NAM-*co*-NAS) homo- and copolymers with M_n between 2 000 g.mol^{-1} and 60 000 g.mol^{-1}, low polydispersity (PDI < 1.2), and controlled end-group functionality (with a high percentage of dithioester terminated chains, >85%). P(NAM-*co*-NAS) random copolymer (M_n=23 000 g.mol^{-1}) were subsequently used as macro-CTA to obtain P[(NAM-co-NAS)-*b*-NAM] block copolymers with a good control over the M_n of the 2nd PNAM block.
In the future, to scale-up the production of chromophore-polymer conjugates, it could be interesting to obtain block copolymers in a one-step process, by adding-up the second monomer in the reaction medium of the macro-CTA (without its prior purification), and thus compare the results of MW and MW distribution with those obtained after a two-step synthesis.

Random and block P(NAM-*co*-NAS) reactive copolymers with different M_n were used to bind amino-functionalized chromophores. Two different hydrophobic two-photon chromophores have been used in this study (Ant and DBB). We have shown that after coupling, water-soluble chromophore-polymer conjugates could be obtained with high coupling yields, controlled numbers of chromophores *per* chain (varying from 1 to 21, determined by SEC/UV, and confirmed by ^{1}H NMR and UV-Vis spectroscopy), and different M_n (ranging from 2 700 to 37 700 g.mol^{-1}).
Structural parameters as the number of chromophore *per* chain (Nc), the chemical nature of the chromophore and the chosen post-treatment influenced the solubility and the physicochemical properties of the final conjugates: i) water-soluble 10Ant-AEM with Nc=10 *vs.* water-insoluble 21Ant-AEM with Nc=21; ii) while carrying the same Nc=10, 10DBB-AEM conjugate was insoluble in water, whereas 10Ant-AEM was water-soluble; iii) all hydrolyzed conjugates exhibited a higher degree of water-solubility when compared to AEM capped conjugates.
The ability to control the number of chromophores *per* chain, can serve to precisely tailor both the brightness of these macromolecular bio-probes and their water-solubility. In this context, it could be interesting to determine the value of Nc where the water-solubility limit is attained, *i.e.* by synthesizing Ant conjugates with Nc between 10 (10Ant-AEM) and 21 (21Ant-AEM).

Developing tools to study the conformation of such conjugates in aqueous solution as a function of Nc would be very helpful in view of biological applications.
In the future, we could suggest the coupling of various chromophores on one single copolymer chain which can subsequently be used as a multiple optical imaging probe, sensitive to different absorption / emission properties all in one single system.

The oriented grafting of these conjugates onto gold nanoparticles will be presented and discussed in Chapter III. Their optical and biological properties will be addressed in Chapters IV and V, respectively.

II.6. Experimental section

Materials

N-acryloyl morpholine (NAM) (Aldrich, 97%) was distilled under reduced pressure (120°C; 10 mmHg) to remove the inhibitor. The comonomer N-acryloxysuccinimide (NAS) was synthesized as previously described.[73] *tert*-Butyl dithiobenzoate (*t*BDB) was synthesized by a one-step process resulting in very high yield and purity (>98%).[10] Azobisisobutyronitrile (AIBN) was purchased from Aldrich (>99%) and purified by crystallization from ethanol. 1,4-Dioxane (Carlo erba, 99%) and tetrahydrofurane (Carlo Erba, 99%), were distilled over $LiAlH_4$ (110°C) and stored at 4°C under nitrogen. Trioxane (Aldrich, 99%), diethyl ether (SDS, 99.5%), decylamine (Aldrich, 95%) and *tris*(*2*-carboxyethyl)phosphine hydrochloride, TCEP (Thermo Scientific Pierce) were used as received.
To obtain chromophore-polymer conjugate, triethylamine (Sigma-Aldrich, ≥99,5%), *4*-(*2*-aminoethyl)morpholine (Aldrich, 99%), dichloromethane (Fischer Scientific, >99%), dimethylformamide (Fischer Scientific, 99,99%), were used without prior modifications.
Two photon chromophores were synthesized at ENS, Laboratore de Chimie (T. Gallavardin, J.-C. Mulatier, P.-H. Lanoe), following a recently published procedure.[74]
Lucifer Yellow Cadaverine ([*N*-(*2*-Aminopentyl)-*4*-amino-*3,6*-disulfo-*1,8*-naphthalene, dipotassium salt]) was purchased from FluoProbes®.

Synthesis and purification of homopolymers and copolymer by RAFT

RAFT (co)polymerization

Monomer(s), AIBN (initiator), *t*BDB (CTA), dioxane (solvent) and trioxane (internal reference for ^{1}H NMR determination of monomer consumption) were introduced in a Schlenk tube or in 12 Radley parallel reactors, each equipped with a magnetic stirrer. The mixture was degassed (by five freeze-evacuate-thaw cycles in Schlenk flask and under nitrogen flux in parallel rectors) then heated at 80°C under nitrogen (in a thermostated oil bath for Schlenk flask and by the automated heating system for parallel reactors). Polymerization time was 3h for PNAM (PNAM_X series) polymers and 13h for P(NAM-*co*-NAS) copolymers (COPO_X series). For Schlenk flask, samples were withdrawn from the polymerization medium *via* a canula (*PNAM*_PX series). Individual monomer conversions were determined by ^{1}H NMR following the decrease of the NAS and NAM vinyl protons in comparison with the protons of trioxane used as previously.[24]
After synthesis, polymers were purified by precipitation in diethylether, and dried under vacuum.

Polymerization conditions in Schlenk flask and in parallel reactors were similar:
- [CTA]/[AIBN]=10;
- $[monomer(s)]_0$=2.0 mol.L^{-1};
- [NAM]/[NAS]=60/40, in the case of RAFT copolymerization;
- [monomer(s)]/[CTA] was adjusted depending on the targeted M_n at 100% conversion from the equation of calculated M_n(calc) (Appendix II.1):
    - M_n=20 200 g.mol^{-1} for PNAM synthesized in Schlenk flask (giving $[NAM]_0/[CTA]_0$ = 142), (Table II. 6);
    - M_n varied from 2 000 to 100 000 g.mol^{-1} for samples synthesized in Radley's Parallel reactor system, PNAM (PNAM_X series) or P(NAM-*co*-NAS) (COPO_X series), (Table II. 7, Table II. 8);
    - Targeted M_n were 18 700 g.mol^{-1} and 31 200 g.mol^{-1} for PNAM block in BLOCK_1 and BLOCK_2 copolymers (Table II. 9), giving $[NAM]_0/[macro\text{-}CTA]_0$ = 107 and 177 respectively.

PNAM_X series	Targeted M_n at 100% conversion (g.mol^{-1})	$[NAM]_0$ / $[CTA]_0$		PNAM_X series	Targeted M_n at 100% conversion (g.mol^{-1})	$([NAM]_0 + [NAS]_0)$ / $[CTA]_0$
PNAM_1	3 000	21		**COPO_1**	2 000	9
PNAM_2	5 000	35		**COPO_2**	5 000	24
PNAM_3	10 000	71		**COPO_3**	10 000	48
PNAM_4	15 000	106		**COPO_4**	15 000	73
PNAM_5	20 000	142		**COPO_5**	20 000	97
PNAM_6	30 000	213		**COPO_6**	20 000	97
PNAM_7	40 000	283		**COPO_7**	25 000	122
PNAM_8	50 000	354		**COPO_8**	25 000	122
PNAM_9	60 000	425		**COPO_9**	30 000	147
PNAM_10	70 000	496		**COPO_10**	50 000	245
PNAM_11	80 000	566		**COPO_11**	80 000	393
PNAM_12	100 000	708		**COPO_12**	100 000	491

AH8T2, AH6T7, AF122T3 copolymer samples were synthesized using the earlier described RAFT polymerization procedure.[22]

Aminolysis of PNAM-DT into PNAM-SH

PNAM (10 mg.mL^{-1}) was dissolved in $CHCl_3$ containing decylamine (10 molar equiv. in comparison with the dithioester end groups). The aminolysis reaction was performed at 40°C in a thermostated oil bath during 48h. TCEP dissolved in water was added to the reaction media to prevent -S-S- bond formation. The reaction may be followed by the change in color – from light orange to light yellow – due to the disappearance of –S-(C=S)- bonds. The polymer recovered by precipitation in diethyl ether was white. ^{1}H NMR spectroscopy confirmed the disappearance of the dithioester end group at 7.4-8.0 ppm.

Synthesis and purification of chromophore-polymer conjugates

Synthesis of Two-Photon chromophore-polymer conjugates

Coupling of Two-Photon chromophores

Coupling reaction was carried out in the dark under stirring for 48 hours, in chloroform at 40°C (for Ant and DBB conjugates). To reach the targeted number of chromophores per chain and to ensure a high coupling yield, 1.1 – 1.2 equivalents of chromophore and 2 equivalents of triethylamine (TEA) were used in the coupling reaction. The polymer concentration was fixed at 10mg.mL^{-1} in the reaction medium. Purification was carried out by precipitation in diethyl ether.
For example, 50 mg of P(NAM-*co*-NAS) copolymer (M_n=12 900 g.mol^{-1}) were dissolved in 0.5mL of chloroform (7.75mM) in a 25mL round bottom flask equipped with a magnetic stirrer. 20.3mg of Ant in chloroform (55.2mM, raw from NH-tBoc deprotection) were then added together with 2 equivalents of triethylamine (TEA). Polymer concentration was then adjusted with chloroform at 10mg.mL^{-1}. After coupling (40°C, 48h, in the dark), the reaction media were analyzed by SEC/UV in order to determine the coupling yield (Table II. 15). The conjugate was then precipitated in a large volume of diethyl ether and isolated from the supernatant by centrifugation. The procedure was repeated until complete discoloration of the supernatant, ensuring the absence of free unreacted chromophore. Purified orange (Ant)/yellow (DBB) conjugates were finally dried under vacuum up to constant weight.

Post-treatment of the remaining activated ester functions

Capping with AEM

After coupling of the TP chromophores onto the polymer backbone, TP conjugates were redissolved in chloroform (10mg.mL^{-1}), and then 10 molar equivalents of amino ethyl morpholine (AEM) (with respect to reactive NAS units on the copolymer) were added to the reaction medium. The reaction was carried

out at 40°C, in $CHCl_3$ in the dark, during 12h, ensuring the complete substitution of succinimide groups with AEM.
AEM capped conjugates were isolated from $CHCl_3$ by precipitation in a large volume of diethyl ether.

Hydrolysis

After coupling of the chromophores onto the polymer backbone, conjugates were redispersed (1mg.mL^{-1}) in a large volume of a borate buffer (50 mM, pH=9). Hydrolysis of the unreacted NAS activated ester groups into carboxylate units proceeded at room temperature under magnetic stirring for 3 days, in the dark.

Synthesis of LY-polymer conjugates

Coupling LY chromophore
The coupling with Lucifer Yellow cadaverine was performed following the procedure previously optimized by Paula Relogio.[68] In a round bottom flask of 25mL equipped with a magnetic stirrer were sequentially added: the copolymer solution in DMF (10 mg.mL^{-1}), LY chromophore solution in water (water/DMF = 10/90:V/V), and triethylamine(TEA) (2 molar equivalents with respect to LY chromophore). The reaction mixture was heated at 40°C in a thermostated oil bath under vigorous stirring during 24 hours, until reaching the maximum chromophore to polymer coupling yield (calculated by SEC/UV).

Post-treatment of the remaining activated ester functions

Capping with AEM

The remaining activated ester groups were capped with a large excess of a water-soluble primary amine, *4*-(*2*-aminoethylmorpholine)(AEM), 10 molar equivalents of AEM (with respect to reactive NAS units on the copolymer) were added to the reaction medium. The reaction was carried out at RT in DMF, in the dark, during 12h, ensuring the complete substitution of succinimide groups with AEM.
LY-polymer conjugate was first isolated from DMF by precipitation in diethyl ether, then dried under vacuum.

Purification
All water soluble conjugates were purified by dialysis against deionized water, using a Spectra/Por® 1-7 regenerated cellulose membrane with MWCO=2000Da, then freeze dried.
The few water-insoluble conjugates were purified only by repeated precipitation in diethyl ether, then purified by dialysis (*cf.* below).

Instruments and methods

SEC/RI
M_n values of PNAM polymers were determined by Waters RI (refractive index) detection using a calibration curve with PNAM etalons produced by RAFT polymerization. Waters 1515 Isocratic HPLC pump coupled with Waters 2410 Refractive Index Detector, Size Exclusion Chromatography Styragel HR4E linear column (7.8x300mm), were used. Data acquisition was performed using Breeze software. Samples were prepared by dissolving 1mg of polymer in 1mL $CHCl_3$.

SEC/LS
Molecular weight distributions were determined by size exclusion chromatography coupled to a multi-angle light scattering detection (SEC/LS). SEC, carried out in amylene stabilized chloroform (Sigma Aldrich, CHROMASOLV® for HPLC, ≥99.8%), at a flow rate of 0.5ml.min^{-1}, 25°C. was performed using a UFLC SHIMADZU LC-20AD pump, PLgel 5µm, MIXED and a differential refractometer (SHIMADZU RID-10A). On-line double detection was provided by a three-angle (47°, 90°, 130°) Wyatt miniDAWN Treos light scattering photometer. Analyses were performed by injection of 50 µl of polymer solution (5mg.mL^{-1}) in chloroform, previously filtered through a 0.22mm Millipore filter. The specific refractive index increment (dn/dc) for poly(NAM) and poly(NAM-*co*-NAS) was 0.16.[22] The molecular weight and polydispersity data were determined using the Wyatt ASTRA SEC/LS software package.

SEC/UV

Coupling yields of the reaction between P(NAM-*co*-NAS) and chromophores were determined (before post-treatment) by size 5 exclusion chromatography (SEC) using UV detection at 510 and 400nm for Ant and DBB conjugates, respectively.

A Varian ProStar Dynamax 800 system fitted with a Varian pump, Size Exclusion Chromatography Styragel HR4E linear column (7.8x300mm²), and 30µl sample loop were used. Data acquisition was performed using Galaxie software. Sample were prepared by dissolving 20-50µL of reaction medium in 1mL DMF stabilized with LiBr (0.05M).

^{1}H NMR spectroscopy

Individual monomer conversions[24] and the number of chromophores *per* chain were determined by ^{1}H NMR in $CDCl_3$, with tetramethylsilane (TMS) as internal reference. ^{1}H NMR spectra were recorded on a Bruker 200MHz spectrometer.

MALDI-TOF MS

The matrix-assisted laser desorption ionization time-of-flight mass spectrometer (MALDI-TOF MS) used to acquire the mass spectra was a Voyager-DE STR (Applied Biosystems, Foster City, CA). This instrument was equipped with a nitrogen laser (wavelength 337nm) to desorb and to ionize the samples. The accelerating voltage used was 20 or 25kV. The positive ions were detected in all cases. The spectra were the sum of 200 shots, and an external mass calibration was used (Sequazyme® peptide mixture). This MALDI instrument used a stainless steel target, on which the samples were deposited and dried. Samples were prepared by dissolving the polymer in THF (or water/DMF) at a concentration of 10g.L^{-1}. In some cases, the polymers were stirred with a strong cation-exchange resin DOWEX 50W-X8, mesh size 200-400 (Supelco, Bellefonte, PA). The matrix used for all experiments was 3-indoleacrylic acid (IAA, Fluka, Milwaukee, WI), used without further purification and dissolved in DMF (0.25M). Matrix and polymer solutions were mixed at 1:1 v/v ratio, and then 0.5µL of the mixture was deposited onto the MALDI target before insertion into the ion source chamber.

UV-Vis spectroscopy

UV-Vis absorption spectra were recorded on a Jasco V-670 spectrophotometer at ambient temperature using 1cm quartz cell.

Precision weighing scale Sartorius LA 230S $\pm$ 0.1mg was used to weigh solid products for sample preparation.

Beer-Lambert law applied for concentration calculations: $A = \varepsilon l c$, where *A* is the absorbance at a given wavelength, *l* is path length of the cell and *c* the concentration of the sample.

Fluorescence spectroscopy (Chapter IV)

Fluorescence emission spectra were recorded on a Horiba-Jobin Yvon Fluorolog-3 spectrofluorimeter equipped with a R928P (PMT) detector. Right Angle geometry, at ambient temperature, a 1 cm optical path length quartz cell, and an excitation wavelengths of were 470nm, 430nm and 390nm for Ant-, LY- and DBB-compounds, respectively. Entrance (excitation)/exit (emission) slits depended on the chromophore and on the reference used: 1nm/2nm for Ant- and LY-derivatives, 3nm/3nm for DBB-derivatives. Integration time = 0.1s.

.

References

[1] **The Chemistry of Radical Polymerization,** G. Moad, D. H. Solomon, *Elsevier Science* **2005**.

[2] a) **''Living'' polymers,** M. Szwarc, *Nature* **1956**, *176*, 1168-1169.

b) **Polymerization initiated by electron transfer to monomer. A new method of formation of block copolymers,** M. Szwarc, M. Levy, R. Milkovich, *J. Am. Chem. Soc.* **1956**, *78*, 2656-2657.

[3] a) **Ion ester equilibriums in the living cationic polymerization of tetrahydrofuran,** K. Matyjaszewski, P. Kubisa, S. Penczek, *J. Polym. Sci. Polym. Chem. Ed.* **1974**, *12*, 1333-1336.

b) **Cationic ringopening polymerization. 2. Synthetic applications,** S. Penczek, P. Kubisa, K. Matyjaszewski, *Adv. Polym. Sci.* **1985**, *68(9)*, 1-298.

[4] **Controlled/living radical polymerization: Features, developments, and perspectives,** W. A. Braunecker, K. Matyjaszewski, *Prog. Polym. Sci.* **2007**, *32*, 93-146.

[5] **Chapter I: Controlled Radical Polymerization: State of the Art in 2008,** K. Matyjaszewski, *In Controlled/Living Radical Polymerization: Progress in ATRP*, ACS Symposium Series, American Chemical Society: Washington, DC, **2009**.

[6] **New polymer synthesis by nitroxide mediated living radical polymerizations,** C. J. Hawker, A. W. Bosman, E. Harth, *Chem. Rev.* **2001**, *101*, 3661-3688.

[7] **Controlled/"Living" Radical Polymerization. Halogen Atom Transfer Radical Polymerization Promoted by a Cu(I)/Cu(II) Redox Process,** J.-S. Wang, K. Matyjaszewski, *Macromolecules* **1995**, *28(23)*, 7901-7910.

[8] **Experimental Requirements for an Efficient Control of Free-Radical Polymerizations via the Reversible Addition-Fragmentation Chain Transfer (RAFT) Process,** A. Favier, M.-T. Charreyre, *Macromol. Rapid Commun.* **2006**, *27*, 653-692.

[9] **Living Free-Radical Polymerization by Reversible Addition-Fragmentation Chain Transfer: The RAFT Process,** J. Chiefari, Y. K. Chong, F. Ercole, J. Krstina, J. Jeffery, T. P. T. Le, R. T. A. Mayadunne, G. F. Meijs, C. L. Moad, G. Moad, E. Rizzardo, S. H. Thang, *Macromolecules* **1998**, *31*, 5559-5562.

[10] **A detailed kinetic study of the RAFT polymerization of a bi-substituted acrylamide derivative: influence of experimental parameters,** A. Favier, M.-T. Charreyre, C. Pichot, *Polymer* **2004**, *45*, 8661-8674.

[11] **Therapeutic proteins: a comparison of chemical and biological properties of uricase conjugated to linear or branched poly(ethylene glycol) and poly(N-acryloylmorpholine),** O. Schiavon, P. Caliceti, P. Ferruti, F. M. Veronese, *Il Farmaco* **2000**, *55(4)*, 264-269.

[12] **Polymers of N-acryloylmorpholine activated at one end and conjugates with bio-active materizals and surfaces,** F. M. Veronese, O. Schiavon, P. Caliceti, L. Sartore, E. Ranucci, P.Ferruti, *US005629384A*, **1997**.

[13] **Poly(N-acryloylmorpholine) as a new soluble support for the liquid-phase synthesis of oligonucleotides,** G. M. Bonora, A. Baldan, O. Schiavon, P. Ferruti, F. M Veronese, *Tetrahedron Lett.* **1996**, *37(27)*, 4761-4764.

[14] **Polymer–drug conjugates: Progress in polymeric prodrugs,** J. Khandare, T. Minko, *Prog. Polym. Sci.* **2006**, *31*, 359-397.

[15] **Narrow Molecular Weight Distribution Precursors for Polymer-Drug Conjugates,** A. Godwin, M. Hartenstein, A. H. E. Müller, S. Brocchini, *Angew. Chem.* **2001**, *113*, 614-617.

[16] a) **Polymer synthesis via activated esters: A new dimension of creativity in macromolecular chemistry,** R. Arshady, *Adv. Polym. Sci.* **1994**, *111*, 1-41.

b) **Advanced Organic Chemistry,** F. A. Carey, R. J. Sundberg, *Science* **2007**, *7.4.2. Aminolysis of esters*, 659-662.

[17] **Study of the RAFT Polymerization of a Water-Soluble Bisubstituted Acrylamide Derivative. 1. Influence of the Dithioester Structure,** A. Favier, M.-T. Charreyre, P. Chaumont, C. Pichot, *Macromolecules* **2002**, *35(22)*, 8271-8280.

[18] **Molecular Weight and Functional End Group Control by RAFT Polymerization of a Bisubstituted Acrylamide Derivative,** F. D'Agosto, R. Hughes, M.-T. Charreyre, C. Pichot, R. G. Gilbert, *Macromolecules* **2003**, *36(3)*, 621-629.

[19] **MALDI-TOF MS Investigation of the RAFT Polymerization of a Water-Soluble Acrylamide Derivative,** A. Favier, C. Ladavière, M.-T. Charreyre, C. Pichot, *Macromolecules* **2004**, *37*, 2026-2034.

[20] **Biotin α-End-Functionalized Gradient Glycopolymers Synthesized by RAFT Copolymerization,** G. Gody, P. Boullanger, C. Ladavière, M.-T. Charreyre, T. Delair, *Macromol. Rapid Commun* **2008**, *29(6)*, 511-519.

[21] **RAFT Homo-and Copolymerization of N-Acryloyl-morpholine, Piperidine, and Azocane and Their Self-Assembled Structures,** Y. S. Jo, A. J. van der Vlies, J. Gantz, S. Antonijevic, D. Demurtas, D. Velluto, J. A. Hubbell, *Macromolecules* **2008**, *41*, 1140-1150.

[22] **Synthesis of N-acryloxysuccinimide copolymers by RAFT polymerization, as reactive building blocks with full control of composition and molecular weights,** A. Favier, F. D'Agosto, M.-T. Charreyre, C. Pichot, *Polymer* **2004**, *45*, 7821-7830.

[23] **Polymères biocompatibles pour la fixation de ligands biologiques,** M-T. Charreyre, F. D'Agosto, A. Favier, C. Pichot, B. Mandrand, Patent WO/2001/92361, **2005**.

[24] **Kinetic Study of Free-Radical Solution Copolymerization of N-Acryloylmorpholine with an Activated Ester-Type Monomer, N-Acryloxysuccinimide,** F. D'Agosto, M.-T. Charreyre, L. Veron, M.-F. Llauro, C. Pichot, *Macromol. Chem. Phys.* **2001**, *202*, 1689-1699.

[25] **New Glycoconjugate Polyacrylamide with Water-Solubility and Additional Activated Groups: Synthesis and Characterization,** D. Teng, W. Yin, X. Zhang, Z. Wang, C. Li, *J. Polym. Res.* **2009**, *16(3)*, 311-316.

[26] **Polymeric Conjugates for Drug Delivery,** N. Larson, H. Ghandehari, *Chem. Mater.* **2012**, *24*, 840-853.

[27] a) **Modern trends in polymer bioconjugates design,** J.-F. Lutz, H. G. Börner, *Prog. Polym. Sci.* **2008**, *33*, 1-39.

b) **Strategies exploiting functions and self-assembly properties of bioconjugates for polymer and materials sciences,** H. G. Börner, *Prog. Polym. Sci.* **2009**, 34, 811-851.

[28] **Overcoming the barriers in micellar drug delivery: loading efficiency, in vivo stability, and micelle–cell interaction,** S. Kim, Y. Shi, J.Y. Kim, K. Park, J. X. Cheng, *Expert Opin. Drug Deliv.* **2010**, *7(1)*, 49-62.

[29] **Polypeptide–polymer bioconjugates,** L. A. Canalle, D. W. P. M. Löwik, J. C. M. van Hest, *Chem. Soc. Rev.* **2010**, *39*, 329-353.

[30] **Polymer-based siRNA delivery: Perspectives on the fundamental and phenomenological distinctions from polymer-based DNA delivery,** D. J. Gary, N. Puri, Y.-Y. Won, *J. Control. Rel.* **2007**, *121*, 64-73.

[31] a) **Lipid-Polymer Hybrid Nanoparticles: Synthesis, Characterization and Applications,** L. Zhang, L. Zhang, *Nano Life* **2010**, *1(1,2)*, 163-173.

b) **A Review on Composite Liposomal Technologies for Specialized Drug Delivery,** M. S. Mufamadi, V. Pillay, Y. E. Choonara, L. C. Du Toit, G. Modi, D. Naidoo, V. M. K. Ndesendo, *J. Drug Deliv.* **2011**, 1-19.

[32] **Effect of Pegylation on Pharmaceuticals,** J. Milton Harris & R. B. Chess, *Nat. Rev. Drug Discov.* **2003**, *2(3)*, 214-221.

[33] **Macromolecular carrier systems for targeted drug delivery: pharmacokinetic considerations biodistribution,** Y. Takakura, M. Hashida, *Pharm. Res.* **1996**, *13*, 820-831.

[34] **Polymers in drug delivery,** O. Pillai, R. Panchagnula, *Curr. Opin. Chem. Biol.* **2001**, *5(4),* 447-451.

[35] **Polymer Architecture and Drug Delivery,** L. Y. Qiu, Y. H. Bae, *Pharm. Res.* **2006**, *23(1)*, 1-30.

[36] **Micro-and nanotechnologies for intelligent and responsive biomaterial-based medical systems,** M. Caldorera-Moore, N. A. Peppas, *Adv. Drug Deliv. Rev.* **2009**, *61*, 1391-1401.

[37] **Hydrogels in drug delivery: Progress and challenges,** T. R. Hoare, D. S. Kohane, *Polymer* **2008**, *49*, 1993-2007.

[38] **Dendrimers as Carriers for Delivery of Chemotherapeutic Agents,** S. H. Medina, M. E. H. El-Sayed, *Chem. Rev.* **2009**, *109*, 3141-3157.

[39] **Structure and properties of pharmacologically active polymers,** H. Ringsdorf, *J. Polym. Sci.*, *Polymer Symposia* **1975**, *51(1)*, 135-153.

[40] **Tumor vascular permeability and the EPR effect in macromolecular therapeutics,** H. Maeda, J. Wu, T. Sawa, Y. Matsumura, K. Hori, *J. Control. Rel.* **2000**, *65(1-2)*, 271-284.

[41] **Cis-trans photoisomerization of azobenzene. Solvent and triplet donors effects,** P. Bortolus, S. Monti, *Phys. Chem.* **1979**, *83(6)*, 648-652

[42] a) **A New Design for Light-Breakable Polymer Micelles,** J. Jiang, X. Tong, Y. Zhao, *J. Am. Chem. Soc.* **2005**, *127*, 8290-8291.

b) **2.3.4. Photoresponsive polymers,** M. W. Urban, *Handbook of Stimuli-Responsive Materials*, Wiley **2011**.

[43] **Photochromic fluorescence switching from diarylethenes and its applications,** C. Yun, J. You, J. Kim, J. Huh, E. Kim, *J. Photochem. Photobiol. C: Photochem. Rev.* **2009**, *10*, 111-129.

[44] **Design, synthesis and biological application of chemical probes for bio-imaging,** K. Kikuchi, *Chem. Soc. Rev.* **2010**, *39*, 2048-2053.

[45] **Biological stains; a handbook on the nature and uses of the dyes employed in the biological laboratory,** H. J. Conn, N. Y. Geneva, *Biotech Publications* **1953**.

[46] a) **Activatable Photosensitizers for Imaging and Therapy,** J. F. Lovell, T. W. B. Liu, J. Chen, G. Zheng, *Chem. Rev.* **2010**, *110*, 2839-2857.

b) **Imaging and Photodynamic Therapy: Mechanisms, Monitoring, and Optimization,** J. P. Celli, B. Q. Spring, I. Rizvi, C. L. Evans, K. S. Samkoe, S. Verma, B. W. Pogue, T. Hasan, *Chem. Rev.* **2010**, *110*, 2795-2838.

[47] **In Vitro Photodynamic Therapy and Quantitative Structure−Activity Relationship Studies with Stable Synthetic Near-Infrared-Absorbing Bacteriochlorin Photosensitizers,** Y.-Y. Huang, P. Mroz, T. Zhiyentayev, S. K. Sharma, T. Balasubramanian, C. Ruzié, M.I Krayer, D. Fan, K. E. Borbas, E. Yang, H. L. Kee, C. Kirmaier, J. R. Diers, D. F. Bocian, D. Holten, J. S. Lindsey, M. R. Hamblin, *J. Med. Chem.* **2010**, *53(10)*, 4018-4027.

[48] **Dye-labelled polymer chains at specific sites: Synthesis by living/controlled polymerization,** M. Beija, M.-T. Charreyre, J. M.G. Martinho, *Progr. Polym. Sci.* **2011**, *36*, 568-602.

[49] a) **Preparation of Azobenzene-Containing Amphiphilic Diblock Copolymers for Light-Responsive Micellar Aggregates,** G. Wang, X. Tong, Y. Zhao, *Macromolecules* **2004**, *37*, 8911-8917.

b) **How Can Azobenzene Block Copolymer Vesicles Be Dissociated and Reformed by Light?,** X. Tong, G. Wang, A. Soldera, Y. Zhao, *J. Phys. Chem. B* **2005**, *109*, 20281-20287.

[50] **Light-Responsive Bioconjugates as Novel Tools for Specific Capture of Biologicals by Photoaffinity Precipitation,** A. Desponds, R. Freitag, *Biotechnol. Bioeng.* **2005**, 91(5), 583-591.

[51] **Rational Design of Light-Controllable Polymer Micelles,** Y. Zhao, *The Chem. Record.* **2007**, *7*, 286-294.

[52] **Polymers for bioimaging,** J.-H. Kim, K. Park, H. Yun Nam, S. Lee, K. Kim, I. Chan Kwon, *Prog. Polym. Sci.* **2007**, *32*, 1031-1053.

[53] **Dual Fluorescent HPMA Copolymers for Passive Tumor Targeting with pH-Sensitive Drug Release: Synthesis and Characterization of Distribution and Tumor accumulation in Mice by Noninvasive**

Multispectral Optical Imaging, S. Hoffmann, L. Vystrčilov , K. Ulbrich, T. Etrych, H. Caysa, T. Mueller, K. Mäder, *Biomacromol.* **2012**, *13*, 652-663.

[54] **Development of Polymeric Cargo for Delivery of Photosensitizer in Photodynamic Therapy,** B. Bae, K. Na, *Int. J. Photoenerg.* **2012**, 1-14.

[55] a) **A polymeric drug delivery system for the simultaneous delivery of drugs activatable by enzymes and/or light,** N. L. Krinick, Y. Sun, D. Joyner, J. D. Spikes, R. C. Straight, J. Kopecek, *J. Biomater. Sci. Polym. Ed.* **1994**, *5*, 303-324.

b) **Combination Chemotherapy and Photodynamic Therapy with N-(2- Hydroxypropyl)methacrylamide Copolymer-bound Anticancer Drugs Inhibit Human Ovarian Carcinoma Heterotranspianted in Nude Mice,** C. M. Peterson, J. M. Lu, Y. Sun, C. A. Peterson, J.-G. Shiah, R. C. Straight, J. Kopecek, *Cancer Res.* **1996**, *56*, 3980-3985.

c) **The effects of subcellular localization of N-(2-hydroxypropyl)methacrylamide copolymer-Mce6 conjugates in a human ovarian carcinoma,** M. Tijerina, P. Kopeckova, J. Kopecek, *Journal of Controlled Release* **2001**, *74*, 269-273.

[56] **Synthesis and Biological Evaluation of Disulfide-Linked HPMA Copolymer-Mesochlorin e6 Conjugates,** V. Cuchelkar, P. Kopeckova, J. Kopecek, *Macromol. Biosci.* **2008**, *8*, 375-383.

[57] **A Smart Polysaccharide/Drug Conjugate for Photodynamic Therapy,** S. Y. Park, H. J. Baik, Y. T. Oh, K. T. Oh, Y. S. Youn, E. S. Lee, *Angew. Chem. Int. Ed.* **2011**, *50*, 1644-1664.

[58] a) **New Developments in Optical Microscopy for Biological Applications,** A. Dixon, *Aust. J. Phys.* **1998**, *51*, 729-750.

b) **Multiphoton excitation cross-sections of molecular fluorophores,** C. Xu, R. M. Williams, W. Zipfel, W. W. Webb, *Bioimaging* **1996**, *4* , 198-207.

[59] **Multiphoton Absorbing Materials: Molecular Designs, Characterizations, and Applications,** S. He, L.-S. Tan, Q. Zheng, P. N. Prasad, *Chem. Rev.* **2008**, *108*, 1245-1330.

[60] **Integrin-Targeting Block Copolymer Probes for Two-Photon Fluorescence Bioimaging,** S. Biswas, X. Wang, A. R. Morales, K. D. Belfield, *Biomacromol.* **2011**, *12*, 441-449.

[61] **Additional Retardation in RAFT Polymerization: Detection of Terminated Intermediate Radicals,** M. Bathfield, F.D'Agosto, R. Spitz, C. Ladavière, M.-T. Charreyre, T. Delair, *Macromol. Rapid Commun.* **2007**, *28*, 856-862.

[62] **Synthèse d'architectures (co)polymerès contrôlées par le procédé RAFT en vue d'une application dans el diagnostique biologique et le transfert de gènes** (Chapitre 5), Thèse A. Favier, **2002**, p. 106.

[63] **Experimental investigation on the reliability of routine SEC–MALLS for the determination of absolute molecular weights in the oligomeric range,** T. Xiea, J. Penellea, M. Verraver, *Polymer* **2002**, **3 (14)** 3973-3977.

[64] a) **Hydrophobic Effect and Substrate Specificity in Reaction of Thioester and Amine in Water,** A. Torihata, C. Kuroda, *Bull. Chem. Soc. Jpn.* **2010**, *83(12)*, 1534-1538.

b) **Mechanism and Kinetics of RAFT-Based Polymerizations of Styrene and Methyl Methacrylate,** A. Goto, K. Sato, Y. Tsujii, T. Fukuda, G. Moad, E. Rizzardo, S. H. Thang, *Macromol.* **2001**, *34*, 402-408.

[65] **Advances in RAFT polymerization: the synthesis of polymers with defined end-groups,** G. Moad, Y.K. Chong, A. Postma, E. Rizzardo, S. H. Thang, *Polymer* **2005**, *46*, 8458-8468.

[66] a) **Photodynamic therapy and two-photon bio-imaging applications of hydrophobic chromophores through amphiphilic polymer delivery,** T. Gallavardin, M. Maurin, S. Marotte, T. Simon A.-M. Gabudean, Y. Bretonnière, M. Lindgren, F. Lerouge, P. L. Baldeck, O. Stéphan, Y. Leverrier, J. Marvel, S. Parola, O. Maury, C.l Andraud, *Photochem. Photobiol. Sci.* **2011**, *10(7)*, 1216-1225.

b) **Water-soluble chromophores with star-shaped oligomeric arms: synthesis, spectroscopic studies and first results in bio-imaging and cell death induction,** C. Monnereau , S. Marotte , P.-H. Lanoë, O. Maury , P. L. Baldeck , D. Kreher , A. Favier , M.-T. Charreyre , J. Marvel , Y. Leverrier, C. Andraud, *New J. Chem.* **2012**, in press.

[67] **Lucifer dyes. Highly fluorescent dyes for biological tracing,** W. W. Stewart, *Nature* **1981**, *292*, 17–21.

[68] a) **PhD, "Water-soluble associative polymers: synthesisi and photophysical of poly(*N*,*N*-dimethylacrylamide) and poly(*N*-acryloylmorpholine)", 2006**, P. Relogio, Instituto Superior Técnico Lisboa.

b) **Fluorescent Polymers Soluble in an Aqueous Solution and a Method for the Production Thereof,** M.-T. Charreyre, B. Mandrand, J. M. G. Martinho, P. Relogio, J. P. Sequeira Farinha, Patent Application WO/2007/003781, **2006**, PCT/FR2006/001544.

[69] **Two-Photon Photosensitized Production of Singlet Oxygen,** P. K. Frederiksen, M. Jørgensen , P. R. Ogilby, *J. Am. Chem. Soc.* **2001**, *123(6)*, 1215-1221.

[70] **Hydrolyzable nonionic surfactants: Stability and physicochemical properties of surfactants containing carbonate, ester, and amide bonds,** M. Stjerndahl, K. Holmberg, *J. Colloid Interface Sci.* **2005**, *291*, 570-576.

[71] PhD **« Synthèse d'agents de contrôle originaux pour l'obtention de copolymères α-fonctionnels par le procédé RAFT. Application à l'élaboration des particules à chevelure contrôlée.** », M. Bathfield, *Chapitre 2*, 83-84.

[72] **Hydrolytic Susceptibility of Dithioester Chain Transfer Agents and Implications in Aqueous RAFT Polymerizations,** D. B. Thomas, A. J. Convertine, R. D. Hester, A. B. Lowe, C. L. McCormick, *Macromolecules* **2004**, *37*, 1735-1741.

[73] **Side product of N-Acryloxysuccinimide synthesis or useful new bifunctional monomer ?,** F. D'agosto, M.T. Charreyre, C. Pichot, *Macromol. Biosci.* **2001**, *1*, 322-328.

[74] **Biocompatible well-defined chromophore–polymer conjugates for photodynamic therapy and two-photon imaging,** C. Cepraga, T. Gallavardin, S. Marotte, P.-H. Lanoë, J.-C. Mulatier, F. Lerouge, S. e Parola, M. Lindgren, P. L. Baldeck, J. Marvel, O. Maury, C. Monnereau, A. Favier, C. Andraud, Y. Leverrier, M.-T. Charreyre, *Polym. Chem*. **2013**, *4(1)*, 61-67.

Chapter III: Grafting chromophore-polymer conjugates onto AuNP in aqueous medium

III.1. Introduction

This chapter will focus on the synthesis and the characterization of gold nanoparticles (AuNP) functionalized in aqueous medium with water-soluble chromophore-polymer conjugates (previously described in Chapter II).

Because of the high affinity of sulfur for gold, thiol-terminated RAFT polymers enable an efficient 'covalent' grafting onto AuNP *via* two different approaches (Figure III. 1): *in situ* and ligand exchange (Figure III. 1).

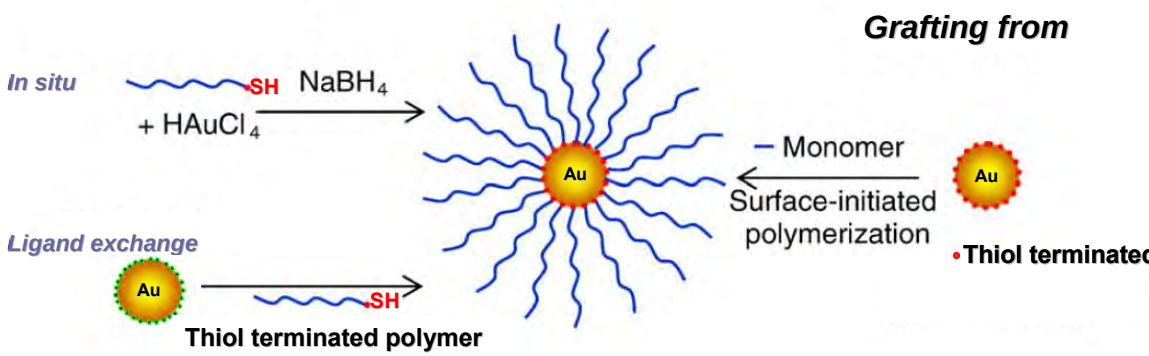

Figure III. 1: Grafting thiol-terminated polymers onto AuNP in aqueous solution *via in situ* or ligand exchange approach.

The 1st part of the chapter (Section III.2) contains a thorough bibliographic study on the grafting of RAFT polymers onto AuNP. It focuses on two main points:

- Grafting strategies used to obtain AuNP-polymer assemblies (Figure III. 1).
- Details on the nature of the RAFT polymers grafted onto AuNP, their properties, and the structure-property relationships of the resulting hybrid nanoparticles.

Then, the grafting of PNAM homopolymers and chromophore-polymer conjugates onto AuNP will be described. PNAM homopolymers were used to optimize the grafting conditions and to study the influence of experimental parameters on the properties the final hybrid nano-objects (Section III.3). Finally, optimized grafting conditions served as a basis for the functionalization of 20 nm spherical AuNP with chromophore-polymer conjugates using "grafting to" strategy and ligand exchange approach (Section III.4).

III.2. Bibliography: AuNP grafted with RAFT polymers

Polymer coated AuNP have been first mentioned when in 1718 Hans Heinrich Helcher reported that starch can significantly stabilize water-soluble colloidal gold. The field of polymer-stabilized AuNP has considerably evolved since then, with great progress in understanding the parameters leading to the stabilization of AuNP.

The main role of the stabilizing polymer was to prevent the nanoparticles from aggregation. Initially, the most commonly used polymers were polyvinylpyrrolidone (PVP) and poly-(ethylene glycol) (PEG).[1] However, during the last decade, the interest of designing polymer grafted AuNP consisted in synergistically combining the properties of colloidal gold with the properties of polymers, in order to produce multifunctional hybrid nano-objects (often addressed as "intelligent/smart" materials) for promising bio- and nanotechnology applications.[2]

Polymers can be synthesized by all available polymerization techniques, however, thanks to their multiple advantages, CRP (Controlled Radical Polymerization) techniques (Chapter II), are more and more used to synthesize and graft polymers onto AuNP. The main benefits in using such polymers are listed below:

- Well-defined polymer compositions and architectures.
- Control over polymer molecular weights.
- Controlled end-group functionalities for oriented grafting onto AuNP.
- Ability to polymerize monomers directly on AuNP surfaces in a controlled manner.
- Possibility to obtain well-defined hybrid AuNP, thus to accurately characterize them.

In this context, the next pages will mainly focus on advances in grafting AuNP with polymers obtained by CRP techniques.

III.2.1. Methods used to synthesize polymer coated AuNP

Regarding the polymer attachment to the AuNP surface, two main strategies could be distinguished: "grafting from" or "grafting to".[3] The first one consists in the synthesis of the polymers from the nanoparticle surface, the latter already functionalized with initiator molecules participation at the surface-initiated polymerization. The second method focuses on the grafting of already synthesized polymers directly on the nanoparticles (either through ligand exchange or *in situ* approach). Each strategy is usually independently used and its choice depends on the polymerization technique used to synthesize the polymers. However, both of them may be combined in the same system to obtain complex polymer coated nanoparticles.[4]

Figure III. 2 summarizes the possible routes allowing to coat AuNP with polymer chains.

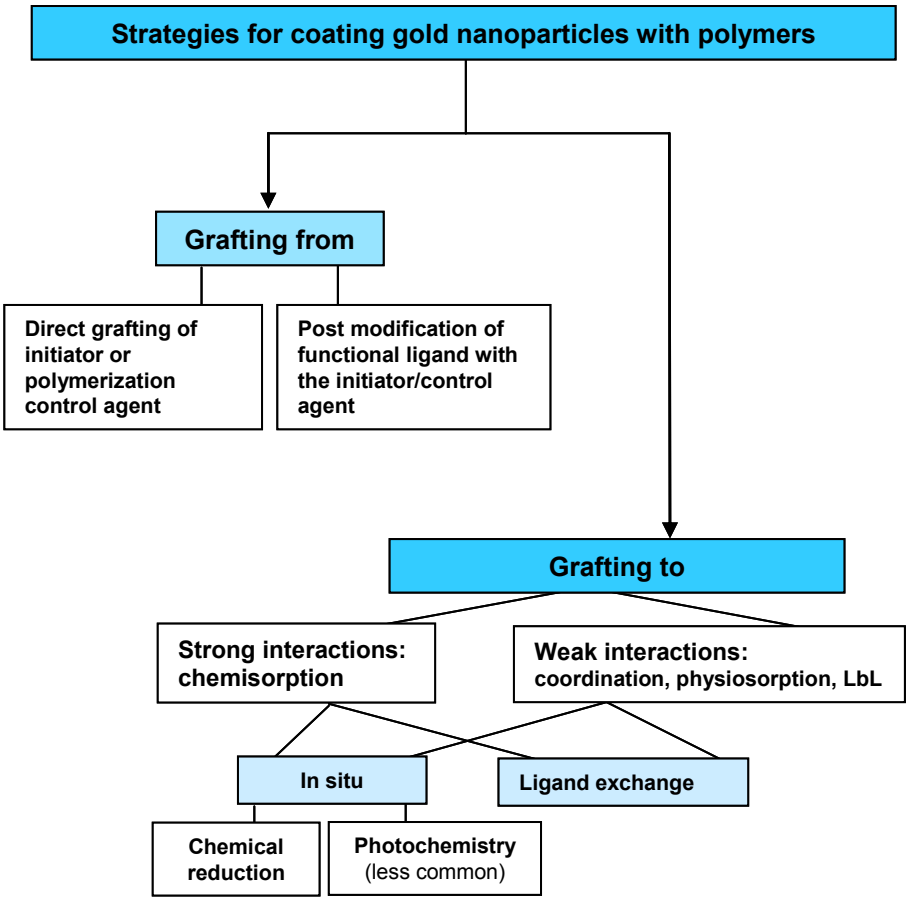

Figure III. 2: Strategies and various synthetic routes allowing to produce AuNP coated with polymers.

Depending on the method used to synthesize the AuNP core, two common approaches could be distinguished: *in situ* and ligand exchange. Unlike "grafting from" and "grafting to" strategies, that are specific for polymer grafting, *in situ* and ligand exchange approaches are general routes for the synthesis and stabilization of AuNP either by small molecular ligands, or by polymer chains. In the framework of polymer grafting, these two approaches relate exclusively to "grafting to" strategy, and consist in using already preformed polymer chains in the role of stabilizing ligands.

All these methods are well illustrated in Figure III. 3 and will be discussed below.

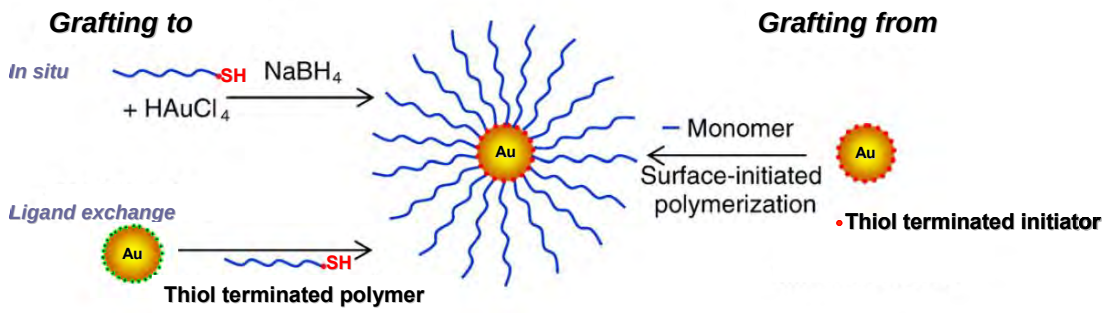

Figure III. 3: Grafting thiol-terminated polymers onto AuNP in aqueous solution. "Grafting to" *vs.* "grafting from" strategy; *in situ vs.* ligand exchange approach.

III.2.1.1. "Grafting from" strategy

"Grafting from" strategy consists of polymer chains synthesized directly from AuNP surfaces, the latter previously coated with molecular initiators or control agents (CA). Surface initiated polymerization occurs then in the presence of monomers, which can easily diffuse to reaction sites situated on AuNP. High polymer coverage of AuNP is ensured through a high grafting density of the initiator/CA, controlling the number of grafted polymer chains.

"Grafting from" strategy is based on surface-initiated controlled radical polymerization (CRP) techniques.[5] [6] ATRP is by far the most used technique in that case and is compatible with a large assortment of monomers and functional groups; it also tolerates a relatively high degree of impurities. RAFT polymerization seems to be less used in surface initiated polymerization than ATRP. Compared to ATRP, where the initiator is directly attached to AuNP surface, in RAFT polymerization, either (i) the initiator, or (ii) the chain transfer agent (CTA) can be grafted.

(i) When the initiator is attached to the surface, a large amount of CTA should be added in the solution* to synthesize RAFT polymers. Because the CTA has a sulfur-containing group with high affinity for gold, early termination by CTA capping to AuNP surface can occur.

(ii) CTA can be grafted by either its R-group or Z-group (Chapter II, Figure III. 4) – both participating in the control of RAFT polymerization.

Figure III. 4: Grafting a CTA used for surface initiated RAFT *via*: a) R-group grafting; b) Z-group grafting.

The R-group grafting implies constant surface detachment of the CTA during RAFT polymerization, which might broaden the molecular weight distribution and also reduce the grafting density. In the case of the Z-group grafting, shorter grafted polymer chains could be obtained. In fact, at high conversion, the growing chains with the CTA become less accessible for monomer addition near AuNP surface.

These drawbacks explain the less popular use of RAFT polymerization in "grafting from" strategy.

To the best of our knowledge, NMP surface initiated polymerization was never used to synthesize polymer coated AuNP. However, TEMPO radical (*2,2,6,6*-tetramethypiperidine-*1*-oxyl radical) has been recently successfully grafted onto ~2 nm AuNP.[7] Compared to ATRP and RAFT, NMP is essentially limited to styrenic monomers and requires relatively high polymerization temperatures, which can explain its lower interest in "grafting from" strategy.

* During RAFT, the concentration of the initiator in very low compared to that of the CTA (Chapter II).

Therefore, two main CRP techniques have been employed to obtain grafted polymers *via* surface initiated polymerization: ATRP[8-10] and RAFT[11-13].

In this context, two approaches could be distinguished when grafting initiators/CA onto AuNP surfaces (Figure III. 5):

a) Direct attachment of a thiol terminated initiator/CA to AuNP surface. [8 9 10]

b) Controlled post-modification of AuNP (functionalized by ligands containing active groups) with functional initiator molecules.[11 12 13]

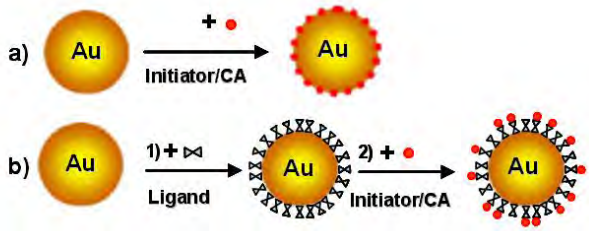

Figure III. 5: Approaches of grafting initiators/CA onto AuNP surface.

a) The 1st approach is rather easy and efficient, leading to polymer-grafted AuNP often by surface initiated ATRP.

Examples include AuNP of 14 nm functionalized with poly(*4*-vinylpyridine) (PVP),[9] or 2.7 nm grafted with poly(methyl methacrylate) (PMMA) with a grafting density of ~0.3 chains/nm².[10]

b) The 2nd approach, involves at least two steps: 1) functionalization of AuNP with a reactive ligand; 2) the post-modification of ligand protected AuNP with reactive initiators. This approach allows to better control the number and the density of initiators linked to AuNP, but usually requires additional steps of synthesis and purification.

This approach has been successfully used in surface initiated ATRP to obtain stable 50 nm AuNP grafted with poly(methyl methacrylate) (PMMA)[11], or to attach poly(*N*-ispropyl acrylamide) (PNIPAM) polymers to 3.2 nm AuNP using RAFT polymerization,[11 13] thus reaching relatively high grafting densities (13 chains/AuNP using a PNIPAM with M_n=21 000 g.mol^{-1}).

To summarize, “grafting from” strategy leads to end-group grafted polymer brushes showing both high densities and good uniformity. However, grafted polymers are more difficult to analyze, because a supplementary step of cleaving the polymers from the AuNP surface is required to properly characterize them. Moreover, this strategy requires multiple synthesis and purification steps, making it tedious and less popular than “grafting to” strategy.

III.2.1.2. "Grafting to" strategy

Polymer grafted AuNP can be prepared directly and easily by "grafting to" strategy. It consists in the grafting of already synthesized, purified, and well characterized polymers onto AuNP.

AuNP can be functionalized and stabilized with polymers either by interacting with the entire polymer backbone or by oriented end-group grafting (Figure III. 6 a)).

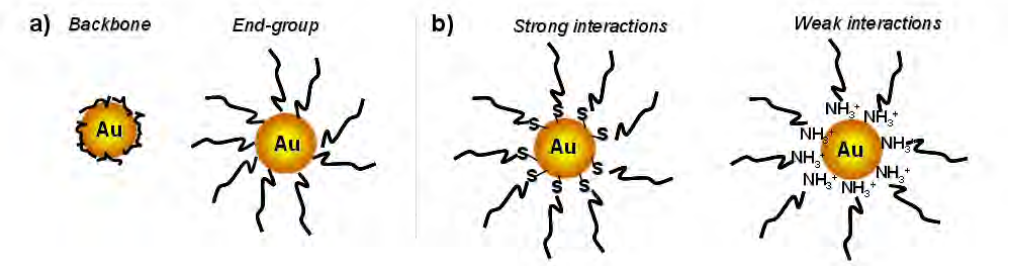

Figure III. 6: Functionalization of AuNP with polymers *via*: a) Backbone *vs.* end-group interactions; b) Strong *vs.* weak polymer-Au interactions.

Depending on the type of bonding between the Au core and the stabilizing polymers, they can be linked to the AuNP surface *via* strong or weak interactions (Figure III. 6 b)).

- Weak interactions referrer to steric and/or electrostatic stabilization of AuNP. They can be achieved *via* coordination chemistry (*e.g.* with amino groups[14]), layer by layer (LbL) approach,[15] electrostatic interactions, physiosorption[16] or encapsulation.[17]
- Strong interactions refer, most of the times, to oriented grafting of polymers bearing sulfur-based groups as thioesters, thiocarbamates, thiols, sulfides, thioctic acids… In this case, chemisorption of polymer chains is possible thanks to the existing strong affinity between Au and sulfur, approaching a covalent bond (Au-S bond strength: 47 kcal/mol).[18] Here the notion of 'covalent grafting' onto AuNP is frequently used.

Two CRP techniques mentioned before, ATRP[19] and RAFT[25-53], have been successfully used to graft polymers onto AuNP surfaces by "grafting to" strategy.
As opposed to "grafting from" strategy, RAFT polymerization was more frequently used in the "grafting to" strategy than ATRP, since RAFT polymers carry a sulfur-containing end-group. Another important advantage of RAFT polymerization relies in its versatility: it can be applied to a broad range of monomers with interesting properties (*e.g.* temperature and pH sensitivity, water-solubility, specific reactivity etc.) to produce copolymers with different architectures (di(tri)block, star, random, comb copolymers).

Examples of AuNP grafted with RAFT polymers *via* "grafting to" strategy will be exhaustively presented in Section III.2.2, providing essential information in terms of their properties and applications.

As explained earlier, the “grafting to” strategy can be processed following two different approaches: either by anchoring the preformed AuNP with already synthesized polymers (ligand exchange approach) or by forming the AuNP in the presence of the stabilizing polymers (*in situ* approach).

III.2.1.2.1. In situ approach

In situ two-phase approach was originally described by Wilcoxon et *al.*[20] and later modified by Brust *et al.*[21] *w*ho reported a one-step preparation of monodisperse AuNP, stabilized by a monolayer of chemisorbed alkanethiloate ligands. Brust method consisted in successive reduction of Au^{3+} to Au^{1+} in a phase transfer process (using tetraoctylammonium bromine (TOAB) as a phase transfer agent), then to Au^0, using a strong reducing agent, $NaBH_4$. Brust AuNP usually exhibit small diameters (<10 nm) and relatively high polydispersity. Due to their alkenthiolate surface coverage these AuNP are mostly soluble in organic solvents.

Water-soluble monodisperse AuNP could later be obtained by Brust’s team, using thioether-terminated polymeric stabilizers.[22] In this case, the one-step aqueous *in situ* approach based on Brust’s initial method consisted in the reduction of a gold precursor ($HAuCl_4$, Au^{3+}) in the presence of water-soluble polymers using a strong reducing agent ($NaBH_4$) (Figure III. 7). If the reduction of Au^{3+} salt takes place in a polar organic solvent, then the reducing agent used is usually $LiB(C_2H_5)_3H$.

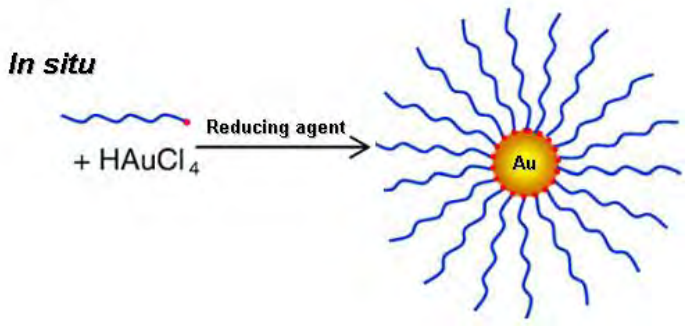

Figure III. 7: Experimental procedure of *in situ* approach allowing to graft polymers onto AuNP.

III.2.1.2.2. Ligand exchange approach

Two-step ligand exchange (or place exchange) approach consists in replacing a weak ligand (*e.g.* citrate) on preformed AuNP by a stronger ligand (thiol or another sulfur-based ligand).

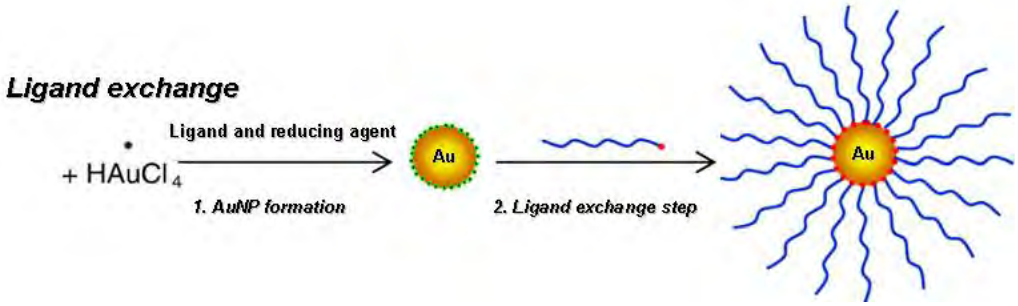

Figure III. 8 : Experimental procedure for ligand exchange "grafting to" approach allowing to obtain, in two steps, polymers grafted AuNP: 1st step – formation of citrate-capped AuNP; 2nd step – polymer grafting *via* surface ligand exchange process.

In a 1st step, preformed AuNP were synthesized using one of the most popular protocols, first described by Turkevich,[23] based on reduction of $HAuCl_4$ salt by sodium citrate in water (Figure III. 8, 1st step – AuNP formation). AuNP size is controlled by trisodium citrate-to-gold ratio and can be varied between 10 and 150 nm (1st study reported by Frens[24] in 1973).
In the 2nd step, preformed AuNP are mixed with thiol-terminated polymers, and undergo a dynamic ligand exchange process during which citrate molecules (weak-interaction ligands) are exchanged with polymers (strong-interaction ligands) at the surface of AuNP (Figure III. 8, 2nd step – ligand exchange).

III.2.2. RAFT polymers grafted onto AuNP

AuNP grafted with RAFT polymers represent a relatively recent filed of research, as RAFT was only discovered in 1998. The first example of such nano objects was reported in 2002 by McCormick.[25]

During the last decade, functionalization of AuNP with RAFT polymers was investigated with respect to the grafting conditions and the properties of grafted systems, the main goal being to prove the grafting as well as its consequences on the properties of the final object. Thanks to their ease of fabrication, spherical AuNP represent >95% of those studies. Another advantage of spheres compared to other geometries is their homogeneous surface coverage. Nonetheless, other AuNP shapes, as nanorods,[26] could be also successfully grafted with RAFT polymers.

Up to date, and mainly during the last decade (with an important amount of articles between 2009 and 2011, published throughout the course of this work) several homopolymers and copolymers produced by RAFT polymerization have been used.

In this section, hybrid systems have been arbitrarily classified with regards to specific surface properties provided by the polymer, nature of RAFT polymers, size of AuNP and the grafting approach are also mentioned.
The following pages will contain some key characteristics of each one of these categories, focusing on AuNP-RAFT polymer systems with a potential interest for biological applications.

A brief review on AuNP grafted with RAFT polymers *via* the "grafting to" strategy will be exposed in the next pages. Hybrid systems were classified with respect to their main functionality:

1) AuNP with controlled water-solubility
2) Stimuli responsive AuNP
3) AuNP as sacrificial templates
4) AuNP for biological applications

A list of analytical techniques allowing to characterize polymer coated AuNP are summarized in Appendix III.1.

III.2.2.1. AuNP with controlled water-solubility

RAFT polymerization is well adapted for polar monomers and can be used to produce a large variety of water-soluble polymers, able to tune and enhance the hydrophilicity of grafted AuNP (Table III. 1).

Table III. 1 : AuNP with controlled water-solubility grafted with RAFT (co)polymers

Grafted polymers	Grafting approach	Solvent	AuNP size	Ref.
PAA	Stabilized preformed AuNP with PEG-*b*-PCL	DMF or water	3.7 nm	[27]
Poly(styrene-*co*-vinyl phenol) (PSVPh)	*In situ* ($NaBH_4$)		5.7 nm	[28]

Fustin *et al.*[27] found an easy technique allowing to increase the hydrophilicity of AuNP by using poly(ethylene glycol)-*b*-poly(ε-caprolactone) (PEG-*b*-PCL) five arm star block copolymer. Those AuNP could be easily transferred from DMF (the synthesis solvent) to water after grafting in one-step trithiocarbonate poly(acrylic acid) (PAA-S-CS-S-PAA) (Figure III. 9). Because PAA is capable of changing its conformation with pH, PAA grafted AuNP (AuNP-PAA) could be investigated as a pH sensitive system; however, the authors did not study the influence of pH on the properties of AuNP-PAA.

Another approach used to control the hydrophilicity has been proposed by Dadmund's group.[28] It consisted in using a grafted poly(styrene-*co*-vinyl phenol) copolymer containing a chosen amount of hydrophilic vinyl phenol groups. In this case, the polarity of the system could be readily controlled by the composition of the initial copolymer poly(styrene-*co*-acetoxystyrene), whose acetoxystyrene groups were transformed into water-soluble vinyl phenol groups before grafting.

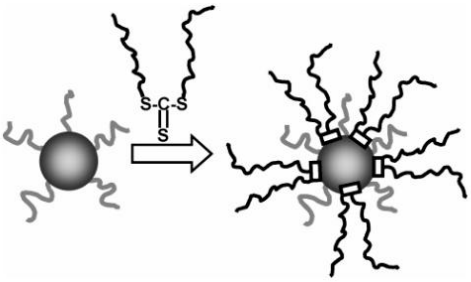

Figure III. 9: Representation of the chemisorption process of PAA-S-CS-S-PAA Chains onto AuNP's prepared in a five-arm PEG-*b*-PCL star block copolymer (the trithiocarbonate moieties are represented by the white rectangles).[27]

III.2.2.2. Stimuli responsive AuNP

More than a half of the works on AuNP grafted with RAFT polymers is related to stimuli responsive systems and in particular, temperature and pH responsive AuNP (Table III. 2). Among them, a great majority concerns poly(*N*-isopropyl acrylamide) (PNIPAM) homo and copolymers (Table III. 2), showing that PNIPAM, is by far the most studied polymer in this context.

Table III. 2 : Temperature and pH responsive AuNP grafted with RAFT (co)polymers.

Grafted (Co)polymer	Grafting approach	Solvent	AuNP size	Ref.
*** PAMPS [a], PVBTAC [b], PDMA [c], P(MAEDAPS-*b*-DMA) [d]**	*In situ* reduction with $NaBH_4$	* Water	* <10 nm	[25]
*** PEG-*b*-PNIPAM**		* THF/EtOH	* 5 -30 nm	[29]
*** PNIPAM**	*In situ* reduction with: $LiB(C_2H_5)_3H$ in	THF	* 1-3 nm	[30] [31] [32]
*** PS-*b*-PNIPAM**			* 6 nm, 15 nm, 30 nm	[33]
- PBuA-*b*-PNIPAM	Direct grafting on preformed AuNP	Water (pH~8)	8 nm	[34]
- PVCm [e]				[35]
- PAA - PNIPAM - PAPTAC [f]				[36]
PNIPAM	Ligand exchange	Water	9 nm	[37]
P(DMAEA) P(AEA) P(AA) P(OEG-A) P(OEG-A-*co*-DEG-A)			20 nm	[38] [39]
P(OEGMA) [g]			6 nm, 12 nm, 30 nm	[40]
PEG-*b*-PDMA			12 nm	[41]

a) PAMPS = poly(sodium *2*-acryl-amido-*2*-methyl propane sulfonate)

b) PVBTAC=poly((vinylbenzyl)-trimethylammonium chloride)

c) PDMA= poly(*N,N*-dimethyl- acrylamide)

d) PMAEDAPS-*b*-PDMA=poly(*3*-[*2*-*N*-methylacrylamido)-ethyl dimethyl ammonio propane sulfonate-*block*-*N,N*-dimethylacryl-amide)

e) PVCm=poly(*N*-vinyl caprolactam).

f) PAPTAC=poly[(*3*-acryl-amidopropyl) trimethylammonium chloride].

g) P(OEGMA)=poly(oligo(ethyleneglycol)methacrylate).

PNIPAM's interesting properties justifying the clear preference for this polymer are listed below:

- PNIPAM is water-soluble at room temperature.
- PNIPAM undergoes thermally reversible phase separation at ~31-32°C (lower critical solution temperature, LCST*).[42]
- PNIPAM is the most studied thermosensitive polymer for bioapplications[43] (*e.g.* immunology, drug delivery, bio-conjugation).

Ultimately, depending on the properties of grafted polymers, AuNP can also be light responsive or multiresponsive.

a) Temperature responsive AuNP

McCormick and co-workers[25] were the first to graft onto AuNP water-soluble well-defined RAFT (co)polymers, composed of an anionic, cationic, neutral, and zwitterionic species (in 2002). They evidenced the efficient grafting *via* thiocarbonylthio end-groups (transformed in thiols during reduction) and the long stability of grafted AuNP. However, limited characterization has been completed with these first systems.

Soon after that, Tenhu's group synthesized highly dense (1 – 4 chains/nm²) AuNP (1-3 nm) grafted with low MW PNIPAM, highlighting the influence of grafted PNIPAM chains confined at the surface of AuNP on phase transition temperature,[30 31] polymer conformation, [30 32] grafting density as a function of both M_n and AuNP size.[31]

In parallel, Moroshima's group[37] grafted PNIPAM chains on larger 9 nm AuNP and found a lower grafting density (0.9 chains/nm²).

Very quickly after the first studies on PNIPAM grafted AuNP, more research groups tried to explore the properties of AuNP-PNIPAM systems by using block copolymers containing a PNIPAM block and a second hydrophobic[33 34] or hydrophilic block.[29] The main goal of using the 2nd block was to influence the thermosensitivity of grafted systems by changing their hydrophobic/hydrophilic balance, thus the LCST of PNIPAM block.

Besides PNIPAM, other thermosensitive copolymers have been grafted onto AuNP: thermosensitive poly(*N*-vinyl caprolactam (PVC),[35] poly(oligoethylene glycol methacrylate) P(OEGMA).[40]

An original use of thermosensitive copolymers has been reported by Luo *et al.*,[41] whose goal was to increase AuNP colloidal stability. Poly(ethylene glycol)-*b*-poly(2-(dimethylamino)ethyl methacrylate), (PEG-*b*-PDMAEMA), obtained by RAFT has been grafted onto 12 nm AuNP. Thermosensitive PDMAEMA block (LCST ~32-50°C depending on its molecular weight), close to AuNP surface was chemically crosslinked (using a crosslinking agent) around the AuNP surface forming a rigid shell. The crosslinking transformed thermosensitive AuNP into a very stable system with respect to temperature and pH variations (Figure III. 10).

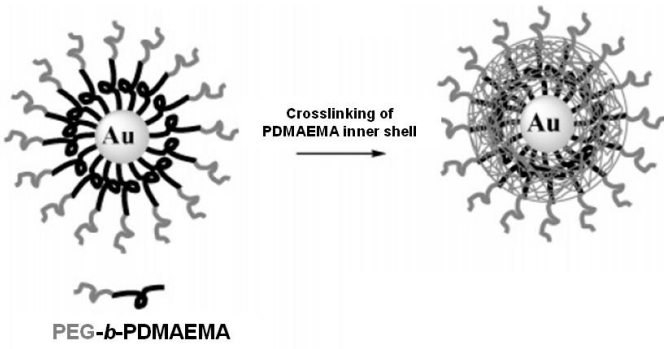

Figure III. 10: Thermosensitive PDMAEMA crosslinking ensuring higher stability of grafted AuNP.[41]

b) pH responsive AuNP

The pH sensitivity of grafted AuNP could be tailored using charged polymers as they undergo pH-induced conformational transitions (Table III. 2). When the charges are distributed along the polymer chain (usually placed on the repeating monomer unit), electrostatic repulsive forces will favor a stretched conformation of the chain. This conformation changes when pH responsive groups (*e.g.* carboxylates) are protonated (at acidic pH).

In this context, negatively charged poly(acrylic acid) (PAA), and positively charges poly(aminoethyl methacrylamide) (PAEMA) polymers have been grafted onto 8 nm AuNP[36] or 20 nm AuNP (Table III. 2).[38] [39] Aggregation behavior as well as grafting density varied with the polymer charge: on 20 nm AuNP grafting density with neutral polymer (PNIPAM) (0.9 chains/nm²) > than with positively charged polymer (0.6 chains/nm²) > than with negatively charged polymer (0.4 chains/nm²)).[39] Charges also can influence the catalytic efficiency of AuNP.[36]

c) Light responsive AuNP

Besides temperature and pH responsive RAFT polymer-AuNP assemblies, a few grafted AuNP systems have been studied regarding their behavior upon light excitation. Light-responsive systems were used to tune the SPR of AuNP, hence their reversible properties (switch "on/off" systems) by simple photoirradiation (Table III. 3).[44] [45]

Table III. 3 : Light responsive AuNP grafted with RAFT (co)polymers.

Grafted (Co)polymer	Grafting approach	Solvent	AuNP size	Ref.
Poly(diarylene) (P(DE))	**In situ* ($NaBH_4$) *Ligand exchange *Seeding method	* Water/toluene; THF/water/toluene) * Water * Water	*6 nm *13 nm *22 nm	[44]
P(DMA-co-Azo)	*In situ* (UV irradiation)	Water/MEOH	10 nm	[45]

Well-defined photochromic diarylethene polymers, poly(DE) (Figure III. 11), were grafted onto AuNP with different sizes (6 nm, 13 nm, 22 nm). All AuNP-poly(DE) exhibited reversible photochromism

[*] The lowest critical solution temperature (LCST) corresponding also to the temperature above which PNIPAM undergoes a phase separation because of the breakdown of the hydrogen bonds present at lower temperature.

upon irradiation either with UV or visible light. This behaviour was triggered by a reversibly breakable bond of DE moiety. Therefore, a reversible SPR band shift, induced by changes in the refractive index of the poly(DE) upon photochromic reaction, was recorded. [44]

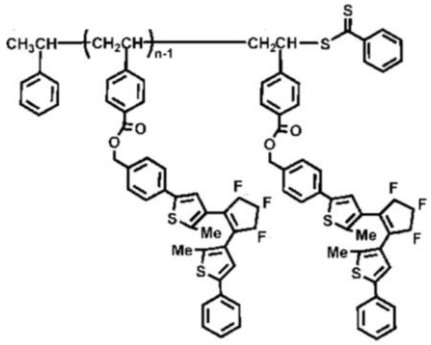

Figure III. 11: The structure of poly(DE).

A 2nd example relates to grafted 10 nm AuNP with water-soluble poly(*N,N*-dimethylacrylamide-*co*-*N*-4-phenylazophenyl), P(DMA-*co*-Azo).[45] Photoresponsive RAFT copolymers coated onto AuNP, could reversibly switch the aggregation state thanks to the *trans*-*cis* photoizomerization of the pending azo-chromophores (Figure III. 12). The photoresponsive aggregation of AuNP could be predicted and monitored by changes in SPR and transmittance of AuNP: the solution was transparent under visible light (*trans* form), but blurred out under UV light (*cis* form).

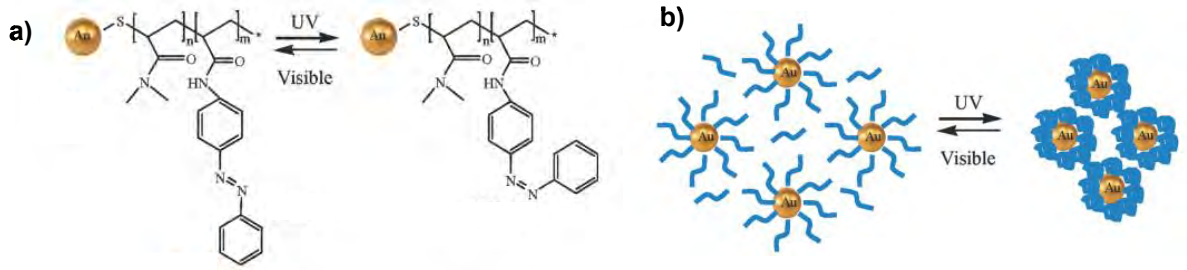

Figure III. 12: a) Chemical structure of the polymer grafted onto gold nanoparticles. b) Schematic illustration of the reversible light-triggered aggregation and dispersion of AuNPs as a result of the trans-cis photoisomerization process.[45]

d) Multiresponsive AuNP

Multistimuli responsive AuNP could be designed by combining temperature with pH or light sensitivity (Table III. 4).

Table III. 4 : Multiresponsive AuNP grafted with RAFT (co)polymers.

Grafted polymer	*Grafting approach*	Solvent	AuNP size	Ref.
PMAA-*b*-PNIPAM	*In situ* reduction with: $LiB(C_2H_5)_3H$ in	THF/MeOH	3 nm	46
PNIPAM	*In situ*	Water/MeOH	10 nm	47

For example, a temperature and pH responsive system was prepared by Tenhu's group who grafted PMAA-*b*-PNIPAM copolymers onto 2.7 nm AuNP.[46] PMAA, poly(methacrylic acid), was the pH

responsive block and PNIPAM, the temperature responsive block. They showed that PNIPAM block, close to AuNP surface, changed the environment polarity near AuNP, and impacted noticeably the SPR, while PMAA block controlled the stability against aggregation of particles upon pH variations.

An interesting example of coupled thermo- and light responsive hybrid system is represented by 10 nm AuNP grafted with PNIPAM functionalized with a BODIPY end-group (Figure III. 13). The distance dependent fluorescence of BODIPY near AuNP has been evidenced: fluorescence intensity increased with the increasing length of the polymer chain (impacted by changes in temperature). The changes in fluorescence intensity (fluorescence emission/quenching) were completely reversible during the heating and cooling cycles.

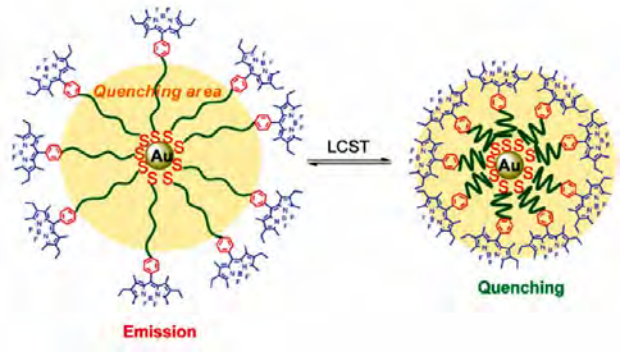

Figure III. 13: AuNP grafted with PNAIPAM-BODIPY.[47]

III.2.2.3. Grafted AuNP as sacrificial template

Grafted AuNP with RAFT polymers have also been used as hard templates for the preparation of hollow polymer nanocapsules (Table III. 5). The cavity size corresponded to the AuNP diameter, after the elimination of the gold core either by pyrolysis,[48] or by chemical dissolution.[49]

Table III. 5 : AuNP grafted with RAFT (co)polymers – as sacrificial templates.

Grafted (Co)polymer	***Grafting approach***	**Solvent**	**AuNP size**	**Ref.**
PAN-*b*-PAA	*In situ*	Water	3 nm	[48]
P[HPMA-*b*-(Sty-*alt*-MA)] [a] **P[OEGA-*b*-(Sty-*alt*-MA)]**	Ligand exchange	Water	13 nm	[49]

[a] Styrene (Sty) or poly(oligoethylene glycol acrylate) (POEGA) and maleic anhydride (MA) alternating copolymer.

One strategy consisted in using 35 nm micelles, composed of amphiphilic poly(acrylonitril-*b*-acrylic acid), PAN-*b*-PAA, as mini reactors for the synthesis of 3 nm AuNP.[48] During pyrolysis (900°C) of those hybrid systems, the Au core inside the micelles fused and diffused out of the organic shell, leaving behind 30 nm stable hollow carbon nanoparticles.

A 2nd strategy consisted in dissolving the AuNP core with aqua regia* (Figure III. 14). In this case, P[HPMA-*b*-(Sty-*alt*-MA)] and P[OEGA-*b*-(Sty-*alt*-MA)] have been grafted onto 13 nm AuNP.[49] In order

* Aqua regia = Nitro-hydrochloric (volume ratio of 1:3) acid mixture.

to ensure a very good stability and a controlled size of the organic polymer shell, the polymer block close to the gold core was chemically crosslinked (*via* diamine-maleic anhydride reaction) before dissolution of the gold core with aqua regia.

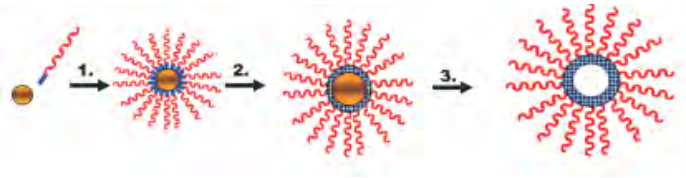

Figure III. 14: Synthesis of nano-capsules using gold nanoparticles as sacrificial templates: 1. Polymer grafting; 2. Inner shell cross-linking; 3. Au core removal.[49]

III.2.2.4. Grafted AuNP for biology

Even if most of water-soluble polymer-grafted AuNP listed above could potentially find an application in biology, not all of them have been evaluated in bio-relevant media.

Moreover, the existing studies on evaluating the biological response of AuNP grafted with RAFT polymers are very recent and focus on proving their potential for bio-oriented applications (Table III. 6).

Table III. 6 : RAFT polymer grafted AuNP for biological applications.

Application	(Co)polymer	Grafting approach	Solvent	AuNP size	Ref.
Water-soluble stable AuNP as effective SERS encoded substrates [a]	Polyacryloyl esters (homo and copolymers) with carbamate end-groups	Ligand exchange	THF/Water	45 nm	50
Molecular recognition of biotinylated AuNP.	Biotin-P(NAM-*co*-ManAm) [b] Biotin-P(NAM-*co*-GlcNAcAm) [b]	*In situ* (UV irradiation)	Water	4-6 nm	51
Influence of AuNP size and surface coverage on cellular translocation and cytotoxicity.	PNIPAM PAA PDHA PAEA	*In situ* Ligand exchange	Water	5 nm 10 nm 17 nm	52
Influence of AuNP size and surface charge on cellular uptake.	PNIPAM PAA PDHA PAEA		Water	5 nm 12 nm 19 nm	53

[a] Surface Enhanced Raman Spectroscopy.

[b] Monomers contain different carbohydrate pendant groups: N-acetyl β-D-glucosaminopyranoside (GlcNAc) or *α-D*-mannopyranoside (Man).

Polymer grafted AuNP can be used in biological sensing and recognition. For example they may serve as efficient SERS (Surface Enhanced Raman Scattering) substrates for sensing applications,[50] since they are capable to increase the SERS effect by avoiding the typical aggregation occurring with 'naked' AuNP. Another example, from studies in our group, is related to AuNP grafted with glycopolymers synthesized by RAFT, which have been proven efficient for specific biomolecular recognition by selective detection of different carbohydrates.[51]

Recently, a range of RAFT polymers were bound onto well-defined spherical AuNP with different sizes (d_{Au} ~5 nm, ~10 nm, ~20 nm) reaching relatively high grafting densities (~1 chain/nm²). Negatively charged (poly(acrylic acid), PAA), positively charges (poly(*2*-aminoethylacrylamide), PAEA) and neutral (poly(*2,3*-hydroxy-propylacrylamide) – P(HPAM), PNIPAM) polymers were used.[52] [53] Grafting AuNP allowed to study cell permeability, cytotoxicity,[52] and cell uptake[53] in Caco-2 cells – epithelia line widely used as *in vitro* model system. It has been demonstrated that cellular uptake was facilitated by charges on the polymer backbone: positively charged AuNP were internalized with greater efficiency compared to negatively charged and neutral AuNP.[53] Moreover, negatively charged AuNP showed a significantly higher translocation, and a lower binding to the cells, compared to positively charged AuNP.

In comparison to these studies a library of RAFT polymethacrylamides derived from poly(pentafluorophenyl methacrylate) precursors were grafted onto AuNP of different sizes (d_{Au}~10 nm, ~25 nm, ~50 nm).[54] Methacrylamide side-chain functionality of the polymer determined the surface charge of nanoparticles (neutral, positively charged or negatively charged). In this study the grafting densities were found to vary between 0.3 and 1.2 chains/nm², depending on the polymer length and its chemical nature. The effect of polymer charge, AuNP size and polymer length on the aggregation of particles was evaluated in 15 different solvents.

In this bibliographic section, the two main strategies leading to AuNP-polymer systems have been presented: “grafting from” and “grafting to”. “Grafting from” strategy, based on surface initiated CRP techniques, seems to be less popular than “grafting to”, since it implies the synthesis of polymer chains directly from the AuNP surface. Although the grafting densities are relatively high by “grafting form”, the polymer growth on the surface of AuNP can interfere and perturb the polymerization process, and usually requires several steps of synthesis and purification.
Unlike “grafting from”, “grafting to” strategy is widely used especially with polymers synthesized by RAFT. These polymers exhibit sulfur-containing end-groups that strongly interact with gold and enable an oriented grafting onto AuNP surface. The “grafting to” strategy of RAFT polymers with different sizes has been proven efficient, enhancing the stability and tailoring the surface properties of grafted AuNP *via* the right polymer choice.

In this context, many RAFT polymers with different properties and functionalities could be successfully used. The general goal of recent studies (2009-2012) consisted in evidencing the grafting, and studying the properties of AuNP-polymer systems before and after grafting.
Thanks to their versatility and controlled structure, AuNP grafted with RAFT polymers exhibit interesting properties for biological applications. In the last couple of years, they have been tested in biological media, giving encouraging results and proving their potential for such applications.

All these benefits motivated the choice of RAFT technique in this work to synthesize chromophore-polymer conjugates for grafting onto AuNP.

III.3. Synthesis, purification and characterization of AuNP-PNAM

Before grafting high added-value chromophore-polymer conjugates onto AuNP, we first used thiol-terminated PNAM-SH homopolymers (Chapter II), to prove the efficient oriented grafting onto AuNP *via* chain end-group and to optimize the experimental conditions of grafting and purification.

Taking into account the information learned about synthesizing polymer coated AuNP, we decided to focus our work on the "grafting to" strategy. For this purpose, *in situ* and ligand exchange approaches used here will be first described, followed by a detailed description of purification and characterization techniques which finally allowed a full study of the properties of AuNP-PNAM systems.
Afterwards, the results obtained by *in situ* and ligand exchange approaches will show the influence of various experimental conditions (*e.g.* concentration of reagents, Au/S ratio) on the properties of the final nano-objects. Special attention will be drawn on the influence of the grafted polymer M_n, as we believe that it can be tuned to control the chromophore-AuNP in the case of grafted linear conjugates.

Our goal was:

- To prove, that PNAM-SH oriented grafting onto AuNP occurs *via* thiol-end group onto the surface of AuNP.
- To study the impact of experimental conditions on the properties of grafted AuNP.
- To properly purify the grafted samples and estimate the grafting density.

III.3.1. Synthesis and purification of AuNP-PNAM: experimental procedure

Grafted AuNP with PNAM polymers could be obtained either by one-step *in situ* approach, or two-step ligand exchange approach (using citrate-capped preformed AuNP).

III.3.1.1. In situ approach

Principle

As mentioned earlier, the one-step aqueous *in situ* approach is based on Brust's method.[21] Grafted AuNP-PNAM were obtained by reducing Au^{3+} salt ($HAuCl_4$) in water, in the presence of water-soluble PNAM-SH (or PNAM-DT) polymers, using a strong reducing agent ($NaBH_4$) (Figure III. 15).
By *in situ* approach, PNAM bearing either a dithioester (DT) or a thiol (SH) end-group could be used for AuNP stabilization. Indeed, they behave in a similar way since rapid and efficient reduction of DT into thiols occurs in the presence of $NaBH_4$.[25] The use of $NaBH_4$ in excess, also prevents the formation of disulfide bonds in water between two polymer chains, thus increasing the degree of AuNP functionalization.

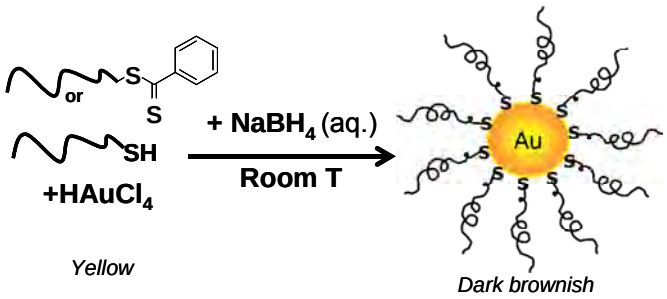

Figure III. 15: Experimental procedure of *in situ* approach leading to grafted AuNP-PNAM (with PNAM-DT or PNAM-SH).

AuNP size control

For *in situ* grafting the role of the ligand (polymer) is to stabilize and control the size of AuNP, as it participates in the nucleation and growth processes of AuNP metallic cores.[55]

Previous studies on *in situ* polymer grafting have shown that polymer concentration, length and chemical structure can influence the size of AuNP. [56] [57] In the case of thiol-ligands (alkanethiols), size-control can be achieved by choosing the suitable Au/S molar ratio.[58] However, when the ligand is a polymer, the impact of Au/S (Au/polymer) ratio for *in situ* approach is limited, giving particles with a diameter between 2 nm – 5 nm.[59]

III.3.1.2. Ligand exchange approach

Principle

Unlike *in situ*, ligand exchange is a two-step process (Figure III. 16).

- In the 1st step, ~20 nm AuNP are obtained by reduction of $HAuCl_4$ salt with sodium citrate under reflux in water (Turkevich method).[23]
- The 2nd step supposes the stabilization of preformed citrate-capped AuNP with thiol-terminated PNAM-SH polymers *via* a dynamic ligand exchange process between a weak (citrate) and a strong ligand (polymer) in solution.

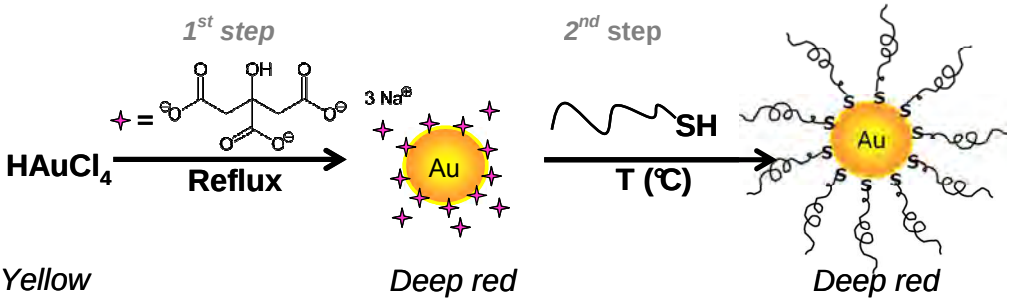

Figure III. 16: Experimental procedure for ligand exchange "grafting to" approach allowing: 1st step – formation of citrate-capped AuNP; 2nd step – polymer grafting *via* surface ligand exchange process.

AuNP size control

The 1st step is responsible for AuNP size control, more specifically through Au/citrate ratio. Here sodium citrate acts both as a reducing agent and an anionic stabilizer. Mechanistic features and kinetics of AuNP formation during citrate reduction have been discussed in literature, showing how Au/citrate ratio controls the size of AuNP.[60]

Before discussing the result obtained using previously mentioned *in situ* and ligand exchange approaches, the following part will focus on the techniques used to purify AuNP-PNAM systems.

III.3.1.3. Purification

Efficient purification of grafted AuNP is essential for further use in bio-related applications, but also to accurately characterize them.

After successful synthesis of water-soluble, stable grafted AuNP, the goal was to isolate them from any other species in solution (molecular species and free ungrafted polymers, Figure III. 17).

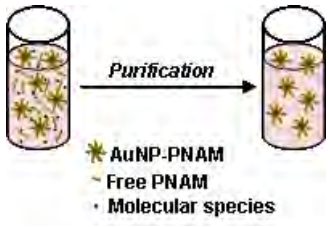

Figure III. 17: PNAM grafted onto AuNP before and after purification.

Initially, purification of AuNP-PNAM systems was a great challenge because AuNP-PNAM and free PNAM exhibited similar solubility properties and could not be purified by selective precipitation for example.

The only significant difference in their properties (apart from the specific optical response of AuNP) was their size and molecular weight. Based on this observation, we tested various purification methods allowing to selectively separate species with different sizes: dialysis, centrifugation,[61] centrifugal ultrafiltration (also called centrifugal solvent displacement) using Amicon Millipore devices,[62] Size Exclusion Chromatography (SEC). Details on each one of these methods are exposed in Appendix III.2.

Table III. 7 illustrates the results of purification techniques used in the case of AuNP-PNAM synthesized by either *in situ* or ligand exchange approach. They will be shortly discussed below.

Table III. 7 : Methods used to purify AuNP-PNAM obtained by in situ grafting.

Purification method	Efficiency		Advantages	Drawbacks
	***In situ* approach**	**Ligand exchange approach**		
1) Dialysis	-	-	Simple and easy	Long and may be

(8 bath changes every 12h) Regenerated cellulose membrane (MWCO=50kDa)				inefficient for macromolecules
2) Centrifugation (8000rpm, 10 min; 3 cycles)	±	+	Fast, costless and efficient.	Less efficient for small water-soluble nanoparticles (⇒ non-negligible losses)
3) Centrifugal ultrafiltration (8000rpm, 10 min; 3 cycles) Regenerated cellulose membrane for tangential flow filtration (MWCO=50/100kDa)	++	++	**Very efficient, rapid and easy**	Expensive

1) Unexpectedly, *dialysis* through a cellulose membrane (with MWCO at least 3 times larger than M_n(PNAM)) was the less efficient method. The recovery of the polymer inside the membrane after more than 4 days of dialysis was >70%. We suppose that, independently on its M_n, PNAM conformation in water prevents its passing though the membrane pores (whose MWCO is calibrated with globular proteins).

2) Because it is easy, fast and less expensive, *centrifugation* is the most widely employed technique to purify grafted AuNP.[61] Indeed, 20 nm AuNP-PNAM obtained by ligand exchange could efficiently be separated from the rest of the solution. However, 2 nm AuNP-PNAM obtained by *in situ* could be only partly recovered after centrifugation, as they exhibited a strong tendency to redispers in water due to their very small size.

3) *Centrifugal ultrafiltration* seemed be the most promising procedure for an efficient separation. In this case, the filtrating membrane placed inside the Amicon device (Appendix III.2) had the same chemical nature and the same MWCO as the membrane used for dialysis. However, the capacity of the polymer to cross the membrane increased significantly thanks to the centrifugal force.

In conclusion, all AuNP-PNAM synthesized in this work were purified by *centrifugal ultrafiltration*.

III.3.2. Characterization of grafted AuNP-PNAM

After the mandatory step of purification, grafted AuNP-PNAM were thoroughly characterized in terms of:

- Degree of purity (by ^{1}H-DOSY NMR – Appendix III.3)
- Size (by TEM and DLS)
- Composition and grafting density (by TGA)
- Optical properties – Surface Plasmon Resonance (SPR) of AuNP (by UV-Vis spectroscopy).

Analytical techniques allowing to access each one of theses characteristics are described are detailed in the Experimental Section III.6.

III.3.3. Properties of AuNP-PNAM

The optimized purification technique (centrifugal ultrafiltration) and the optimized characterization techniques were used to properly study the influence of various experimental parameters on the properties of grafted AuNP-PNAM obtained either by *in situ* or ligand exchange approaches.
The results corresponding to previously listed studies (III.3.1) will be discussed as follows.

III.3.3.1. In situ approach

Trying to influence the AuNP properties, we investigated the impact of different experimental conditions.
Several experimental conditions were kept unchanged:

- Au/polymer or Au/S ratio = 3: taking into account previous studies pointing to a limited influence of this parameter on AuNP size.
- $NaBH_4$/Au ratio = 10: the ratio between Au and reducing agent may influence the kinetics of AuNP *in situ* formation. Because of a very rapid nucleation step, a large excess of reducing agent (>7 molar eq.) is recommended in order to avoid undesired precipitation and destabilization of AuNP.

While these two parameters were fixed, two experimental conditions were varied allowing to study:

→ The influence of Au initial concentration ($[Au]_0$): by varying the total volume of reaction medium, $[Au]_0$= 1,7mM / 3,3mM / 5,7 mM.

→ The influence of PNAM molecular weight M_n(PNAM): on the final size of grafted AuNPs: M_n(PNAM) = 3 300 / 14 100 g/mol – discussed in a separate section ((III.2.3.3)).

The "*in situ*" grafting experiments will allow to:

- Evaluate the purity of AuNP-PNAM by ^{1}H-DOSY NMR.
- Prove the grafting *via* thiol end groups of PNAM-SH polymers.

- Study the influence of the initial gold concentration $[Au]_0$ on the size of AuNP.

III.3.3.1.1. Evaluation of the purity of AuNP-PNAM

After showing (qualitatively) that centrifugal ultrafiltration was the most efficient technique for AuNP-PNAM purification, we also wanted to quantitatively prove the efficiency of this method by evaluating the degree of purity of AuNP-PNAM. For this purpose, 2D ^{1}H-DOSY NMR (or NMR diffusion) experiments were performed (Appendix III.3). This analysis provides a way to detect different compounds in a mixture based on the differences between their diffusion coefficients and therefore on the differences in their size and shape. 2D ^{1}H-DOSY NMR experiments were possible thanks to a fruitful collaboration with C. Chamignon, F. Boisson from INSA Lyon and S. Denis-Quanquin from ENS Lyon, who implemented the experiments and optimized the complex data processing.

Previously, NMR diffusion analysis with 45 nm AuNP grafted with polymer were used to prove the functionalization of AuNP by evidencing the presence of the grafted polymer on the surface of the AuNP.[50] In our work, 2D ^{1}H-DOSY NMR was recorded on *in situ* AuNP-PNAM purified samples (by centrifugal ultrafiltration) in D_2O and compared with the results of AuNP-PNAM reaction mixture containing an excess of free PNAM (unpurified sample) (Figure III. 18 a)).

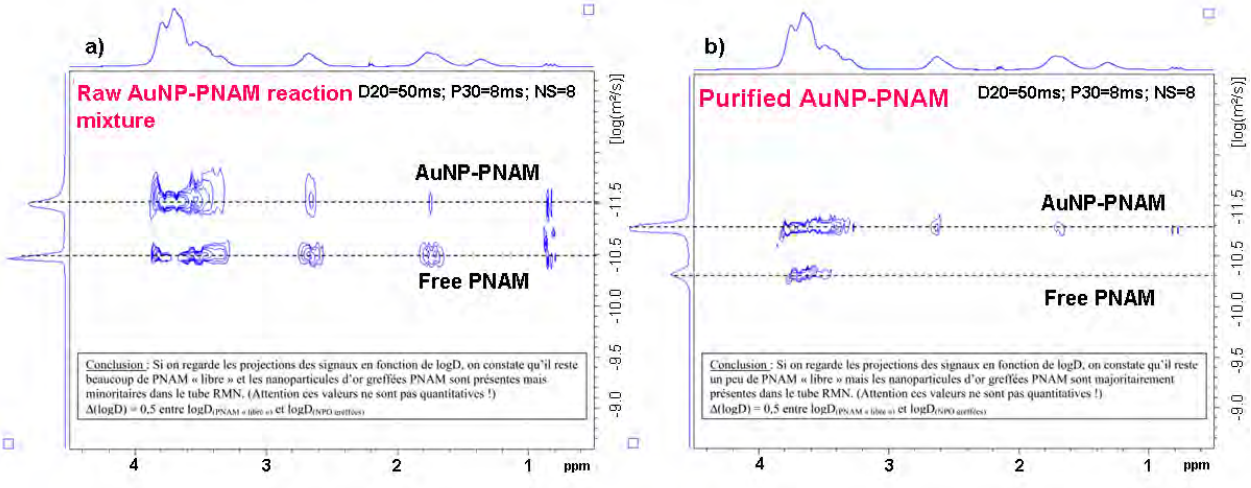

Figure III. 18: ^{1}H-DOSY NMR charts of: a) Raw AuNP-PNAM reaction mixture in D_2O; b) Purified AuNP-PNAM in D_2O.

The 2D ^{1}H DOSY NMR spectra of grafted AuNP-PNAM contain the ^{1}H NMR chemical shifts of PNAM on the horizontal axes, and the diffusion parameter on the vertical axes. The difference between grafted AuNP-PNAM and free PNAM in solution can be noticed through differences in their diffusion (Figure III. 18). The comparison between raw AuNP mixture (Figure III. 18 a)) and purified AuNP-PNAM (Figure III. 18 b)) shows a significant decrease in the amount of free PNAM after purification.

Even if the optimization of data processing, allowing to quantify the amount of free polymer in solution *vs.* grafted polymer, is still in progress, these first results allowed to clearly evidence the efficiency of the chosen purification method (centrifugal ultrafiltration).

III.3.3.1.2. Proof of oriented grafting via thiol end-groups

The main goal in this chapter was to graft chromophore-polymer conjugates onto AuNP, controlling the chromophore-AuNP distance by tuning the polymer chain length. Therefore, it seemed important to first prove that grafting with RAFT polymers occurred *via* the thiol (SH) end-groups and formed brushes on the surface of AuNP.

In this context, *in situ* grafting was an extremely easy technique. During the AuNP formation *in situ* (by reduction with $NaBH_4$), the stability of AuNP could be observed visually, since unstable AuNP quickly sedimented forming a black precipitate.

In order to evidence the oriented grafting through thiol end-groups, the following experiments were carried out (Figure III. 19):

1) Au^{3+}(aq.) reduction in the presence of thiol terminated PNAM-SH obtained by RAFT polymerization.
2) Au^{3+}(aq.) reduction without any polymer.
3) Au^{3+}(aq.) reduction in the presence of PNAM obtained by free radical polymerization (without any sulfur-containing end-groups).
4) Au^{3+}(aq.) reduction in the presence of PNAM-**X,** where **X** should be a modified end-group without sulfur atoms (resulting from a PNAM-DT polymer prior submitted to end-group modification reaction in the presence of AIBN (large excess) – Appendix III.4).[63]

In order to highlight the stabilizing capacity of RAFT polymers, and also to anticipate it in the case of chromophore-polymer conjugates (capped with AEM or hydrolyzed, Chapter II), two other tests have been completed (Figure III. 19).

5) Au^{3+}(aq.) reduction in the presence of P(NAM-*co*-NAS) random copolymer after quantitative hydrolysis of succinimide pendant groups.
6) Au^{3+}(aq.) reduction in the presence of P(NAM-*co*-NAS) random copolymer after quantitative aminolysis of succinimide pendant groups with AEM (4-(2-aminoethyl)morpholine).

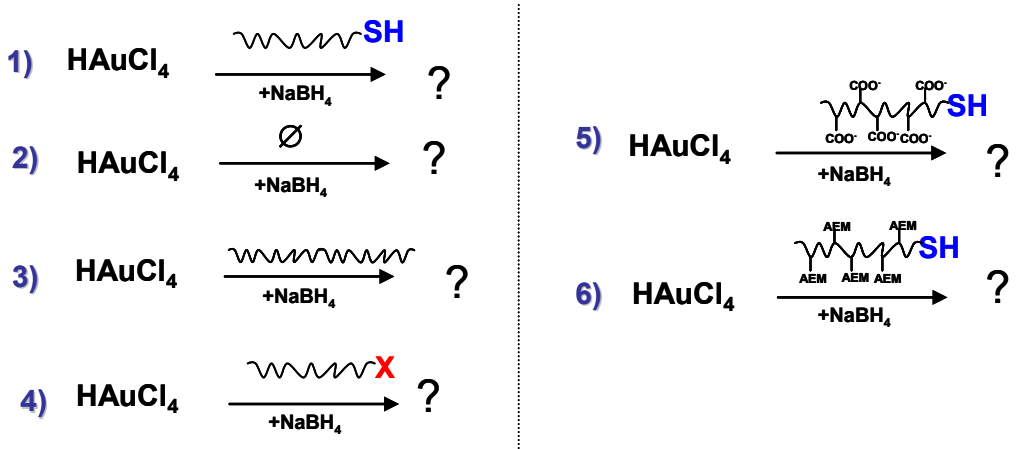

Figure III. 19: List of tests performed in the framework of *in situ* grafting onto AuNP.

Qualitative results on the immediate stability of PNAM grafted AuNP are summarized in Table III. 8. The stability of *in situ* grafted AuNP has been evaluated by observing their color, aggregation behavior and size (by TEM).

Table III. 8 : Qualitative results of AuNP grafted in situ with different PNAM based polymers

N°	Grafted polymer	M_n (g.mol^{-1})	*In situ* grafting results		
			AuNP(aq.) color	Stability [b]	Comments
1	**PNAM-SH**	14 100	Black-brown	**+**	No sedimentation
2	**No polymer**	-	Black precipitate formed after reduction of Au^{3+} with $NaBH_4$		
3	**PNAM-rad.** [a]	64 800	Red	**+**	~4 nm AuNP observed by TEM
4	**PNAM-X**	3 000	Grey	**-**	Polydisperse aggregates observed by TEM
5	**P(NAM/NAS) (AH7T7) after hydrolysis** [c]	13 800	Brown	**+**	No sedimentation
6	**P(NAM/NAS) (AH7T7) after AEM Capping** [d]	19 500	Brown	**+**	No sedimentation

[a] PNAM synthesized by free radical polymerization.

[b] No precipitation and no sedimentation after 2 weeks of storage ⇒ "+", otherwise "-".

[c] P(NAM/NAS) modified by hydrolyses into PNAM-*co*-PAA (negatively charged at pH > 5).

[d] P(NAM/NAS) modified by AEM capping into PNAM-*co*-PNAEM (poly(*N*-acryloyl morpholine-*co*-*N*- acrylamido-4-(2-aminoethyl)morpholine).

1) The observed homogenous and clear solution shows that PNAM-SH homopolymer bearing a thiol end-group leads to stable grafted AuNP.

2) After reduction with $NaBH_4$ in the absence of polymer, a black solid precipitated immediately, proving that the formation of a colloidal AuNP suspension is entirely due to the polymer present in solution.

3) When using PNAM obtained by free radical polymerization, ~4 nm AuNP were obtained (TEM). Even if PNAM-rad. does not contain sulfur atoms it may contain carbonitrile groups (from the polymerization initiator) which can stabilize AuNP *via* weak interactions.[48] Moreover steric effects, due to a higher polymer M_n, could also contribute to AuNP stabilization in this case.

4) In order to prove that stability was much stronger when using thiol-terminated polymers, we tried to modify the dithioesther (DT) group of the PNAM-DT (Appendix III.4) into PNAM-**X**. DT modification reaction was tricky: after reaction we could only note that **X** was not a DT, but still containing sulfur atoms (study under investigation). Regardless these incomplete results, PNAM-**X** showed poor stability towards AuNP *in situ* formation.

5) and 6) Stable AuNP could be obtained in experiments 5) and 6), proving that the highest stability was achieved with thiol-terminated polymers, *via* oriented thiol grafting onto AuNP.

III.3.3.1.3. Influence of experimental conditions

As mentioned before, Au/S (Au/polymer) ratio, which was supposed to influence the AuNP size, had in fact a limited impact.[59]

In this study we varied Au initial concentration ($[Au]_0$), hoping to influence the growth of AuNP and their final size. $[Au]_0$ was changed from 1.7 mM to 3.3 mM and 5.7mM (Table III. 9) by varying the total reaction volume. The PNAM used for grafting was the same (M_n = 14 100 g.mol^{-1}), and Au/S ratio – kept constant.

Table III. 9: Influence of $[Au]_0$ during *in situ* grafting on the properties of gold nanoparticles.

Studied parameter	Concentration $[Au]_0$	PNAM M_n (g.mol^{-1})	UV-Vis maximum wavelength	Average diameter (TEM) (nm)
$[Au]_0$ initial concentration	1.7	14 100	Shoulder 500-510 nm	1.9 ± 0.5
	3.3		Shoulder 500-510 nm	2.3 ± 0.5
	5.7		Shoulder 500-510 nm	2.4 ± 0.6

Figure III. 20 illustrates the UV-Vis absorption spectra and TEM images obtained for *in situ* AuNP-PNAM samples.

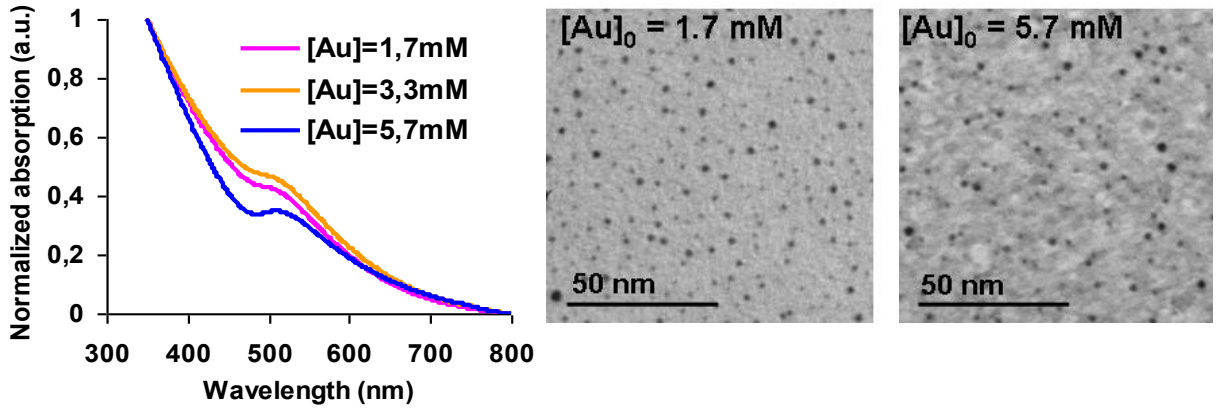

Figure III. 20: Influence of $[Au]_0$ initial concentration on the properties of grafted AuNP, $[Au]_0$=1.7 mM / 3.3 mM / 5.7 mM: (left curves) UV-Vis absorption; (right) TEM pictures black dots correspond to ~2-3 nm AuNP, (the substrate is a carbon thin film prone to damaging under the electron beam).

Results reported in Table III. 9 are similar showing 2-3nm AuNP with a relatively high polydispersity, leading to a weak SPR band (shoulder at ~500-510 nm, typical for small AuNP). Nevertheless, these results are in good agreement with previously reported *in situ* AuNP functionalized with thiol-polymer ligands.[64]

Considering the extensive studies described in literature and the tests performed here, we concluded that Au core size is only marginally sensitive to experimental conditions, resulting in small AuNP (d<5 nm).

Up to date, only one recent example exists with *in situ* grafted AuNP with diameters between 1.5 and 18 nm. In this study Oh *et al.* [65] proposed a new procedure using polymers terminated with thioctic acid functions, offering a much stronger binding and ensuring a more efficient growth of AuNP. In that case the size of AuNP was controlled *via* the amount of ligands used, while AuNP stabilization was ensured by a supplementary passivation step (supplementary addition of ligand and reducing agent).

III.3.3.1.4. Grafting density

The grafting density of *in situ* AuNP-PNAM could be calculated using TEM and TGA results (Experimental section III.6). We found a value of 0.73 chains/nm², corresponding to ~15 PNAM chains/AuNP, and 67% wt. of PNAM (Appendix III.6).
Tenhu's group obtained higher grafting densities (between 1-4 chains/nm²) for PNIPAM oligomers grafted *in situ* onto similar 2-3 nm AuNP. The lower grafting density obtained with PNAM *vs.* PNIPAM may be due to the higher molecular weight of the PNAM polymer (14 100 $g.mol^{-1}$), but also to differences in its conformation on the surface of AuNP. In the same context, a slightly higher coverage of PEG-SH onto 2.8 nm AuNP has been reported by Wuelfing *et al.* (79% organic part)[64] suggesting that PEG-SH is distorted into a cone-shaped volume when grafted onto AuNP.

In conclusion, by *in situ* approach, small 2-3 nm AuNP-PNAM could be successfully synthesized *via* oriented thiol end-group chemisorption onto AuNP surface. *In situ* AuNP-PNAM showed a weak SPR band and a relatively high grafting density. Experimental conditions influenced only marginally the final size of grafted AuNP.
In the framework of *in situ* grafting, we could have investigated more extensively the influence of various experimental parameters; however we decided to focus on the well-known ligand exchange approach allowing to produce bigger AuNP within a larger size regime.

III.3.3.2. Ligand exchange approach

Two-step ligand exchange

Ligand exchange approach is a two-step process (Figure III. 21). While the 1st step determines the size of AuNP, the 2nd step involves the grafting PNAM-SH polymers *via* a dynamic ligand exchange at the surface of AuNP.

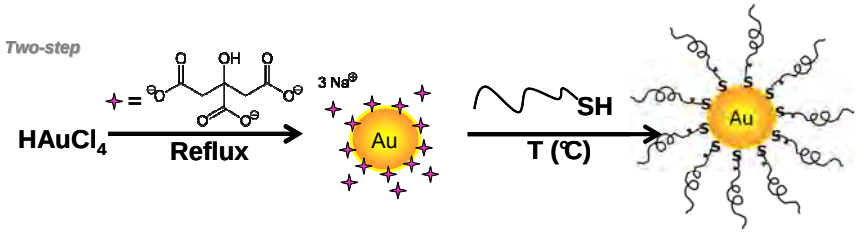

Figure III. 21: Experimental procedure for two-step ligand exchange approach: 1st step – formation of citrate-capped AuNP; 2nd step – polymer grafting via surface ligand exchange process.

1st step

In our studies we worked on 20 nm AuNP as a model for grafting. Therefore, the citrate/Au molar ratio was kept unchanged:

- Citrate/Au ratio = 4.4: giving ~20 nm AuNP.

Citrate reduction of gold undergoes a multi-step complicated mechanism[66] and is very sensitive to experimental conditions. Their variation can lead to poor size distribution control, especially during scaling-up.

In order to increase the amount of produced citrate-capped AuNP, we studied:

→ The influence of a moderate scaling-up (V_1 = 3x V_0) on AuNP size distribution, by tripling the reaction volume.

2nd step

Because the ligand exchange step is a dynamic process, its efficiency may be dependent on experimental parameters used here: *e.g.* the amount of PNAM (expressed through Au/S ratio) and its molecular weight, as well as the temperature at which the exchange occurs.

In order to find the optimal conditions we investigated:

→ The influence of Au/S ratio: allowing to minimize the amount of polymer involved in the exchange process, Au/S = 3 / 10 / 20.*

→ The influence of the temperature (T°): expected to accelerate the ligand exchange at the surface of AuNP, T° = 25 / 50 / 80°C.

Similar to *in situ* grafting, we searched to determine the impact of PNAM molecular weight on the grafting efficiency and conformation of PNAM chains at the surface of AuNP.

→ The influence of PNAM M_n: Mn = 14 100 / 26 400 / 47 300 g.mol^{-1} – discussed in a separate section (III.3.3.3).

One-step ligand exchange

Finally, by varying the experimental conditions, we tried to go from a two-step ligand exchange process to a single step process and analyze its impact on the properties of grafted AuNP (size, shape, stability).

→ One-step ligand exchange process was studied: Au^{3+}citrate reduction, under reflux, in the presence of the polymer (Figure III. 22).

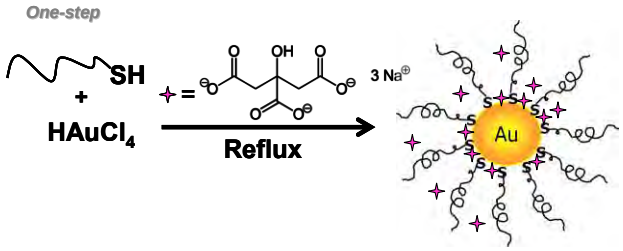

Figure III. 22: One-step ligand exchange approach to graft PNAM-SH onto AuNP formed by citrate reduction.

* Au/S ratio = Au/PNAM ratio

Each one of previously mentioned studies will be further discussed.

III.2.3.2.1. Influence of scaling-up

The goal of this experiment was to increase the amount of synthesized citrate-capped AuNP by scaling-up the reaction, still following the Turkevitch method (Figure III. 23).

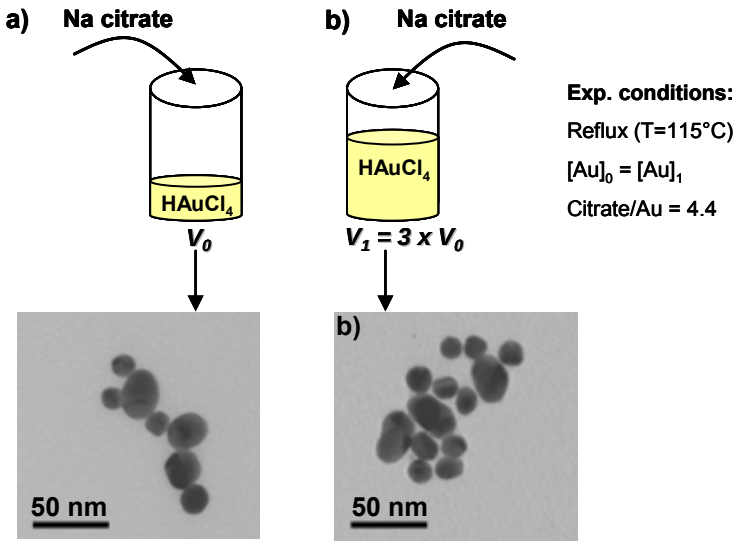

Figure III. 23: Moderate scaling-up of $HAuCl_4$ citrate reduction: a) V_0=37.5mL; b) V_1 = 3 x V_0 = 112.5 mL (same Au III concentration in both batches).

TEM pictures illustrate that the scaling-up (x 3) did not change the mean size of citrate-capped AuNP (Figure III. 23). Quantitative analyses showed however ~+10 % increase in size polydispersity when tripling the reaction volume.

Reducing the AuNP polydispersity was not a first priority in these studies, nonetheless it could be improved by modifying the sequence of reagent addition as reported recently.[67]

III.3.3.2.2. Influence of temperature during ligand exchange

Ligand exchange is always performed at room temperature, during at least 24 hours, due to relatively slow exchange rate between citrate molecules and PNAM-SH.

The goal of this study was to increase the reaction rate, working at higher temperature, the main idea being to reach a rapid exchange and a maximum grafting density of the polymer on AuNP. Three different temperature values have been tested: 25°C, 50°C, 80°C, while keeping all other experimental parameters fixed (M_n(PNAM)=14 100 g.mol^{-1}; Au/S=3) and a reaction time of 3 hours.

First, we have proven that the exchange rate between citrate and PNAM increased with the increasing temperature. It was evidenced by qualitative DLS measurement, monitoring the increase of AuNP hydrodynamic radius with time (Appendix III.5). TGA analysis allowed further quantifying the impact of the temperature on the grafting density (Figure III. 24, Appendix III.6). TEM imaging allowed

measuring the mean polymer corona thickness surrounding the gold core (Figure III. 24, Figure III. 25).

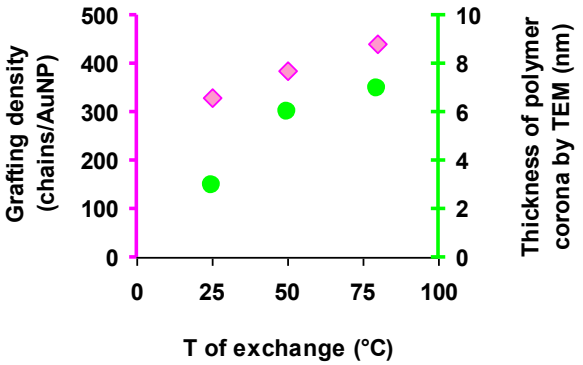

Figure III. 24 : Effect of temperature during grafting by ligand exchange on the grafting density (pink squares), and the thickness of polymer corona measured from TEM images (green circles).

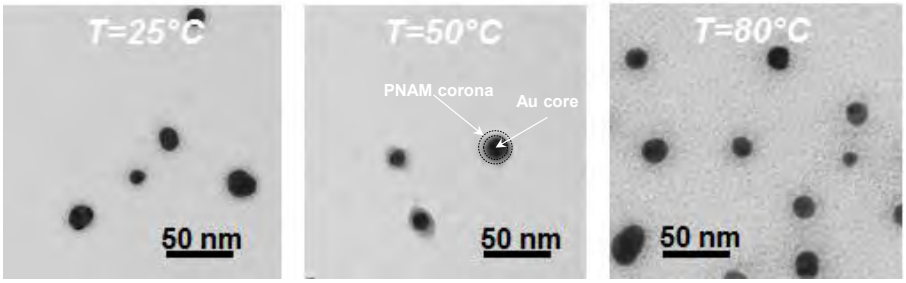

Figure III. 25 : TEM images correspond to PNAM (Mn=14 000 g/mol) grafted AuNP by ligand exchange, at T=25°C / 50°C / and 80°C (staining with RuO_4).

According to these results, TEM and TGA measurements show that whatever the temperature, efficient grafting of the polymer on the AuNP occurs. Even if previous studies mention that Au-S bond can be cleaved at T=80°C,[49] TEM images of experiments performed at 80°C show a homogenous corona around the AuNP. It can also be noted in Figure III. 24 that the highest grafting density is achieved at T=80°C (440 chains/AuNP). Based on this optimization, all ligand exchange experiments were performed at 80°C ensuring a rapid and a high coverage of PNAM-SH onto AuNP.

III.3.3.2.3. Influence of Au/S ratio

In order to favor the ligand exchange process, a large excess of polymer is used (when Au/S ratio = 3, more than 90% free PNAM is recovered after AuNP-PNAM purification). The goal of this study was to decrease the amount of polymer used during ligand exchange, while keeping a high grafting density.
In literature, different Au/S ratios have been used (Au/S=1/15[13], or Au/S=100[41]), but no systematic study on the influence of this parameter was completed so far.
For this purpose, we tested the following Au/S ratios: 3, 10 and 20 (Figure III. 26, Figure III. 27), while keeping all other parameters unchanged (M_n(PNAM)=14 100 g.mol^{-1}; $T_{exchange}$=80°C, time=3h).

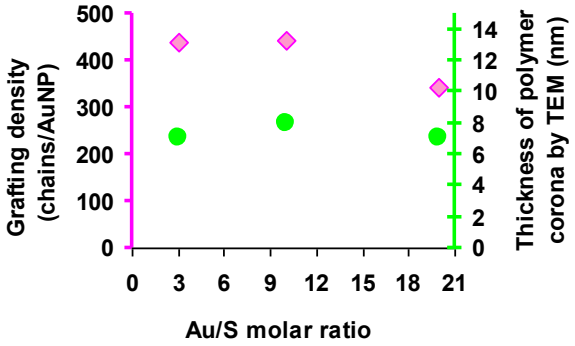

Figure III. 26 : Influence of increasing initial Au/polymer (Au/S) molar ratio during grafting by ligand exchange on the grafting density (with a thiol terminated PNAM).

Grafting density remained almost unchanged when Au/S ratio increase from 3 to 10 (Figure III. 26), meaning that a decrease (by 2/3) of PNAM amount does not significantly impact the grafting density.

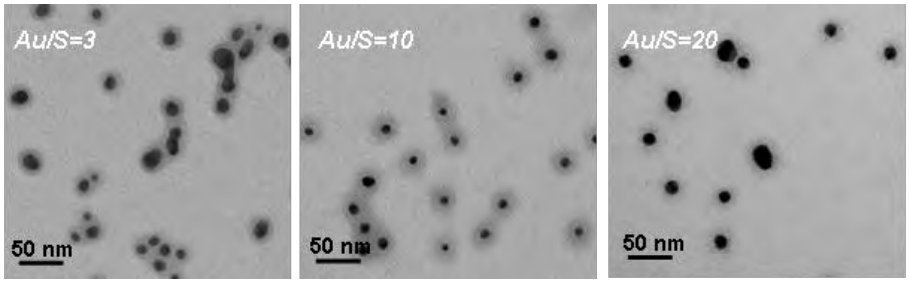

Figure III. 27 : TEM images of PNAM (Mn=14 000 g/mol) grafted by ligand exchange onto AuNP using Au/S ratio = 3, 10, or 20 respectively (staining with RuO_4).

On the other hand, TEM images showed no significant impact on polymer corona thickness (7-8 nm mean thickness), Figure III. 27.

Nonetheless, under the same staining conditions, the polymer corona with Au/S=20 is less contrasted and less visible on TEM images, in agreement with the lowest grafting density found in this case. This study demonstrates that by increasing Au/S ratio from 3 to 10 we could spare two-thirds of the polymer used for grafting without significantly affecting the grafting density. This optimization will be even more valuable when saving important amounts of high added-value chromophore-polymer conjugates (Section III.4).

III.3.3.2.4. One step ligand exchange

Another short study consisted in performing the two-step ligand exchange process in a one single step, by reducing the Au^{3+}(aq.) salt in the presence of PNAM-SH polymer with sodium citrate under reflux (Figure III. 22).

The one-step process (AuNP formation and polymer grafting) resulted in stable 15 nm AuNP-PANM (Table III. 10).The smaller AuNP diameter (15 nm) compared to the two-step process (17 nm) can suggest a quicker stabilization of AuNP in the two step process.

Table III. 10 : TEM results after ligand exchange one-step process compared to the two-step process.

AuNP-PNAM properties	Two-steps process *1) Au^{3+} reduction* *2) Ligand exchange*	One-step process **"Reduction + ligand exchange"**
TEM diameter AuNP core (nm)	18 ± 5	15 ± 3
TEM PNAM corona thickness	7 ± 1	3 ± 1
SPR maximum (nm) (UV-Vis spectroscopy)	528*	524*

***** No difference was recorded in the width UV-Vis spectra (Appendix III.7).

TEM results showed however a thinner (3-4 nm) and a less dense polymer corona after one-step grafting compared to 7 nm found after the two-step process. The UV-Vis spectrum of AuNP-PNAM after one-step process is slightly blue shifted, corroborating with smaller diameter recorded by TEM (Appendix III.6).

Even if complementary testing and analyses would be needed to conclude on the influence of one-step process (*e.g.* TGA), this preliminary experiment proved that AuNP formation and stabilization by PNAM-SH can occur during citrate-reduction.

III.3.3.2.5. Grafting density

AuNP-PNAM obtained by ligand exchange under optimized conditions are characterized by grafting densities varying between 0.3 and 0.5 chains/nm² (300 – 400 chains/AuNP), almost twice lower than for *in situ* AuNP-PNAM (Appendix III.6). These results are in good agreement (similar order of magnitude) with previously reported values for ~20 nm citrate-capped AuNP coated with RAFT polymer. [38 49 52 53]

To conclude, ligand exchange approach allowed producing well-defined 20 nm AuNP-PNAM. The most important difference and advantage characterizing AuNP-PNAM formed by ligand exchange (vs. *in situ*) is that the size of AuNP core and the grafting of polymer shell can be separately tuned. By varying experimental parameters during ligand exchange (temperature, Au/S ratio), in was possible to optimize the grafting conditions leading to high grafting densities while using a minimum amount of PNAM.

III.3.3.3. Influence of PNAM molecular weight (M_n)

The length of the PNAM polymer used for grafting is the last studied parameter. It is expressed through the molecular weight (M_n) of linear polymers.

It was shown that the polymer chemical nature[56] and molecular weight[68] can have a significant impact on the grafting density of AuNP.

Our goal was to find how the molecular weight of hydrophilic PNAM polymer could affect the grafting density and the thickness of polymer corona (TEM) using the previously described experimental conditions.

III.3.3.3.1. In situ

In the framework of *in situ* approach, two different PNAM have been considered, with M_n = 3 300 g.mol^{-1} and 14 100 g.mol^{-1}. UV-Vis spectroscopy and TEM imaging results obtained for functionalized AuNP are illustrated in Figure III. 28.

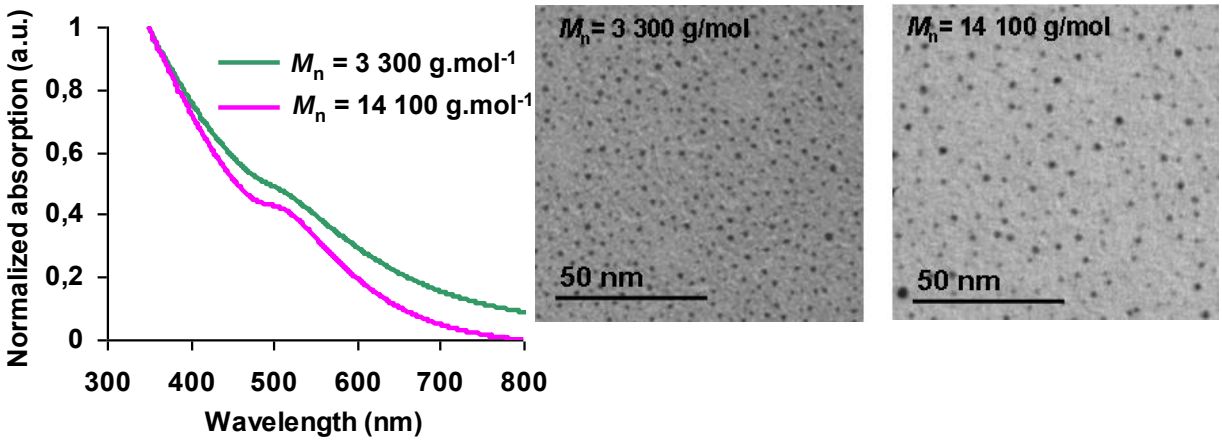

Figure III. 28 : Influence of polymer M_n on the properties of grafted AuNP, using PNAM Mn=3 300 g.mol^{-1} or Mn=14 100 g.mol^{-1}.: (left graphic) UV-Vis absorption; (right) TEM imaging – black dots correspond to ~2 nm AuNP, the substrate is a carbon thin film.

In situ 2-3 nm AuNP-PNAM are characterized by a typical weak SPR band (shoulder at ~510 nm), Figure III. 28. These results show that PNAM M_n had little impact on the size of *in situ* AuNP-PNAM. Presuming that, thanks to the oriented end-group grafting, PNAM chains form uniform brushed around AuNP, the thickness of polymer corona should then be influenced by the polymer length although the latter statement could not be proven by TEM (impossible to see the polymer corona).

III.3.3.3.2. Ligand exchange

The influence of PNAM molecular weight was easier to study on 20 nm AuNP-PNAM obtained by ligand exchange, as both the Au core and the polymer corona could be seen and measured by TEM.

In this context, different PNAM polymers have been grafted by ligand exchange on ~20 nm citrate-capped AuNP: M_n(PNAM)=14 100 g.mol^{-1}, M_n(PNAM)=26 400 g.mol^{-1}, M_n(PNAM)=47 300 g.mol^{-1}, Figure III. 29 illustrates the changes in grafting density and polymer corona thickness (TEM – Figure III. 30) as a function of PNAM M_n.

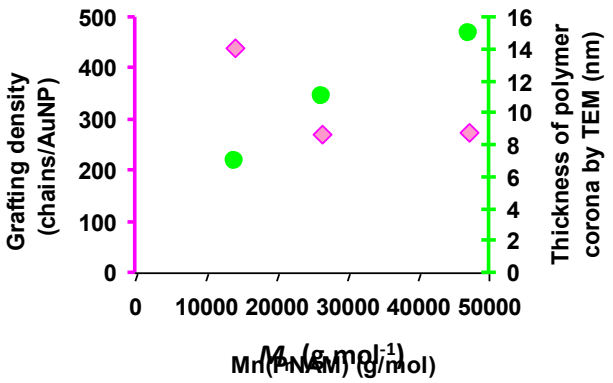

Figure III. 29 : Effect of PNAM M_n on grafting density (pink squares), and thickness of polymer corona measured (TEM) (green circles).

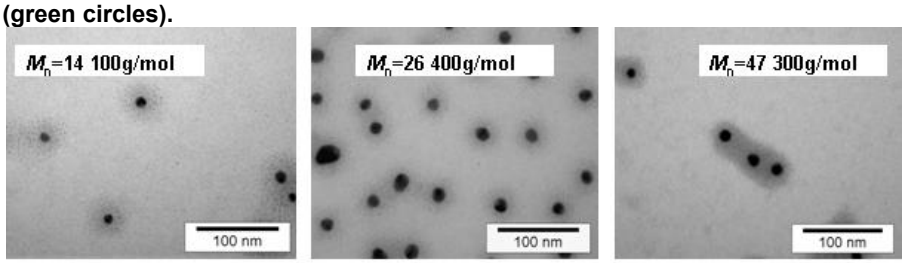

Figure III. 30 : TEM images of AuNP-PNAM obtained by ligand exchange respectively with M_n = 14 100 / 26 400 / 47 300 g.mol^{-1} (staining with RuO_4).

According to TEM pictures, the polymer corona thickness increases with increasing length (M_n) of the polymer, while the grafting density decreases. This is consistent with previous studies by Kang and Taton who reported a similar behavior using PS-*b*-PAA block copolymers grafted onto 12 nm AuNP.[17] These findings are of great importance for the rest of this project, justifying the role of polymers for tuning and controlling the distance between the coupled chromophores on the polymer chain and AuNP surface (Section III.4.).

In this section the grafting of PNAM-SH polymers onto AuNP has been presented using two different approaches in aqueous medium: *in situ* (one step process) and ligand exchange (two-step-process). The most important results for each one of these approaches are summarized in Table III. 11.

In situ approach gave generally small 2-3 nm stable AuNP-PNAM with high polydispersity and high grafting density. These hybrid nano-objects were difficult to analyze by TEM (due to their small size) and presented a weak SPR band. Despite the limitations of *in situ* grafting approach, which made it inadequate for the next step of the project, this easy one-step process allowed to quickly and efficiently evidence the thiol end-group oriented grafting of PNAM-SH polymers onto AuNP.

In parallel, larger 20 nm AuNP-PNAM were synthesized using the two-step ligand exchange approach. They could be easily visualized and characterized by TEM (Au core diameter and thickness of PNAM corona). In this way the ligand exchange experimental conditions could be optimized to achieve high PNAM grafting densities, while using low quantity of PNAM.

Ligand exchange process allowed to separately tune the AuNP size and shape in a 1st step and then control the polymer grafting by ligand exchange on preformed AuNP in a 2nd step. Thanks to its versatility, ligand exchange approach appears more adequate for SPR driven applications.

Table III. 11 : Comparison between *in situ* and ligand exchange approaches with PNAM M_n=14 100 g.mol^{-1}.

Grafting approach	UV-Vis maximum (nm)	TEM imaging		Grafting density			Advantages	Limitations
		Diameter (nm)	Polymer corona (nm)	Chains/ AuNP	Surface density (chains/nm²)	Au/polymer weight ratio		
In situ	Shoulder 500-510 nm	**2-3 ±1**	Invisible	**15**	**0.73**	**0.5**	- Easy, quick one-step process - High grafting densities	- Limited size (d<10 nm) - Weak SPR band ⇒ no potential in fluorescence enhancement
Ligand exchange	525	**18±5**	~5-7	**440**	**0.49**	**4.8**	- Good control over structure - Visible polymer corona by TEM - Size can be easily tuned in the 1st step	- Two-step process - Lower grafting density

The differences between these two approaches can be observed on UV-Vis spectra and TEM imaging as illustrated in Figure III. 31

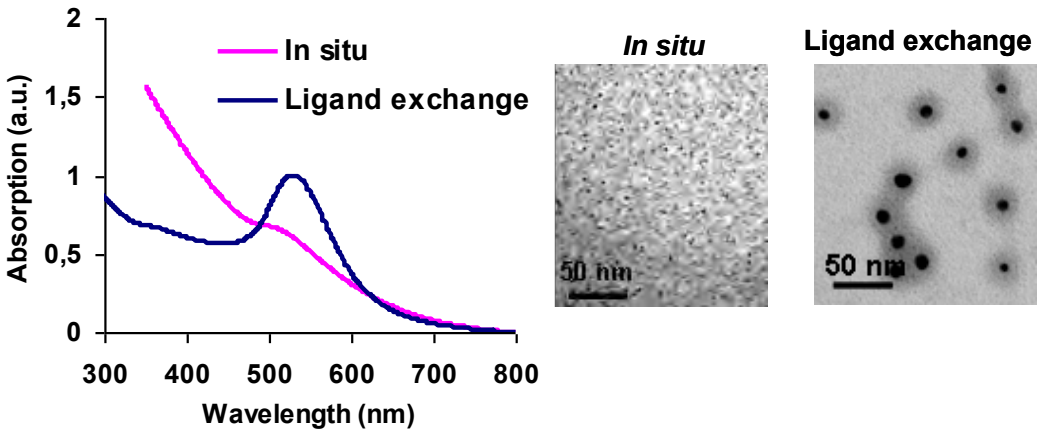

Figure III. 31 : (left) Comparative UV-Vis spectra of 2 nm AuNP-PNAM by *in situ* approach *vs.* ~20 nm AuNP-PNAM grafted by ligand exchange. (right) TEM images corresponding to *in situ vs.* ligand exchange grafted AuNP (black dots or spheres are AuNP cores).

The final goal in this project is to increase the optical response of chromophores *via* SPR enhancement. It is known that bigger AuNP with anisotropic shapes exhibit a stronger SPR field. This would bring us to further study the grafting capacity of PNAM polymer onto AuNP with various sizes and shapes (work in progress in collaboration with J. Navarro, ENS Lyon).[69]

This is the main reason why ligand exchange approach has been chosen for grafting chromophore-polymer conjugates onto AuNP in the last section of this chapter. In this context, 20 nm citrate-capped AuNP will be used as a reference model.

III.4. Grafting chromophore-polymer conjugates onto AuNP

After proving the efficient grafting of PNAM polymers onto AuNP, the last part of this chapter will focus on grafting various chromophore-polymer conjugates, derived from P(NAM-*co*-NAS) copolymers obtained by RAFT (Chapter II), onto the surface of ~20 nm citrate-capped AuNP. The preparation of these nano-objects will be based on previously optimized conditions for ligand exchange two-step process.

Chromophore-polymer conjugates used for grafting were water-soluble and functionalized with Lucifer Yellow Cadaverine (LY), Anthracene (Ant), or Dibromobenzene (DBB) chromophores (Figure III. 32) coupled along the copolymer chain. These conjugates exhibited different backbone structures, as they were post-treated by AEM capping or hydrolysis (Chapter II), different chain lengths and architectures (random or block) (Figure III. 33).

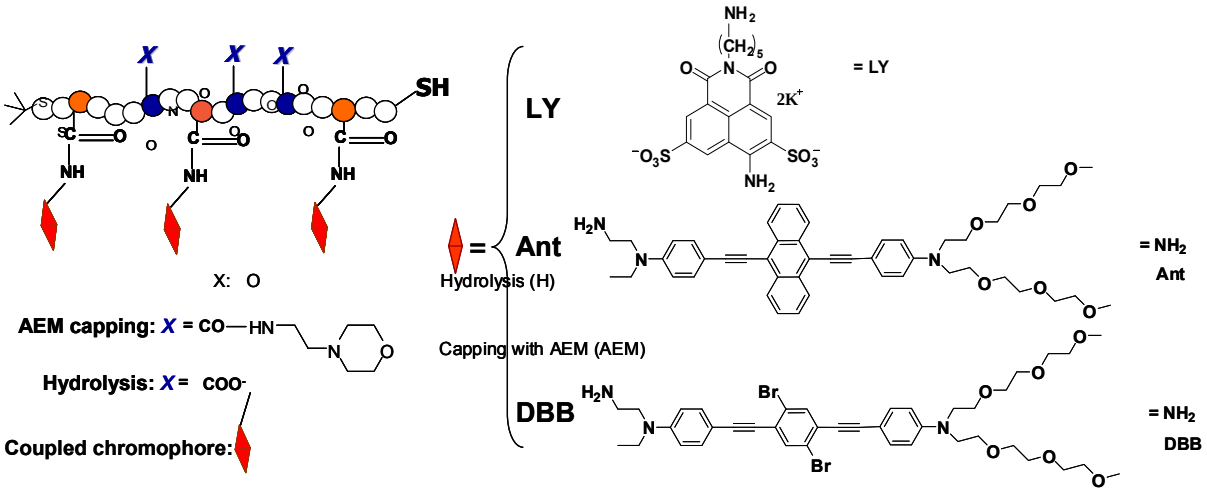

Figure III. 32: Schematic structure of chromophore-polymer conjugates with LY, Ant, or DBB conjugates.

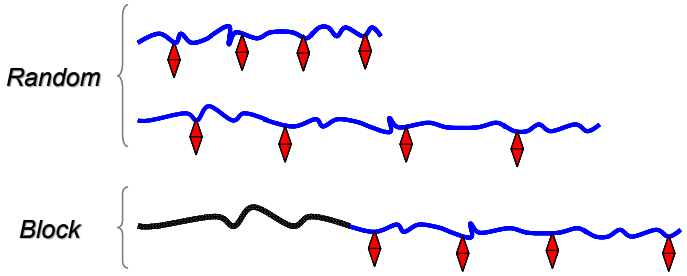

Figure III. 33: Schematic representation of conjugates with random or block architectures, bearing different numbers of chromophores *per* chain.

- LY-conjugates (bright yellow color) were used as a model systems, to study the properties of grafted AuNP. All LY-conjugates are capped with AEM and are negatively charged due to two sulfonate groups on the LY chromophore molecule.

Ant and DBB conjugates were designed for two-photon applications (Imaging and PDT).

- Water-soluble Ant-conjugates (red-orange color) are neutral if capped with AEM, or negatively charged if hydrolyzed and exhibit a random architecture.

- Water-soluble DBB-conjugates (drab yellow color) are negatively charged because all of them were hydrolyzed (H), with either random or block architectures (Figure III. 33).

Grafting procedure, characterization and properties of AuNP coated with conjugates will be further discussed.

III.4.1. Grafting and purification

Grafting conditions

As mentioned earlier, the optimized two-step ligand exchange approach in water was applied to graft conjugates onto ~20 nm citrate-capped AuNP: Au/S molar ratio = 10; $T_{exchange}$=80°C; reaction time = 3h.

Purification

Prior to any analyses, AuNP grafted with conjugate have been purified from free conjugates in solution by centrifugal ultrafiltration or size exclusion chromatography (SEC).[70]

- AuNP-LY conjugates

Centrifugal ultrafiltration was very efficient for hydrophilic LY conjugates (see results in Appendix III.8), but failed to purify two-photon Ant or DBB conjugates, because of their strong, irreversible absorption on the membrane of the centrifugal filter device.

- AuNP-Ant conjugates and AuNP-DBB conjugates

An alternative method of purification was to use size exclusion chromatography (SEC) in order to separate grafted AuNP from free Ant- or DBB-polymer conjugates in solution. In this context a thorough and time-consuming optimization procedure has been carried out before reaching efficient purification conditions (Appendix III.8).

III.4.2. Characterization of grafted AuNP

Two analytical techniques, UV-Vis spectroscopy and TEM, were used to first prove the grafting efficiency and, more importantly, study the properties of AuNP functionalized with polymer conjugates. TEM and UV-Vis results are all summarized in Table III. 12. TGA analyses were not possible in this case, due to the limited disposable amount of grafted AuNP.

The length of conjugates (expressed through the M_n of P(NAM-*co*-NAS) copolymer before chromophore coupling), the number of chromophores *per* chain (Nc), and the post treatment technique (AEM capping (AEM), or hydrolyses (H)) are reported for each grafted AuNP sample.

Grafting densities could be estimated from UV-Vis spectra (for DBB grafted conjugates), or fluorescence spectroscopy using the Au core dissolution with cyanide (for LY conjugates) (Appendix III.9, Chapter IV).

Table III. 12 : List of ~20 nm AuNP grafted with chromophore-polymer conjugates. TEM results of Au core diameter and conjugates corona thickness; maximum wavelength of SPR band after grafting.

Chromophore	Conjugate grafted-AuNP	Copolymer M_n (before coupling) (g/mol)	Conjugate M_n (g/mol)	Nc	TEM results		UV-Vis maximum (nm)	Grafting density (chains/AuNP // chains/nm²)
					Core (nm)	Corona (nm)		
LY	AuNP-LY2KDa	2 200	2 700	1.1	16 ± 5	1 ± 1	525	419 // 0.52 [b]
	AuNP-LY9KDa	7 900	9 500	4.2	17 ± 5	4 ± 1	531	395 //0.43 [b]
	AuNP-LY15KDa	12 900	15 000	4.6	17 ± 5	12 ± 2	527	313 // 0.34 [b]
	AuNP-LY37KDa	34 600	37 700	4.4	18 ± 5	20 ± 5	528	463 // 0.39 [b]
	AuNP-LY32KDa(B)*	29 400	32 400	5.2	16 ± 5	18 ± 3	528	320 // 0.45 [b]
Ant	AuNP-6Ant-H	12 900	14 800	6.1	17 ± 5	6 ± 1	531	-
	AuNP-6Ant-AEM	12 900	17 300	6.1	17 ± 5	4 ± 1	533	-
	AuNP-10Ant-AEM	12 900	20 000	10.3	17 ± 5	Aggregated AuNP in water		-
DBB	AuNP-DBB13KDa	12 900	13 800	4.4	17 ± 5	4 ± 1	542	913 // 1.01 [c]
	AuNP-DBB28KDa(B)[a]	29 400	28 800	4.6	17 ± 5	8 ± 1	536	750 // 0.82 [c]
	AuNP-DBB33KDa(B) [a]	35 000	33 300	4.0	16 ± 5	13 ± 3	534	740 // 0.92 [c]

[a] B stands for block copolymer (see chapter II).

[b] Calculated by fluorescence spectroscopy after Au core dissolution with cyanide (detailed in Chapter IV).

[c] Calculated from UV-Vis spectroscopy (Appendix III.9).*

Variation in AuNP size and shape will not be taken into account in the following discussion, as all citrate capped AuNP used for grafting are obtained following the same protocol.

III.4.2.1. Absorption properties

UV-Vis spectroscopy

UV-Vis spectra of grafted AuNP show a red-shift of the SPR maximum absorption band (Table III. 12, Figure III. 34), indicating the efficient grafting of conjugates.[71] The red-shift increased with decreasing M_n of grafted conjugates. This phenomenon, dependent on the hydrophilic/hydrophobic balance of the system, seems favored with amphiphilic And and DBB conjugates (red-shift: $\Delta\lambda$ = 7-9 nm) compared to hydrophilic LY grafted conjugates (red-shift: $\Delta\lambda$ = 3-4 nm).

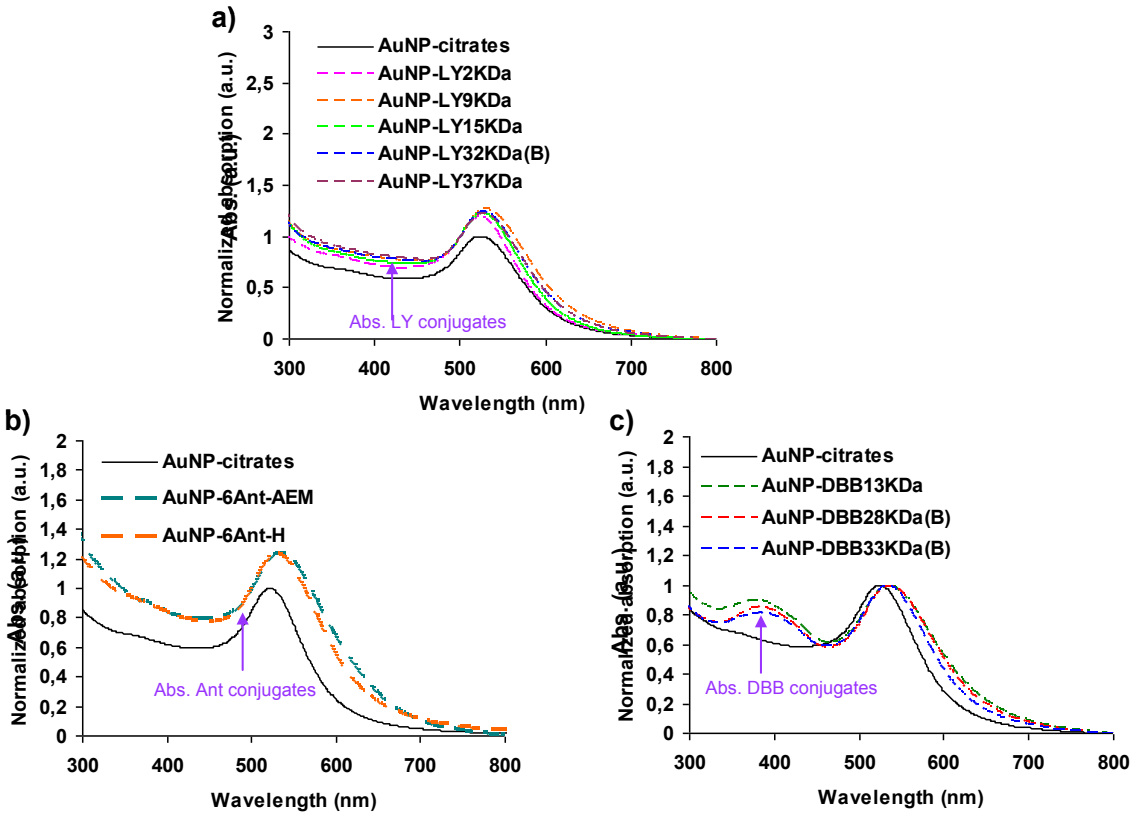

Figure III. 34 : UV-Vis absorptions in water of grafted AuNP with: a) LY-conjugates; b) Ant-conjugate; c) DBB-conjugates, compared to the absorption of citrate-capped AuNP before grafting. Purple flashes point to the maximum absorption of LY, Ant and DBB free conjugates.

UV-Vis spectroscopy could be used to determine the amount of grafted conjugates onto AuNP, if the absorption (*i.e.* the concentration) of these conjugates was possible to substract from the UV-Vis spectra of grafted AuNP. Nevertheless, the difference between the extinction coefficient of ~20 nm AuNP (ε_{AuNP}~10^{+9} $cm^{-1}.M^{-1}$), and the one of polymer conjugates ($\varepsilon_{conjugate}$~10^{+3}–10^{+4} $cm^{-1}.M^{-1}$, Chapter IV), makes the contribution of conjugates difficult to detect. Indeed, on UV-Vis spectra of grafted LY and Ant conjugates (Figure III. 34 a) b)), no absorption band is observed at the maximum absorption wavelengths of LY or Ant chromophores (430 nm and 490 nm respectively). In the case of DBB conjugates, a shoulder at ~400 nm was observed, wich would correspond to grafted conjugates, although the latter observation seems unexpected, giving the previous argument. In order to confirm the last result, a quantification of AuNP degree of purity would serve as a reliable confirmation.

III.4.2.2. Structural characterization

TEM imaging

TEM analyses confirmed the grafting by visualizing the organic part (polymer conjugates) surrounding AuNP metallic core (revealed with RuO_4).

TEM quantitative results are listed in Table III. 12. TEM images corresponding to LY, Ant and DBB conjugates are illustrated in Figure III. 35, Figure III. 36, Figure III. 37, respectively, where the AuNP core and the grafted polymer coronae can be distinguished.

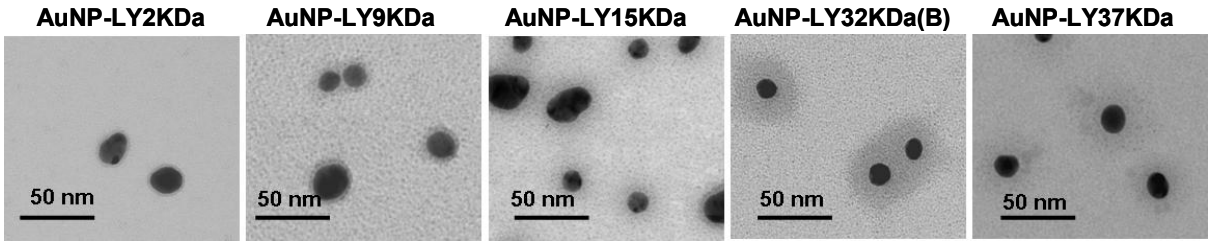

Figure III. 35 : TEM images of ~20 nm AuNP grafted with LY-conjugates having different lengths (staining with RuO_4).

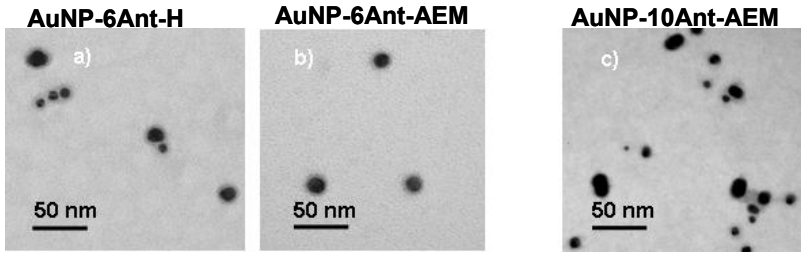

Figure III. 36 : TEM images of ~20 nm AuNP grafted with Ant-conjugates: a) 6Ant-H; b) 6Ant-AEM; c) 10Ant-AEM casted from $CHCl_3$ solution (staining with RuO_4).

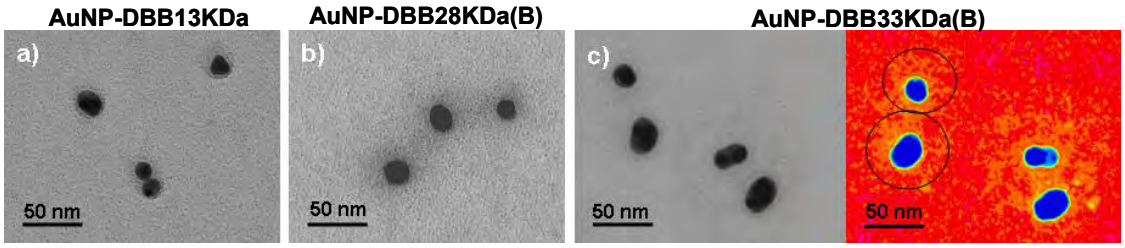

Figure III. 37 : TEM images of ~20 nm AuNP grafted with hydrolyzed DBB-conjugates: a) DBB13KDa; b) DBB28KDa(B); c) DBB33KDa(B) – the red image corresponds to a multicolor scale used to visualize and properly measure the DBB33KDa corona thickness (staining with RuO_4).

We can notice that generally all AuNP seem stable towards aggregation and appear well-dispersed on TEM grids, except AuNP-10Ant-AEM sample in $CHCl_3$ (Figure III. 36).

Cryo-TEM imaging

Although TEM gives a good idea about the organic corona homogeneity around the particles, it characterizes only the dry samples. The way the polymers chains spread in solution is expected to be different than in the dried state, impacting the corona thickness. In order to find a better agreement with the real thickness in aqueous medium, cryo-TEM imaging has been performed (P. Alcouffe).

Cryo-TEM imaging was tested on a thin film of frozen AuNP-LY32kDa(B) sample in solution. No staining agents were used in this case and the polymer corona was only revealed by differences in contrast between metallic and organic materials (Figure III. 38).

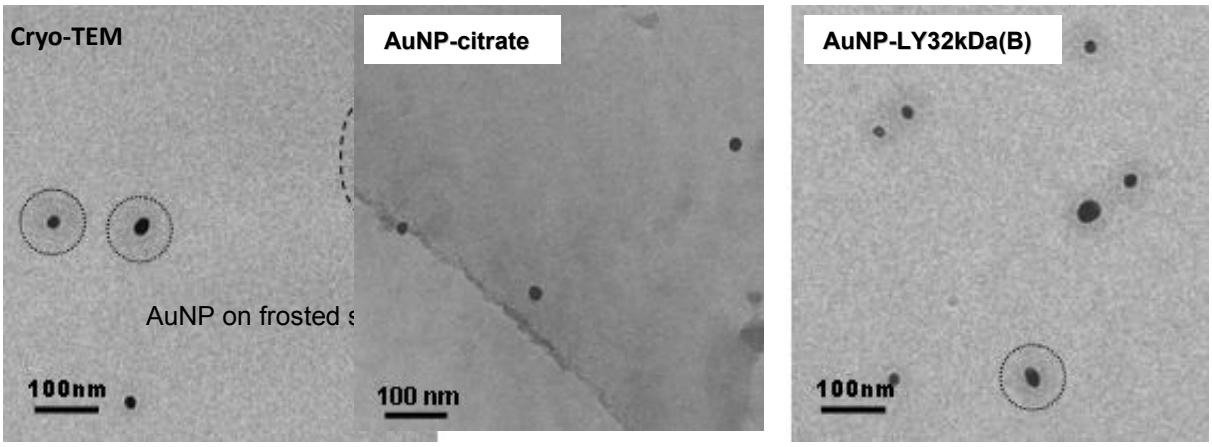

Figure III. 38 : Cryo-TEM images of AuNP-citrate before grafting (left), and AuNP-LY32KDa(B) after grafting (right).

The hydrated polymer corona of LY32KDa(B) conjugates grafted onto 20 nm AuNP could be measured from cryo-TEM analyses (Figure III. 38) and compared to the results found by classical TEM (Table III. 13).

Table III. 13 : : Comparison between classical TEM and cryo-TEM results of AuNP-LY32KDa(B).

AuNP-LY32KDa(B) analyzed by:	Au core diameter (nm)	Conjugate corona thickness (nm)
Classical TEM (dried sample)	17 ± 5	**18 ± 3**
Cryo-TEM (frozen hydrated sample)	17 ± 5	**30 ± 4**

While no visible corona is observed for citrate-capped AuNP, a slightly contrasted grayish corona could be distinguished in the case of grafted AuNP with LY32kDa(B) conjugate. Interestingly, the same sample exhibits a 18 nm corona thickness in classical TEM, which is 12 nm larger in the case of cryo-TEM (Figure III. 38, Figure III. 39). This result clearly points out the presence of a hydrated state of the grafted polymer in solution.

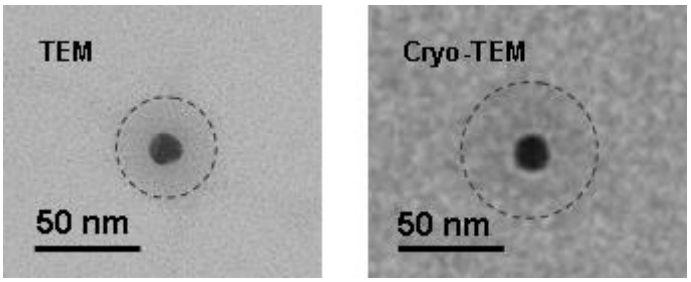

Figure III. 39 : Comparison between (left) classical TEM with RuO_4 staining; (right) cryo-TEM (no staining) on one grafted nanoparticles of AuNP-LY32KDa(B) sample.

III.4.2.2. Grafting density

As mentioned above, grafting density of high-added value conjugates onto 20 nm AuNP could not be carried out using TGA analyses. TGA is a destructive technique requiring at least several milligrams of product to obtain accurate results.

Two alternative methods, fluorescence spectroscopy and UV-Visible spectroscopy, could be however applied to estimate the grafting density of LY and DBB conjugates. They are based on determining the ratio between the concentration of grafted conjugates and that of AuNP in the sample. The grafting density can be expressed as:

$$Grafting\_density = \frac{c_{conjugates}}{c_{AuNP}}$$

While the concentration of AuNP (c_{AuNP}) was easily determined from their UV-Vis spectra, the concentration of grafted conjugates ($c_{conjugates}$) was deduced either by fluorescence (LY grafted conjugates) or by UV-Vis spectroscopy (DBB grafted conjugates).

- AuNP-LY conjugates

The grafting density with LY conjugates was calculated by fluorescence spectroscopy, after recovering the grafted conjugates, by dissolution of Au cores with cyanide.[72] The principle of this method is discussed in Chapter IV and calculations detailed in Appendix III.9. Briefly, the dissolution of Au core leads to a solution of free conjugates. The fluorescence emission of recovered conjugates allowed to deduce their concentration, using a reference solution of the same conjugate.

- AuNP-DBB conjugates

UV-Vis absorption of grafted DBB conjugates (visible in Figure III. 34 c) ~400 nm) was determined from UV-Vis absorption of grafted AuNP-DBB conjugates, by subtracting the absorption corresponding to citrate-capped AuNP before grafting (Appendix III.9).

Results obtained by each one of these methods are reported in Table III. 12.
- Grafting density of water-soluble LY-conjugates onto 20 nm AuNP is similar to previously studied AuNP-PNAM systems (~400 chains/AuNP). Nonetheless, the effect of the molecular weight seems less obvious in the case of grafted LY-conjugates.
- The density of grafted DBB-conjugates is twice higher (~800 chains/AuNP) compared to LY conjugates.

We have to keep in mind that both AuNP-conjugate systems, LY and DBB, give negatively charged AuNP. It has been previously reported that grafting density depends of the charges along the grafted polymers.[34] [38] Boyer *et al.*[38] found a decrease in packing density, caused by electronic repulsion between grafted polymer chains, for ~18 nm AuNP functionalized with negatively charged polymers (PAA). On the other hand, the opposite trend was observed for negatively charged ~18 nm AuNP-PAA studied by Liang *et al.*.[53] The differences between these contradictory examples may come from not taking into account the molecular weights of studied polymers involved in grafting.

It is not difficult to imagine that negatively charged polymers may have a different packing when compared to neutral polymers. The question, however, would be how negative charges should influence the grafting density: i) on one hand, packing density may decrease because of repulsive

interchain forces, limiting the grafting; ii) on the other hand, the interchain repulsive forces contributing to a more stretched polymer chain conformation would probably decrease the steric hindrance between two neighboring grafted chains, thus increasing the grafting density. In reality, both phenomena probably occur, leading to an optimum grafting density.

When calculating the grafting densities we suppose that all samples are 100% pure. Moreover, UV-Vis spectroscopy and especially fluorescence spectroscopy technique used there are sensitive to any traces of ungrafted conjugates (especially fluorescence) affecting the results of calculated grafting densities. In order to confirm the purity of grafted AuNP, ^{1}H-DOSY NMR would serve as a reliable proof. Subsequently a double check using two different methods would be required here should give more insights on the precision of calculated grafting densities.

III.4.3. Influence of conjugate structure on the properties of grafted AuNP

According to the results from Table III. 12, most of the well-defined AuNP grafted with conjugates are stable in aqueous medium, which is not the case for the AuNP-10Ant-AEM.
10Ant-AEM conjugate (AEM-capped neutral conjugate, bearing 10 Ant chromophores/chain) triggered a partial precipitation of AuNP during grafting in water. We know that the aggregation behavior of grafted AuNP depends on the hydrophilic/hydrophobic balance of the system, the strength of interactions being related to the chromophore nature (hydrophilic or hydrophobic), the post treatment technique (AEM or H), and also the grafting density (number of chromophores *per* chain).
In the case of 10Ant-AEM conjugates, aggregation occurs due to an important local concentration of amphiphilic conjugates onto AuNP, limiting their solubility in water. AuNP-10Ant-AEM recovered precipitate could be redissolved in organic solvents ($CHCl_3$), and then analyzed by TEM illustrating the aggregation tendency of these nanoparticles (Figure III. 36 c)).
On the contrary, all hydrolyzed conjugates (6Ant-H and DBB conjugates) and hydrophilic LY conjugates remained water-soluble after grafting on AuNP.
Moreover, we note in Table III. 12 that the thickness of grafted corona is also dependent on the chromophore type. Using the same copolymer backbone (the same length), the thickness of polymer corona obtained with LY-conjugates is approximately twice larger than the thickness of DBB or Ant grafted conjugates (Figure III. 40).
Figure III. 40 illustrates the dependency between the M_n (length) of the copolymer backbone used to synthesize the conjugate synthesis and the thickness of polymer corona (TEM). As earlier shown for AuNP-PNAM systems, polymer corona thickness increases with the increasing polymer length.

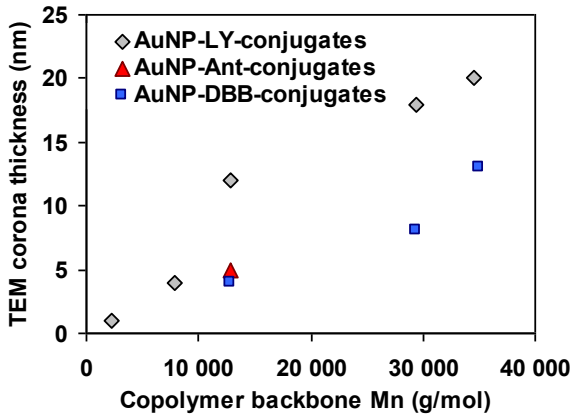

Figure III. 40 : The influence of the length of the conjugate on the thickness of polymer corona measures by TEM: grey diamonds – AuNP-LY-conjugates; red triangles – AuNP-Ant conjugates; blue squares – AuNP-DBB-conjugates.

We conclude that the chromophore chemical nature controls the conformation of grafted conjugates. Unlike hydrophilic LY conjugates, Ant and DBB conjugates carrying hydrophobic chromophores are probably characterized by stronger chromophore-chromophore interactions leading to the shrinking of the grafted polymer chain (Figure III. 41), thus to a thinner polymer corona measured by TEM.

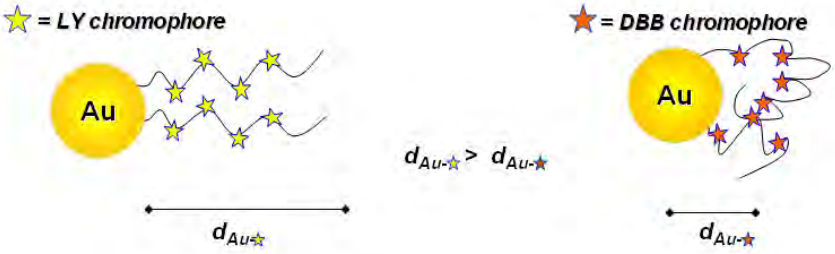

Figure III. 41: Possible conformations of grafted TP conjugates *vs.* LY conjugate onto AuNP.

We should however remind here that the corona thickness calculated by classical TEM characterizes dried grafted AuNP samples and is probably less extended than in solution, as suggested by the results obtained using cryo-TEM analysis (Section III.4.2.2.).

Chromophore-polymer conjugates have been successfully grafted onto ~20 nm citrated-capped AuNP and resulted in water-soluble hybrid well-defined nano-objects. Grafting has been evidenced by UV-Vis spectroscopy and TEM.

Water-solubility, conformation of grafted conjugates and grafting density turned out to be dependent on the chemical nature of the chromophore (hydrophilic *vs.* hydrophobic), the length and the structure of the polymer backbone (capped with AEM or hydrolyzed).

Polymer corona thickness measured by TEM increased with the increasing M_n of the polymer backbone suggesting a potential increase in chromophore-AuNP distance.

III.4.4. Grafting LY32KDa(B) conjugate onto spherical AuNP with different diameters

In order to study the influence of AuNP size on grafting, AuNP spherical nanoparticles with larger diameters (d > 20 nm) were synthesized by J. Navarro (post-doc 2011-2012) using a novel modified Turkevich-Frens method.[73] The LY32KDa(B) conjugate, synthesized in Chapter II, has been grafted on all these spherical AuNP following the previously described ligand exchange approach.

UV-Vis spectroscopy before and after grafting LY32KDa(B) conjugate onto 13 nm, 50 nm and 90 nm AuNP (Figure III. 42 a)) shows a red-shift of the SPR band. This phenomenon, likely due to the changes in the refractive index of the environment surrounding the AuNP, was previously discussed in the case of 20 nm AuNP (Section III.4.2.1).
As reported in literature, larger spherical AuNP exhibit increased scattering and broadened SPR bands, shifted towards longer wavelengths.[74]

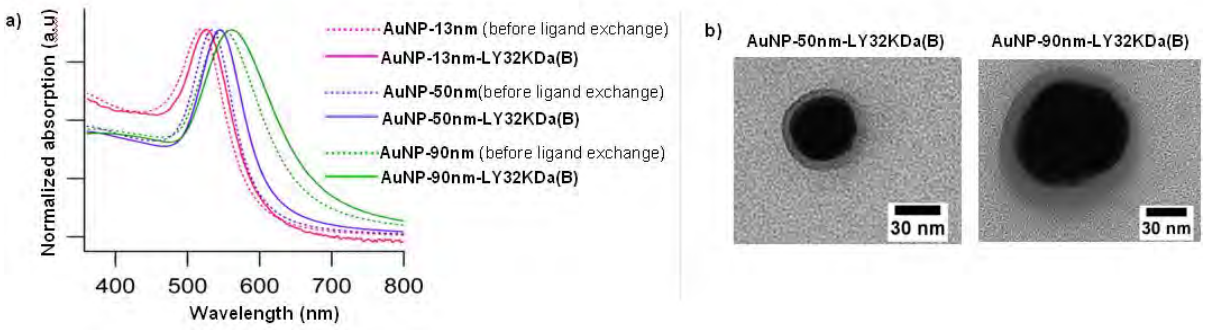

Figure III. 42: a) UV-Vis spectra of AuNP before and after grafting with LY32KDa(B) conjugate: 13nm AuNP (pink), 50nm AuNP (purple), 90nm AuNP (green); b) TEM images of 50nm and 90nm AuNP grafted with LY32KDa(B).

TEM images enabled to calculated the AuNP core mean diameter and the thickness of the grafted polymer corona (~6 nm for AuNP-50nm-LY32KDa(B) and to ~12 nm for AuNP-90nm-LY32KDa(B)). When compared to 20 nm AuNP grafted with the same conjugate (polymer corona thickness ~18 nm), a decrease of polymer corona thickness was observed. This would probably suggest that the size of AuNP influences the conformation of grafted polymer conjugates, thus the overall grafting density.

This ongoing work, proves the versatility of such nano-objects, and is being completed by studies on AuNP with different shapes (stars, bipyramids, and rods).
The influence of AuNP core size on the photophysical properties of grafted LY32KDa(B) conjugate will be discussed in Chapter IV.

III.5. Conclusion of Chapter III

Taking into account the extensive work already completed on AuNP functionalized with RAFT polymers, it has been shown in literature how the properties of coated polymers can tune the final properties of grafted AuNP, emphasizing the advantages of using RAFT polymerization.

The first step to obtain AuNP grafted with RAFT polymers, consisted in the optimization of experimental conditions using PNAM-SH polymers *via* two different synthetic approaches: one-step *in situ* and two-step ligand exchange. The first approach led to 2-3 nm diameter stable AuNP-PNAM, with high grafting densities (0.7 chains/nm²). Control *in situ* experiments evidenced that grafting onto AuNP occurred *via* the SH polymer end-groups (oriented grafting).
The ligand exchange approach resulted in well-defined 20 nm AuNP-PNAM. Using this approach, it was possible to separately control the size of the AuNP and the polymer grafting procedure, to optimize the grafting conditions (temperature, Au/S molar ratio) and to accurately characterize the grafted AuNP-PNAM, as well as to visualize and measure the Au core diameter and the polymer corona thickness by TEM. Compared to *in situ*, lower grafting densities have been reached by ligand exchange approach (0.5 chains/nm²).

The possibility to change AuNP size and shape, to control the polymer grafting, together with the ease of characterization led us to choose the ligand exchange approach for grafting high-added value chromophore-polymer conjugates. Thus, based on previously optimized synthesis and characterization techniques with AuNP-PNAM systems, well-defined water-soluble AuNP-conjugates have been elaborated. The final properties of these grafted AuNP were dependent on the properties of the grafted conjugate (water-solubility, density of chromophores *per* chain, chromophore chemical nature, charges along the chain, length of the polymer backbone). Most importantly, it has been demonstrated that the polymer corona thickness (TEM) increased with the increasing polymer length.

- For LY conjugates, the corona thickness increased from 1 nm to 20 nm when the polymer M_n increased from 2 000 g.mol^{-1} to 37 000 g.mol^{-1}.
- For DBB grafted conjugates, the corona thickness it increased from 4 nm to 13 nm when the polymer M_n increased from 13 000 g.mol^{-1} to 35 000 g.mol^{-1}.

This last result is of great importance for the rest of this work, as it justifies the use of multifunctional polymers to potentially control the photophysical properties of chromophores near AuNP by modifying the chromophore-AuNP distance (Chapter IV).

Even if 20 nm AuNP were discussed as a model system for grafting, some current work is focusing on the grafting of conjugates on larger AuNP with different sizes and shapes.

III.6. Experimental section

Materials

Gold salt ($HAuCl_4 \times 3H_2O$, 99.99%, metal basis 49.5% min) was purchased from Alfa Aesar GmbH & Co KG; trisodium dihydrate citrate (95%) – from Merk, $NaBH_4$ (99%) – from Sigma Aldrich; and used as received.
Sodium chlorate 1112-A, enzyme and endotoxyne free used to prepare the eluent for the purification step was obtained from Euromedex.
Modified cellulose Cellufine GCL-2000 particles (90-140µm diameter) purchased from Chisso Corporation was used for the preparation of SEC column.
Amicon Ultra-15 (regenerated cellulose membrane, MWCO=100kDa or 50kDa) was purchased from Millopore.
Purified Grafted Milli-Q water was used as solvent for almost all syntheses, purifications and analyses.
$CHCl_3$ (stabilized with EtOH) used to dissolve AuNP-10Ant-AEM was purchased from Carlo Erba (analytical grade).

Grafting RAFT polymers onto AuNP

In situ approach

On a mixture of 15mg $HAuCl_4x3H_2O$ (1.7mM) and 41mg PNAM (0.6mM) was added dropwise a freshly prepared $NaBH_4$(aq.) solution (10 molar eq. with respect to Au), under vigorous stirring at room temperature. The color of the reaction medium changed suddenly from light yellow to dark brown. The reaction mixture was kept under stirring during another 2 hours.

- $[Au]_0$ = 1.7mM
- PNAM/Au molar ratio = 1/3
- $NaBH_4$/Au molar ratio = 10/1
- Reaction time = 2 hours.

Ligand exchange approach

1st step: Synthesis of citrate capped AuNP

In a round bottom flask, 15mg $HAuCl_4x3H_2O$ aqueous solution (0.9mM $[Au]_0$, 45 mL) was heated at 115°C in an oil bath. The flask was fitted with a refrigerator and brought to reflux under stirring. Sodium citrate solution of 56.6mM was added in one shot to the boiling gold salt and left under stirring for another 30 minutes. The color of the solution changed suddenly from light yellow to colorless, then to dark blue, and finally to violet-red. Reaction mixture containing citrate-capped AuNP was then cooled at RT.

- $[Au]_0$ = 0.9mM
- Citrate/Au molar ratio = 4.5
- Reaction time = 30 min.

2nd step: grafting of thiol-terminated polymers (conjugates) onto ~20 nm preformed AuNP

In a round bottom flask, previously synthesized citrate-capped AuNP in water (0.9 mM) were mixed at room temperature with a solution of PNAM (or conjugates), molar ratio Au/polymer (Au/S) = 10. The reaction mixture was stirred at 80°C during 3h, under vigorous stirring.

- $[Au]_0$ = 0.9 mM
- polymer/Au molar ratio = 1/10
- Temperature during ligand exchange = 80°C
- Reaction time: 3 hours.

Purification techniques

Centrifugal ultrafiltration

Centrifugal ultrafiltration was achieved using Amicon Ultra-15 purchased from Millipore with MWCO = 50/100kDa. The aqueous solution of grafted AuNP (obtained by either *in situ* approach – MWCO=50kDa, or ligand exchange approach – MWCO = 100kDa) was centrifuged 3 times (10 min,

8000 rpm) to remove the excess of free ungrafted polymer in solution. Centrifugation was performed on Eppendorf Centrifugal 5810 R centrifuge.

SEC chromatography

Size Exclusion Chromatography (SEC) was performed in a (20cm x 1cm) Econo Pac glass column fitted with polyethylene oxide filter from BioRad. The SEC column (15cm x 1cm) was prepared using Cellufine GCL-2000 gel (Chisso Corporation) and 0.25% (wt.) NaCl(aq.) eluent. A concentrated solution (~5mg Au / mL) of grafted AuNP (~500µL) is eluted on the column under gravity.

Several gels were used to optimize the SEC method. The characteristics of chromatography gels used for SEC purification are summarized in the table below.

Gel	Supplier	Chemical nature	Particle size (µm)	Exclusion limit ($g.mol^{-1}$)	pH range	Organic solvent tolerance (%)
Sephadex G-50 Fine DNA Grade	Sigma-Aldrich	Dextran	~40 - 350	$1,5x10^3$ – $3x10^4$	4 -10	< 20
Gel Sephacryl S200-HR	General Electric Healthcare	Crosslinked allyl dextran with N,N-bisacrylamide	~ 47	5×10^3 – 2.5×10^5	3 - 11	< 20
Bio-Gel P-100 Gel Medium	BIO-RAD	Polyamide	~ 90 - 80	$5x10^3$ – 10^5	2 - 10	< 20
Cellufine GCL-2000	Chisso	Crosslinked cellulose	~40 - 130	10^3 – 10^6	1 - 14	-

Instruments and methods

UV-Vis absorption

UV-Vis absorption spectra were recorded on a Jasco V-670 spectrophotometer at ambient temperature using 1 cm quartz cell.

Precision weighing scale Sartorius LA 230S ± 0.1mg was used to weigh solid products for sample preparation.

Beer-Lambert law applied for concentration calculations: $A = \varepsilon l c$, where *A* is the absorbance at a given wavelength, *l* is path length of the cell and *c* the concentration of the sample.

For example, for 20 nm AuNP, a red shift of 3-4 nm was recorded, corresponding to the difference between maxima of SPR bands before and after PNAM grafting (figure below).

UV-Vis spectra of citrate-capped AuNP (sky blue dashed line) and PNAM-grafted AuNP (dark blue straight line) – 3 nm red-shift of SPR band after grafting

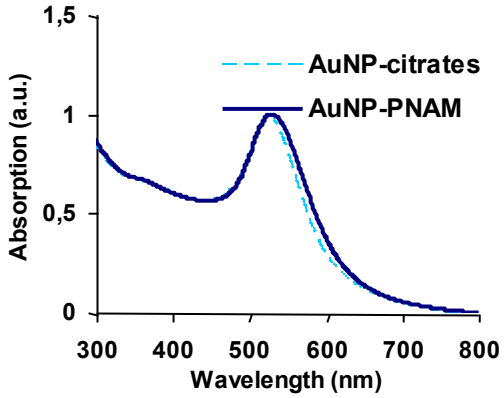

TEM imaging

TEM of gold nanoparticles was carried out on Philips CM 120 electron microscope operated at an accelerating voltage of 80 keV.

A drop of AuNP aqueous suspension was placed on a carbon-coated copper grid (300/600 mesh) and the excess liquid was removed before the grid was air dried.
The polymer shell was revealed by positive staining using RuO_4: the dried grid was exposed during 20-30 min to RuO_4 vapors.
The particle size distribution was determined with the ImageJ software by statistical analysis of more than 40-100 nanoparticles taken from 1 to 3 images for each sample.
For polymer corona thickness measurements with Image J, a multicolor scale was applied to TEM images in order to better visualize the contrast zones (figure below).

TEM imaging of AuNP-PNAM (staining with RuO_4): (left) grey-color scale; (right) multicolor scale.

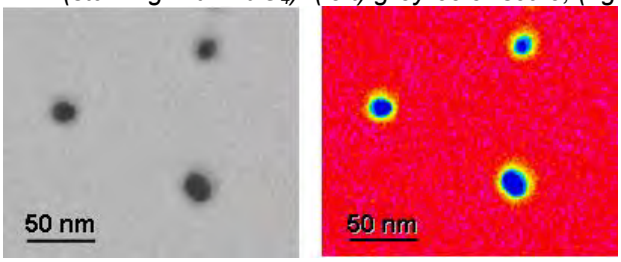

Example of results obtained with AuNP-PNAM obtained by in situ and ligand exchange approaches will be given below.

In situ AuNP-PNAM

Generally, in the case of *in situ* AuNP-PNAM samples (figure below), black dots on TEM images correspond to 2-3 nm AuNP cores. The polymer shell stabilizing these AuNP was not visible by TEM due to limited resolution of the microscope and to insufficient contrast between small AuNP and the thin layer of grafted polymer. Moreover the staining with RuO_4 increased the background noise on TEM photos, impeding the accurate detection of small AuNP, and did not reveal the grafted polymer corona.

TEM imaging of in situ AuNP-PNAM (no staining).

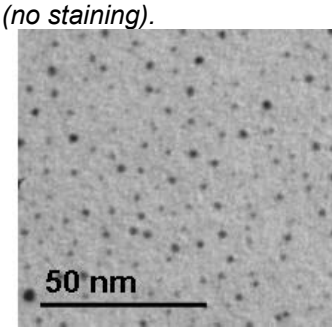

AuNP-PNAM obtained by ligand exchange

In the case of larger AuNP-PNAM obtained by ligand exchange, both the AuNP core and PNAM corona could be visualized (figure below). AuNP metallic cores are represented by black spots and grafted polymers around AuNP appear as dark grey coronae around each AuNP (figure below).

TEM imaging AuNP-PNAM obtained by ligand exchange (staining with RuO_4): a) agglomerated citrate-capped AuNP; b) AuNP-PNAM after the ligand exchange step (PNAm, M_n=14100 g.mol^{-1}).

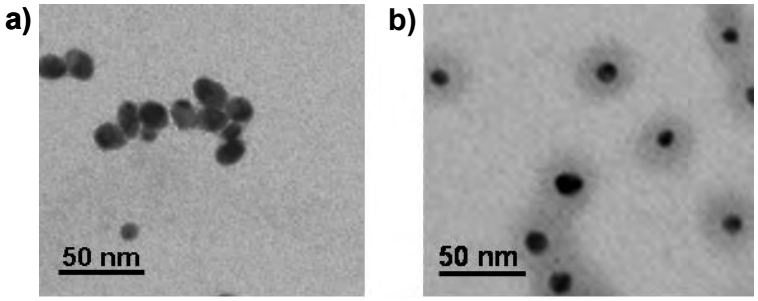

Cryo-TEM imaging

Cryo-TEM samples were prepared using holey carbon film Cu grids (400 mesh). 5µL of concentrated solution of AuNP was placed on the holey grid. After drying to a thin film with blotting paper, the sample was immediately dipped into liquid ethane (-186°C).. The freezed sample was transferred into the Philips CM 120 electron microscope chamber and imaged under a lower electron dose (60kV).

DLS

Diffusion Light Scattering (DLS) was performed on Nanosizer from Malvern with diluted solutions ($10M^{-12}$ $[Au]_0$), using 1 cm polystyrene cuvettes. We used this technique to monitor the grafting of preformed citrate-capped AuNP *via* ligand exchange approach.*

Thermogravimetric Analysis (TGA)

Weight loss of free polymer and polymer coated AuNPs was measured on a TGA instrument (NETZSCH STA 409 PC/PG LuxxR) with alumina pans. The samples were heated from 25 to 1000°C at a heating rate of 10°C/min under nitrogen (flow rate 40mL/min). The weight ratio between Au and grafted polymer could be estimated form TGA data.

During TGA of AuNP-PNAM (figure below), only PNAM grafted on nanoparticles decomposes into volatile residual compounds, corresponding to a sudden loss of weight at ~400-450°C.

TGA thermograms of AuNP-PNAM vs. free PNAM (Heating rate 10°/min, N_2 atmosphere).

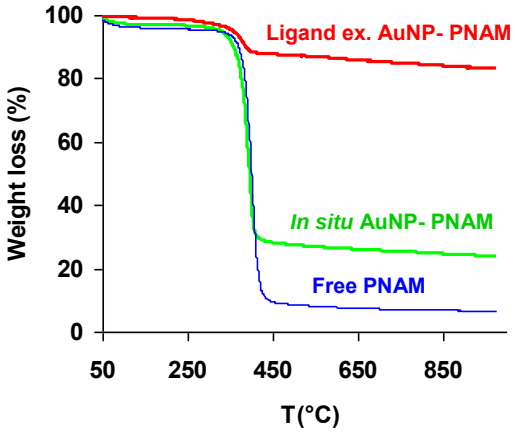

The remaining weight would represent then the amount of Au in the initial sample. It has however been shown that TGA of free PNAM results in only 92% weight loss (corresponding to volatile decomposition products), the remaining of 8% from initial weight was attributed to non-volatile organic products. Taking into account this data, the amount of PNAM and Au could be estimated for in situ grafted AuNP-PNAM and ligand exchange AuNP-PNAM.

Grafting density

Using TEM and TGA results the grafting density of AuNP-PNAM in chains/nm² could be determined using the equation below. [37]

$$\frac{\frac{W_{PNAM} \times N_A}{M_{PNAM}}}{\frac{W_{Au}}{\rho_{Au} \times V_{AuNP}} \times S_{AuNP}}$$

Here, W_{PNAM} is the percentage of weight loss corresponding to the decomposition of the PNAM chains, ρ_{Au} is the density of bulk gold (19.32 g/cm3), W_{Au} is the percent weight corresponding to Au, V_{AuNP} is

* The size of grafted AuNP could not be properly determined by DLS (interference between DLS laser, and SPR of AuNP?).

the volume of a bare gold nanoparticle calculated from the AuNP diameter determined by TEM. N_A is Avogadro's number, M_{PNAM} is the molecular weight of grafted PNAM chain (M_n), and S_{AuNP} is the specific surface area of bare gold nanoparticle calculated from AuNP diameter determined by TEM.

^{1}H-DOSY NMR

High-resolution liquid NMR spectroscopy was carried out with a Bruker spectrometer operating at 400 MHz for $_1$H, using D_2O (99.8% as solvent). For 2D spectra, were recorded under a field gradient. The gradient pulses have no effect on stationary species, and have a greater effect on species that diffuse rapidly.

NMR experiments were carried out at 300 K on a Bruker Avance III spectrometer operating at 400,13 MHz for proton with a 5 mm BBFO+ probe equipped with z-gradient coil delivering up to 52,8 G/cm. Gradient coil strength was calibrated with "doped water" NMR reference standard. Temperature was calibrated with "80% ethylene glycol in DMSO-d6" NMR reference standard and was set and controlled with an adapted regulation to avoid fluctuations due to sample heating.

DOSY experiments were recorded in D_2O using "ledbpgppr2s" Bruker pulse sequence with water presaturation. Gradients were linearly sampled from 2,41 G/cm to 45,74 G/cm in 16 points. 8 scans were acquired on 32k data points, and recycle time of 3,5 s. The gradient pulse length δ was optimized with each sample (5 to 8 ms) and the diffusion delay Δ was set to 50 ms. Fourier transform was applied in F2 with 1 Hz exponential broadening. The DOSY spectra were obtained by fitting independently all columns of the F2 transformed spectrum, using a Levenberg-Marquardt algorithm embedded into the commercial software BRUKER TopSpin™. Careful polynomial correction was applied along the F2 dimension before the processing, which was computed on 128 points.

Diffusion ordered NMR spectroscopy (DOSY) relates the chemical shifts of NMR resonances from a given molecular species to the translational diffusion coefficient of that species. Diffusion coefficients of molecules are related to hydrodynamic radius and molecular weights.

Fluorescence spectroscopy

Fluorescence emission spectra were recorded on a Horiba-Jobin Yvon Fluorolog-3 spectrofluorimeter equipped with a R928P (PMT) detector. Right Angle geometry, at ambient temperature, a 1 cm optical path length quartz cell, and an excitation wavelength of 430 nm were used for LY-derivatives. Entrance (excitation)/exit (emission) slits: 1nm/2nm; integration time = 0.1s.

References

[1] **Gold Nanoparticles: Assembly, Supramolecular Chemistry, Quantum-Size-Related Properties, and Applications toward Biology, Catalysis, and Nanotechnology**, M.-C. Daniel, D. Astruc, *Chem. Rev.* **2004**, *104*, 293-346.

[2] **Smart core/shell nanocomposites: Intelligent polymers modified gold nanoparticles,** D. Li, Q. He, J. Li, *Adv. Colloid. Interface Sci*. **2009**, *149*, 28-38.

[3] **Recent advances in polymer protected gold nanoparticles: synthesis, properties and applications,** J. Shan, H. Tenhu, *Chem. Commun.* **2007**, 4580-4598.

[4] **Amphiphilic Janus Gold Nanoparticles via Combining "Solid-State Grafting-to" and "Grafting-from" Methods,** B. Wang, B. Li, B. Zhao, C. Y. Li, *J. Am. Chem. Soc.* **2008**, *130*, 11594-11595.

[5] **Surface-Initiated Polymerization I,** R. Advincula, M. R. Buchmeiser, D. J. Dyer, Heidelberg, Volume Editor R. Jordan, Springer-Verlag Berlin **2006**.

[6] **Polymer Brushes via Surface-Initiated Controlled Radical Polymerization: Synthesis, Characterization, Properties, and Applications,** R. Barbey, L. Lavanant, D. Paripovic, N. Schüwer, C. Sugnaux, S. Tugulu, H.-A. Klok, *Chem. Rev.* **2009**, *109*, 5437-5527.

[7] **Gold Nanoparticles Tethered to Gold Surfaces Using Nitroxyl Radicals,** O. Swiech, N. Hrynkiewicz-Sudnik, B. Palys, A. Kaim, R. Bilewicz, *J. Phys. Chem. C* **2011**, *115*, 7347-7354.

[8] **One-Pot Synthesis of Robust Core/Shell Gold Nanoparticles,** H. Dong, M. Zhu, J.A. Yoon, H. Gao, R. Jin, K. Matyjaszewski, *J. Am. Chem. Soc.* **2008**, *130*, 12852-12853.

[9] **Two-Stage pH Response of Poly(4-vinylpyridine) Grafted Gold Nanoparticles**, D. Li, Q. He, Y. Yang, H. Möhwald, J. Li, *Macromolecules* **2008**, *41*, 7254-7256.

[10] **Synthesis of Gold Nanoparticles Coated with Well-Defined, High-Density Polymer Brushes by Surface-Initiated Living RadicalPolymerization,** K. Ohno, K. Koh, Y. Tsujii, T. Fukuda, *Macromolecules* **2002**, *35*, 8989-8993.

[11] **Preparation of Polymer Coated Gold Nanoparticles by Surface-Confined Living Radical Polymerization at Ambient Temperature,** T. K. Mandal, M. S. Fleming, D.R. Walt, *Nano Lett.* **2002***, 2(1)*, 3-7.

[12] **Synthesis of Gold Nanoparticles Grafted with a Thermoresponsive Polymer by Surface-Induced Reversible-Addition-Fragmentation Chain-Transfer Polymerization,** J. Raula, J. Shan, M. Nuopponen, A. Niskanen, H. Jiang, E. I. Kauppinen, H. Tenhu, *Langmuir* **2003**, *19*, 3499-3504.

[13] **Thermoresponsive Nanohydrogels Cross-Linked by Gold Nanoparticles**, X. Lian, J. Jin, J. Tian, H. Zhao, *ACS Appl*. *Mater*. *Interfaces* **2010**, *2(8)*, 2261-2268.

[14] a) **Photochemical Approach toward Deposition of Gold Nanoparticles on Functionalized Carbon Nanotubes**, F. B. Lollmahomed, R. Narain, *Langmuir* **2011**, *27*, 12642-12649.

b) **Supramolecular Colloidal Systems of Gold Nanoparticles/Amphiphilic Cyclodextrin: a FE-SEM and XPS Investigation of Nanostructures Assembled onto Solid Surface,** A. Mazzaglia, L. Monsu Scolaro, A. Mezzi, S. Kaciulis, T. De Caro, G. M. Ingo, G. Padeletti, *J. Phys. Chem. C* **2009**, *113*, 12772-12777.

c) **Polymer-Induced Synthesis of Stable Gold and Silver Nanoparticles and Subsequent Ligand Exchange in Water,** R. Sardar, J.-W. Park, J. S. Shumaker-Parry, *Langmuir* **2007**, *23*, 11883-11889.

[15] **Glycopolymer Decoration of Gold Nanoparticles Using a LbL Approach,** C. Boyer, A. Bousquet, J. Rondolo, M. R. Whittaker, M. H. Stenzel, T. P. Davis, *Macromolecules* **2010**, *43*, 3775-3784.

[16] **Recent advances in polymer protected gold nanoparticles: synthesis, properties and applications,** J. Shan and H. Tenhu, *Chem. Commun.* **2007**, 4580-4598.

[17] **Controlling Shell Thickness in Core-Shell Gold Nanoparticles via Surface-Templated Adsorption of Block Copolymer Surfactants,** Y. Kang, T. A. Taton, *Macromolecules* **2005**, *38*, 6115-6121.

[18] **Adsorption modes of cysteine on Au(111): Thiolate, amino-thiolate, disulfide,** R. D Felice, A. J. Selloni, *Chem. Phys.* **2004**, *120*, 4906-4914.

Monolayer-Protected Cluster Molecules, A. C Templeton, W. P. Wuelfing, R. W Murray, *Acc. Chem. Res.* **1999**, *33*, 27-36.

[19] **Gold Nanoparticles Protected with Thiol-Derivatized Amphiphilic Poly(E-caprolactone)-b-poly(acrylic acid),** I. Javakhishvili, S. Hvilsted, *Biomacromol.* **2009,** *10,* 74-81.

[20] **Optical properties of gold colloids formed in inverse micelles,** J. P.Wilcoxon, R. L. Williamson, R. Baughman, *J. Chem. Phys.* **1993**, *98(12)*, 9933-9950.

[21] **Synthesis of Thiol-Derivatized Gold Nanoparticles in a Two-phase Liquid-Liquid System,** M. Brust, M. Walker, D. Bethell, D. J. Schiffrin, R. Whyman, *J. Chem. Soc. Chem. Commun.* **1994,** *7*, 801-802.

[22] **Size-controlled synthesis of near-monodisperse gold nanoparticles in the 1-4 nm range using polymeric stabilizers,** I. Hussain, S. Graham, Z. Wang, B. Tan, D. C. Sherrington, S. P. Rannard, A. I. Cooper, M. Brust, *J. Am. Chem. Soc*. **2005**, *127(47),* 16398-9.

[23] **Nucleation and growth process in the synthesis of colloidal gold,** J. Turkevitch, P.C. Stevenson, J. Hillier, *Discussion Faraday Soc.* **1951**, *11*, 55-75.

[24] **Controlled Nucleation for the Regulation of the Particle Size in Monodisperse Gold Suspensions,** G. Frens, *Nature: Phys. Sci.* **1973**, *241*, 20-22.

[25] **Facile Preparation of Transition Metal Nanoparticles Stabilized by Well-Defined (Co)polymers Synthesized *via* Aqueous Reversible Addition-Fragmentation Chain Transfer Polymerization,** A. B. Lowe, B. S. Sumerlin, M. S. Donovan, C. L. McCormick, *J. Am. Chem. Soc.* **2002**, *124*, 11562-11563.

[26] **Surface Modification of Gold Nanorods with Polymers Synthesized by Reversible Addition-Fragmentation Chain Transfer Polymerization,** J. W. Hotchkiss, A. B. Lowe, S. G. Boyes, *Chem. Mater.* **2007**, *19*, 6-13.

[27] **Tuning the Hydrophilicity of Gold Nanoparticles Templated in Star Block Copolymers,** C.-A. Fustin, C. Colard, M. Filali, P. Guillet, A.-S. Duwez, M. A. R. Meier, U. S. Schubert, J.-F. Gohy, *Langmuir* **2006**, *22*, 6690-6695.

[28] **Facile synthesis of thiol-terminated poly(styrene-*ran*-vinyl phenol) (PSVPh) copolymers via reversible addition-fragmentation chain transfer (RAFT) polymerization and their use in the synthesis of goldnanoparticles with controllable hydrophilicity,** C.-U. Lee, D. Roy, B. S. Sumerlin, M. D. Dadmun, *Polymer* **2010**, *51*, 1244-1251.

[29] **Synthesis of poly(ethylene oxide)-based thermoresponsive block copolymers by RAFT radical polymerization and their uses for preparation of gold nanoparticles,** H. J. Jeon, D. H. Go, S. Choi, K. M. Kim, J. Y. Lee, D. J. Choo, H.-O. Yoo, J. M. Kim, J. Kim, *Colloids and Surfaces A*: *Physicochem. Eng. Aspects* **2008**, *317*, 496–503.

[30] **Two Phase Transitions of Poly(N-isopropylacrylamide) Brushes Bound to Gold Nanoparticles,** J. Shan, J. Chen, M. Nuopponen, H. Tenhu, *Langmuir* **2004**, *20*, 4671-4676.

[31] **Tuning the Structure of Thermosensitive Gold Nanoparticle Monolayers,** C. A. Rezende, J. Shan, L.-T. Lee, G. Zalczer, H. Tenhu, *J. Phys. Chem. B* **2009**, *113*, 9786-9794.

[32] **Thermoresponsive Properties of N-Isopropylacrylamide Oligomer Brushes Grafted to Gold Nanoparticles: Effects of Molar Mass and Gold Core Size,** J. Shan, Y. Zhao, N. Granqvist, H. Tenhu, *Macromolecules* **2009**, *42 (7)*, 2696-2701.

[33] **Synthesis of Gold Nanoparticles Coated with Polystyrene-block-poly(N-isopropylacrylamide) and Their Thermoresponsive Ultraviolet-Visible Absorbance,** Y. Liu, W. Tu, D. Cao, *Ind. Eng. Chem. Res.* **2010**, *49*, 2707-2715.

[34] **Thermoresponsive Amphiphilic Diblock Copolymers Synthesized by MADIX/RAFT: Properties in Aqueous Solutions and Use for the Preparation and Stabilization of Gold Nanoparticles,** S. Sistach, M. Beija, V. Rahal, A. Brûlet, J.-D. Marty, M. Destarac, C. Mingotaud, *Chem. Mater.* **2010**, *22*, 3712-3724.

[35] **Thermoresponsive poly(N-vinyl caprolactam)-coated gold nanoparticles: sharp reversible response and easy tenability,** M. Beija, J.-D. Marty, M. Destarac, *Chem. Commun.* **2011**, *47*, 2826-2828.

[36] **Control of the catalytic properties and directed assembly on surfaces of MADIX/RAFT polymer-coated gold nanoparticles by tuning polymeric shell charge,** M. Beija, E. Palleau, S. Sistach, X. Zhao, L. Ressier, C. Mingotaud, M. Destarac, J.-D. Marty, *J. Mater. Chem.* **2010**, *20*, 9433-9442.

[37] **Salt Effect on the Heat-Induced Association Behavior of Gold Nanoparticles Coated with Poly(N-isopropylacrylamide) Prepared via Reversible Addition-Fragmentation Chain Transfer (RAFT) Radical Polymerization,** S. Yusa, K. Fukuda, T. Yamamoto, Y. Iwasaki, A. Watanabe, K. Akiyoshi, Y. Morishima, *Langmuir* **2007**, *23*, 12842-12848.

[38] **Modulation of the Surface Charge on Polymer-Stabilized Gold Nanoparticles by the Application of an External Stimulus,** C. Boyer, M. R. Whittaker, K. Chuah, J. Liu, and T. P. Davis, *Langmuir* **2010**, *26(4)*, 2721-2730.

[39] **Design and Synthesis of Dual Thermoresponsive and Antifouling Hybrid Polymer/Gold Nanoparticles,** C. Boyer, M. R. Whittaker, M. Luzon, T. P. Davis, *Macromolecules* **2009**, *42*, 6917-6926.

[40] **The critical importance of size on thermoresponsive nanoparticle transition temperatures: gold and micelle-based polymer nanoparticles,** N. Sze Ieong, K. Brebis, L. E. Daniel, R. K. O'Reilly, M. I. Gibson, *Chem. Commun.* **2011**, *47*, 11627-11629.

[41] **Double Hydrophilic Block Copolymer Monolayer Protected Hybrid Gold Nanoparticles and Their Shell Cross-Linking**, S. Luo, J. Xu, Y. Zhang, S. Liu, C. Wu, *J. Phys. Chem. B* **2005**, *109*, 22159-22166.

[42] **Influence of Additives on the Thermoresponsive Behavior of Polymers in Aqueous Solution,** K. Van Durme, H. Rahier, B. Van Mele, *Macromolecules* **2005**, *38*, 10155-10163.

[43] **Thermoresponsive hydrogels in biomedical applications,** L. Klouda, A. G. Mikos, *Eur. J. Pharm. Biopharm.* **2008***, 68(1)*, 34–45.

[44] **Light-Controllable Surface Plasmon Resonance Absorption of Gold Nanoparticles Covered with Photochromic Diarylethene Polymers,** H. Nishi, T. Asahi, S. Kobatake, *J. Phys. Chem. C* **2009**, *113*, 17359-17366.

[45] **Using Polymers To Photoswitch the Aggregation State of Gold Nanoparticles in Aqueous Solution,** A. Housni, Y. Zhao, Y. Zhao, *Langmuir* **2010**, *26(14)*, 12366-12370.

[46] **Gold Nanoparticles Protected with pH and Temperature-Sensitive Diblock Copolymers,** M. Nuopponen, H. Tenhu, *Langmuir* **2007**, *23*, 5352-5357.

[47] **BODIPY-Based Chain Transfer Agent: Reversibly Thermoswitchable Luminescent Gold Nanoparticle Stabilized by BODIPY-Terminated Water-Soluble Polymer,** A. Nagai, R. Yoshii, T. Otsuka, K. Kokado, Y. Chujo, *Langmuir* **2010**, *26(19)*, 15644-15649.

[48] **Controlled RAFT Synthesis of Polyacrylonitrile-b-poly(acrylic acid) Diblocks as Precursors of Carbon Nanocapsules with Assistance of Gold Nanoparticles,** A. Aqil, C. Detrembleur, B. Gilbert, R. Jérôme, C. Jérôme, *Chem. Mater.* **2007**, *19*, 2150-2154.

[49] **Synthesis of Hollow Polymer Nanocapsules Exploiting Gold Nanoparticles as Sacrificial Templates,** C. Boyer, M. R. Whittaker, C. Nouvel, T. P. Davis, *Macromolecules* **2010**, *43*, 1792-1799.

[50] **Self-Assembly and Encoding of Polymer-Stabilized Gold Nanoparticles with Surface-Enhanced Raman Reporter Molecules,** Z. Merican, T. L. Schiller, C. J. Hawker, P. M. Fredericks, I. Blakey, *Langmuir* **2007**, *23*, 10539-10545.

[51] **Synthesis of Biotinylated α-D-Mannoside or N-Acetyl β-D-Glucosaminoside Decorated Gold Nanoparticles: Study of Their Biomolecular Recognition with Con A and WGA Lectins,** X. Jiang A. Housni, G. Gody P. Boullanger, M.-T. Charreyre, T. Delair, R. Narain, *Bioconjugate Chem.* **2010**, *21*, 521-530.

[52] **Interaction of Densely Polymer-Coated Gold Nanoparticles with Epithelial Caco-2 Monolayers,** I-C. Lin, M. Liang, T.-Y. Liu, Z. M. Ziora, M. J. Monteiro, I. Toth, *Biomacromolecules* **2011**, *12*, 1339-1348.

[53] **Cellular Uptake of Densely Packed Polymer Coatings on Gold Nanoparticles,** M. Liang, I-C. Lin, M. R. Whittaker, R. F. Minchin, M. J. Monteiro, I. Toth, *ACS Nano* **2010**, *4(1)*, 403-413.

[54] **Sequentially Modified, Polymer-Stabilized Gold Nanoparticle Libraries: Convergent Synthesis and Aggregation Behavior,** M. I. Gibson, M. Danial, H.-A. Klok, *ACS Comb. Sci.* **2011**, *13*, 286-297.

[55] **Probing in situ the Nucleation and Growth of Gold Nanoparticles by Small-Angle X-ray Scattering,** B. Abécassis, F. Testard, O. Spalla, P. Barboux, *Nano Lett.* **2007**, *7(6)*, 1723-1727.

[56] **Colloidal Gold Nanoparticles Protected by Water-Soluble Homopolymers and Random Copolymers,** A. B. R. Mayer, J. E. Mark, *Eur. Polym.* **1998**, *34*, 103-108.

[57] **Thermodynamic Control of Gold Nanocrystal Size: Experiment and Theory,** D. V. Leff, P. C. Ohara, J. R. Heath, W. M. Gelbart, *J. Phys. Chem.* **1995**, *99*, 7036-7041.

[58] **Alkanethiol molecules containing an aromatic moiety self-assembled onto gold clusters,** S.R. Johnson, S.D. Evans, S.W. Mahon, A. Ulman, *Langmuir* **1997**, *13*, 51-57.

[59] **Alkanethiolate Gold Cluster Molecules with Core Diameters from 1.5 to 5.2 nm: Core and Monolayer Properties as a Function of Core Size,** M. J. Hostetler, J. E. Wingate, C. Zhong, J. E. Harris, R. W. Vachet, M. R. Clark, J. D. Londono, S. J. Green, J. J. Stokes, G. D. Wignall, G. L. Glish, M.D. Porter, N. D. Evans, R.D. Murray, *Langmuir* **1998**, *14*, 17-30.

[60] a) **New Insights on the Nanoparticle Growth Mechanism in the Citrate Reduction of Gold(III) Salt: Formation of the Au Nanowire Intermediate and Its Nonlinear Optical Properties,** B.-K. Pong, H. I. Elim, J.-X. Chong, W. Ji, B. L. Trout, J.-Y. Lee, *J. Phys. Chem. C* **2007**, *111*, 6281-6287.

b) **Modeling of Formation of Gold Nanoparticles by Citrate Method,** S. Kumar, K. S. Gandhi, R. Kumar, *Ind. Eng. Chem. Res. 2007*, *46*, 3128-3136.

[61] **Characterization, purification, and stability of gold nanoparticles,** S. K. Balasubramanian, L. Yang, L.-Y. L. Yung, C.-N. Ong, W.-Y. Ong, L. E. Yu, *Biomaterials* **2010**, *31*, 9023-9030.

[62] **Amphiphilic Gold Nanoparticles with V-Shaped Arms,** E. R. Zubarev, J. Xu, A. Sayyad, J. D. Gibson, , *J. Am. Chem. Soc.* **2006**, *128*, 4958-4959.

[63] **Reversible Addition-Fragmentation Chain Transfer Polymerization: End Group Modification for Functionalized Polymers and Chain Transfer Agent Recovery,** S. Perrier, P. Takolpuckdee, C. A. Mars, *Macromolecules* **2005**, *38*, 2033-2036.

[64] **Nanometer Gold Clusters Protected by Surface-Bound Monolayers of Thiolated Poly(ethylene glycol) Polymer Electrolyte,** W. P. Wuelfing, S. M. Gross, D. T. Miles, R. W. Murray, *J. Am. Chem. Soc.* **1998**, *120*, 12696-12697.

[65] **One-Phase Synthesis of Water-Soluble Gold Nanoparticles with Control over Size and Surface Functionalities,** E. Oh, K. Susumu, R. Goswami, H. Mattoussi, *Langmuir* **2010**, *26(10)*, 7604-7613.

[66] **a) Formation of the Au Nanowire Intermediate and Its Nonlinear Optical Properties,** B.-K. Pong, H. I. Elim, J.-X. Chong, W. Ji, B. L. Trout, and J.-Y. Lee, *J. Phys. Chem. C* **2007**, *111*, 6281-6287.

b) Modeling of Formation of Gold Nanoparticles by Citrate Method, S. Kumar, K. S. Gandhi, R. Kumar, *Ind. Eng. Chem. Res.* **2007**, *46*, 3128-3136.

[67] **Influence of the Sequence of the Reagents Addition in the Citrate-mediated Synthesis of Gold Nanoparticles,** I. Ojea-Jiménez, N. G. Bastús, V. F. Puntes, *J. Phys. Chem. C*, **2011**, *115 (32)*, 15752-15757.

[68] **Two-Dimensional Self-Organization of Polystyrene-Capped Gold Nanoparticles,** H. Yockell-Lelièvre, J. Desbiens, A. M. Ritcey, *Langmuir* **2007**, *23*, 2843-2850.

[69] **Synthesis, electron tomography and single-particle optical response of twisted gold nano-bipyramids,** J. R. G. Navarro, D. Manchon, F. Lerouge, E. Cottancin, J. Lermé, V. Bonnet, F. Chaput, A. Mosset, M. Pellarin, S. Parola, *Nanotechnology* **2012**, *23(14)*, 145707-145715.

[70] **Purification of Molecularly Bridged Metal Nanoparticle Arrays by Centrifugation and Size Exclusion Chromatography,** J. P. Novak, C. Nickerson, S. Franzen, D. L. Feldheim, *Anal. Chem.* **2001**, *73*, 5758-5761.

[71] **The plasmon band in noble metal nanoparticles: an introduction to theory and applications,** A. Moores, F. Goettmann, *New J. Chem.* **2006**, *30*, 1121-1132.

[72] **Synthesis, Stability, and Cellular Internalization of Gold Nanoparticles Containing Mixed Peptide-Poly(ethylene glycol) Monolayers,** Y. Liu, M.K. Shipton, J. Ryan, E. D. Kaufman, S. Franzen, D. L. Feldheim, *Anal. Chem.* **2007**, *79*, 2221-2229.

[73] **Gold nanoparticles and functional polymers as efficient nanoplatform towards luminescent probes**, J. R. G. Navarro, F. Lerouge, C. Cepraga, G. Micouin, D. Chateau, A. Favier, M.-T. Charreyre, P.-H. Lanoë, C. Monnereau, N. P. Blanchard, J. Lermé, F. Chaput, A.-M. Gabudean, K. Kamada, C. Andraud, P. L. Baldeck, S. Parola, in preparation.

[74] **Determination of Size and Concentration of Gold Nanoparticles from UV-Vis Spectra,** W. Haiss, N. T. K. Thanh, J. Aveyard, and D. G. Fernig, *Anal. Chem.* **2007**, *79*, 4215-4221.

Chapter IV: Photophysical characterization

IV.1. Introduction

In Chapter II of this thesis, the coupling of two-photon (TP) chromophores onto water-soluble P(NAM-*co*-NAS) copolymer chains was demonstrated. Despite the hydrophobic character of TP chromophores (Ant and DBB), water-soluble chromophore-polymer conjugates were successfully synthesized. Their solubility was dependent on two parameters: the density of chromophores *per* chain and the chosen post-treatment method (AEM capping or hydrolysis).

In Chapter III, it was shown how water-soluble chromophore-polymer conjugates were successfully grafted onto 20 nm AuNP by the ligand exchange approach. It was evidenced by TEM that grafted polymer corona thickness increased with the increasing length of the grafted polymer chain, suggesting an increase of the distance between chromophores and AuNP surface. Chromophore-AuNP distance is considered as one of the main parameters controlling the photophysical response of chromophores in the vicinity of AuNP.

Before evaluating these systems (conjugates and grafted AuNP) in biological media (Chapter V), it was of great value to study their photophysical behaviour in solution.

One important part of this chapter will focus on photophysical properties of chromophore-polymer conjugates (Section IV.4):

- LY-polymer conjugates (capped with AEM) – used as model system.
- Ant-polymer conjugates (AEM or H) – aimed for bioimaging applications.
- DBB-polymer conjugates (AEM and H) – aimed for PDT applications.

The influence of the polymer chain on the photophysical properties of bound chromophores will be discussed; chromophore-polymer conjugates will be compared with free chromophores in solution.

A chromophore linked to a AuNP can have its fluorescence quenched or enhanced, strongly depending on its distance from the AuNP surface. At short distances (directly grafted chromophores), quenching[1] is usually the dominant process (Figure IV. 1 a)). In order to limit quenching and recover the fluorescence, a spacer can be used (Figure IV. 1 b)). Moreover, it was demonstrated that at a longer distance, chromophore fluorescence may even be enhanced *via* interaction with the SPR field of AuNP (Figure IV. 1 c)).

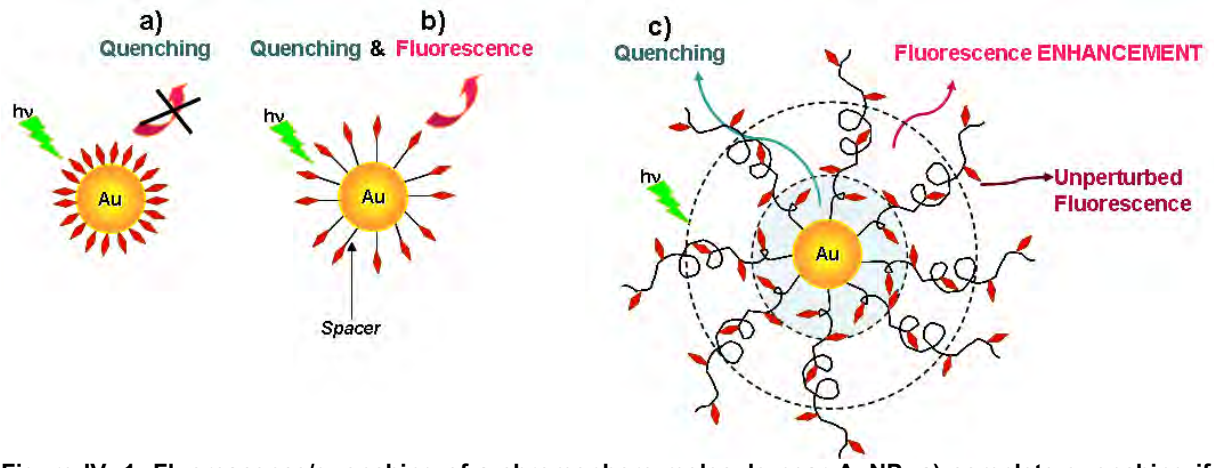

Figure IV. 1: Fluorescence/quenching of a chromophore molecule near AuNP: a) complete quenching if the chromophore is too close to AuNP surface; b) fluorescence can be partly recovered using a spacer; c) fluorescence enhancement at an optimal distance.

Since this work was based on the synthesis of chromophore-polymer conjugates with controlled length and composition, we will study how spherical 20 nm diameter AuNP influence the photophysical properties of such conjugates grafted on their surface. Additionally, the influence of polymer length and architecture will be discussed (Section IV.5).

A short introduction on photophysical properties of a chromophore molecule ((Section IV.2) followed by some insights on its behavior near metallic nanosurfaces (Section IV.3) is given at the beginning of this chapter.

IV.2. Photophysical parameters and methods considered in this chapter

Some basic principles of possible photophysical processes in molecular systems will be addressed below.

IV.2.1. Photophysics of chromophores

A chromophore molecule can undergo several photophysical radiative/non-radiative processes when excited by light (Figure IV. 2), listed below.

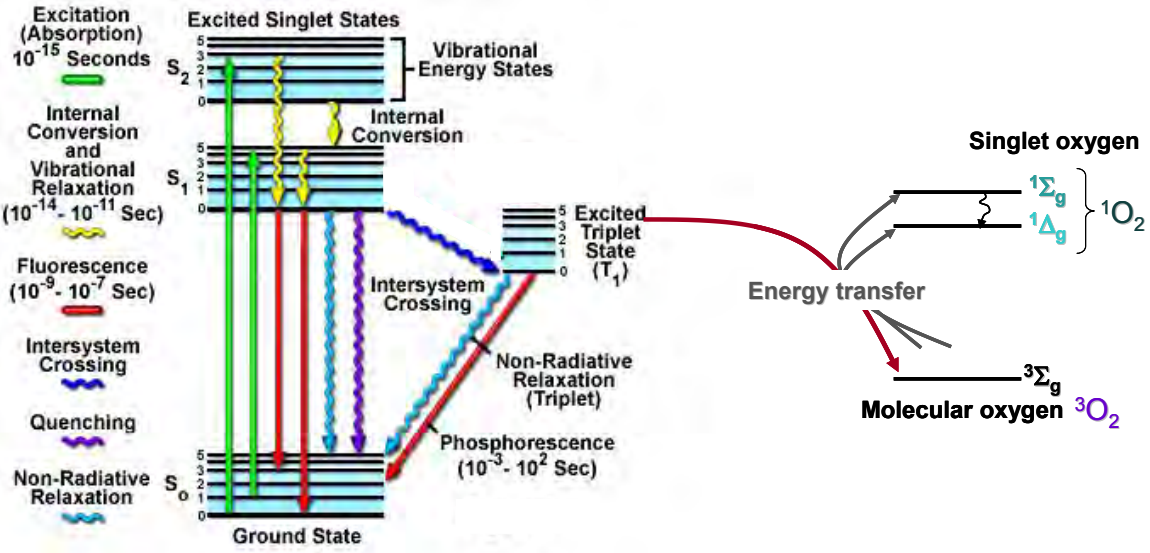

Figure IV. 2: Perrin-Jablonski diagram characterizing possible pathways upon photoactivation of a chromophore.[*]

1) Absorption: after excitation with light, the chromophore transits from its ground state S_0 to its excited state S_n *via* photon absorption, which occurs very fast (in approximately a femtosecond).

After light absorption, several pathways of de-excitation can occur:

2) Internal conversion (IC) is a process that occurs via inter- (mainly) and intramolecular vibrational relaxation (loss of energy) in the absence of light emission. IC generally occurs in a picosecond or less.

3) Fluorescence is a radiative process, emission of a photon, usually occurring from the lowest excited singlet state S_1 back to the ground state S_0. Emission is produced in a wide range of photon energies due to the closely spaced vibrational energy levels of the ground state S_0 (0-5). As a result, fluorescence is normally observed over a large band of wavelengths rather than a sharp band.

4) Quenching of fluorescence is a non-radiative deactivation of fluorescent molecules leading to reduction of fluorescence intensity. It can occur during the excited state lifetime – for example

[*] http://www.olympusfluoview.com/theory/fluoroexciteemit.html

collisional quenching, energy transfer, charge transfer reactions or photochemistry; or can occur due to formation of complexes in the ground state.

5) Intersystem crossing (ISC) is the energy transfer from the excited singlet state to the more stable excited triplet state T_1. ISC is an improbable process, because excited molecules must first undergo spin conversion to produce unpaired electrons, which is normally a forbidden process due to the spin-flip. This process is mediated by spin-orbit coupling. Depending on orbital configuration this becomes more or less probable and is more common in molecules with orbitals with large degree of freedom, oxygen lone-pairs, halogens, metal ion complexes, etc.

6) Phosphorescence corresponds to the radiative de-activation of the excited triplet state. Because it is a spin-forbidden transition, triplet state emission (phosphorescence) is several orders of magnitude slower than fluorescence.

7) Triplet state energy transfer to molecular oxygen (Figure IV. 2) in an important consequence of the high chemical reactivity exhibited by molecules in triplet state. Ground state oxygen molecule (normally a triplet $^3\Sigma_g$), can be excited to a reactive singlet state ($^1\Sigma_g$ or $^1\Delta_g$), by energy transfer, resulting in photobleaching and production of cytotoxic free radicals (e.g. singlet oxygen, $^1O_2$). Chromophores containing heavy atoms, such as halogens and many transition metals, often facilitate the production of singlet oxygen.

From Perrin-Jablonski diagram two radiative processes can be distinguished: fluorescence and phosphorescence, characterized by their respective radiative decay rate constants k_r and k_r^T. The non-radiative processes corresponding to de-excitation pathways from S_1 to S_0 are competing with fluorescence: IC and ISC processes, characterized by the total non-radiative decay rate constant $k_{nr}=k_{IC}+k_{ISC}$.

IV.2.2. Photophysical parameters and methods

The key parameters enabling to properly characterize and quantify photophysical behaviour of chromophores excited by light are defined as follows.

IV.2.2.1. Absorbance parameters

Molar extinction coefficient (ε)

The molar extinction coefficient, ε (in [$cm^{-1}.mol^{-1}.L$]), is an intrinsic property of a molecule, determined by its electronic/chemical structure, and characterizes its capacity to absorb light ($S_0 \rightarrow S_1$) at a given wavelength. It can be deduced from the absorbance of a solution of the sample (A), by using the Beer-Lambert's Law:[2] $A=\varepsilon lc$, with l – the photophysical path length (in [cm]) and c – the sample concentration (in [$mol.L^{-1}$]). It is emphasized that the extinction, or absorbance (as it is measured) probes the ground state configuration of a molecule in an environment.

IV.2.2.2. Fluorescence parameters

Fluorescence quantum yield (ϕ)

The fluorescence quantum yield, ϕ (dimensionless parameter), is the fraction of excited molecules that return from S_1 excited state to S_0 ground state emitting fluorescence photons. It corresponds to the number of emitted photons during the entire duration of the fluorescence decay, reflecting the total number of absorbed photons and can be expressed as in Eq. (1); with k_r / k_{nr} – the ratio of radiative/non-radiative decay rate constants, respectively.

$$\phi = \frac{k_r}{k_r + k_{nr}} \quad (1)$$

Fluorescence quantum yields are generally determined by two methods: direct measurement of absorption and emission, the latter by using an integrating sphere. This is common for solids samples and thin films. For molecules in solution it is more conveniently obtained from a comparative method with respect to a known reference sample, and using a variant of the Stern-Volmer equation – Eq. (2).[3]

$$\phi = \phi_r \times \frac{A_r}{A} \times \frac{F}{F_r} \times \frac{n^2}{n_r^2} \quad (2)$$

A and A_R, F and F_r are the absorbance and fluorescence (area or intensity ratios) of the sample and the reference, respectively; while n/n_r is the ratio of the refractive indexes of the respective solvents.

Brightness

The brightness of a fluorescent species (in [$cm^{-1}.mol^{-1}.L$]) reflects its luminescence efficacy, and depends on both absorption and emission, Eq. (3). It is widely employed in biology to compare various chromophores, and can be tuned either by increasing the molar absorption of a molecule, ε, and/or its fluorescence quantum yield, ϕ.

$$Brightness = \varepsilon \times \phi \quad (3)$$

Fluorescence lifetime (τ)

Fluorescence decay time[4] $\tau(t)$, in [ns], is one of the most important characteristics of a fluorescent molecule since it defines the time span of observation of the fluorescence dynamic phenomenon. Also it is a direct measure of the excited state properties as methods based on fluorescence quantum yield can be hampered by parasitic effects such as local solvent effects (inducing Stoke's shift) and energy exchange effects. Fluorescence lifetime "τ" is conventionally defined as the time needed for the concentration of excited molecules to decrease to "1/e". "τ" depends on the radiative (k_r) and the non-radiative (k_{nr}) decay rate constants, Eq. (4), thus can be directly related to fluorescence quantum yield, Eq. (5).

$$\tau = \frac{1}{k_r + k_{nr}} \quad (4)$$

$$\phi = k_r \times \tau \quad (5)$$

Fluorescence anisotropy (r)

Fluorescence anisotropy (a dimensionless parameter) characterizes the dynamic behaviour of a chromophore using polarized excitation. It provides information about the rotational mobility originating from Brownian motion, molecular binding, macromolecular association, local viscosity changes.[5]

When polarized light is applied to a group of randomly oriented chromophores, those with transition dipole moments aligned parallel to the polarization plane of the light will be preferentially excited, while those with perpendicular absorption will not be excited at all. The excited chromophores will reorient before re-emitting fluorescence. Then the degree of de-polarization of the emitted light will be reduced depending on the time-scale of the reorientation. Thus, anisotropy measures the degree of depolarization and is usually defined as in Eq. (6).

$$r = \frac{I_{II} - GI_{\perp}}{I_{II} + 2GI_{\perp}} \quad (6)$$

where I_{II} and $I_{\perp}$ are the fluorescence intensities according to parallel and perpendicular orientations to that of the excitation light, and G is a calibration factor that accounts for the different detection sensitivity for lights of different polarizations of the detector and spectral arrangement (usually a grating).

F. Perrin related the observed anisotropy to the excited state lifetime and the rotational diffusion of a chromophore, Eq. (7).[6]

$$r = \frac{r_0}{1 + \frac{\tau}{\theta}} \quad (7)$$

with r_0 – the initial or intrinsic anisotropy, τ - the fluorescence lifetime and θ - the rotational correlation time. The rotational correlation time θ is directly related to the diffusion of molecules, hence to their hydrodynamic radius, which can be expressed for a spherical model *via* Stokes-Einstein-Debye relation ($\theta \propto V_h$), with V_h the hydrodynamic volume.

In this work measurements of time-resolved anisotropy, Eq. (8), will be performed, giving access to $r_\infty(t\rightarrow\infty)$ – the residual anisotropy characterizing the restriction of chromophore rotation, $r_0(t=0)$ – the intrinsic anisotropy, and θ – the rotational correlation time.

$$r(t) = r_\infty + r_0 \times \exp(-\frac{t}{\theta}) \quad (8)$$

IV.2.2.3. Singlet oxygen production

Principle

Excited triplet states of organic molecules have much longer lifetimes compared to excited singlet states, and thus are more susceptible to quenching by diffusion/collisions, and by collisions with paramagnetic molecules such as oxygen. Hence, phosphorescence is much more difficult to be detected especially at room temperature.

A deactivation pathway of the excited triplet state (T_1) consists in its energy transfer to molecular oxygen ($^3O_2$), called photosensitization, resulting in the recovery of the chromophore (also referred as photosensitizer or PS) in its ground state (S_0) and the production of singlet oxygen ($^1O_2$) (Figure IV. 2, (9)). Oxygen has two single excited states, $^1\Sigma_g$ and $^1\Delta_g$, (Figure IV. 3), with respectively 95 and 158 kJ.mol^{-1} above its ground triplet state, $^3\Sigma_g$.[7]

$$\mathbf{T_1 + {}^3O_2 \rightarrow S_0 + {}^1O_2} \text{ (9)}$$

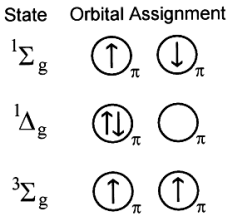

Figure IV. 3: Representations of molecular oxygen lowest singlet and triplet states.[7]

The electronic configuration of $^1\Sigma_g$, the short-lived excited state, is very similar to that of the ground state, except the fact that the last two electrons have antiparallel spins while these electrons in the ground state have parallel spins. The other excited singlet state $^1\Delta_g$ is a metastable state often referred as singlet oxygen ($^1O_2$), and is more important than $^1\Sigma_g$ due to its longer lifetime (45 min *vs.* 7–12 s for $^1\Sigma_g$).[8]

The ability of a chromophore (photosensitizer) to produce singlet oxygen is measured by its quantum yield Φ_Δ which depends on the triplet state formation quantum yield (ϕ_T) and on the efficiency of energy transfer to molecular oxygen, Eq. (10), with f_{ET} – the energy transfer efficiency factor.

$$\Phi_\Delta = \phi_T \times f_{ET} \text{ (10)}$$

Measurement of singlet oxygen production (Φ_Δ)

Φ_Δ (dimensionless parameter) of $^1O_2$ is measured by detecting its characteristic luminescence at 1270 nm by comparison with the luminescence of a standard photosensitizer in the same solvent Eq. (11).[8] This approach has been firmly established since the middle of the 1980s. However, $^1O_2$ luminescence remains difficult to detect, especially in protic solvents where it undergoes strong quenching, which explains why other alternative methods have also been developed.[9]

$$\Phi_{\Delta} = \Phi_{\Delta\_r} \times \frac{A_r}{A} \times \frac{L}{L_r} \quad (11)$$

with $\Phi_{\Delta\_r}/\Phi_{\Delta}$ – is the ratio of the singlet oxygen luminescence quantum yield of the reference and the sample, respectively; A_r/A – is the ratio of absorbance at the excitation wavelength and L_r/L – the ratio of the luminescence (intensity or area) .

IV.2.2.4. Two-photon absorption (TPA)

Principle

Compared to one photon absorption which depends linearly on the excitation intensity, the phenomenon of two-photon absorption (TPA) involves the simultaneous absorption of two photons, (Figure IV. 4), and increases with the square of the intensity of excitation (the 2nd term of the Eq. (12)). This is the reason why TPA induced processes need intense laser beams to be observed, especially focused pulsed lasers, generating high instantaneous photon densities.

In the simple case of a material containing a concentration *N* (in cm^{-3}) of absorbing molecules, under steady state conditions, the linear and two-photon absorption processes are given by Eq. (12):

$$\frac{dI}{dz} = -N\varepsilon I - N\sigma_{TPA} I^2 \quad (12)$$

where 'I' is the photon flux (in [photons.cm^{-2}.s^{-1})]), z (in [cm]) – the propagating distance, 'ε' is the one-photon absorption cross section (in [cm^2]) and 'σ_{TPA}' is the two-photon absorption cross section (in [cm^4.s]).

σ_{TPA} is the key photophysical parameter describing the nonlinear TPA, which becomes more probable with highly energetic excitations.

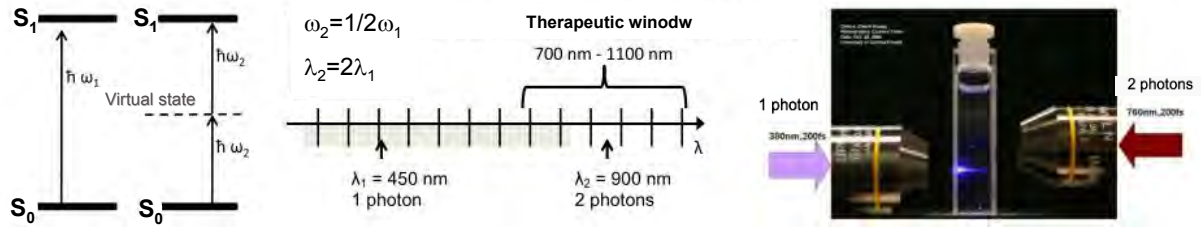

Figure IV. 4: Comparing one-photon absorption with two-photon absorption (left); TPA → excitation in the Near IR region, therapeutic window (middle); high spatial resolution of excitation due to increased intensity of light and no linear TPA process (right).*

TPA was first analyzed theoretically in the 1930s by Maria Göppert-Mayer.[10] The unit for the TPA cross section is often given as cm^4.s/(photon molecule), and, for practical reasons, 10^{-50}.cm^4.s has been adopted as a unit of the cross section, called a Göppert-Mayer (1GM = 10^{-50}.cm^4.s).

* Information from T.Gallavardin, PhD – http://belfield.cos.ucf.edu/

Measurement of TPA cross section (σ_{TPA})

Up to date, two different methods are being used to measure σ_{TPA}: the Z-scan technique[11] and Two Photon Excited Fluorescence[12] (TPEF). In this work TPEF was used to determine σ_{TPA}.

TPEF experiments require the use of a pulsed femtosecond laser and are performed on rather dilute solutions (~10^{-4} mol.L^{-1}). The intensity of the TPEF signal increases with the square of the laser intensity and is dependent on σ_{TPA}, Eq. (13).

$$I_{TPEF} = \sigma_{TPA} \times I_{laser}^2 \times \phi \times c \times K \quad (13)$$

where I_{TPEF} is the fluorescence intensity, I_{laser} – the laser intensity (in [photons.cm^{-2}.s^{-1})]), c – the concentration of the chromophore (in [mol.L^{-1}]), K –experimental constant (dimensionless).

σ_{TPA} values are deduced using the comparative method, where the TPA of the sample is compared with the TPA of a known reference compound, Eq. (14), 'r' stands for the reference sample.

$$\sigma_{TPA} = \sigma_{TPA\_r} \times \frac{\phi_r}{\phi} \times \frac{I_{TPFE}}{I_{TPFE\_r}} \times \frac{c_r}{c} \quad (14)$$

IV.3. Scientific context: chromophores near nanostructured metals

Before discussing the changes in chromophore photophysical properties near metallic nanoparticles it is necessary to understand the specific interaction of nanostructured metals with electromagnetic radiation and light, called the Surface Plasmon Resonance (SPR).

IV.3.1. Surface Plasmon Resonance (SPR)

When the wavelength of light is much larger than the size of a metallic nanoparticle, the electronic cloud of the particle is polarized and can create resonance conditions. When the frequency of light matches the natural frequency of metal surface electrons, resonance conditions are reached resulting in a strong oscillation of free electrons (Figure IV. 5). This phenomenon is called Surface Plasmon Resonance and was described in terms of excited 'evanescent' electromagnetic waves at the surface of the metal.[13] The amplitude of the evanescent field decreases exponentially with the distance from the surface, and its intensity depends on the size, the shape, and the dielectric constants of both the metal and the surrounding material.[14]

Experimentally SPR band can be observed by UV-Vis spectroscopy measurements through its extinction spectrum (absorption and scattering being the two contributing mechanisms).

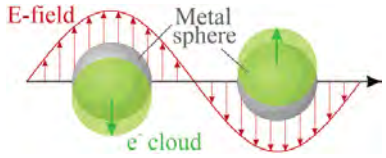

Figure IV. 5: Schematic of plasmon oscillation for a sphere.[15]

Absorption and scattering contributions

The extinction cross section (C_{ext}) characterizing SPR of metal particles can be expressed by a combination of both absorption (C_{abs}) and scattering (C_{sca}) factors. For spherical nanoparticles with sizes comparable to the incident wavelength of light, C_{ext} can be expressed as in Eq. (15):

$$C_{ext} = C_{abs} + C_{sca} = k\,\mathrm{Im}(\alpha) + \frac{k^4}{6\pi}|\alpha|^2 \quad (15)$$

where $k = 2\pi\frac{n_1}{\lambda_0}$ and is the wave vector of the incident light in medium with refractive index n_1 and α is the polarizability of the sphere with radius r: $\alpha = 4\pi r^3 \frac{\varepsilon_p - \varepsilon_m}{\varepsilon_p + 2\varepsilon_m}$, where ε_p is the complex dielectric functions of the particle, ε_m – the dielectric constant of the medium, and Im(α) is the imaginary part of the expression containing the complex function.

From Eq. (15): $C_{abs} \propto r^3$ and $C_{sca} \propto r^6$. This observation is important, as it was demonstrated that the behavior of chromophores next to metallic nanoparticles is mainly underpinned by the scattering component, suggesting that the size and shape of metallic nanoparticles are critical parameters enabling to tune photophysical properties near their surfaces.[16]

IV.3.2. Influence of metal SPR on photophysical properties of a chromophore

It is known that the presence of nearby metallic nanoparticles can alter photophysical behavior of chromophores after light absorption. Remarkably, the interaction between free electrons in the metal and the chromophores can modify the radiative decay rate, or amplify the excitation rate.

Several phenomena are likely to occur near metallic nanoparticles:

- *Quenching*
- *Enhancement*

Up to date, the occurrence of either one of these phenomena seems to strongly depend on the distance between the chromophore and the nanoparticle, as illustrated in Figure IV. 6. Fluorescence emission near metallic nanoparticles can either be quenched, enhanced or unperturbed depending mainly on the distance (but also other parameters as orientation of transition dipole) between a chromophore and the nanoparticle.[17]

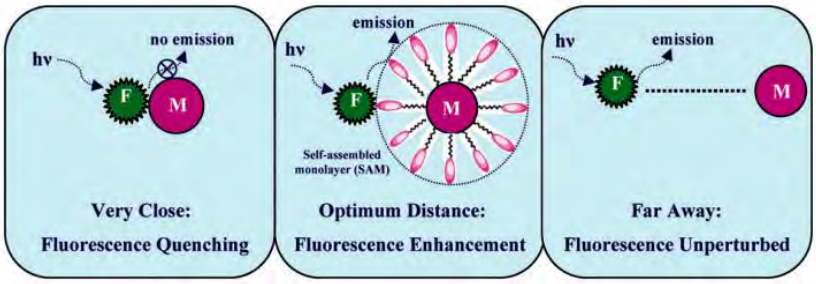

Figure IV. 6: Schematic presentation showing the effect of the distance between a metallic nanoparticle and a chromophore on its fluorescence emission. [17]

IV.3.2.1. Quenching

Excited chromophores can be quenched by energy transfer and/*or* electron transfer to the metal surface.[17]

- The electron transfer mechanism characterizes mainly nanoparticles with sizes < 5 nm, as in this size range, nanoparticles exhibit a very weak SPR band in the visible region.
- Energy transfer can occur for larger nanoparticles, from the excited state of the chromophore (donor) to the metallic nanoparticle (acceptor). This phenomenon occurs if there is overlap between the emission spectrum of the donor and the absorption spectrum of the acceptor, and can be understood in terms of FRET (Förster/Fluorescence Resonance Energy Transfer), whose transfer constant varies as $1/d^6$ (d – the distance between donor and acceptor species).

  In the context of metal resonance energy transfer the interaction of chromophores with metal surface is also distance-dependent. Compared to FRET, theoretical and experimental studies indicate that near metallic nanoparticles, metal resonance energy transfer rate varies as $1/d^{\delta}$

with δ=3-4 at intermediate distances, while recovering the Förster $1/d^6$ dependence at large separations,[18] (with d < 5 nm).

IV.3.2.2. Enhancement

Enhancement phenomenon (or metal-enhancement) is the result of SPR interaction with the chromophore ground state (absorption) or its excited state (emission) (Figure IV. 7, Figure IV. 8), affecting one of the previously described photophysical phenomena: absorption ($S_0 \rightarrow S_1$), fluorescence ($S_1 \rightarrow S_0$), phosphorescence ($T_1 \rightarrow S_0$), and/or triplet state energy transfer to molecular oxygen ($T_1 \rightarrow {}^3O_2$) (Figure IV. 8).

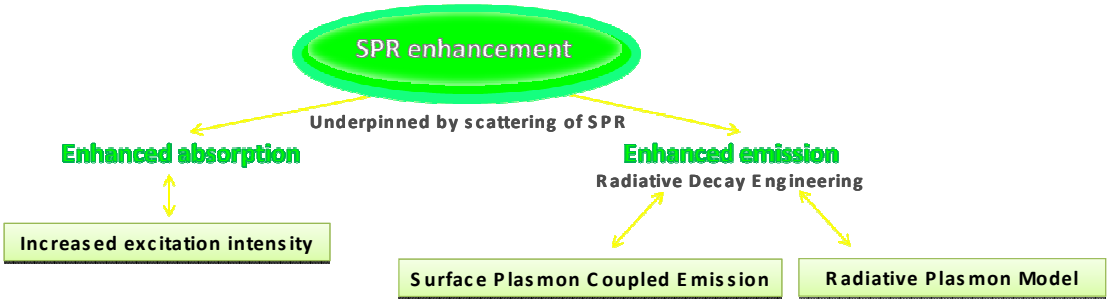

Figure IV. 7: Possible mechanisms of SPR enhanced photophysical properties of chromophores.

Extensive work on near-field interaction between a fluorescent chromophores and metals were carried out by Lakowicz and Geddes.[19] They studied metal-enhanced-fluorescence (MEF) phenomenon and describe it from the point of view of its possible mechanisms.

Besides MEF, Geddes also showed that radiative metal-enhanced-phosphorescence (MEP),[20] observed at low temperature, can occur in the same system. On the other hand, metal-enhanced-singlet oxygen production (ME^1O_2) can also occur;[21] it is a non-radiative process of the excited triplet state that competes with MEP, both depending on changes in the dynamics of the excited triplet state near metallic nanoparticles.[22]

Figure IV. 8 illustrates these metal enhancement phenomena using the example of Ag nanoislands studied by Geddes and coworkers. [23]

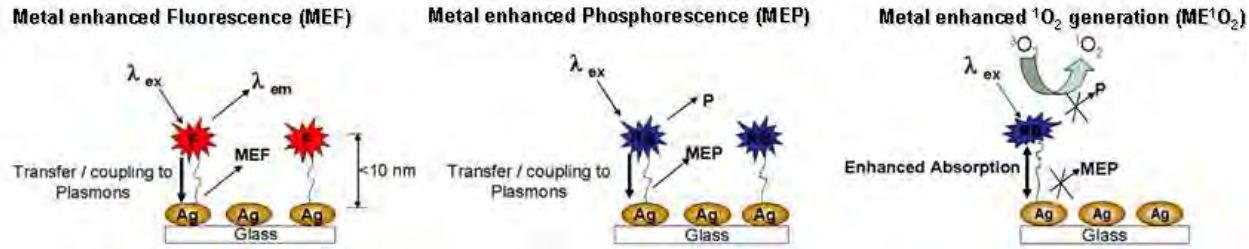

Figure IV. 8: Graphical representations of metal enhanced fluorescence; metal enhanced phosphorescence, and metal enhanced generation of singlet oxygen. [23]

Enhanced absorption

Enhanced absorption results from the interaction of the ground state of the chromophore with SPR; the increased local electric field induces an enhancement in the excitation rate, thus increasing the amount of light absorbed by the chromophore.

In order to occur, resonance (spectral overlap) between chromophore absorption and SPR is required.

The increased electric field, responsible for enhanced absorption, can be simulated by theoretical models. Its distribution depends strongly on the size and the shape of the nanoparticle. Novotny and coworkers[24] showed that there exists an optimum distance (~15 nm) from the surface of gold nanoparticles where a maximum enhancement is achieved. They used the multiple-multipole method (MMP) to calculate the emission of a chromophore considered as a single dipole placed at variable distances from the surface of spherical gold nanoparticles.[25] In another study, from MMP it was demonstrated that, in the case of small spherical gold nanoparticles (d < 30 nm), the non-radiative component will dominate the molecular dipole decay, due to increased absorption over negligible scattering, thus impeding the enhancement.[26]

Enhanced emission

Enhanced emission results from the interaction of the chromophore in its excited state with SPR.

Up to date, two models describing the enhanced emission of chromophores near metals have been proposed:

- *Surface Plasmon Coupled Emission* (SPCE), resulting from the interaction between chromophore emission and SPR. SPCE generates an increased radiative decay rate constant leading to lower fluorescence lifetime, but higher fluorescence quantum yield.[19]
- *Radiative Plasmon Model* (RPM) is defined as the capacity of plasmons to radiate the non-radiative energy transferred from excited state of the chromophore to the metal (mirror dipole effect). [27] [28]

Due to the expected and observed changes in radiative/non-radiative decays, these phenomena are often addressed in the framework of Radiative Decay Engineering.

Enhanced two-photon absorption near metallic nanoparticles

Although less examined, non-linear photophysical properties of chromophores near metallic nanoparticles can also be enhanced mainly by absorption enhancement *via* SPR. Different groups have shown two-photon induced fluorescence enhancement by factors of 90, 80, 480 or 40 with chromohores near thin metal films, silver islands, aggregated fractal metal clusters or nanoparticles, respectively.[29] Enhancement in two-photon absorption was mainly evidenced *via* the increased T¨PA cross section, σ_{TPA}, measured by Z-scan technique. It should be mentioned that optimum enhancement conditions under two-photon excitation might not follow the same distance-dependence as under one-photon excitation. In a recent article Murphy's group reported the highest TPA enhancement at 3 nm distance from the surface of Au nanorods.[29d)]

It has been difficult to experimentally distinguish among various enhancement mechanisms (plasmon enhanced absorption *vs.* plasmon enhanced emission), especially for samples in solution. In order to better understand parameters controlling metal-enhanced photophysics of chromophores, they have been studies focusing on quantifying the enhancement factors, trying to isolate each phenomenon at a time.[30]

To conclude, it was briefly summarized how luminescence properties of a chromophore can be altered by the presence of metallic nanoparticles. They can either be quenched at short distances (~0-5 nm), or enhanced with variations in the incident light (enhanced absorption: ~0-15nm) and/or changes in the radiative decay rate (enhanced emission: ~0-20nm).

- While absorption enhancement (modifying the excitation rate) can act on all (radiative and non-radiative) photophysical phenomena (fluorescence, phosphorescence, and singlet oxygen production), emission enhancement acts only on radiative photophysical processes (fluorescence and phosphorescence).
- It is believed that enhancement arises from the scattering component of nanoparticle extinction (SPR), the absorption component being responsible for quenching processes.
- Resonance between chromophore emission/absorption bands and SPR band is required in order to reach optimized enhancement.
- As mentioned above, all photophysical phenomena seem to strongly depend on the chromophore-nanoparticle distance. However, other factors such as chromophore orientation with respect to nanoparticle surfaces, which can significantly change its photophysical luminescence.
- Also non-linear photophysical properties of chromophores have been reported to be enhanced by SPR absorption enhancement.

Taking into account the scientific context presented above, the following two parts of this chapter will focus on photophysical characterization of chromophore-polymer conjugates, before and after grafting them onto ~20 nm gold nanoparticles (AuNP).

IV.4. Chromophore-polymer conjugates: the influence of the polymer chain on the photophysical properties of chromophores

This part describes and analyses the influence of the polymer chain on the photophysical properties of bound chromophores. Three types of polymer conjugates reported in Chapter II will be investigated: LY conjugates – used as a model system, and TP conjugates: Ant and DBB conjugates.
Fluorescence properties will be described comparing the chromophore-polymer conjugates with the corresponding free chromophores in solution:

- Absorption / Emission spectra
- Molar extinction coefficient
- Fluorescence quantum yield
- Fluorescence lifetime
- Fluorescence anisotropy
- Brightness
- Two photon absorption properties (for TP conjugates)
- Production of singlet oxygen (for DBB conjugates)

IV.4.1. LY-polymer conjugates

For simplicity, LY cadaverine will be marked as 'LY'. LY polymer-conjugates were synthesized as a model system (and a cheaper one) for the grafting studies onto AuNP. Their photophysical properties will be described below, and compared with those obtained by Paula Relogio in a previous PhD thesis.[31]

IV.4.1.1. Background: brief review on photophysical properties of LY chromophores

Photophysical properties of Lucifer Yellow chromophore family have been previously determined in aqueous and in polar organic solvents.[32] It is known that Lucifer Yellow is rather insensitive to pH, exhibiting high fluorescence quantum yields in acidic, neutral or basic aqueous solutions (pH = 2 to pH = 10). Previously, P. Relogio checked its stability with pH using Biotin-LY.[31]
In a relatively recent article, the photophysical properties of a Lucifer Yellow derivative, Lucifer Yellow ethylenediamine (LYen), have been thoroughly investigated.[33] In this study, Fürstenberg *et al.* reported the photophysical properties of LYen in different solvents (Table IV. 1), and evidenced the quenching of LYen in water induced by the excited-state proton transfer (ESPT) of the chromophore to water molecules, leading to lower fluorescence quantum yield and shorter lifetime, compared to polar organic solvents. On the other hand, ε and Stokes shifts are larger in water (Table IV. 1).

Table IV. 1: Photophysical properties of LYen in different solvents.[33]

Solvent	Max abs/em (nm)	ε_{400} ($cm^{-1}.M^{-1}$)	ε_{430} ($cm^{-1}.M^{-1}$)*	ϕ	τ (ns)
H_2O	428 / 530	7 900	11 600	0.27	5.7
D_2O	428 / 528	/	/	0.53	11.5
DMSO	439 / 518	4 700	6 900	0.68	10.6
DMF	435 / 510	5 700	8 400	0.70	11.3

* Calclated from spectra in ref.33.

It is important to take into consideration these findings, before investigating the photophysical properties of LY- polymer conjugates in water.

IV.4.1.2. Photophysical properties of LY- polymer conjugates

LY conjugates are negatively charged thanks to the two sulfonate groups from the chromophore, the polymer backbone is neutral (as capped with AEM), (Figure IV. 9).

a) **b)**

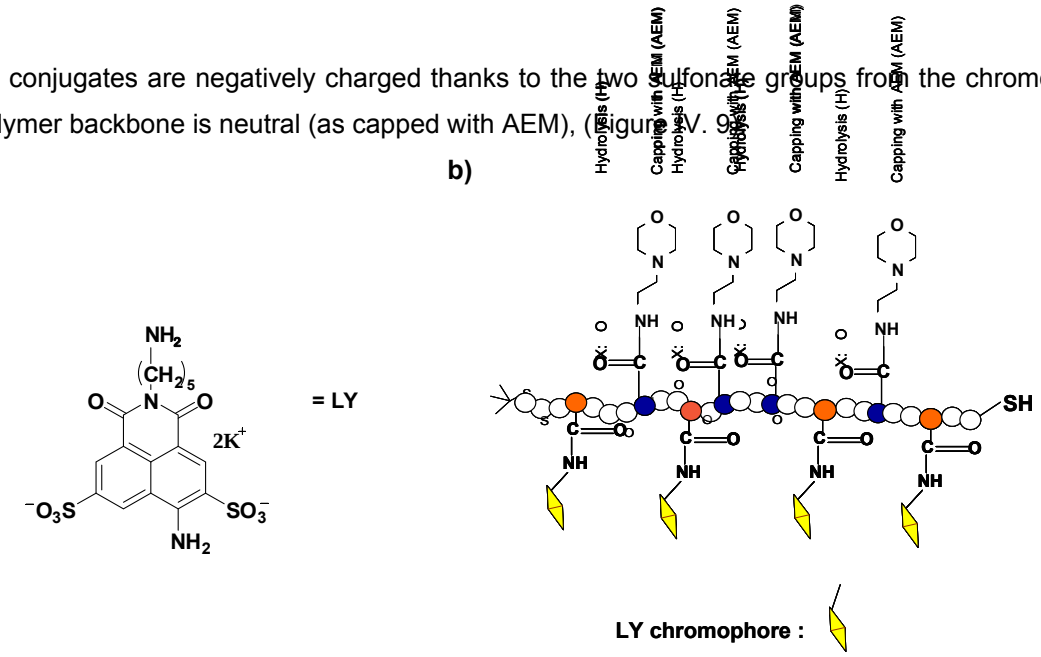

Figure IV. 9: a) Structures of Lucifer Yellow Cadaverine chromophore (LY). b) Schematic representation of LY- polymer conjugates.

Table IV. 2 summarizes the physicochemical properties of LY conjugates. The five different conjugates differ from each other by the length of the polymer chain (from 2 000 to 35 000 $g.mol^{-1}$), the number of bound chromophores *per* chair (Nc = 1 to 5), thus the density of chromophores (expressed as the average distance between two neighbouring LY chromophores, varying from 16 to 52, Table IV. 2), and by the polymer architecture (random or block copolymer).

Table IV. 2: Physicochemical properties of LY-polymer conjugates.

LY conjugates	Nc	Post-treatment	M_n (P(NAM-*co*-NAS) before coupling (g.mol^{-1})	M_n after coupling (g.mol^{-1})	Average LY-LY distance (monomer units)
LY2KDa	1.1	AEM	2 200	2 700	-
LY9KDa	3.3		7 900	9 500	16
LY15KDa	3.8		12 900	15 000	22
LY37KDa	4.4		34 600	37 700	52
LY32KDa(B)*	5.2		Block1: P(NAM-*co*-NAS)_21 600 g.mol^{-1} Block2: PNAM_7 800 g.mol^{-1}	32 400	27

*B=block copolymer backbone

Photophysical properties of LY chromophore before and after coupling on the polymer chain are presented in Table IV. 3 and will be discussed below.

Table IV. 3: Photophysical properties of LY- polymer conjugates in water.

Conjugate *vs.* free chromophore	ε (cm^{-1}.M^{-1})$_{430nm}$*		λ abs /em (nm)	ϕ* in water [b]	Brightness (cm^{-1}.M^{-1})	$\langle\tau\rangle$ [c,**]
	per conj	per chromophore				
Free LY Cadaverine	-	11 600[a]	427 / 537	0.33	3 800	6.1
LY2KDa	12 800	11 600	429 / 537	0.29	3 700	n.d.
LY9KDa	29 900	9 100	429 / 532	0.24	7 200	7.6
LY15KDa	42 600	11 200	430 / 534	0.26	11 100	7.5
LY37KDa	46 600	10 600	429 / 535	0.33	14 900	n.d.
LY32KDa(B)	55 000	10 600	429 / 534	0.27	13 400	8.2

* Experimental estimated errors: $\varepsilon \sim \pm$ 10-15%; $\phi \sim \pm$ 10-15%; $\tau <$ 5%.

[a] From Paula's PhD Thesis[31]

[b] Relative to ϕ(Coumarin 153 in MeOH)=45%

[c] $\langle\tau\rangle = \dfrac{\sum_i A_i \tau_i^2}{\sum_i A_i \tau_i}$ = average lifetime

[d] n.d.=not determined

IV.4.1.3. Steady state fluorescence analyses

Insignificant changes are observed in absorption / emission spectra of LY-polymer conjugates (Figure IV. 10). Apparently, coupling to the polymer does not affect the ground or excited states of bound LY chromophore. A systematic slight red-shift (in absorption) and blue-shift (in emission), ~2-3 nm (red curves), could be noticed for conjugates compared to free LY chromophore. It might arise from small modifications in polarity due to the polymer chain, which can possibly limit the extent of hydrogen bonding with water molecules (inducing a blue-shift[34]). A similar tendency was found by Paula Relogio.[31]

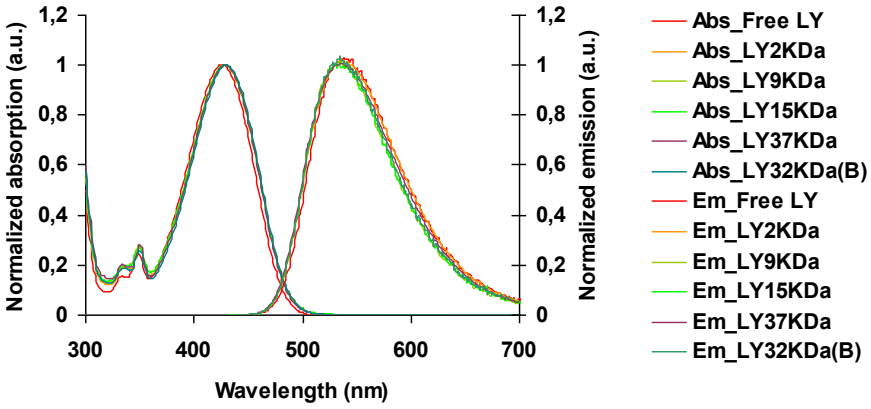

Figure IV. 10: Absorption / emission spectra of LY- polymer conjugates in water (λ_{ex}=430nm).

The absorption and emission processes could be quantified through the determination of ε and ϕ values, respectively (Table IV. 3). Molar extinction coefficients (ε) are of the same order of magnitude (considering the experimental error ±15%). These results are consistent with previous findings showing little influence of the bounding on the photophysical properties of LY chromophore.[31] Moreover, ε values are in good agreement with previously reported values for this class of chromophores (Table IV. 1).*

As previously reported by Paula Relogio,[31] a higher LY density (shorter LY-LY average distance), results in a decrease in the fluorescence quantum yield (Table IV. 2). Stronger chromophore-chromophore interactions would *a priori* favor additional nonradiative routes. On the other hand, when considering the increasing density of LY chromophores along the chain (LY chromophores coming closer to each other), repulsive interactions of negatively charged LY chromophores would allow a more extended conformation of the polymer chain, resulting in a higher extent of LY chromophore exposure to water (leading to enhanced quenching by ESPT, see above). Both these phenomena, the possible formation of hydrogen bonding in water and ESPT with water molecules,[33] lead to a decrease in ϕ.

Regardless of the (small) changes in ϕ (Figure IV. 11 a)) with the increasing LY-LY average distance on the chain, the overall brightness of LY conjugates (Table IV. 3) increases with the number of LY *per* chain (Figure IV. 11 b)), justifying the interest of LY-polymer conjugates for highly sensitive imaging applications.

* In Table IV. 1, ε(LYEn) is 7 900 $cm^{-1}.M^{-1}$ at 400 nm in water. Calculation at 430 nm gives a corresponding value of 11 600 $cm^{-1}.M^{-1}$.

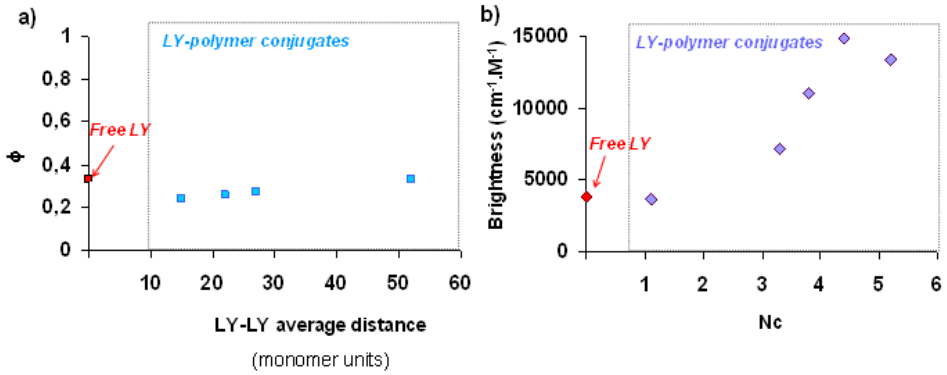

Figure IV. 11: a) Fluorescence quantum yield as a function of LY-LY average distance; b) Fluorescence brightness as a function of Nc.

IV.4.1.4. Time-resolved fluorescence analyses

Fluorescence decays were measured for 3 LY conjugates and compared to that of free LY chromophore (Figure IV. 12, Table IV. 4).

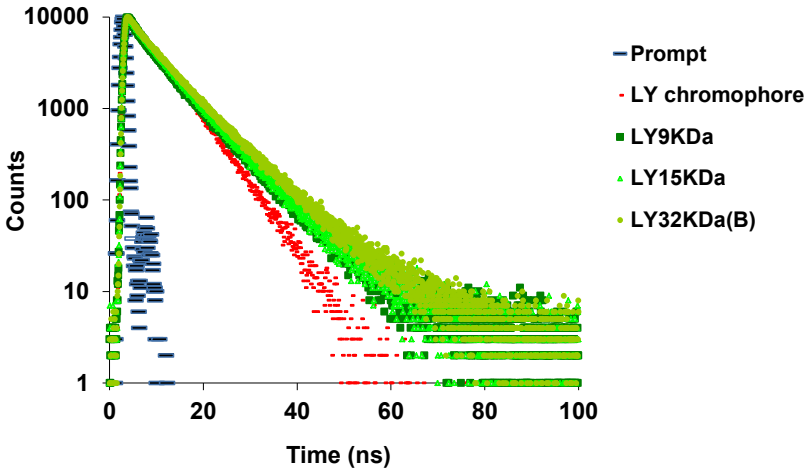

Figure IV. 12: Fluorescence decay of LY conjugates vs. free LY in water (λ_{ex}=440nm; λ_{em}=530nm).

Table IV. 4: Fluorescence decay parameters for LY-polymer conjugates vs. free LY chromophore in water.

Sample	Mono-exponential model		Bi-exponential model [a]				$\langle\tau\rangle$ [b] (ns)	χ^2
	τ (ns)	A (%)	τ_1 (ns)	A1 (%)	τ_2 (ns)	A2 (%)		
Free LY	6.1	100%	-	-	-	-		1.24
LY9KDa	-	-	2.9	17	7.9	83	7.6	1.17
LY15KDa	-	-	4.1	22	8.0	78	7.5	1.19
LY32KDa(B)	-	-	4.0	21	8.7	79	8.2	1.20

[a]) On purpose, none of the components was fixed at 6.1 ns, because the fit was less accurate (χ^2 >1.2).

[b] $\langle \tau \rangle = \frac{\sum_i A_i \tau_i^2}{\sum_i A_i \tau_i}$ = average lifetime.

The influence of the polymer is illustrated in Figure IV. 12: compared to the mono-exponential fluoresce decay of free LY chromophore, LY-polymer conjugates present a bi-exponential profile composed of a fast component – attributed to LY more exposed to the solvent (water), and a slow component – attributed to LY "protected" by a less polar polymer environment (Table IV. 4).
As reported by Paula Relogio,[31] even if the average fluorescence lifetime $<\tau>$ of conjugates is longer compared to free LY, lifetime decreases when LY-LY average distance decreases, corroborating with the observed changes in fluorescence quantum yields ($\phi \propto \tau$).
Such a multi-exponential fluorescence decay, observed after coupling of the chromophore to a polymer chain, was previously reported with HPMA-camptothecin polymer conjugates (HPMA=*N*-(2-hydroxypropyl) methacrylamide), which was attributed to changes in polymer conjugate conformation after coupling with a fluorescent drug.[35]

In order to better understand the impact of the polymer chain on photophysical properties of bound LY, radiative (k_r) and nonradiative (k_{nr}) decay rate constants were calculated for 3 LY conjugates using Eq. (4) and Eq. (5) (Table IV. 5). The results are in good agreement with Paula Relogio's earlier findings who noted: i) a decrease in radiative (k_r) and nonradiative (k_{nr}) decay rate constants after LY coupling to the polymer chain, due to changes in the local environment of the chromophore; ii) a decrease in nonradiative decay rate constants with increasing LY-LY average distance: less quenching, thus higher fluorescence quantum yields and longer corresponding lifetimes.

Table IV. 5: Fluorescence decay parameters for LY-polymer conjugates vs. free LY chromophore in water.

Sample	ϕ	$<\tau>$ (ns)	k_r x 10^8 (s^{-1}) [a]	k_{nr} x 10^8 (s^{-1}) [b]	LY-LY distance (monomer units)
Free LY	0.33	6.1	0.54	1.10	-
LY9KDa	0.24	7.6	0.32	1.01	15
LY15KDa	0.26	7.5	0.34	0.99	21
LY32KDa(B)	0.27	8.2	0.33	0.89	26

a) $k_r = \frac{\phi}{<\tau>}$

b) $k_{nr} = \frac{1}{<\tau>} - k_r$

Note: Although weak, two-photon properties of LY chromophore were determined here and corresponded with values previously reported in literature[36] (Appendix IV.1).

IV.4.1.5. Conclusion on LY conjugates

In conclusion, the influence of the polymer chain on photophysical properties of LY conjugates can mainly be attributed to slight changes in the local environment of bound LY chromophores.
While absorption / emission spectra do not change significantly for LY bound chromophores, fluorescence quantum yields and lifetimes generally decreased slightly with increasing LY density along the chain.

Since various LY-polymer conjugates studied here exhibit similar photophysical properties, it will be possible to study them comparatively after their grafting onto AuNP, in order to highlight the existing interactions between bound LY chromophores and spherical AuNP.

VI.4.2. Two-photon chromophore-polymer conjugates

TP polymer conjugates synthesized in Chapter II, bearing Ant or DBB chromophores along the chain (Figure IV. 13), have been characterized with respect to their one-photon and two-photon photophysical properties.

Unlike LY chromophores, TP chromophores are not soluble in water[37] and lead to the production of amphiphilic TP polymer conjugates soluble in organic and/or aqueous solvents. We expect thus a different behavior in water compared to LY-polymer conjugates.

In the following section, due to similarities in their photophysical behavior, Ant and DBB conjugates will be discussed in parallel.

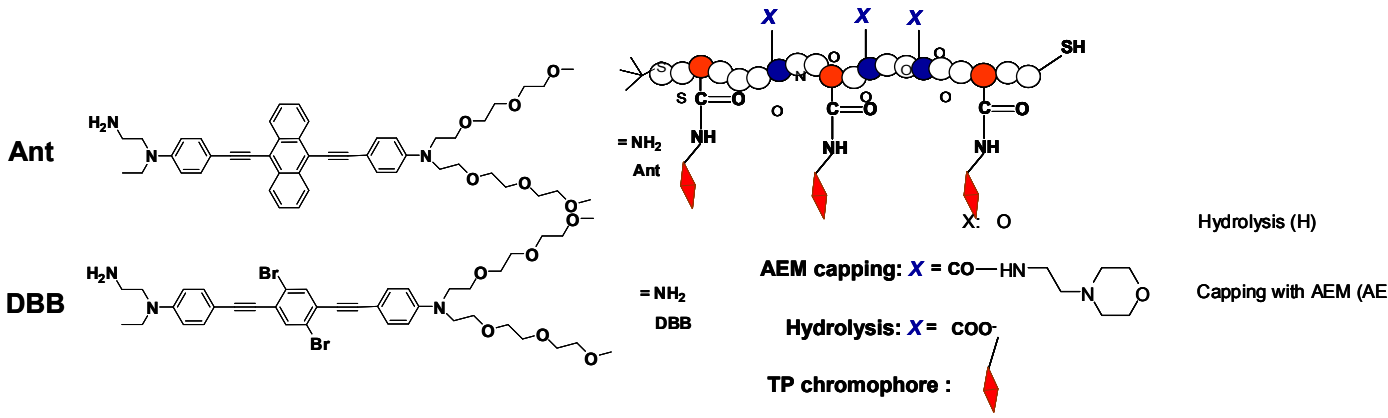

Figure IV. 13: Structure of Ant- and DBB-polymer chromophores, and schematic representation of corresponding TP-polymer conjugates.

Ant conjugates

Physicochemical properties of Ant-conjugates are reported in Table IV. 6. It is worth mentioning that all Ant-polymer conjugates have all the same length (as the same copolymer backbone was used for chromophore coupling), but carry different numbers of Ant chromophore *per* chain (Nc= 6 / 10 / 21) and are either capped with AEM (AEM) or hydrolyzed (H) (Figure IV. 13).

Table IV. 6: Physicochemical properties of Ant-polymer conjugates.

Ant conjugate	Nc	Post-treatment	Solubility	M_n (P(NAM-*co*-NAS)) before coupling (g.mol^{-1})	M_n after coupling (g.mol^{-1})	Ant-Ant average distance (monomer units)
6Ant-H*	6.1	H	Water	12 900	14 800	14
6Ant-AEM	6.1	AEM	Water, $CHCl_3$		17 300	14
10Ant-AEM	10.3	AEM	Water, $CHCl_3$		20 000	8
21Ant-AEM	20.6	AEM	$CHCl_3$		26 600	4

All photophysical properties of Ant-polymer conjugates are summarize in Table IV. 7.

Table IV. 7: Photophysical properties of Ant-polymer conjugates.

Ant conjugate vs. free chromophore	ε (cm^{-1}.M^{-1})$_{470nm}$ **		Solvent	λ abs /em (nm)	ϕ** a)	Brightness	$<\tau>$ b)** (ns)	σ_{TPA} (740 nm) (GM c))** *per* conj. / *per* chromophore
	per conj	per chromophore						
Free Ant *	-	33 000	$CHCl_3$	480 / 557	0.87	28 700	2.6	420
6Ant-H	108 000	17 700	H_2O	485 / 609	0.02	1 600	Multicomp.	760 / 124
6Ant-AEM	175 000	28 700	$CHCl_3$	480 / 557	0.76	131 300	2.97	1930 / 316
	107 000	17 500	H_2O	486 / 602	0.045	4 800	Multicomp.	840 / 138
10Ant-AEM	341 000	33 100	$CHCl_3$	480 / 564	0.65	221 700	3.02	4340 / 420
	199 700	19 400	H_2O	485 / 605	0.02	2 400	Multicomp.	1270 / 123
21Ant-AEM	608 000	29 500	$CHCl_3$	480 / 564	0.42	255 400	3.12	5200 / 252

* The amino group is protected with *t*Boc (*tert*-butoxycarboxyl) group

** Experimental estimated errors: $\varepsilon \sim \pm$ 10-15%; $\phi \sim \pm$ 10-15%; $\tau <$ 5%, $\sigma_{TPA} \sim \pm$ 20%.

a) Reference: fluoresceine at pH=10, ϕ=92%

b) $<\tau>=\frac{\sum_i A_i \tau_i^2}{\sum_i A_i \tau_i}$ = average lifetime

c) 1 GM (Goeppert–Mayer) = 10^{-50}.cm^4.s.photon^{-1}. Reference Coumarin-307 (ϕ= 0.56 in ethanol).

DBB conjugates

As for the Ant conjugates, four different DBB conjugates 1) to 4) were designed, with the same polymer length but with different numbers of DBB *per* chain (Nc= 4 / 10), either post-treated by AEM capping or hydrolysis. However, two different DBB conjugates with a block architecture, 5) and 6), have lower chromophore densities and higher molecular weights (higher DBB-DBB distance) (Table IV. 8).

Table IV. 8: Physicochemical properties of DBB-polymer conjugates.

Conjugate	Nc	Post-treatment	M_n (P(NAM-*co*-NAS)) before coupling (g.mol^{-1})	M_n after coupling (g.mol^{-1})	DBB-DBB average distance (monomer units)
1) 4DBB-H (DBB13KDa)	4.4	H	12 900	13 800*	19
2) 4DBB-AEM	4.4	AEM		16 700	19
3) 10DBB-H	9.8	AEM		18 100*	8
4) 10DBB-AEM	9.8	AEM		20 400	8
5) DBB28KDa(B)*	4.6	H	Block1: P(NAM-*co*-NAS)_21 600 g.mol-1 Block2: PNAM_7 800 g.mol-1	28 800	31
6) DBB33KDa(B)*	4.0	H	Block1: P(NAM-*co*-NAS)_23 000 g.mol-1 Block2: PNAM_12 000 g.mol-1	33 800	38

*B – the polymer backbone is a block copolymer.

Photophysical properties of DBB conjugates *vs.* DBB free chromophore are given in Table IV. 9. Most of the properties follow the trends identified for Ant conjugates, however there are also differences induced by specific properties of the DBB chromophore:

- DBB is less fluorescent than Ant, but exhibits a relatively stable triplet state capable to interact with molecular oxygen in order to produce cytotoxic singlet oxygen.
- Fluorescence lifetime of free DBB is very short (< 200 ps) and could not be properly quantified as 200 ps was close to the detection limit of the measurement.

In the following section, photophysical properties of DBB conjugates will be further compared to that of Ant conjugates, pointing out the similarities and differences between them.

Table IV. 9: Photophysical properties of DBB-polymer conjugates.

Conjugate vs. free chromophore	ε (cm^{-1}.M^{-1})$_{390nm}$*		Solvent	λ abs /em (nm)	ϕ* a)	Φ_Δ b)*	Brightness	σ_{TPA} (740 nm) (GM c)* *per* conj. / *per* chromophore
	per conj	*per* chromophore						
Free DBB	-	58 000	$CHCl_3$	390 / 460	0.23	0.33	13 300	450
4DBB-H (DBB13KDa)	176 000	40 000	H_2O	387 / 510	< 0.01		< 1 400	1370 / 311
4DBB-AEM	190 000	43 100	H_2O	384 / 510	< 0.01	-	< 1 100	1390 / 315
	229 000	52 000	$CHCl_3$	390 / 460	0.18	0.47	41 200	610 / 138
10DBB-H	335 000	36 200	H_2O	384 / 510	< 0.01	-	< 2 300	2615 / 267
10DBB-AEM	477 000	48 600	$CHCl_3$	390 / 460	0.16	0.47	76 300	1600 / 163
DBB28KDa(B)	174 500	37 900	H_2O	384 / 510	0.05	-	8 700	-
DBB33KDa(B)	151 100	37 700	H_2O	384 / 510	0.06	-	9 100	-

* Experimental estimated errors: $\varepsilon \sim \pm$ 10-15%; $\phi \sim \pm$ 10-15%; τ < 5%, $\sigma_{TPA} \sim \pm$ 20%.

a) Reference: Coumarine 153 in MeOH, ϕ=45%.

b) Reference: Phenalenone in $CHCl_3$, Φ_Δ=100%.

c) 1 GM (Goeppert–Mayer) = 10^{-50}.cm^4.s.photon. Reference Coumarin-307 (ϕ= 0.56 in ethanol).

IV.4.2.1. Steady state fluorescence analyses

Ant conjugates

Influence of Ant binding to the polymer chain

In order to investigate if the binding of Ant chromophore on the copolymer chain has an influence on its photophysical properties, the absorption and fluorescence emission spectra of Ant-polymer conjugates were compared with those of free Ant chromophore in chloroform (Figure IV. 14).

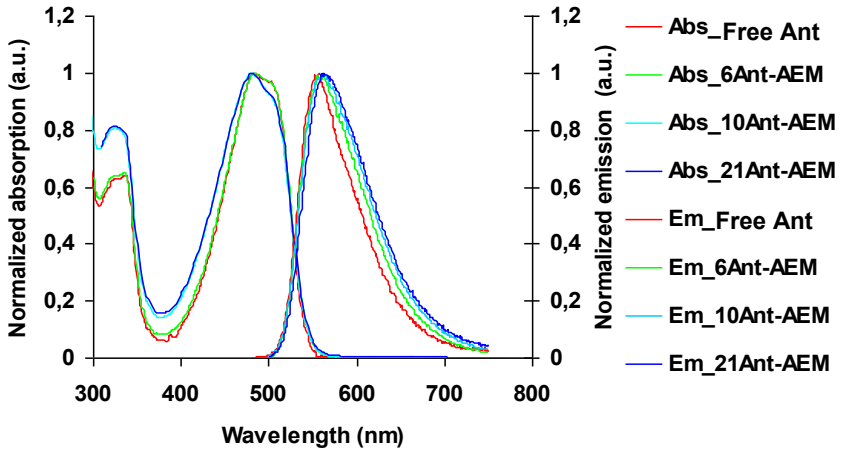

Figure IV. 14: Absorption / emission spectra of Ant-polymer conjugates vs. free Ant in $CHCl_3$ (λ_{ex}=470nm).

As expected, in a good solvent ($CHCl_3$) the bonding to the polymer chain and the polymer environment do not significantly change the ground or excited electronic states of Ant molecules after coupling (almost unchanged absorption / emission spectra). However, the slight broadening and the small blue-shifted absorption / red-shifted emission of Ant polymer conjugates indicate some influence of the polymer, possibly increasing the local polarity around Ant chromophores.

Similarly to LY conjugates, the binding of Ant chromophores induced ~10% decrease in ε_{470nm} compared to free Ant, and a decrease in fluorescence quantum yields (0.87 for free Ant to 0.76 for 6Ant-AEM conjugate) (Table IV. 7).

Influence of Ant density along the polymer chain

No changes were noticed in the absorption of various Ant conjugates in chloroform (ε_{470nm}~30 000 $cm^{-1}.M^{-1}$). Fluorescence quantum yields decreased with the increasing number of chromophores/chain (Figure IV. 15 a)): from 0.76 for 6Ant-AEM, carrying 6 Ant *per* chain, to 0.42 for 21Ant-AEM conjugate bearing 21 Ant *per* chain.

However, as in the case of LY conjugates, the overall brightness of conjugates increases with the increasing number of Ant chromophores *per* chain (Figure IV. 15 b)).

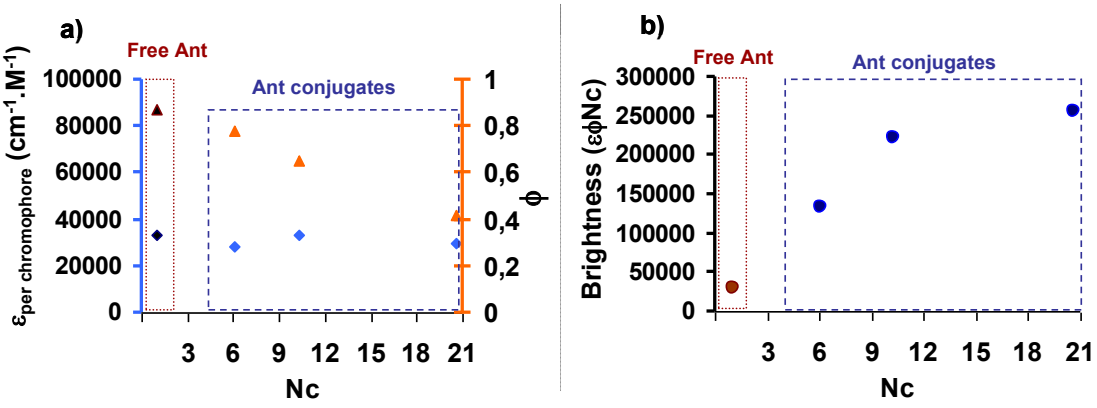

Figure IV. 15: Influence of the number of Ant chromophores per chain (Nc) on: a) molar extinction coefficient (ε) and fluorescence quantum yield (ϕ); b) and on brightness of Ant-polymer conjugates in $CHCl_3$. Comparison with free Ant chromophore.

Influence of the solvent

As discussed in Chapter II, some of Ant conjugates were water-soluble. The goal here was to investigate if their photophysical properties in water change with respect to those in chloroform;
As shown in Chapter II and Table IV. 7, 6Ant-AEM and 10Ant-AEM conjugates are soluble in both $CHCl_3$ and water. These two conjugates were analyzed in these two different solvents (Figure IV. 16).

Figure IV. 16: Absorption / emission of 6Ant-AEM and of 10Ant-AEM conjugates in water vs. $CHCl_3$ (λ_{ex}=470nm).

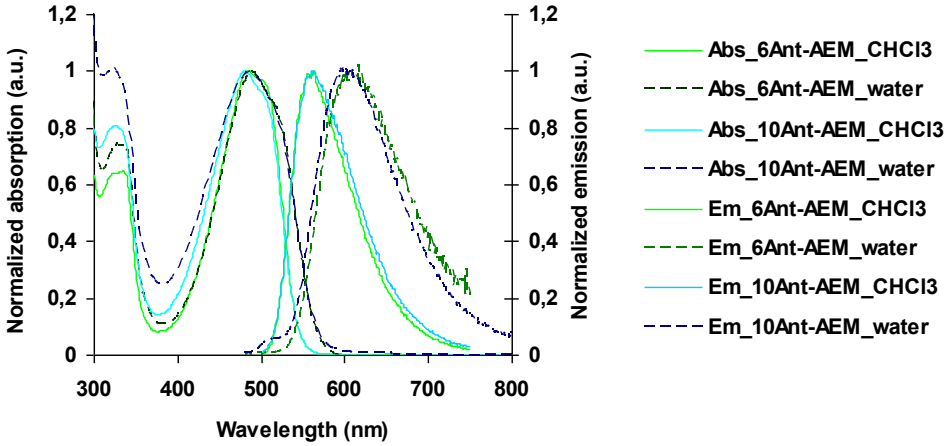

As predicted by theory, the increasing solvent polarity (from $CHCl_3$ to water) induces an increase in the Stokes shift. While the absorption spectrum is less sensitive to the solvent, suggesting a reduced polarity of its ground state, a significant red-shift (~40 nm) in emission curve was recorded in water compared to $CHCl_3$ (Figure IV. 16). These changes can be explained by the existence of charge transfer (CT) transitions in Ant chromophore, inducing a strongly polarized excited state.[37]

Molar extinction coefficients, and even more significantly fluorescence quantum yields of Ant-polymer conjugates (Table IV. 7) decreased in water compared to $CHCl_3$.

- The increased number of electronic transitions in water *vs.* $CHCl_3$ can explain the broadening in absorption spectra and the decrease (~40%) in molar extinction coefficients at 470 nm.
- Nonradiative processes seem to be highly favored in aqueous media, due to stronger chromophore-chromophore interactions (by π stacking) between water-insoluble Ant chromophores, leading to an almost complete loss of fluorescence ($\phi_{water} < 0.05$).

  Belfield and coworkers, who studied the photophysical behavior of TP chromophore-polymer bioconjugates with a norbornen polymer backbone, reported a similar decrease of florescence quantum yields in water *vs.* DMSO.[38]

Further on, the positive solvatochromism was evidenced by recording absorption and emission spectra of water-soluble 6Ant-H conjugate in different solvents: water, ethanol (EtOH), methanol (MeOH), dimethylformamide (DMF), and dioxane (Figure IV. 17), confirming the existence of a strongly polarized exited state, characterizing the Ant chromophore (little changes in absorption, but significant changes in emission maximum wavelengths).[37]

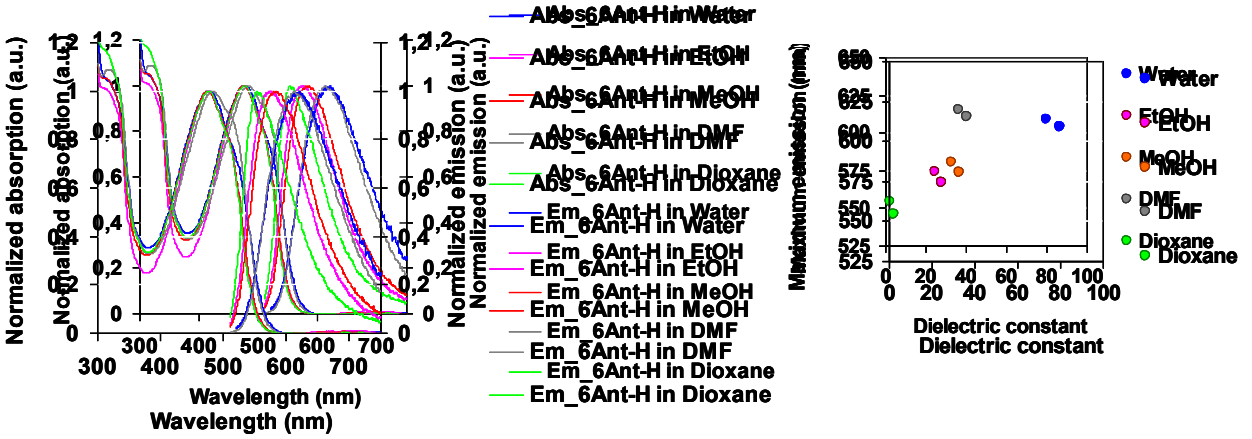

Figure IV. 17: Influence of solvent polarity on absorption / emission properties of 6Ant-H conjugate (λ_{ex}=470nm): absorption / emission spectra (left graph); maximum wavelength of fluorescence emission plotted against the dielectric constant of the corresponding solvent (right graph).

The same studies allowed to determine the fluorescence quantum yields in these different solvents (Table IV. 10).

Table IV. 10: Fluorescence properties of 6Ant-H conjugates in different solvents; ϕ was determined at λ_{ex}=390 nm, reference Rubrene in methanol (ϕ=0.09)

6Ant-H in different solvents	ϕ	λ abs / em (nm)	Stokes shifts (nm)	Dielectric constant
Water	0.02	480 ; 609	133	80.1
Dioxane	0.07	476 ; 554	78	2.25
EtOH	0.07	475 ; 574	99	24.5
MeOH	0.05	474 ; 580	106	32.7
DMF	0.13	483 ; 615	132	36.7

Compared to water, organic environment favors a more extended conformation of Ant conjugates (by better solubilizing them), thus limiting Ant-Ant interactions and quenching processes related to those interactions. As a consequence the fluorescence quantum yields increase significantly in polar organic solvents: ϕ_{water} = 0.02 *vs.* ϕ_{DMF} = 0.13.

Influence of the post-treatment of Ant conjugates (AEM capping *vs.* hydrolysis)

Absorption / emission spectra of 6Ant-AEM conjugate *vs.* 6Ant-H conjugate were recorded in water (Appendix IV.2).

The chemical nature of the polymer backbone (either neutral after AEM capping – 6Ant-AEM, or negatively charged after hydrolysis – 6Ant-H), has no impact on ε (17 500 *vs.* 17 700$cm^{-1}.M^{-1}$). However a slight decrease in ϕ for the hydrolyzed conjugates is noticed (0.02 for 6Ant-H vs. 0.05 for 6Ant-AEM), probably due to and increased polarity of the environment surrounding Ant chromophores.

DBB conjugates

Similar photophysical studies were carried out on DBB-polymer conjugates (Figure IV. 18).

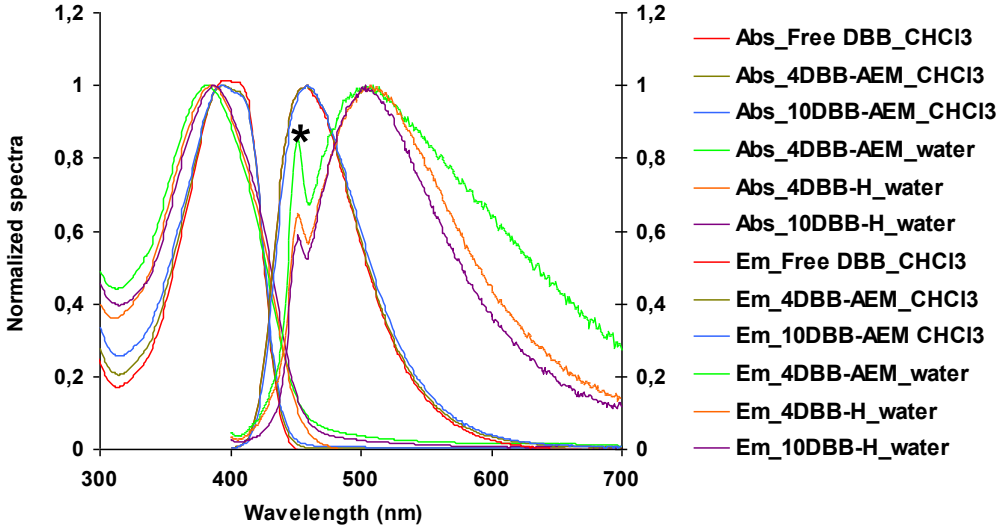

Figure IV. 18: Absorption / emission spectra of DBB-polymer conjugates vs. free DBB in $CHCl_3$ and of hydrophilic DBB conjugates in water (λ_{ex}=390nm).

Note: The sharp peak at ~450 nm on emission spectra corresponds to the Raman scattering of water.

Influence of the DBB binding to the polymer chain

Like in the case of Ant conjugates, the absorption / emission spectra of DBB conjugates in $CHCl_3$ were similar to those of free DBB, suggesting no changes in ground or excited state of DBB after coupling (Figure IV. 18).

Influence of DBB density along the chain

range limits

Similarly to Ant conjugates in $CHCl_3$, ε and ϕ of DBB conjugates decreased with the increasing number of DBB *per* chain (Nc) due to increased contribution of intrachain chromophore-chromophore interaction (Figure IV. 19 a)), while the overall brightness significantly increased as a function of Nc (Figure IV. 19 b)).

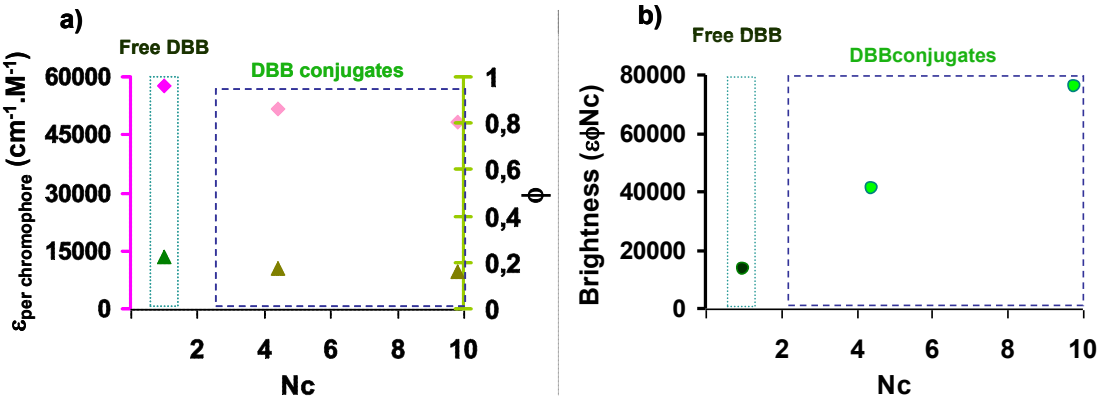

Figure IV. 19: Influence of the number of DBB chromophores per chain (Nc) on: a) absorption (ε) and emission (ϕ) properties in $CHCl_3$; b) and on brightness of DBB-polymer conjugates in $CHCl_3$. Comparison with free DBB chromophore.

In the case of water-soluble hydrolyzed DBB conjugates, the influence of DBB-DBB average distance along the polymer chain was also investigated in water and in dioxane. When the DBB-DBB distance increased, a significant increase in fluorescence quantum yield of DBB conjugates in water is observed (Figure IV. 20, Table IV. 11).

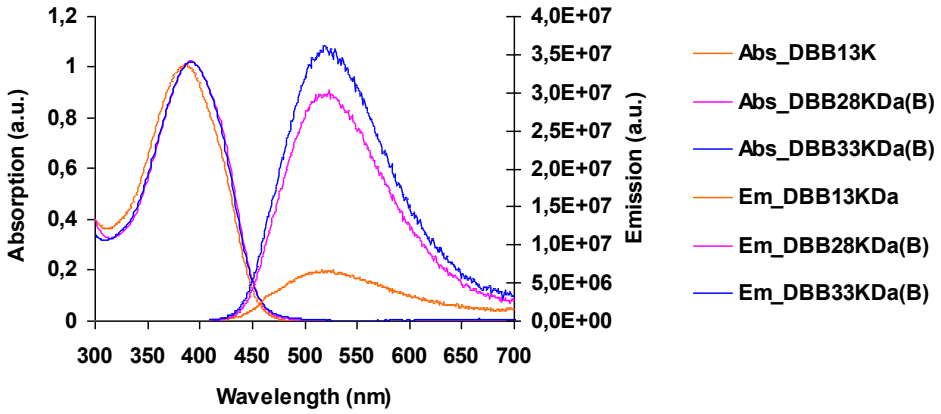

Figure IV. 20: Absorption / emission spectra of DBB-polymer conjugates in water (λ_{ex}=400nm).

Table IV. 11: Fluorescence quantum yield of water-soluble DBB-polymer conjugates in water and dioxane.

Conjugate	ϕ H2O	ϕ Dioxane	DBB-DBB average distance (monomer units)
Free DBB	-	0.17	-
DBB13KDa	< 0.01	0.08	19
DBB28KDa(B)	0.05	0.11	31
DBB33KDa(B)	0.06	0.13	38

Influence of the solvent

As previously mentioned, the changes in solvent polarity have the same impact on DBB conjugates: compared to $CHCl_3$ that is a blue-shifted absorption due to stronger hydrogen bonding in water and a red-shifted emission (Figure IV. 18).

Like Ant conjugates, DBB conjugates exhibit a positive solvatochromism: Stokes shift ~60 – 70 nm in dioxane and $CHCl_3$ and ~140 nm in water (Appendix IV.3).
In water, both ε and ϕ decrease significantly. Moreover, the better solubility of DBB in polar organic solvents significantly improves fluorescence quantum yields of water-soluble conjugates: $\phi_{dioxane} > \phi_{water}$ (Appendix IV. 2).

Influence of the post-treatment technique (AEM capping *vs.* hydrolysis)

As previously observed for Ant-polymer conjugates, the chemical nature of the polymer backbone of DBB-polymer conjugates, seem to have limited impact on their absorption / emission properties (Figure IV. 18): comparison between 4DBB-AEM and 4DBB-H curves.

IV.4.2.2. Time-resolved fluorescence analyses

Ant conjugates

The phenomenon leading to important losses in quantum efficiency with the increasing number of Ant *per* chain (Figure IV. 15) was revealed by measuring the corresponding fluorescence decays of Ant-polymer conjugates in $CHCl_3$ (Figure IV. 21).

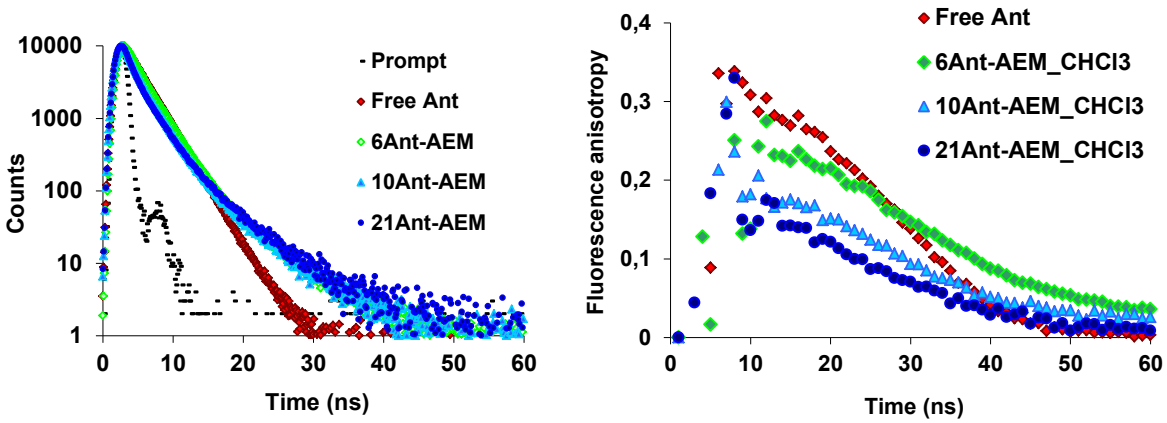

Figure IV. 21: Fluorescence lifetime (left graph) and anisotropy (right graph) of Ant-polymer conjugates compared to free Ant chromophore in $CHCl_3$ (λ_{ex}=469nm; λ_{em}=560nm).

Similarly to LY conjugates, an increase in average fluorescence lifetime was observed for Ant bound chromophore compared to free Ant chromophore in $CHCl_3$. However, unlike fluorescence quantum yields, fluorescence decays of all Ant conjugates seemed almost insensitive to the number (density) of chromophores *per* chain (Figure IV. 21, left graph). This behaviour suggested a decrease in the radiative decay rate constants (k_r) and possibly an increase in nonradiative decay rate constants (k_{nr}) of the bound Ant chromophore. The decay rate constants were estimated and are given in Table IV. 12.

Table IV. 12: Fluorescence parameters of Ant-polymer conjugates vs. free Ant chromophore.

Sample	One exponential model		Two exponential model				<τ> (ns)	χ^2	ϕ	k_r x 10^8 (s^{-1} a)	k_{nr} x 10^8 (s^{-1} b)
	τ (ns)	A (%)	τ_1 (ns)	A1 (%)	τ_2 (ns)	A2 (%)					
Free Ant*	2.6	100%	-	-	-	-	-	1.1	0.87	0.34	0.05
6Ant-AEM	-	-	2.1	82	4.7	18	2.97	~3	0.76	0.26	0.08
10Ant-AEM	-	-	1.7	73	4.4	27	3.02	~4	0.65	0.21	0.12
21Ant-AEM	-	-	1.4	65	4.2	35	3.12	~3	0.42	0.13	0.19

* NH_2 protected with *t*Boc group

a) $k_r = \frac{\phi}{<\tau>}$

b) $k_{nr} = \frac{1}{<\tau>} - k_r$

The latter results confirm that fluorescence quenching is directly related to the concentration of chromophores on the chain (increasing from 6, to 10 and to 21 for the same polymer length). Quenching seems to be induced by a stronger distance-dependent interaction (energy transfer) between neighboring Ant chromophores situated closer to each other. Homo-FRET[39] phenomenon, attributed to the energy transfer between 'identical' chromophore molecules, can possibly explain this behavior. Homo-FRET is characterized by a decrease in the apparent quantum yields when

chromophore concentration increases, without affecting the fluorescence lifetimes as the excited state is not actually reduced during energy transfer.

Homo-FRET can be evidenced by monitoring the loss in fluorescence anisotropy in the emission, upon excitation with polarized light.[40] Indeed, time-resolved anisotropy measurements (Figure IV. 21, right graph) with Ant conjugate show significant changes in fluorescence anisotropy. As predicted by homo-FRET, decreased anisotropy values were found with the increasing number of Ant chromophores *per* chain:[41] the initial anisotropy r_0 (at t=0), which depends on the orientation of Ant absorption dipole moment, was found 0.34 for the free Ant chromophore and decreased to 0.25, 0.20, 0.15 for Ant conjugates bearing 6, 10, and 21 Ant *per* chain, respectively (Appendix IV.4).

Time-resolved fluorescence decays were determined for all water soluble conjugates (Figure IV. 22). Fluorescence decays were much faster in water compared to $CHCl_3$, supporting previously discussed increased quenching in aqueous medium. A multiexponential distribution was found in this case, explained by the existence of multiple micro-environments surrounding the bound Ant chromophores leading to a much broader distribution of the excited states.

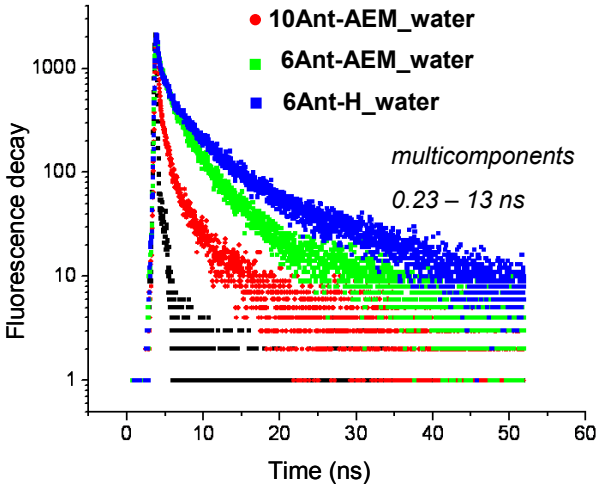

Figure IV. 22: Fluorescence lifetime of water-soluble Ant-polymer conjugates in water (λ_{ex}=489nm; λ_{em}=585nm) – measurements performed in Norway by M. Lindgren. Black dots represent the prompt.

DBB conjugates

As mentioned in the introduction of this part, DBB conjugates like DBB free chromophore exhibited very short fluorescence lifetimes (Figure IV. 23). This is the reason why quantitative analyses in $CHCl_3$ or water could not be carried out.

Although quantitative analyses of their fluorescence decays could not be evaluated, due to similarities in their chemical structures, we expect DBB-polymer conjugates to follow the same behaviour as Ant chromophores with respect to chromophore-chromophore interactions (Homo-FRET phenomenon).

Following this hypothesis, fluorescent decays seem to be faster in water (Figure IV. 23, right graph).

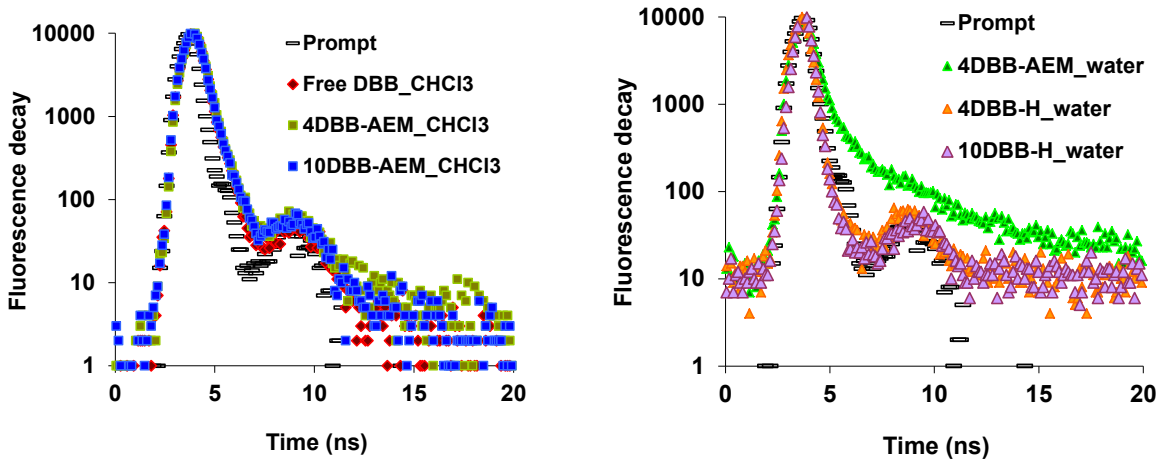

Figure IV. 23: Fluorescence decays of DBB conjugates: (left graph) in $CHCl_3$; (right graph) in water (λ_{ex}=440nm; λ_{em}=500nm).

Note 1: A strong scattering background could be recovered in aqueous medium.

Note 2: Peak ~9 ns – background noise (detector).

It should be noted here that DBB-derived conjugates exhibit a long-living triplet state that could also quench fluorescence. However, the influence of Nc on this quenching was not be evidenced here, but should be considered in the future (transient absorption measurements).

V.4.2.3. Two-Photon absorption properties

Two-photon excitation measurements were carried out with the assistance of Jean Bernard, at UJF Grenoble, in the team of P. Baldeck.

Ant conjugates

Two photon absorption cross sections (σ_{TPA}) of Ant-polymer conjugates in $CHCl_3$ and water have been determined by Two-Photon Excited Fluorescence (TPEF) (Figure IV. 24) and maximum values reported in Table IV. 7.

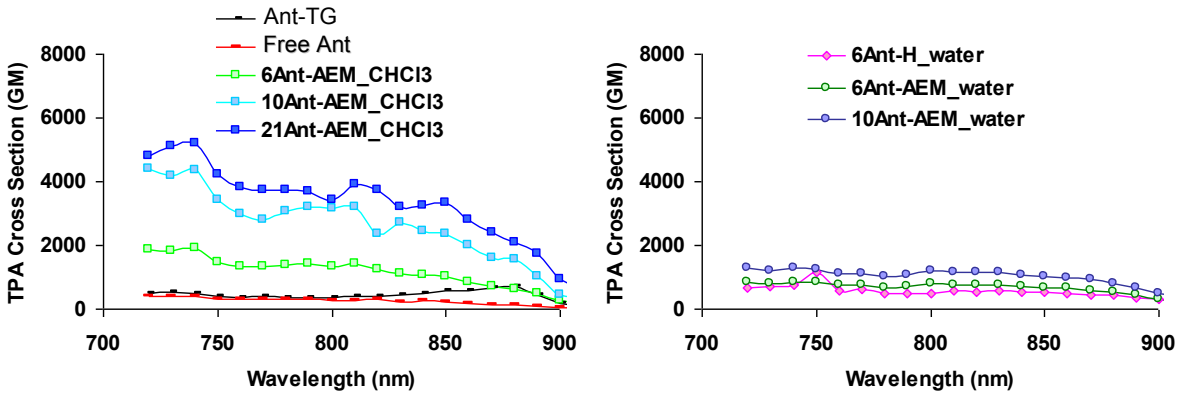

* Ant-TG = Ant chromophore synthesized by T. Gallavardin during his PhD.[37]

Figure IV. 24: Two-Photon Absorption Cross Section of Ant-polymer conjugates and Ant chromophore: (left) in $CHCl_3$; (right) water (relative to Coumarine 307 in CH_2Cl_2, measurement accuracy ± 20%).

Ant chromophore used for coupling (PEGylated derivative) exhibits high σ_{TPA}, 420 GM at 740 nm, in agreement with previously determined 518 GM found for similar chromophores.[37]

As expected, σ_{TPA} of Ant conjugates varied similarly to one-photon absorption properties (ε): i) compared to free Ant chromophore, σ_{TPA} of bound Ant decreased after coupling on the polymer chain; ii) $\sigma_{TPA}(CHCl_3) > \sigma_{TPA}(water)$.

Although water-soluble Ant conjugates are characterized by low fluorescence quantum yields, relatively high σ_{TPA} values (Table IV. 7) (Figure IV. 24) contribute to obtain a sufficiently high brightness values under TP excitation, justify their potential use for TP fluorescence bioimaging (Chapter V).

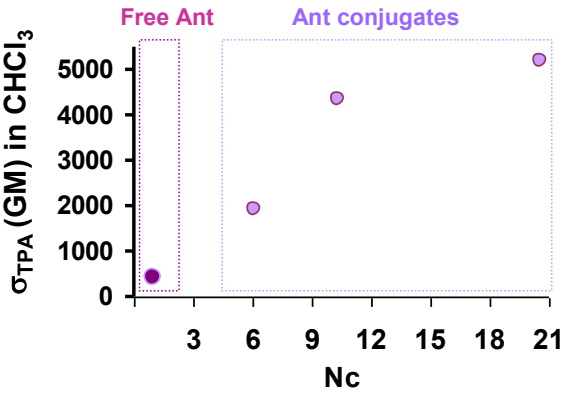

Figure IV. 25: Two-Photon Cross section of Ant-polymer conjugates vs. free Ant chromophore in $CHCl_3$.

DBB conjugates

Slightly similar behavior (and similar orders of magnitude) has been found for σ_{TPA} of DBB-polymer conjugates (Figure IV. 26).

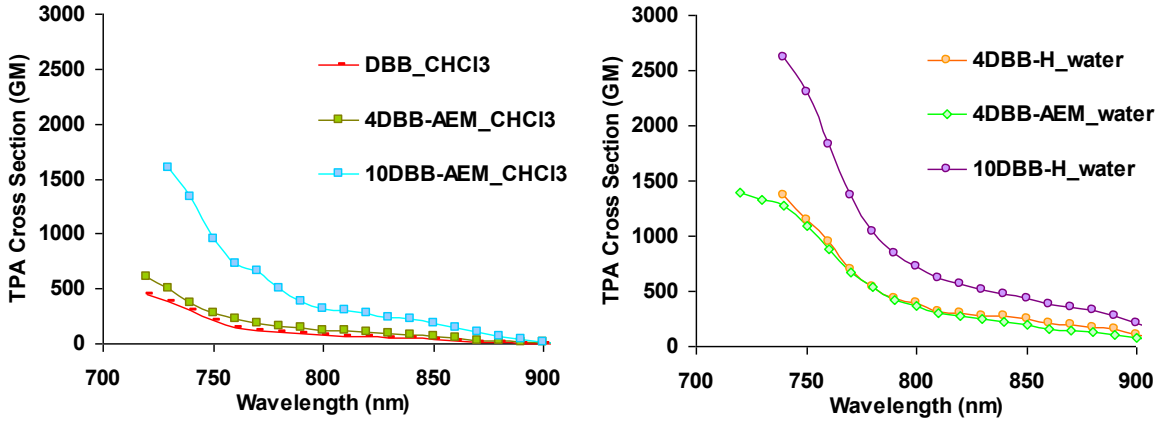

Figure IV. 26: Two-Photon Absorption Cross Section of DBB conjugates and DBB chromophore: (left) in $CHCl_3$; (right) water (relative to Coumarine 307 in CH_2Cl_2, measurement accuracy ± 20%).

However and unexpectedly, σ_{TPA}(water) > σ_{TPA}($CHCl_3$) (Figure IV. 26). In principle, this is a very positive observation considering the final biological application. Nonetheless the uncertainties related to TPEF technique may have biased these trends.

As previously mentioned, σ_{TPA} of DBB conjugates in $CHCl_3$ and water increased with the increasing number of DBB *per* chain (Figure IV. 27), highlighting the benefits of the polymers chain.

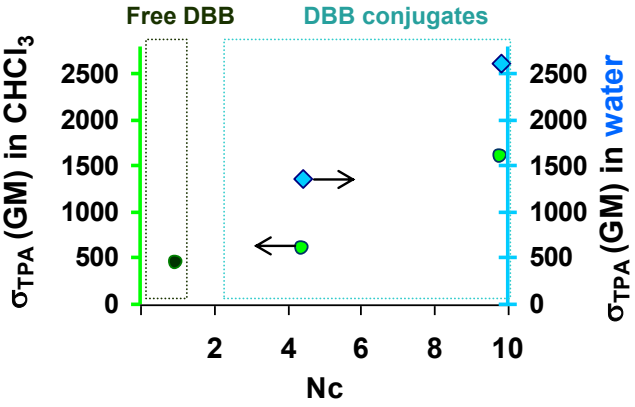

Figure IV. 27: Two-Photon Cross section of DBB-polymer conjugates vs. free DBB chromophore in $CHCl_3$ and water.

IV.4.2.4. Singlet oxygen production

Ant conjugates

It was shown earlier that Ant chromophore has only 1% photons potentially reaching the triplet sate after light absorption. Therefore, Ant-polymer conjugates were not the object of this analysis.

DBB conjugates

DBB chromophore has been designed for singlet oxygen production and exhibited a quantum yield of singlet oxygen production of Φ_Δ=0.33 in $CHCl_3$.

Singlet oxygen produced by free DBB and DBB-conjugates was recorded in $CHCl_3$ by detecting its phosphorescence at 1270 nm as previously reported (Figure IV. 28).[37]

The quantum yields of singlet oxygen production (Φ_Δ) were calculated using phenalenone[42] molecule as reference ($\Phi_\Delta^{phenalenone}$=1) and Stern-Volmer model.

Calculated values were reported in Table IV. 9 .

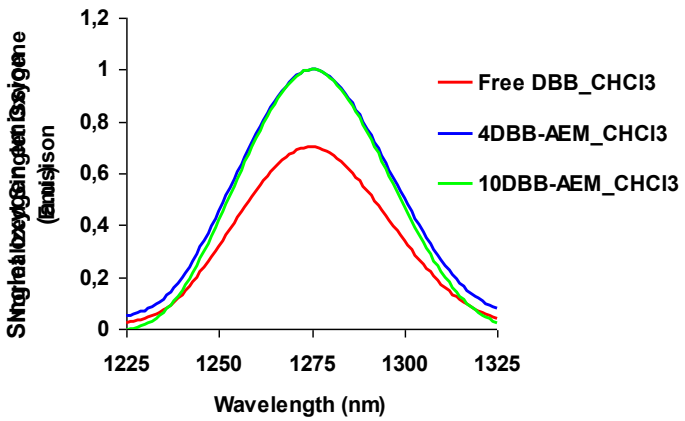

Figure IV. 28: Singlet oxygen emission of DBB-polymer conjugates *vs.* free DBB chromophore in $CHCl_3$ (λ_{ex}=390nm).

After coupling, $^1O_2$ production (Φ_Δ) of DBB conjugates increases (to 0.47) compared to $^1O_2$ produced by free DBB (0.33).
We suppose that, in the case of free amino-derived DBB chromophore, Φ_Δ is partly quenched due to the presence of primary amine-groups on the structure of DBB chromophore, known as efficient quenchers of $^1O_2$.[43]

Unlike fluorescence quantum yields (ϕ), singlet oxygen production yields (Φ_Δ) seem to be apparently not influenced by the number of DBB *per* chain. This observation suggests that quenching induced by stronger chromophore-chromophore interactions would only influence the radiative deactivation of excited singlet state S_1 (by homo-FRET), although without affecting the Intersystem Crossing (ISC) efficiency and triplet state T_1 energy transfer to oxygen. The latter deduction would still require confirmation (also in the case of water-soluble conjugates); however, it provides promising expectations for PDT applications.

In water, phosphorescence of singlet oxygen could not be detected. $^1O_2$ is a very reactive electrophile; its phosphorescence is additionally attenuated in water by resonance energy transfer from $^3O_2$ to the O-H vibrations of water molecules and by partial re-absorption of the emitted phosphorescence.[44] Consequently the $^1O_2$ generation in water could not be determined in solution. Nonetheless, the PDT potential of water-soluble DBB conjugates will be tested directly in biological media (Chapter V).

Kinetics of $^1O_2$ production was not investigated in this study. However, the luminescence lifetime of $^1O_2$ with a similar DBB chromophore has been determined to be 7.4 µs,[45] encouraging its use for PDT applications.

IV.4.2.5. Conclusion on TP conjugates

Photophysical properties of TP chromophore-polymer conjugates were compared with those of free chromophore in organic medium. While little changes were noticed in the absorption of bound chromophores (slight decrease of ε *per* chromophore), fluorescence emission decreased significantly with the increasing number of chromophores *per* chain, due to homo-FRET energy transfer.
TP conjugates exhibited positive solvatochromism in polar solvents, proving the existence of a highly polarized excited state, sensitive to the surrounding environment.
Due to a favored static and dynamic quenching in water, fluorescence emission of conjugates decreased drastically (one order of magnitude) compared to organic solvents.
One- and two-photon absorption properties (ε and σ_{TPA} *per* conjugate) increased with the increasing number of chromophores *per* chain, contributing to enhanced fluorescence brightness on conjugates.

Singlet oxygen production in $CHCl_3$ could be evaluated for DBB conjugates (Φ_Δ =0.47) and free free DBB chromophore (Φ_Δ =0.33) in $CHCl_3$. Unlike fluorescence, the triplet state energy transfer seemed little dependent on the number of DBB *per* chain.

Thanks to the water-solubility of several Ant and DBB-polymer conjugates, it was possible to determine their photophysical properties in water, which was not possible with free Ant and DBB chromophores.

At this point, we have shown that after coupling on the polymer chain, one- and two photon absorption properties of bound chromophores were relatively preserved. Generally, the same trends were found for LY (one-photon) conjugates and Ant / DBB (two-photon) chromophores after coupling on the polymer chain in terms of absorption / fluorescence emission properties, with however bigger differences in the case of TP polymer conjugates.

The evaluation of multiple photophysical parameters (ε, ϕ, brightness, and τ) enables to properly correlated the steady state fluorescence properties with time-resolved fluorescence results.

In the case of water-soluble TP polymer conjugates, significant decrease of fluorescence efficiency was recorded in aqueous medium, due to stronger chromophore-chromophore interactions leading to important fluorescence quenching.

This would constitute a supplementary reason of using AuNP to enhance the properties of TP conjugates *via* SPR interaction (next Section).

IV.5. Grafted AuNP: the influence of AuNP on the photophysical properties of chromophores bound to a polymer spacer

The aim of this part was to study the changes in photophysical properties of chromophore-polymer conjugates after their grafting onto spherical 20 nm AuNP (Chapter III).

As described in the 3rd part of this chapter, fluorescence quenching or enhancement near AuNP surface is governed by chromophore-AuNP distance.
Since chromophore-polymer conjugates, with different lengths and different chromophore densities, have been grafted onto AuNP, the fluorescence properties of the resulting nano-objects will depend on chromophore-AuNP distance.
However, for 20 nm AuNP, chosen as a model system in this work, little or no enhancement is expected, as SPR of 20 nm AuNP is characterized by a strong absorption component and a negligible scattering component (it is believed that SPR enhancement is controlled by scattering only).

In order to determine the influence of 20 nm AuNP on fluorescence properties of grafted conjugates, a comparative method was implemented here (with J. Navarro, F. Lerouge).*
Grafted AuNP were submitted to NaCN treatment. Cyanides are known to quantitatively dissolve Au^0, and releasing the grafted layer (Figure IV. 29).[46] The complete dissolution of gold core was indicated by the absence of SPR on absorption spectrum. Fluorescence emission of dissolved AuNP solutions (corresponding to the fluorescence emission of released conjugates) was compared with the fluorescence emission of the grafted AuNP (the same amount) before the dissolution.

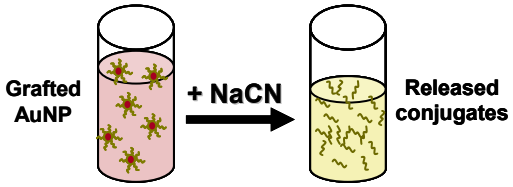

Figure IV. 29: Au core dissolution with cyanide.

Several control tests had to be performed before using cyanide on grafted AuNP:

- the influence of cyanide on the stability of chromophore-polymer conjugates;
- the influence of cyanide on citrate capped AuNP.

Note: to be significant, this method must be performed on perfectly purified grafted AuNP.

*Fluorescence emission measured before and after dissolution of gold core, i.e. from grafted to free released conjugates.

IV.5.1. AuNP-LY conjugates

20 nm AuNP grafted with LY conjugates of various sizes (2 000 to 37 000 $g.mol^{-1}$) and architectures (Figure IV. 30) have been submitted to the cyanide treatment, in order to study how structural differences between grafted LY conjugates may impact on the distance between LY chromophores and AuNP surface, and then on their fluorescence properties.

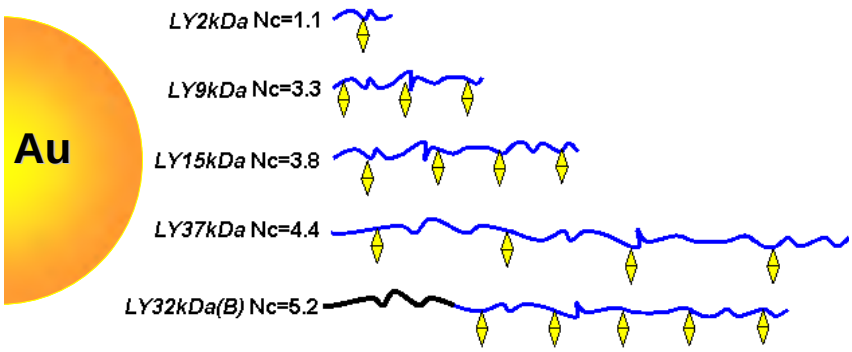

Figure IV. 30: Schematic representation of the various LY-polymer conjugates bound to 20 nm spherical AuNP.

Control tests indicated no degradation of free LY conjugates by cyanide. On the other hand, a weak residual fluorescence could be recovered after cyanide treatment of citrate-capped AuNP, corresponding to the newly formed Au^{1+} fluorescent complex.[5] This residual emission was taken into account when calculating the overall fluorescence emission of released conjugates in the presence of cyanide.

The quenching characterizing AuNP-LY conjugates systems can be the resultant of three different phenomena:

- intramolecular quenching (due to the density of LY chromophores *per* chain);
- intermolecular quenching (due to the grafting density if LY-polymer conjugates on the AuNP surface);
- quenching *via* metal resonance energy transfer (due to the interaction with the AuNP).

IV.5.1.1.Steady state fluorescence analyses

Analyzed samples contained the same amount of AuNP (the same absorption intensity at the maximum wavelength of the SPR band, ~530 nm, (Figure IV. 31). While no qualitative changes could be detected in the shape of emission spectra (corresponding to that of free LY chromophore), relative emission intensity increased with the increasing length of the polymer chain (Figure IV. 31, dashed lines), possibly due to an increasing LY-AuNP distance leading to less quenching.

At this stage of the study, comparative observation does not take into account the potential differences coming from variations of the chain grafting density (LY conjugates *per* AuNP), or variation of the chromophore density *per* chain (Nc) – both correlated to the number of LY chromophores *per* AuNP. In order to quantify the quenching (enhancement), the fluorescence emission of those samples was compared before and after Au dissolution (Figure IV. 32, Table IV. 13).

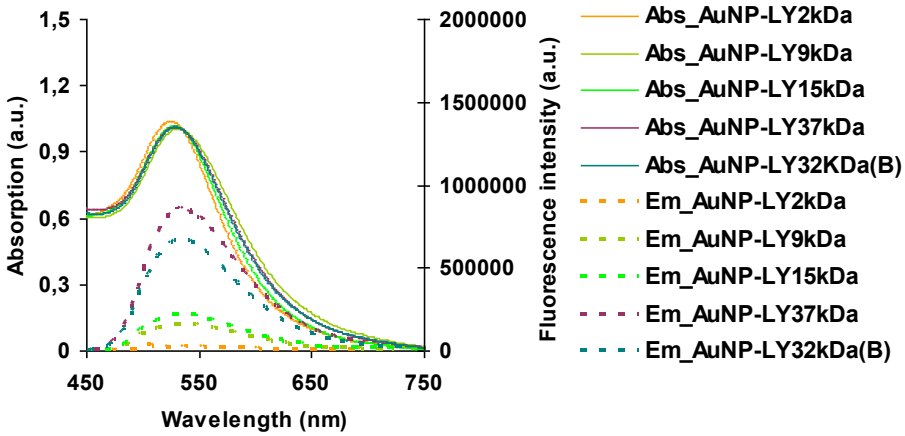

Figure IV. 31: Absorption/ Emission spectra (dashed lines), (λ_{ex}=470nm) of grafted AuNP-LY conjugates.

No changes could be noted on the fluorescence emission spectra of LY-conjugates after grafting onto AuNP, suggesting that the AuNP does not alter the excited state of the chromophore and that the environment of LY chromophore inside the hydrated polymer corona is similar to that in the free conjugate.

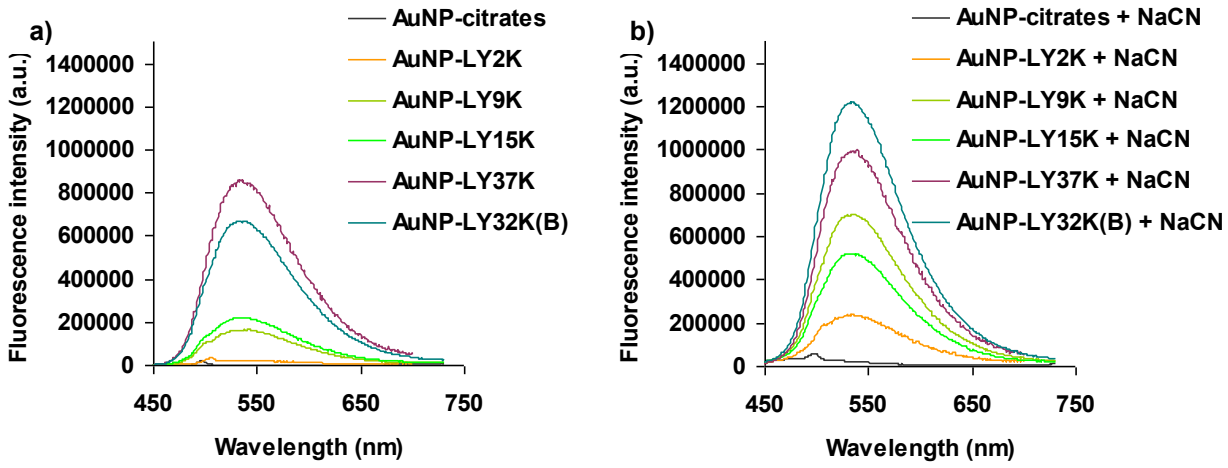

Figure IV. 32: Emission of grafted AuNP-LY conjugate samples before a), and after b) AuNP core dissolution with cyanide (λ_{ex}=470nm).

Nonetheless, a decrease in fluorescence emission of LY conjugates is noted after grafting onto AuNP, indicating that quenching of fluorescence occurs in this case.

Table IV. 13: Fluorescence, quenching, and grafting density of 20 nm AuNP grafted with LY conjugates.

Grafted AuNP-LY conjugate	Copolymer M_n (before coupling) (g.mol^{-1})	Polymer shell TEM (nm)	Length of stretched polymer chain (nm)*	'Fluorescence recovery"** / Quenching (%)	Grafting density (chains/AuNP)	Grafting density (chains/nm²)	Nb. LY / AuNP
AuNP-LY2KDa	2 200	1 ± 1	3	10 / 90	419	0.52	460
AuNP-LY9KDa	7 900	4 ± 1	12	30 / 70	395	0.43	1303
AuNP-LY15KDa	12 900	12 ± 2	20	50 / 50	313	0.34	1189
AuNP-LY37KDa	34 600	20 ± 5	55	90 / 10	463	0.45	2037
AuNP-LY32KDa(B)	29 400	18 ± 3	49	65 / 35	320	0.39	1664

**Calculated using the DP_n of the initial copolymer (degree of polymerization) and using –C–C– single bond length as 1.54A° and 109.5° as a bond angle between two –C–C– bonds.

** "Fluorescence recovery" = the ratio between the area under the fluorescence emission curve before and after dissolution of Au core by cyanide (fluorescence emission of grafted LY conjugate *vs.* free LY conjugate).

This steady state study demonstrates the distance dependence of fluorescence emission (and quenching) of LY-polymer conjugates grafted onto 20 nm AuNP.

For a better understanding of these phenomena, several interpretations of results listed above are possible (Figure IV. 33).

- LY-AuNP distance is related to the polymer corona thickness (measured by TEM, Figure IV. 33 a)): when the length of the chains increases, the average distance between chromophores and AuNP surface also increases (Chapter III). For an increased LY-AuNP distance, corresponding to an increased polymer corona thickness, the quenching decreases significantly. This is the reason why, for the shortest grafted conjugate (LY2KDa), fluorescence seems almost completely quenched (emission barely detected, strongly impacted by the background noise, Figure IV. 32). Nevertheless, after Au core dissolution, the fluorescence recovered from the released free LY2KDa conjugate is significantly higher, indicating a strong quenching of this conjugate after grafting onto AuNP.

  Even if little or no enhancement is expected with 20 nm AuNP, an almost complete recovery (90%) of fluorescence is reached with AuNP-LY37KDa exhibiting 90% of free LY37KDa fluorescence intensity.

  A very similar trend for fluorescence quenching is observed with respect to the theoretical length of the stretched polymer (Figure IV. 33 b)), highlighting the role of the polymer M_n (length) as an efficient spacer in the recovery of fluorescence at the surface of AuNP. Moreover, the two calculated and measured polymer corona thicknesses (theoretical and determined by TEM) represent the two limits (maximum and minimum) of the polymer corona thickness in solution.

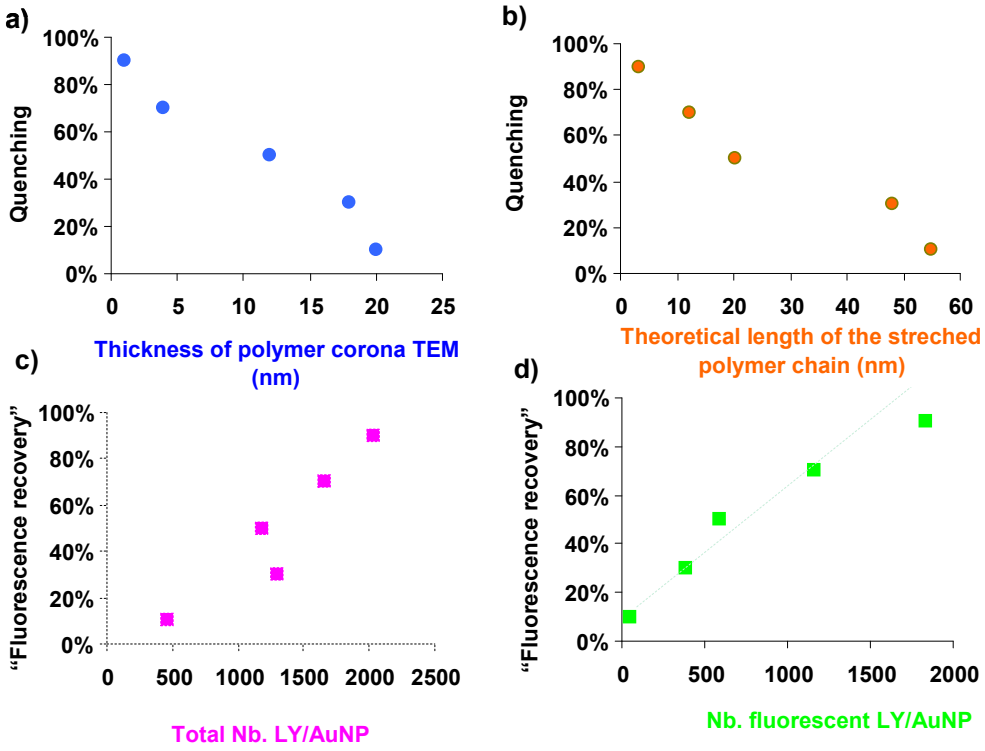

Figure IV. 33: Fluorescence quenching of grafted AuNP-LY conjugates as a function of the thickness of grafted polymer corona a); of the theoretical length of the stretched polymer chain b). Fluorescence of grafted AuNP-LY conjugates as a function of the total number of LY chromophores *per* AuNP c); and of the number of fluorescent LY chromophores d) (λ_{ex}=470nm).

- Thanks to fluorescence data, the chain grafting density could be calculated for each AuNP sample (Table IV. 13) (Chapter III, Appendix III.6). The same order of magnitude was found for all AuNP grafted with LY grafted conjugates, independently of their length. Grafting density values (310 – 460 chains *per* AuNP) allowed to further calculate the total amount of LY chromophores *per* AuNP. Fluorescence intensity increased with the increasing number of LY *per* AuNP (500 – 2000 LY *per* AuNP) (Figure IV. 33 c)).
- Moreover, if no enhancement were possible with 20 nm AuNP, fluorescence would depend exclusively on the number of fluorescent chromophores *per* chain Eq. (16), calculated from the percentage of recovered fluorescence and the total number of LY *per* AuNP. As a proof, Figure IV. 33 d) illustrates the dependence of fluorescence emission with the number of fluorescent LY chromophores *per* AuNP.

$$Nb._{LY}^{fluo} = Nb._{LY}^{total} \times Fluorescence(\%) \quad (16)$$

IV.5.1.2. Time-resolved fluorescence analyses

Fluorescence decays of three AuNP samples (AuNP-LY9KDa, AuNP-LY15KDa, AuNP-LY32KDa(B)), were recorded (Figure IV. 34) and analyzed (Table IV. 14). In all cases, decays were faster for the grafted AuNP compared to free conjugates.

While free LY conjugates (recovered after Au core dissolution)*, were characterized by a bi-exponential decay profile (Section IV.4), grafted AuNP, could be correctly fitted with a three-exponential profile, displaying a supplementary very short lifetime component (τ_3 < 1 ns, Table IV. 14), τ_1 and τ_2 remaining similar to those found for free LY conjugates before grafting. We suppose that this component corresponds to the contribution of quenching *via* metal resonance energy transfer (Section IV.3), leading to an increased non-radiative rate constant, and lower fluorescence emission intensity.[1b)]

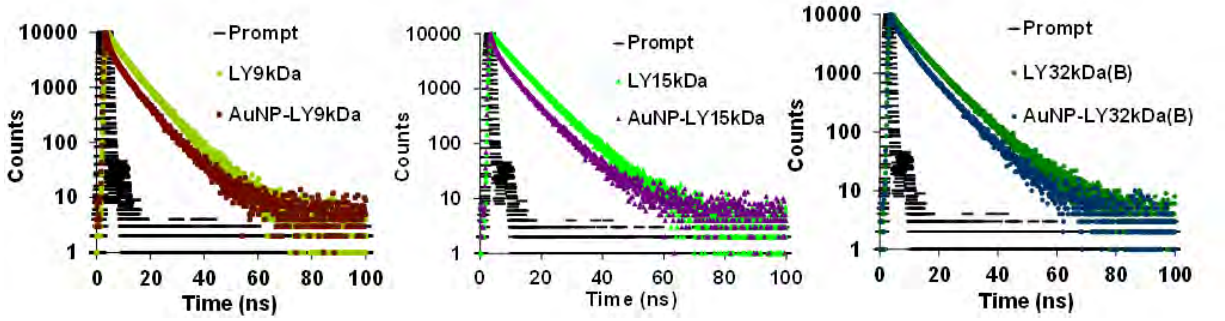

Figure IV. 34: Fluorescence decays of grafted AuNP vs. free LY conjugates: (left) AuNP-LY9KDa, (middle) AuNP-LY15KDa, (right) AuNP-LY32KDa(B), (λ_{ex}=440nm, λ_{em}=530nm,).

Table IV. 14: Fluorescent decay parameters of of LY conjugates grafted onto AuNP.

Sample	3-exponential model						<τ> (ns)	χ^2
	τ_1 (ns)	A1 (%)	τ_2 (ns)	A2 (%)	τ_3 (ns)	A3 (%)		
AuNP-LY9KDa	3.5	26	7.9	60	0.6	14	7.1	1.06
AuNP-LY15KDa	3.0	24	7.5	64	0.5	12	6.8	1.14
AuNP-LY32KDa(B)	3.6	32	8.4	62	0.6	6	7.5	1.09

The shorter lifetime component τ_3 (Table IV. 15) after grafting would correspond to the quenching of fluorescence by resonance energy transfer to AuNP, also characterized by the non-radiative decay rate constant k_{nr_AuNP}.

* We verified that cyanide had no impact on fluorescence decays of those conjugates, by comparing them with fluorescence decays of new samples of free conjugates (⇒ equivalent decays).

Table IV. 15: Calculated radiative and non-radiative rates of LY conjugates grafted onto AuNP.

Sample	*Before grafting* $\langle\tau\rangle_{conj.}$ *(ns)*	After grafting $\langle\tau\rangle_{conj.@AuNP}$ (ns)	k_r x 10^8 (s^{-1}) a)	k_{nr} x 10^8 (s^{-1}) b)	k_{nr_AuNP} x 10^8 (s^{-1}) c)
AuNP-LY9KDa	*7.6*	7.1	0.032	0.100	0.009
AuNP-LY15KDa	*7.5*	6.8	0.035	0.099	0.014
AuNP-LY32KDa(B)	*8.2*	7.5	0.033	0.089	0.011

a) $k_r = \frac{\phi}{\langle\tau\rangle_{conj.}}$; b) $k_{nr} = \frac{1}{\langle\tau\rangle_{conj.}} - k_r$; c) $k_{nr\_AuNP} = \frac{1}{\langle\tau\rangle_{AuNP}} - \frac{1}{\langle\tau\rangle_{conj.}}$;

$$\langle\tau\rangle_{AuNP} = \frac{1}{k_r + k_{nr} + k_{nr\_AuNP}}$$

Similar behaviour near 13 nm AuNP has been found with fuorescein and lissamine chromophores distanced from AuNP surface using LbL (layer-by-layer) assemblies around the Au core.[47]

Compared to other existing core-shell systems (e.g. silica coated,[48] LbL[47]), where the shell is rather rigid/static, with little conformation variability, LY chromophore-polymer shell is more flexible. We suggest that a more complex photophysical behaviour may characterize grafted LY conjugates on AuNP surface, where distance-dependent properties – as quenching (by either inter/intrachain interactions or energy transfer to AuNP) or (if allowed) SPR enhancement – coexist. In this context, fluorescence measurements would be a resultant of all these possible pathways.

IV.5.1.3. Conclusion on AuNP-LY conjugate systems

The benefits of random and block P(NAM-*co*-NAS) copolymers, obtained by RAFT, to be used as multifunctional platforms allowing to tune the fluorescence properties of chromophores near AuNP surfaces, has been demonstrated with LY-polymer conjugates, since the fluorescence of LY in the polymer corona near AuNP increased when the polymer length (M_n) increased (Figure IV. 35).

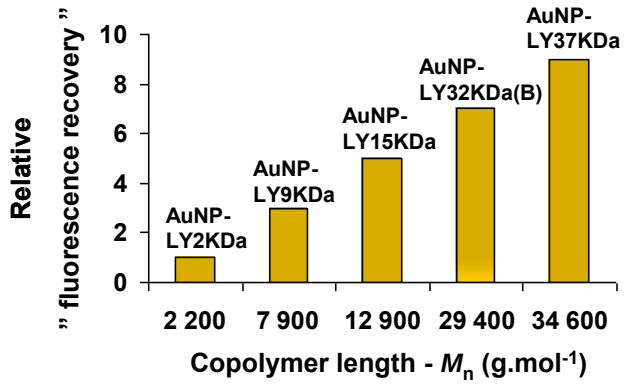

Figure IV. 35: Relative "fluorescence recovery" of LY-polymer conjugates grafted onto 20 nm AuNP surface as a function of the P(NAM-*co*-NAS) copolymer molecular weight, calculated as the ratio of the "fluorescence recovery" for the different grafted LY conjugates in comparison with the shortest grafted conjugate (LY2KDa).

The distance-dependent fluorescence of grafted LY-polymer conjugates at the surface of 20 nm AuNP has therefore been evidenced showing that fluorescence emission could be almost completely recovered ("fluorescence recovery" = 90%) in the case of the longest polymer chain (AuNP-LY37KDa). In this case, the relative "fluorescence recovery" reached a factor 9, in comparison with the shortest polymer chain (AuNP-LY2KDa).

IV.5.2. AuNP grafted with Two-Photon chromophore-polymer conjugates

Photophysical properties of water-soluble 20 nm AuNP grafted with TP conjugates were studied in the last part of this chapter.

Note: The fluorescence intensity of TP conjugates decreased significantly in the presence of cyanide ions, the reason why AuNP grafted with those conjugates could not be studied by cyanide method.

AuNP-Ant conjugates

Very weak fluorescence emission was recorded after the grafting of Ant-conjugates onto 20 nm AuNP, was strongly impacted by the background noise (Appendix IV.5).

We conclude that in the case of Ant-polymer conjugates (M_n=12900g.mol^{-1}), the Ant chromophores are probably too close to AuNP surface, thus their fluorescence is completely quenched by energy transfer to Au. It may probably be due to the shrinked conformation of Ant conjugates compared to LY conjugate with a similar length (Chapter III, indicated by a 3 times thinner polymer corona found for Ant- (4 nm) *vs.* LY-polymer conjugates (12 nm)).

AuNP-DBB conjugates

Unlike Ant-polymer conjugates, 3 DBB-polymer conjugates (Figure IV. 36), of various sizes, architectures and DBB densities, were grafted onto AuNP and studied by fluorescence spectroscopy.

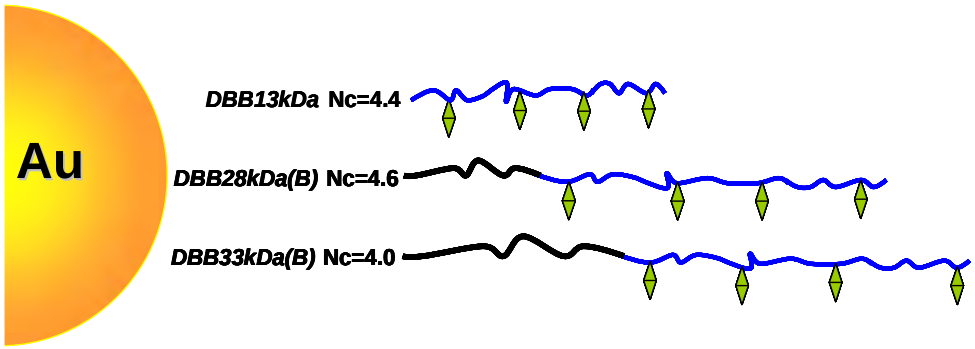

Figure IV. 36: DBB conjugates with different polymer lengths and different DBB density/chain used for grafting onto 20 nm AuNP: DBB13KDa – random copolymer; DBB28KDa(B) –block copolymer with 8 000 g.mol-1 spacer; DBB33KDa(B) – block copolymer with 12 000 g.mol^{-1} spacer.

IV.5.2.1. Steady state fluorescence analyses

Because DBB conjugates exhibit higher absorption (higher ε) compared to LY conjugates, and because their absorption maxima do not overlap with the maximum of the SPR band of AuNP, we could observe their presence on absorption spectra of grafted AuNP (peak at ~400 nm) (Figure IV. 37) and estimate the corresponding concentration and grafting density (Chapter III, Appendix III.6).

First, unlike grafted Ant-polymer conjugates, we note that, for the same polymer length (M_n=12 900g.mol^{-1}), the fluorescence signal recovered from AuNP-DBB13KDa could be properly detected. This is rather surprising, because in water free Ant-polymer conjugates showed higher fluorescence quantum yields (ϕ~0.02-0.045) in water compared to free DBB-polymer conjugate (ϕ < 1%). This observation confirms the complexity of studying chromophores in the vicinity of AuNP, depending on numerous parameters related to the chromophore (structure of ground and excited state, intrinsic photophysical characteristics: absorption / emission), suggesting that Ant-polymer conjugates chromophores are more prone to quenching in the presence of AuNP than DBB conjugates.

The 2nd observation was carried out by analyzing the relative emission intensities of grafted AuNP with different DBB conjugates (Figure IV. 37). While the number of chromophores *per* chain was similar (~4-5 DBB *per* chain), their length and architecture varied significantly (length: DBB13KDa < DBB28KDa(B) < DBB33KDa(B), B –block copolymer structures).
Like for LY grafted conjugates, the shape of TP chromophore-polymer conjugates emission spectra did not change after grafting onto AuNP.

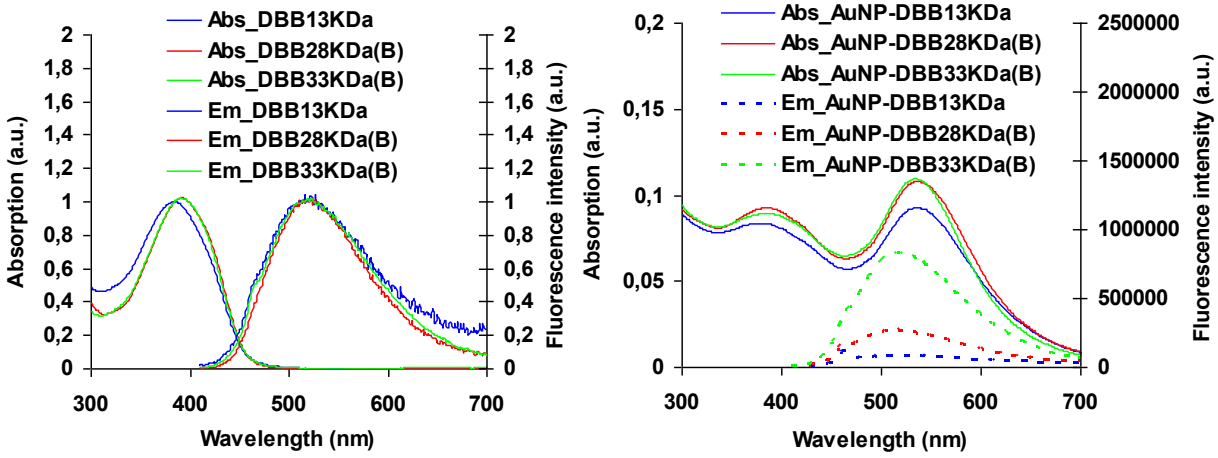

Figure IV. 37: Absorption/Emission spectra of DBB conjugates before (left) and after (right) grafting onto AuNP (λ_{ex}=400nm).

We note that for the same amount of absorbed light (similar absorptions at 400 nm), DBB conjugates grafted onto AuNP exhibited very different fluorescence intensities – increasing with the increasing

length of the grafted polymer, trend of fluorescence intensity: AuNP-DBB13KDa < AuNP-DBB28KDa(B) < AuNP-DBB33KDa(B)) (similar to previous observations with LY conjugates).
However, relative comparison between different AuNP-DBB grafted systems is not accurate, since DBB conjugates, exhibit significant differences in their quantum yields in water (0.01 for the short DBB13KDa *vs.* 0.05 and 0.06 for DBB longer block copolymer conjugates, Table IV. 11). Thus DBB block copolymer conjugates emit at least 5-6 times more than DBB13KDa in water. It appears then logical to record higher fluorescence intensities with these conjugates compared to the shorter DBB13KDa random conjugate (Table IV. 16).

We can however note (Table IV. 16) that relative emission of AuNP grafted with DBB conjugates does not correspond to the relative ratios differences between their fluorescence quantum yields. We believe that a higher extent of quenching exists in AuNP-DBB13KDa sample compared to the other two (AuNP-DBB28KDa(B) and AuNP-DBB33KDa(B)), due to the absence of a spacer between the AuNP surface and DBB chromophores (Figure IV. 36).
Moreover, these first results even point out that the "fluorescence recovery" of the longest DBB33KDa(B) grafted conjugates would be higher than that of DBB28KDa(B) grafted onto AuNP (Table IV. 16, Relative Emission). This last data still requires supplementary confirmation and a thorough quantitative study.

Table IV. 16: Fluorescent emission of DBB conjugates grafted onto AuNP. Grafting density calculated from their absorption at ~400nm.

Sample	ϕ	Fluorescence intensity	Relative Emission (to AuNP-DBB13KDa)	DBB conjugate absorption @400 nm	Polymer shell TEM (nm)	Length of stretched polymer chain (nm)*	Grafting density (chains/AuNP // chains/nm²)	Nb. DBB/ AuNP
(1) AuNP-DBB13KDa	*< 1%*	6,65 x 10^{+6}	1	0.024	4 ± 1	20	913 // 1.01	4017
(2) AuNP-DBB28KDa(B)	*5 %*	1,83 x 10^{+7}	(2)/(1) ~ 3	0.024	8 ± 1	48	750 // 0.82	3450
(3) AuNP-DBB33KDa(B)	*6 %*	4,95 x 10^{+7}	(3)/(1) ~8	0.021	13 ± 3	58	740 // 0.92	2960

*Calculated using the DP_n of the initial copolymer (degree of polymerization) and using –C–C– single bond length as 1.54A° and 109.5° as a bond angle between two –C–C– bonds.

As discussed for LY conjugates, the fluorescence emission of DBB conjugates grafted onto 20 nm AuNP increases with the increasing length of the polymer, illustrated by the increased polymer corona thickness measured by TEM, and the theoretical one (calculated as the length of the completely stretched polymer chain) (Figure IV. 38 a) and b)).

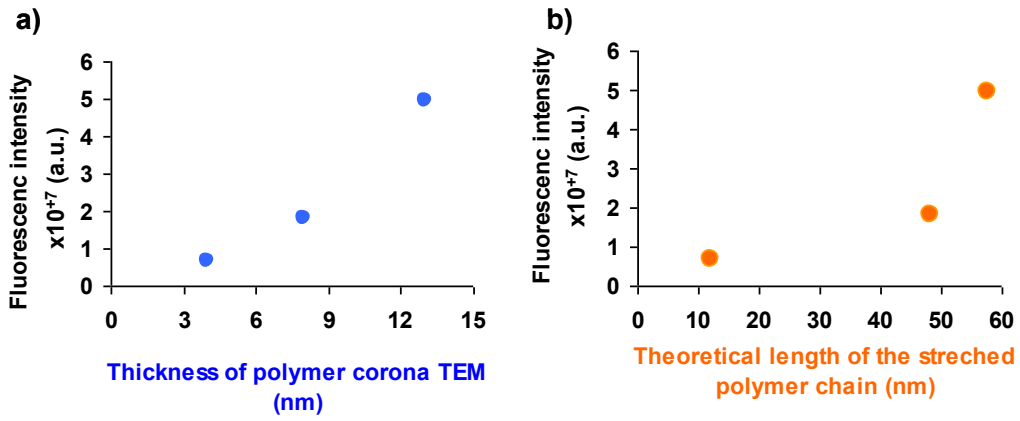

Figure IV. 38: Fluorescence intensity of DBB conjugates as a function of: a) TEM polymer corona thickness; b) theoretical length of the stretched polymer chain.

IV.5.2.2. Time-resolved fluorescence analyses

The quenching *via* metal resonance energy transfer was confirmed by time-resolved fluorescence analyses of AuNP-DBB13KDa *vs.* AuNP-DBB28KDa(B), showing faster decays for the grafted AuNP than for the free DBB13KDa conjugates (Figure IV. 39).

Figure IV. 39 illustrated how chromophores separated from AuNP surface *via* a spacer block (AuNP-DBB28KDa(B)), preserve their fluorescence showing a smaller decrease in fluorescence decay after grafting onto AuNP.

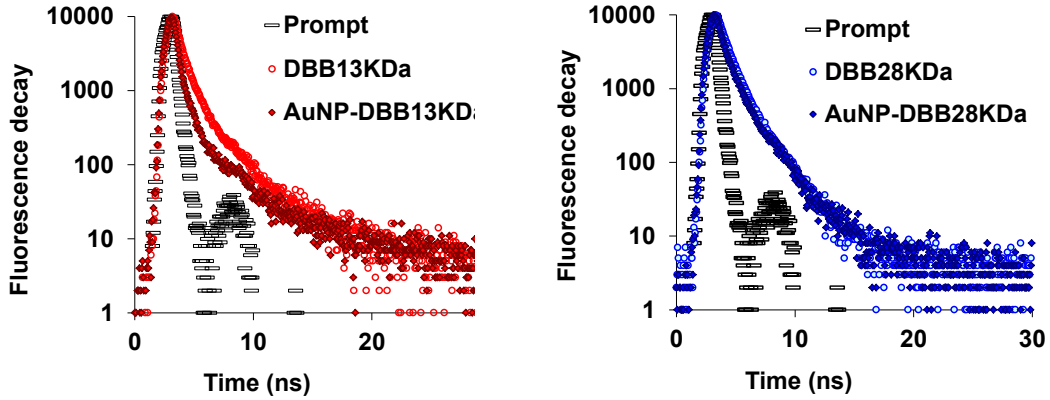

Figure IV. 39: Fluorescence decays of DBB conjugates:. Comparative fluorescence decays of DBB conjugates (DBB13KDa – red; DBB28KDa(B) – blue) before and after grafting onto AuNP (λ_{ex}=440nm, λ_{em}=500nm).

Even if the quantification of fluorescence decay rate constants and average lifetimes for DBB conjugates was not possible (τ < 200 ps, the instrumental detection limit), the presence of 20 nm AuNP has a significantly higher impact on the fluorescence decay of the shorter grafted DBB conjugate (DBB13KDa).

IV.5.2.3. Conclusion on AuNP-DBB conjugate systems

Like for LY conjugates, longer DBB conjugates exhibited higher fluorescence intensities after grafting onto AuNP, suggesting a distance-dependent behavior of DBB conjugates near AuNP. A thorough investigation of photophysical properties is still required with DBB grafted systems to better understand the photophysical phenomena in the vicinity of AuNP.

In the future, it would be interesting to determine the influence of AuNP on fluorescence properties under two-photon excitation and compare them with these data.

To summarize, this study described how fluorescence properties of grafted chromophore-polymer conjugates were affected by the presence of 20 nm AuNP.

As expected, fluorescence emission depended on the distance between chromophores and AuNP surface. High quenching was recorded at small chromophore-AuNP distances, which decreased with the increasing length of the polymer chain.

This distance was controlled by the density and the chemical nature of chromophores bound to the copolymer chain, influencing its conformation. We could show that TP Ant- and DBB-polymer conjugates (displaying stronger chromophore-chromophore and chromophore-Au interactions) are possibly located closer to AuNP surface than LY conjugates, leading to an increased fluorescence quenching (Figure IV. 40).

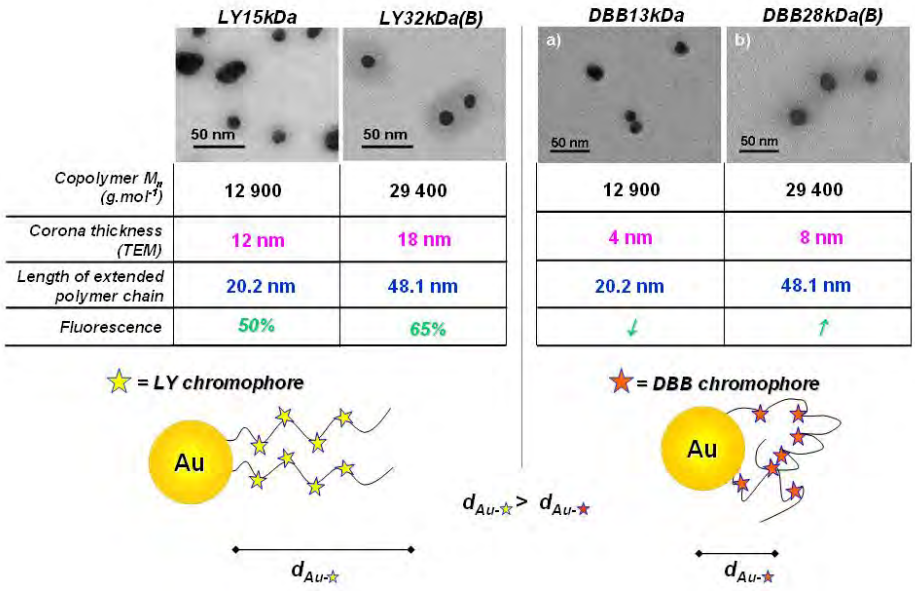

Figure IV. 40: Possible conformations of grafted TP conjugates *vs.* LY conjugate onto AuNP.

The representation above correlates the length of the polymer chain, the type of bound chromophore, and the corresponding fluorescence properties, partly explaining the higher fluorescence quenching of TP chromophore-polymer conjugates compared to LY conjugates, after grafting onto AuNP.

It should be recalled that a complete quenching has been recorder for Ant grafted conjugates, whereas LY and DBB conjugates partially preserved their fluorescence properties (Table IV. 17).

Table IV. 17: Correlation between SPR, and λ_{abs} / λ_{em} of chromophore-polymer conjugates on grafted AuNP fluorescence.

AuNP d~20 nm	Grafted conjugates	λ_{abs} / λ_{em}	Fluorescence?
SPR ~ 530 nm	LY conjugates	~430 / **~530**	YES
	Ant conjugates	**~500** / ~600	NO
	DBB conjugates	~400 / **~500**	YES

Could this be a consequence of a potential interaction between SPR and the spectral properties of the conjugates? This hypothesis would be sustained by the existing resonance between LY and DBB emission spectra (maxima at ~500-530 nm) and AuNP SPR band (maximum at ~530 nm), not present in the case of Ant conjugates. Further studies are needed to better understand these effects.

IV.5.3. The influence of AuNP diameter on photophysical properties of LY32KDa(B) conjugate

As exposed at the end of Chapter III (Section III.4.4), AuNP with increasing diameters (13 nm, 50 nm and 90 nm) have been grafted with LY32KDa(B) conjugate (J. Navarro). The photophysical properties of this conjugate before and after grafting onto 13 nm, 50 nm and 90 nm AuNP were determined using the cyanide method presented above.

In all the three cases, after dissolution of the Au core, a quantitative determination showed that the fluorescence of the grafted LY conjugate was lower than fluorescence of the corresponding free LY conjugate. The percentage of "fluorescence recovery" increased from 60% to 70% and 85% with the increasing Au core diameter (form 13 nm, to 50 nm and 90 nm, respectively) (Figure IV. 41). In the case of the ~20 nm AuNP, 'florescence recovery' was 65%.

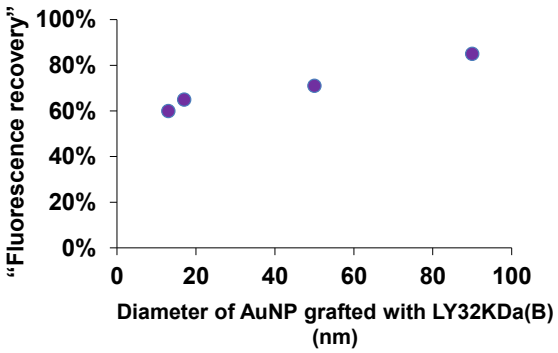

Figure IV. 41: Fluorescence recovery of LY32KDa(B) conjugates grafted onto 13 nm, 50 nm and 90 nm AuNP

LY32KDa(B) grafted onto 13 nm AuNP exhibit roughly the same fluorescence recovery (60%) compared to the value obtained after grafting onto 20 nm AuNP (65%). These similar results could be explained by the weak scattering component of AuNP with diameters $d_{Au} < 30$ nm (no enhancement). In the case of small AuNP, the only evidenced photophysical phenomenon would be the distance-dependent quenching of the fluorescence of chromophores near AuNP (evidenced in Section IV.5.1).

On the other hand, for 50 nm and 90 nm AuNP, the scattering component increases significantly along with the SPR intensity, inducing an increase in the overall fluorescence of grafted conjugates.

However, because the recorded fluorescence emission of grafted AuNP is the sum of quenching and enhancement processes, we can conclude that for spherical AuNP, with diameters $d_{Au} \leq 90$ nm, fluorescence quenching prevails over fluorescence enhancement.

This study experimentally evidenced the role of AuNP size in tuning the photophysical properties of chromophores near AuNP surfaces. The influence of AuNP shape (bipyramids, stars) on these properties is under investigation.

IV.6. Conclusion of Chapter IV

Photophysical properties of chromophore polymer conjugates have been studied from two different perspectives: i) the influence of the polymer chain on photophysical properties of bound chromophores; ii) the influence SPR after grafting of conjugates onto 20 nm AuNP.

The absorption and fluorescence emission properties of three classes of conjugates (LY, Ant and DBB) have been determined:

- LY-polymer conjugates: ε~10 000 $cm^{-1}.M^{-1}$; ϕ~0.30 (in water);
- Ant-polymer conjugates: ε~30 000 $cm^{-1}.M^{-1}$; 0.40 < ϕ < 0.80 (in chloroform); ε~20 000 $cm^{-1}.M^{-1}$; ϕ < 0.05 (in water);
- DBB-polymer conjugates: ε~50 000 $cm^{-1}.M^{-1}$; 0.15 < ϕ < 0.20 (in chloroform); ε~40 000 $cm^{-1}.M^{-1}$; $\phi \leq 0.05$ (in water).

It has been demonstrated that after coupling onto the polymer chain the local environment of the chromophores was sensitively changed, slightly decreasing the photophysical processes (absorption / emission) of bound chromophores compared to free chromophores. The decrease in fluorescence quantum yields strongly depended on the density of chromophores *per* chain, and on the type of chromophore-chromophore interactions. This phenomenon was more significant in the case of conjugates carrying hydrophobic TP chromophores.

TP water-soluble conjugates displayed very weak fluorescence quantum yields in water compared to organic media (chloroform). However, their strong one- and two-photon absorptions ensured high brightness values in water (reaching 9 000 $cm^{-1}.M^{-1}$), justifying their future testing for bioimaging and PDT applications (Chapter V). TP chromophore-polymer conjugates (Ant and DBB) exhibited high TPA cross section (σ_{TPA}~1000 GM) in water.

It has been also suggested that another advantage of the polymer chain could be its ability to increase the resistance to photobleaching of bound chromophores. This latter statement still requires experimental proof.

The influence of the AuNP was studied after grafting the water-soluble conjugates onto 20 nm AuNP. We evidenced that fluorescence quenching by energy / electron transfer to Au surface, controlled by chromophore-AuNP distance, could be reduced (and even avoided) by increasing the length of the conjugates. It has been shown, using the model system of LY-polymer conjugates, that fluorescence recovery increased form <10% to 90% when M_n increased from 2 000 $g.mol^{-1}$ to 35 000 $g.mol^{-1}$. While Ant-polymer conjugates grafted onto 20 nm AuNP had their fluorescence completely quenched in water by energy transfer to the AuNP, DBB and LY conjugates grafted onto 20 nm AuNP could retain some fluorescence thanks to their higher molecular weight.

These first studies, proved the interest of using multifunctional linear polymers to increase the photophysical response of chromophores near the surface of AuNP.

20 nm AuNP were however not the best choice to study enhancement phenomena. In this context, preliminary studies with larger AuNP (d_{Au} ~ 50 nm, 90 nm) and with AuNP with different shapes

(nanorods, nanobipyramids and nanostars) resulted in increased fluorescence recovery and even fluorescence enhancement (with nanobipyramids)[49] (post-doc of J. Navarro).

While one-photon properties (absorption / emission, fluorescence lifetime) were investigated and compared between bound and free chromophores, two-photon absorption properties, by TPEF technique, could not be evaluated in the presence of AuNP (first tests resulted in a completely attenuated fluorescence emission signal).
We suggest that Z-scan measurements, usually used to estimate TPA enhancement of chromophores *via* SPR, should be more appropriate than TPEF in this case. These experiments would provide preliminary information about the two-photon potential of hybrid AuNP in biology.

DBB-polymer conjugates, showed high quantum yields of singlet oxygen generation (Φ_{Δ}=0.47, in organic media ($CHCl_3$), proof of their potential for PDT applications. However, due to the lack of a proper analytic technique, this could not be carried out in aqueous medium, but would represent a perspective for the future. One possibility could be to estimate its generation in D_2O, where $^1O_2$ lifetime increases up to detectable levels (compared to the strong quenching in water). Other efficient indirect methods could also be implemented (*e.g.* using selective singlet oxygen sensors).[50]

In order to evaluate their potential for bioimaging and PDT applications, first biological results with TP conjugates and their corresponding grafted AuNP will be discussed in Chapter V.

IV.7. Experimental section

Materials

Lucifer Yellow Cadaverine ([N-(2-Aminopentyl)-4-amino-3,6-disulfo-1,8-naphthalene, dipotassium salt]) was purchased from FluoProbe®.
The synthesis of free TP chromophores was previously described in the literature.[37]
All solvents (analytical grades) were purchased from Sigma Aldrich or Fischer Scientific and used without further purification.

Instruments and analytical methods

UV-Vis spectroscopy

UV-Vis spectra were recorded on a Jasco V-670 spectrophotometer at ambient temperature using 1 cm optical path length quartz cell. Extinction coefficients ε were calculated using Beer-Lambert law at 430 nm for LY-polymer conjugates, at 470 nm for Ant-polymer conjugates, and at 390 nm for DBB-polymer conjugates (as well as for grafted AuNP).

Steady-state fluorescence spectroscopy

Fluorescence emission spectra were recorded on a Horiba-Jobin Yvon Fluorolog-3 spectrofluorimeter equipped with a R928P (PMT) detector. Measurements were performed under Right Angle geometry, at ambient temperature, using a 1 cm optical path length quartz cell. Excitation wavelengths were 470 nm, 430 nm and 390 nm for Ant-, LY- and DBB-compounds, respectively. Entrance (excitation) / exit (emission) slits depended on the chromophore and on the reference used: 1nm / 2nm for Ant- and LY-derivatives, 3nm / 3nm for DBB-derivatives. Integration time = 0.1s.

Fluorescence quantum yields

Fluorescence quantum yield, ϕ, was calculated according to Eq. (2) for diluted solutions having an photophysical density (absorbance) lower than 0.1. References were rubrene (ϕ=0.27 in methanol) and Coumarin 153 (ϕ=0.45 in methanol) for Ant- and DBB-derivatives, respectively.

Quantum yields of singlet oxygen generation

Singlet oxygen generated by DBB derivatives in $CHCl_3$ solution (Abs_{max}=0.1) was recorded by detection of $^1O_2$ phosphorescence at 1270 nm. The instrumental setup for singlet oxygen detection is similar to the one used for fluorescence spectroscopy. Samples were excited at 390 nm using a flash-lamp and the response signal was recorded between 1225nm and 1325nm using SPEX® DSS-IGA020L InGaAs detector which operates at liquid N_2 temperature to minimize thermal noise. The slit apertures are much larger than for fluorescence measurements: entrance slit=14, exit slit=40; integration time – 1s. Quantum yield of singlet oxygen generation (Φ_Δ) was calculated using Stern-Volmer model and phenalenone molecule as reference (Φ_Δ=1), according to Eq. (11).

Time-resolved fluorescence spectroscopy

Time-resolved fluorescence decays were were measured by the method of time-correlated single-photon counting using a picosecond spectrofluorimeter from Horiba Jobin Yvon iHR320. The instrument was equipped with a FluoroHub single photon counting controller and a R928P (PMT) detector. A laser head or a nano-LED pulsed diode powered by a pulsed diode controller (IBH) was used as the excitation light source. The excitation wavelength was 469 nm for Ant-derivatives, or 440 nm for LY- and DBB-derivatives, respectively. The emission monochromator was set to 560 nm, 530 nm and 500 nm for Ant-, LY-, and DBB-derivatives, respectively. Data Station software was used for running the spectrometer, and for the deconvolution and the analysis of decays.

Fluorescence anisotropy decays

Fluorescence anisotropy decay measurements were carried out using the same experimental set-up and detection system, by recording the fluorescence with a polarizer alternating between parallel and perpendicular orientations to the excitation polarization, with a dwell time of 30 s in each position to

correct for excitation intensity drifts: emission collected at 560 nm at four different polarization configurations, VV, VH, HH, and HV, in the case of Ant-polymer conjugates.
All samples were analyzed in diluted water or chloroform solutions (10^{-7} – 10^{-8} mol.L^{-1} chromophore).

Two-Photon Fluorescence Excitation spectroscopy

Two-photon Absorption (TPA) cross-section spectra were obtained between 700-950 nm by up-conversion fluorescence using a Ti:sapphire femtosecond laser (Coherent Verdi-V5 pump coupled with a femtoseconde MIRA 900 cavity) with an intensity power fixed at 50 mW and a S2000 Ocean Optics Spectrometer. The excitation beam was collimated over the quartz cell (10mm) with a pulse frequency of 80MHz. The measurements were conducted in an intensity regime where the fluorescence signal showed a quadratic dependence on the intensity of the excitation beam, as checked for all samples. Detector integration time was set at 1s. Measurements were performed at room temperature in chloroform or water, at a concentration of 10^{-4} mol.L^{-1} chromophore.

Two-photon absorption cross section

TPA cross-section values (σ_{TPA}) were obtained using Eq. (14). Calibration was performed by comparison with the published two-photon absorption spectrum of Coumarin-307 (σ_{TPA}=0.56 in ethanol) between 700 and 900 nm.[12] The uncertainty in the measured cross-sections is about 20%.

References

[1] a) **Gold Nanoparticles Quench Fluorescence by Phase Induced Radiative Rate Suppression,** E. Dulkeith, M. Ringler, T. A. Klar, J. Feldmann, *Nano Lett.* **2005**, *5(4)*, 585-589.

b) **Fluorescence Quenching of Dye Molecules near Gold Nanoparticles: Radiative and Nonradiative Effects,** E. Dulkeith, A. C. Morteani, T. Niedereichholz, T. A. Klar, and J. Feldmann, S. A. Levi, F. C. J. M. van Veggel, D. N. Reinhoudt, M. Möller, D. I. Gittins, *Phys. Rev. Lett.* **2002**, *89 (20)*, 203002.1-203002.4.

[2] **Spectrochemical Analysis,** J. D. J. Ingle and S. R. Crouch, Prentice Hall, **1988**, New Jersey.

[3] **Standard for Measuring Quantum Yield,** Protocol for fluorescence quantum yield determination employed by Nanoco Technologies Ltd. **2008**.

[4] C**hapter 3: Characteristics of fluorescence emission, Molecular Fluorescence: Principles and Applications,** B. Valeur, **2001.**

[5] a) **Analysis of time-resolved rfluorescence anisotropy decays,** A. J. Cross, G. R. Fleming, *Biophys. J. Biophysical Society* **1984**, 45-56.

b) **Porphyrin-Cored 2,2-Bis(methylol)propionic Acid Dendrimers,** R. Vestberg, A. Nyström M. Lindgren, E. Malmström, A. Hult, *Chem. Mater.* **2004**, *16*, 2794-2804.

[6] **Polarisation de la Lumiere de Fluorescence. Vie Moyene des Molecules Fluorescentes,** F. Perrin, *J. Physique* **1926**, *7*, 390-401.

[7] **Physical Mechanisms of Generation and Deactivation of Singlet Oxygen,** C. Schweitzer, R. Schmidt, *Chem.Rev.* **2003**, 1685-1757.

[8] **Singlet Oxygen Quantum Yields of Different Photosensitizers in Polar Solvents and Micellar Solutions,** W. Spiller, H. Kliesch, D. Wöhrle, S. Hackbarth, B. Röder, G. Schnurpfeil*. J. Porph. Phthaloc.* **1998**, 145-158.

[9] **Quantum Yields for the Photosensitized Formation of the Lowest Electronically Excited Singlet State of Molecular Oxygen in Solution,** F. Wilkinson, W. P.Helman, A. B. Ross, *J. Phys. Chem. Ref. Data* **1993**, *22*, 113-262.

[10] **Über Elementarakte mit zwei Quantensprüngen,** M. Göppert-Mayer, *Ann. Phys.* **1931**, *401*, 273-294.

[11] **Sensitive measurement of optical nonlinearities using a single beam,** M. Sheik-Bahae, A. A. Said, T.-H. Wei, D. J. Hagan, E. W. Van Stryland*, IEEE J. Quantum Electron* **1990**, *26*, 760-769.

[12] **Measurement of two-photon excitation cross sections of molecular fluorophores with data from 690 to 1050 nm,** C. Xu, W. W. Webb, J. *Opt. Soc. Am. B* **1996**, *13*, 481-491.

[13] **Surface polaritons - propagating electromagnetic modes at interfaces,** E. Burstein, *J.Vac.Sci.Technol.* **1974**, *11*, 1004-1019.

[14] **Optical Properties of Metal Clusters; Springer-Verlag,** U, Kreibig, M. Vollmer, Heidelberg, Germany, **1995**, Vol. *25*.

[15] **The optical properties of metal nanoparticles: the influence of size, shape and dielectric environment,** K.L. Kelly, E. Coronado, L. L. Zhao, G. C. Schatz, *J Phys Chem B* **2003**, *107*, 668-677.

[16] **Calculated Absorption and Scattering Properties of Gold Nanoparticles of Different Size, Shape, and Composition: Applications in Biological Imaging and Biomedicine,** P. K. Jain, K.Seok Lee, I. H. El-Sayed, M. A. El-Sayed, *J. Phys. Chem. B* **2006**, *110*, 7238-7248.

[17] a) **Photophysical aspects of molecular probes near nanostructured gold surfaces,** S. Kumar Ghosh, T. Pal, *Phys. Chem. Chem. Phys.* **2009**, *11*, 3831-3844.

b) **Chromophore-Functionalized Gold Nanoparticles,** K. G. Thomas, P. Kamat, *Acc. Chem. Res.* **2003**, *36*, 888-898.

[18] **Resonance energy transfer from a fluorescent dye to a metal nanoparticle,** S. Bhowmick, S. Saini, V. B. Shenoy, B. Bagchi, J. *Chem. Phys.* **2006**, *125*, 181102 (1-6).

[19] a) **Radiative decay engineering 3. Surface plasmon-coupled directional emission,** J. R. Lakowicz, *Anal. Biochem.* **2004**, *324*, 153-169.

b) **Radiative decay engineering 5: metal-enhanced fluorescence and plasmon emission,** J. R. Lakowicz, *Anal. Biochem.* **2005**, *337*, 171–194.

c) **Plasmonics in Biology and Plasmon-Controlled Fluorescence,** J. R. Lakowicz, *Plasmonics* **2006**, *1*, 5-33.

d) **Plasmon light scattering in biology and medicine: new sensing approaches, visions and perspectives,** K. Aslan, J. R. Lakowicz, C. D. Geddes, *Curr. Opin. Chem. Biol.* **2005**, *9*, 38-544.

e) **Metal-enhanced fluorescence: an emerging tool in biotechnology,** K. Aslan, I. Gryczynski, J. Malicka, E. Matveeva, J. R. Lakowicz, C.D Geddes, *Curr. Opin. Chem. Biol.* **2005**, *16*, 55-62.

[20] a) **Metal-enhanced phosphorescence,** Y. Zhang, K. Aslan, S. N. Malyn, C. D. Geddes, *Chem. Phys.Lett.* **2006**, *427*, 432-437.

b) **Metal-Enhanced Phosphorescence: Interpretation in Terms of Triplet-Coupled Radiating Plasmons,** Y. Zhang, K. Aslan, Mi. J. R. Previte, S. N. Malyn, C. D. Geddes, *J. Phys. Chem. B* **2006**, *110*, 25108-25114.

[21] **Metal-enhanced Singlet Oxygen Generation: A Consequence of Plasmon Enhanced Triplet Yields,** Y. Zhang, K. Aslan, M. J. R. Previte, C. D. Geddes, *J. Fluoresc.* **2007**, *17*, 345-349.

[22] **Surface Plasmons Control the Dynamics of Excited Triplet States in the Presence of Gold Nanoparticles,** N. L. Pacioni, M. Gonzalez-Bejar, E. Alarcon, K. L. McGilvray, J. C. Scaiano*, J. Am. Chem. Soc.* **2010**, *132*, 6298-6299.

[23] **Plasmonic engineering of singlet oxygen generation,** Y. Zhang, K. Aslan, M. J. R. Previte, C. D. Geddes, *PNAS* **2008**, *105(6)*, 1798-1802.

[24] a) **Enhancement and Quenching of Single-Molecule Fluorescence,** P. Anger, P. Bharadwaj, L. Novotny, *Phys. Rev. Lett.* **2006**, *96*, 113002

b) **Spectral dependence of single molecule fluorescence enhancement,** P. Bharadwaj, L. Novotny, *Opt. Express* **2007**, *15(21)*, 14266-14274.

[25] **The generalized multiple multipole technique for computational electromagnetics,** C. Hafner, Artech, **1990**.

[26] Near-field coupling of a single fluorescent molecule and a spherical gold nanoparticle, T. Härtling, P. Reichenbach, and L. M. Eng, *Opt. Express* **2007**, *15(20)*, 12806-12817.

[27] **Radiative decay engineering 5. Non-quenching metallic surfaces and plasmon emission, J. R.** Lakowicz, *Anal. Biochem.* **2005**, in press.

[28] ***Metal-enhanced fluorescence: Surface plasmons can radiate a fluorophore's structured emission,*** Y. Zhang, K. Aslan, and M. J. R. Previte, C. D. Geddes, *Appl. Phys. Lett.* **2007**, *90*, 053107(1-3).

[29] a) **Two-photon-excited fluorescence enhanced by a surface plasmon,** H. Kano, S. Kawata, *Opt. Lett.* **1996**, *21*, 1848-1850.,

b) **Multiphoton excitation of fluorescence near metallic particles: Enhanced and localized exciation,** I. Gryczynski**,** J. Malicka, Y. Shen, Z. Gryczynski, J. R. Lakowicz, *J. Phys. Chem. B* **2002**, *106*, 2191-2195.

c) **Near-Field Probing Surface Plasmon Enhancement Effect on Two-Photon Emission,** Y. Shen, J. Swiatkiewicz, T.-C. Lin, P. Markowicz, N. Prasad Paras*, J. Phys. Chem. B* **2002**, *106*, 4040-4042.

d) **Plasmonic Enhancement of the Two Photon Absorption Cross Section of an Organic Chromophore Using Polyelectrolyte-Coated Gold Nanorods,** S. T. Sivapalan, J. H. Vella, T. K. Yang, M. J. Dalton, R. N. Swiger, J. E. Haley, T. M. Cooper, A. M. Urbas, L.-S. Tan, C. J. Murphy, *Langmuir* **2012**, *28*, 9147-9154.

[30] **Surface Plasmon Enhanced Fluorescence of Dye Molecules on Metal Grating Films,** Y. Jiang, H.-Y. Wang, H. Wang, B.-R. Gao, Y.Hao, Y. Jin, Q.-D. Chen, H.-B. Sun, J*. Phys. Chem. C* **2011**, *115*, 12636-12642.

[31] **PhD, "Water-soluble associative polymers: synthesisi and photophysical of poly(*N*,*N*-dimethylacrylamide) and poly(*N*-acryloylmorpholine)", 2006**, P. Relogio, Instituto Superior Técnico Lisboa, Chapter IV –"Highly Fluorescent Poly(NAM)".

[32] a) **Synthesis of 3,6-disulfonated 4-aminonaphthalimides,** W. W. Stewart, *J. Am. Chem. Soc.* **1981**, *103*, 7615-7620

b) **Lucifer dyes—highly fluorescent dyes for biological tracing,** W. W. Stewart, *Nature* **1981**, *292*, 17-21.

[33] Excited-state dynamics of the fluorescent probe Lucifer Yellow in liquid solutions and in heterogeneous media, A. Fürstenberg, E. Vauthey, *Photochem. Photobiol. Sci.* **2005**, *4*, 260-267.

[34] **Hydrogen Bonding and Electronic Transitions : The Role of the Franck-Condon Principle,** G. C. Pimentel, *J. Am. Chem. Soc.* **1957***, 79(13)*, 3323-3326.

[35] **Aggregation properties of a HPMA-camptothecin copolymer in isotonic solutions,** G. Chirico, M. Collini, F. Olivini, M. Zamai, E. Frigerio, V. R. Caiolfa, *Biophysical Chemistry* **2004**, *110*, 281-295.

[36] **Two-photon absorption standards in the 550-1600 nm excitation wavelength range,** N. S. Makarov, M. Drobizhev, A. Rebane, *Optics Express* **2008**, *16(6)*, 4029-4047.

[37] a) **Photodynamic therapy and two-photon bio-imaging applications of hydrophobic chromophores through amphiphilic polymer delivery,** T.Gallavardin, M. Maurin, S. Marotte, T. Simon, A.-M. Gabudean,Y. Bretonnière, M. Lindgren, F. Lerouge, P. L. Baldeck, O. Stéphan, Y. Leverrier, J. Marvel, S. Parola, O. Maury and C. Andraud, *Photochem Photobiol Sci.* **2011**, *7*, 1216-1225.

b)) **Biocompatible well-defined chromophore–polymer conjugates for photodynamic therapy and two-photon imaging,** C. Cepraga, T. Gallavardin, S. Marotte, P.-H. Lanoë, J.-C. Mulatier, F. Lerouge, S. e Parola, M. Lindgren, P. L. Baldeck, J. Marvel, O. Maury, C. Monnereau, A. Favier, C. Andraud, Y. Leverrier, M.-T. Charreyre, *Polym. Chem*. **2013**, *in press.*

[38] **Integrin-Targeting Block Copolymer Probes for Two-Photon Fluorescence Bioimaging,** S. Biswas, X. Wang, A. R. Morales, H.-Y. Ahn, K. D. Belfield, *Biomacromol.* **2011**, *12*, 441-449.

[39] **La fluorescence des solutions. Polarisation. Vie moyenne des molécules dans l'état excité, Francis Perrin,** *J. de Phys.* **1926**, *7*, 390-401.

[40] **HomoFRET Fluorescence Anisotropy Imaging as a Tool to Study Molecular Self-Assembly in Live Cells,** F. T. S. Chan, C. F. Kaminski, G. S. Kaminski Schierle, *ChemPhysChem* **2011**, *12(3)*, 500-509.

[41] **Molecular Fluorescence: Principles and Applications,** V. Bernard **200**, Wiley-VCH, p.29.

[42] **Phenalenone, a universal reference compound for the determination of quantum yields of singlet oxygen $O_2(^1\Delta_g)$ sensitization,** R. Schmidt, C. Tanielian, R. Dunsbach, C. Wolff, *J. Photochem. Photobiol. A: Chem* **1994**, *79*, 11-17.

[43] a) **Charge-Transfer Quenching of Singlet Oxygen $O_2(\Delta g)$ by Amines and Aromatic Hydrocarbons,** A. P. Darmanyan, W. S. Jenks, *J. Phys. Chem. A* **1998**, *102*, 7420-7426.

b) **Quenching of Singlet Oxygen by Aliphatic Amines,** B. M. Monroe, *J. Phys. Chem.* **1977**, *81* (19), 1861-1864.

[44] Singlet Oxygen Chemistry in Water. 2. Photoexcited Sensitizer Quenching by O2 at the Water-Porous Glass Interface, J. Giaimuccio, M. Zamadar, D.Aebisher, G. J. Meyer, A. Greer, *J. Phys. Chem. B* **2008**, *112*, 15646–15650.

[45] **PhD 2010, Chromophore à absorption biphotonique pour l'imagerie et la photothérapie dynamique : synthèse, vectorisation, greffage sur nanoparticules d'or et propriétés spectroscopique,** T. Gallavardin.

[46] Synthesis, Stability, and Cellular Internalization of Gold Nanoparticles Containing Mixed Peptide-Poly(ethylene glycol) Monolayers, Y. Liu, M.K. Shipton, J. Ryan, E. D. Kaufman, S. Franzen, D. L. Feldheim, *Anal. Chem.* **2007**, *79*, 2221-2229.

[47] **Distance-Dependent Fluorescence Quenching on Gold Nanoparticles Ensheathed with Layer-by-Layer Assembled Polyelectrolytes,** G. Schneider and G.Decher, N. Nerambourg, R. Praho, M. H. V. Werts, M.Blanchard-Desce, *Nano Lett.* **2006**, *6(3)*, 530-536.

[48] **Fluorescent Core-Shell Ag@SiO2 Nanocomposites for Metal-Enhanced Fluorescence and Single Nanoparticle Sensing Platforms,** K. Aslan, M. Wu, J. R. Lakowicz, C. D. Geddes, *J. Am. Chem. Soc.* **2007**, *129*, 1524-1525.

[49] **Synthesis, electron tomography and single-particle optical response of twisted gold nano-bipyramids,** J. R. G. Navarro, D. Manchon, F. Lerouge, E. Cottancin, J. Lermé, V. Bonnet, F. Chaput, A. Mosset, M. Pellarin S. Parola, *Nanotechnology* **2012**,*23(14)*, 145707-145715.

[50] **Highly reactive oxygen species: detection, formation, and possible functions,** W. Freinbichler, M. A. Colivicchi, C. Stefanini, L. Bianchi, C. Ballini, B. Misini, P. Weinberger, W. Linert, D. Vareslija , K. F. Tipton, L. Della Corte, *Cell. Mol. Life Sci.* **2011**, *68*, 2067-2079.

Chapter V: Biological evaluation

All biological tests were performed by Sophie Marotte, Yann Leverrier, Jacqueline Marvel at INSERM U851 Lyon

V.1. Introduction

The TP conjugates and their corresponding grafted AuNP were designed to be used as nano-probes for TP bioimaging and photodynamic therapy (PDT) applications.

Taking into account their optical properties (Chapter IV), the goal in this chapter was to evaluate the properties of the TP chromophore-polymer conjugates in cells, before and after grafting onto AuNP, by addressing the following questions:

i) Are TP-polymer conjugates (and their corresponding grafted AuNP) non-toxic in the absence of photoactivation?

ii) Is their cell uptake favored compared to free chromophores?

iii) Can TP-polymer conjugates (and grafted AuNP) be used as probes for fluorescence microscopy under one- and two-photon excitation?

iv) Can DBB-polymer conjugates (and grafted AuNP) induce the death of cancer cells upon photoactivation?

It is important to note that an efficient bio-probe, aimed for bioimaging or PDT, would ideally exhibit the following behavior in cells (Figure V. 1):

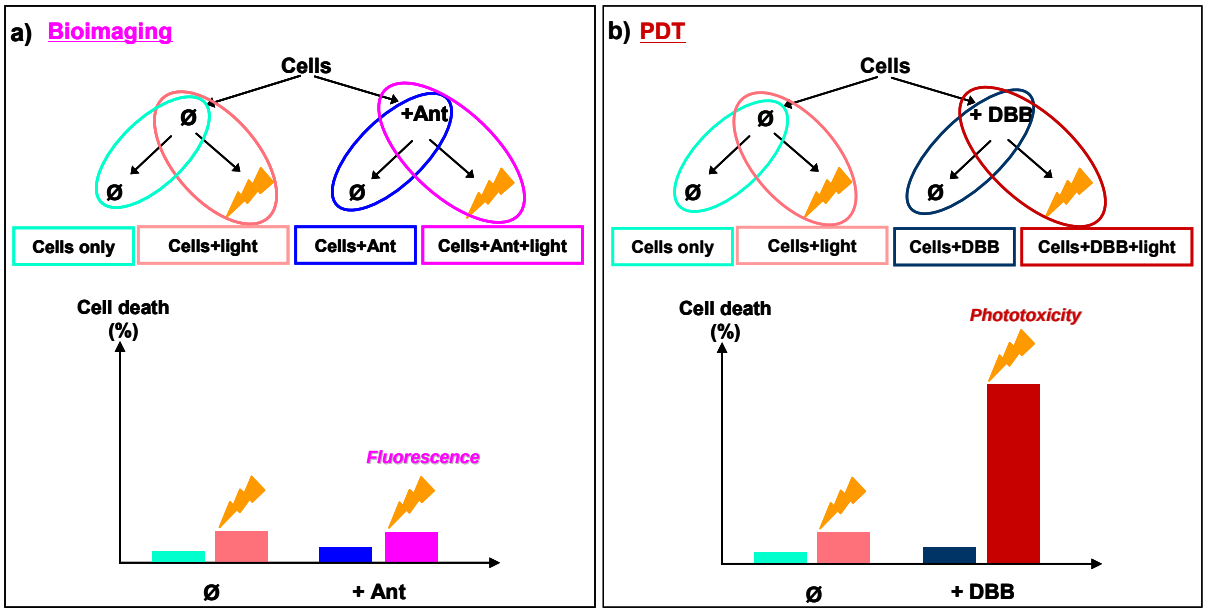

Figure V. 1: a) The effect of light excitation on fluorescent probes (Ant-conjugates) incubated into cells; b) The effect of light excitation on photosensitizing probes (DBB-conjugates) incubated into cells.*

a) An ideal fluorescent probe for bioimaging should be non-toxic for cells (in the dark and under light excitation) and exhibit efficient fluorescence properties in cellular medium after light excitation (Figure V. 1 a)).

b) An ideal photosensitizing probe (PS) for PDT should be non-toxic in the dark, but become phototoxic and induce cell death upon light irradiation (Figure V. 1 b)).

* Sophie Marotte, INSERM Lyon.

Toxicity and phototoxicity depend both not only on the nano-probes (concentration, way of encapsulation, etc.), but also on the conditions of light excitation.

In order to better understand the biological activity of our nano-probes, the principles of TP microscopy and the possible mechanisms of PDT will be briefly reported in the first part of the chapter (Section V.2).
Then, the cell uptake and cytotoxicity of the polymer probes will be first investigated in Section V.3. Additionally, one- and two-photon bioimaging (Section V.4) and phototoxicity effects (Section V.5) will be discussed.

The samples tested in this chapter are listed below:

- 6Ant-H and 4DBB-H, 10DBB-H, and 4DBB-AEM polymer conjugates;
- 45 nm / 65 nm / 80 nm spherical AuNP grafted with DBB32KDa(B) polymer conjugate compared with the free conjugate.
- 20 nm AuNP were not tested due to lack of time.

V.2. Two-Photon Excited Fluorescence bioimaging and Photodynamic Therapy

In order to better understand the results presented in Section V.4 and V.5 using our nano-probes, a brief presentation of TPEF microscopy and PDT will be exposed below.

V.2.1. Two-Photon Excited Fluorescence microscopy

The development of TPEF microscopy[1] was pioneered by Winfried Denk in the laboratory of Watt W. Webb at Cornell University, who combined the idea of two-photon absorption (TPA) with the use of a laser scanner.[2] The investigators noted that the TPA process (detailed in Chapter IV) can be exploited to implement microscopy imaging in three dimensions (3D), thanks to its unique advantages resulting from TPA phenomenon, which will be briefly highlighted below.

Advantages and Limitations

Conventional microscopy enables an enlarged image by shinning light right through the sample. In this case, the information inside the thickness of the sample is blurred out, due to the out-of-focus noise created by the diffraction of light.

This important limitation of conventional microscopy could be overcome with the invention of confocal microscopy in the 1960s, which applies a new method referred as 'optical sectioning', enabling to selectively image a particular levels within a section of the sample. The information above that level and below that level is thus discarded from the image. Moreover, by reassembling the 2D confocal microscopy images at various depths, a 3D reconstructed picture of the entire sample can be obtained.

Unlike confocal microscopy, which allows 3D reconstruction of multiple 2D images by limiting the observation volume (restricted to the focal plane), TPEF microscopy enables to achieve 3D resolved images by limiting the excitation volume (~1μm^3).[3 4]

One important difference between confocal microscopy, which operates in the visible range of the spectrum, and TPEF microscopy, which operates in the NearIR spectral region (at twice the wavelength of one-photon microscopy), is that TPEF microscopy enables to obtain images deeper inside tissues (2-3 times deeper).[5]

Nonetheless, TPEF microscopy results in a lower spatial resolution compared to confocal microscopy, since the diffraction-limited focal spots widen as the excitation wavelength increases.[3]

A thorough comparison of two latter microscopy techniques is given in Table V. 1.

Table V. 1: Advantages and limitations of TPEF vs. confocal microscopy.[3]

Description	Advantages	Limitations
Confocal microscopy	- Capable of optical sectioning ability. - Rejects the light coming from out-of-focus regions above and below the scanned section. - 3D reconstruction is possible, using a sequence of sections taken at various depths. - Can generate images based on specimen refractive index variation.	- Requires the use of pinhole apertures to reject out-of-focus light. - Is alignment-sensitive due to the presence of pinholes. - Inside thick specimens, scattering of fluorescent photons is inevitable, causing a significant loss of these photons at the confocal pinhole. - Usually uses UV-Vis light excitation.
TPEF microscopy	- Requires no pinhole aperture and minimizes signal loss (less alignment sensitive). - Two-photon excitation wavelengths are typically about twice the one-photon excitation wavelengths, ensuring higher penetration depth of the light. - Is characterized by a limited focal volume (sub-femtolitre), leading to decreased photodamage and 3D resolved images.	- Is characterized by lower spatial resolution, (approximately half the resolution under one-photon microscope), because of higher excitation wavelengths. (The microscope resolution is inversely proportional to the wavelength of light used for excitation.)

TPEF is an expensive technique, still in development, but its potential for noninvasive biological studies (two-photon imaging, diagnostic or even therapy) is well demonstrated,[6] thanks to the following characteristics:

- The two-photon excitation wavelength is typically in the 700–1100 nm spectral range (called “therapeutic window”), where water, biomolecules and tissue are less absorbing and scattering, allowing *in vivo* deep-tissue imaging and therapy.
- Limited excitation volume restricts the irradiation to an approximately 1 μm^3, limiting the out-of-focus photodamage of living tissues and the photobleaching of fluorescent probes; it also makes the technique ‘self-confocal’ allowing 3D resolved imaging.

V.2.2. Photodynamic therapy (PDT)

PDT is a real opportunity to replace many invasive treatments. Even if it is often discussed in the framework of cancer therapy, PDT appears well placed for use in different non-oncological indications as for example AMD (Age-related Macular Degeneration), ophthalmology, virology, or atherosclerosis.[7 12]

Regarding its way of action, PDT requires the use of i) a photoactivable probe, referred as photosensitizer, (PS), ii) light of an appropriate wavelength, iii) and molecular oxygen (*cf.* General Introduction).[8]

After activation by light of an appropriate wavelength, a PS can undergo in biological medium mainly three types of reactions (Figure V. 2).[9 10]

- In its excited singlet state (^{1}PS*, Figure V. 2), the PS can directly interact with species present in the biological medium (type III reactions).

- When the PS decays to its triplet excited state (^{3}PS*, Figure V. 2), it can either interact with oxygen to form radicals or radical ions, by proton or electron transfer (type I reactions),
- or it can transfer its energy to molecular oxygen, leading to the formation of singlet oxygen ($^1O_2$), which is generally accepted as the main damaging species in PDT, (type II reactions).

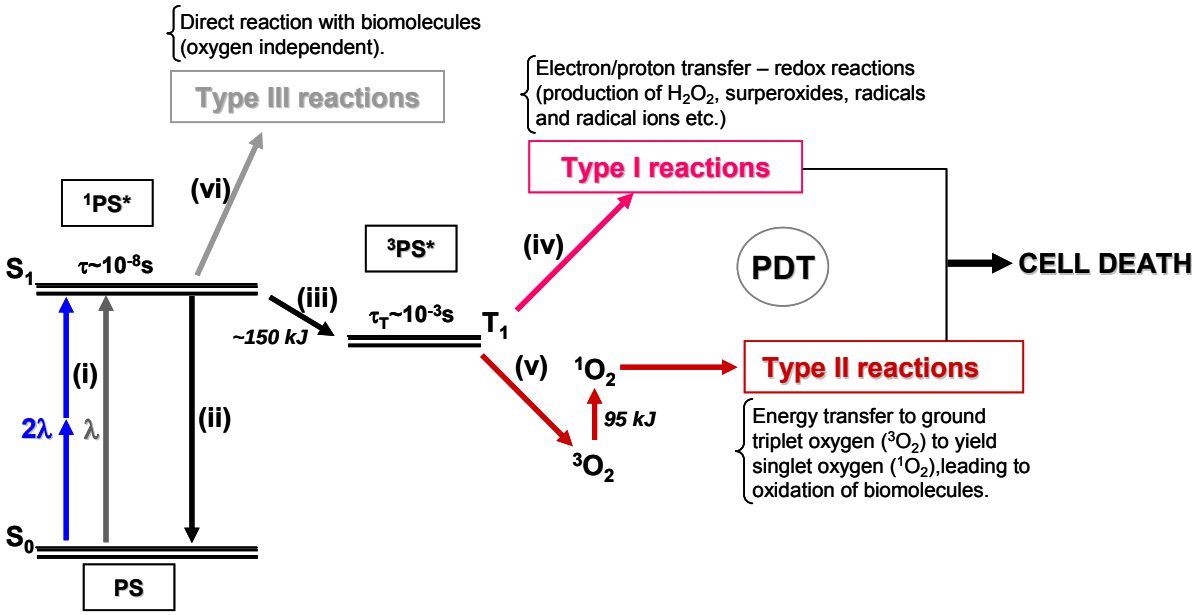

Figure V. 2: Simplified Perrin-Jablonski diagram explaining the mechanisms triggering PDT process: (i) one- or two-photon absorption; (ii) fluorescence; (iii) intersystem crossing; iv) excited triplet state direct reaction with species in the environment (by proton or electron transfer) to form cytotoxic radicals or radical ions; (v) excited triplet state energy transfer to molecular oxygen to form cytotoxic singlet oxygen; (vi) excited singlet state direct reaction with biomolecules (oxygen independent reactions).

Type I and type II reactions occur in the presence of oxygen and have been classified as possible mechanisms of photodynamic action (defined in 1941 as the photooxidation of biological substrates in the presence of molecular oxygen and a sensitizing agent).[11]

Therefore, PDT depends on at least 4 factors: (i) the concentration of the PS; (ii) the concentration of molecular oxygen ($^3O_2$); (iii) the appropriate excitation wavelength; (iv) the intensity of the excited light. It is clear that appropriate choices of PS type and dose, excited light wavelength, and light dose determine the efficacy and safety of PDT.[12]

Advantages and Limitations

In cancer therapy, PDT has several advantages:[13]

- It works virtually on all types of cancers.
- Because there are no cumulative toxic effects, the procedure can be repeated several times.
- Localized illumination enables specific tumor treatment without destruction of normal tissues.
- It is usually an outpatient procedure (not requiring the stay overnight) and leaves minimal scarring of the treated zone.
- PDT has been proven to be cost-effective and to provide increased life expectancy, compared with other treatments (surgery or chemotherapy).

Despite the numerous benefits described above, there are some limitations:

- PDT is a local treatment, therefore inefficient for widespread metastases.
- Due to light depth limitation of one-photon linear PDT (excitation in the UV-Vis spectral range, characterizing most existing molecular PS), PDT is more effective for small tumors accessible for light excitation. Bulky tumors may also be treated by PDT, however requiring repeated light exposure.
- The risk of light absorption and scattering of biological species (particularly between 400 nm – 600 nm) is one of the most important limitations in PDT.

  Typically, the useful range of wavelengths for therapeutic activation of the PS is 700 nm – 900 nm, in order to avoid interference with biological medium, increase the penetration depth inside tumors, thus improve the PDT treatment efficacy.

In this context, PS molecules absorbing in the NearIR region would be clinically relevant for PDT, allowing the treatment of tumors deeper and safer into the tissues.

Photosensitizers use in clinic

The very first generation of PS used in PDT was based on hematoporphyrin derivatives (HpD). Photofrin®, composed of a mixture of HpD with several absorption wavelengths, is the first PDT drug receiving FDA approval. In clinic, Photofrin® is usually excited at 630 nm, where light can penetrate deeper inside tissues. However, at 630 nm its absorption is relatively weak and high light doses are required for tumor treatment. Other significant limitations of the first generation PS consist in the lack of tumor specificity, and a high photosensitivity due to PS poor clearance (requiring 4-12 weeks to be completely eliminated from the body).[13]

Because of these multiple limitations, the second generation PS has focused on synthetic compounds with intense absorption bands in the red and NearIR regions (e.g. chlorines, bacteriochlorins, phthalocyanines), or on limiting the skin photosensitivity by increasing the PS clearance rate from the organism (e.g. Levulan® based on ALA (5-aminolevulinic acid)).

Along with the second generation PS, the synthesis of third generation PS, with improved tumor specificity thanks to targeting moieties, is now under active investigation.[14]

Although many efforts have been done to increase and shift the absorption wavelength of the PS, as well as to improve the PS specificity in tumors and decrease the PS clearance time after treatment, currently FDA-approved PS for PDT are mostly all excited below 700 nm, limiting the penetration depth to less than 2 mm.[15]

Two-photon PDT

One way to mitigate some of the inherent limitations of PDT related the excitation wavelength and to penetration depth inside tissues is two-photon excitation (TPE). The advantages of TPE have been extensively mentioned above.

In the framework of PDT, TPE (in the NearIR region) would reduce the background scattering and absorption from biological media, while increasing the depth of penetration inside tumors. It will

therefore reduce the side effects of irradiation by limiting the photodamage and improving the 3D control of photoactivation and treatment.[15]

While its potential for deep tissue therapy has been already proven,[16 17] a driving motivation currently exists in advancing the research and the development of two-photon PDT.

In the future, two-photon PDT should allow a better control of the photodynamic action, thanks to the highly localized excitation of the treated zone, thus preventing damages to healthy tumor neighboring tissues.

However, because of this high spatial localization of the excitation used in two-photon PDT compared to one-photon linear PDT, larger tumors will be probably harder to treat with the first method, requiring longer time to entirely scan the laser beam over the tumor.

In this short introductory section we could notice how using TPE may significantly improve the results of *in vivo* diagnosis (TPEF microscopy) and therapy (two-photon PDT).

In this context, macromolecular two-photon chromophore-polymer conjugates (alone or grafted onto AuNP), all carefully elaborated during this project, should enable localized treatment and/or tumor imaging thanks to TPE.

V.3. Cell uptake and cytotoxicity

In order to address the first two questions stated in the introduction of this chapter:

i) Are the conjugates (and their corresponding grafted AuNP) non-toxic in the absence of photoactivation?

ii) Is their cell uptake favored compared to free chromophores?

cell uptake and cytotoxicity have been assessed for all TP bio-probes.

Note:

Cell uptake is the process of retention by cells of a bio-probe, including its permanent or temporary retention.

Cytotoxicity is the degree at which a bio-probe possesses a specific destructive action on cells.

Cell viability – the determination of living cells, based on a total cell sample.

Cell mortality – the determination of dead cells, based on a total cell sample

There are two methods allowing to monitor the cell uptake: fluorescence confocal microscopy and flow cytometry. The latter one will be thoroughly presented below, as long as results obtained by fluorescence confocal microscopy will be detailed in Section V.4.

V.3.1. Flow Cytometry

Principle

Flow cytometry is a well-established technique allowing to quantify the cell viability and determine the cell uptake (Figure V. 3).

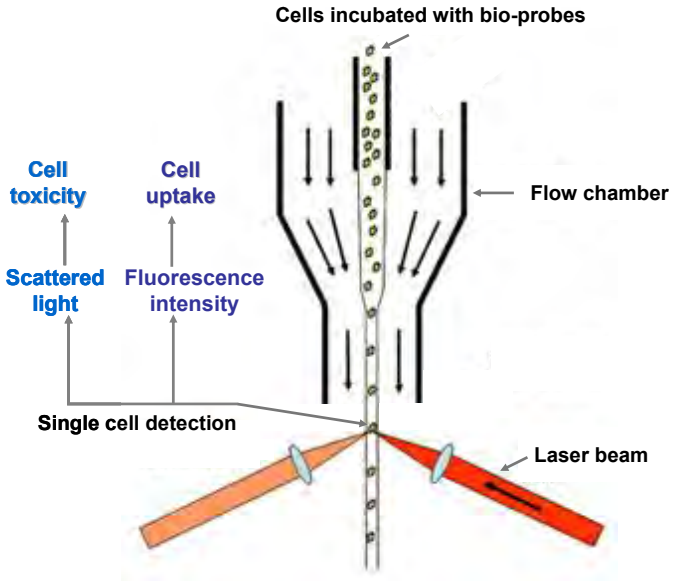

Figure V. 3: Experimental set-up used in flow cytometry to analyze cells incubated with fluorescent bio-probes.

More precisely, flow cytometry simultaneously measures and analyzes multiple physical characteristics of single cells, prior incubated with fluorescent bio-probes.

- Based on the detection of fluorescence intensity *per* cell, flow cytometry enables to measure the amount of cells that have taken up the fluorescent bio-probes; the detected fluorescence signal is therefore proportional to the number of fluorescent species internalized or attached to the cells.
- Based on the scattering detection of single cells, flow cytometry allows to quantify their size and granulometric features, two important factors related to cell viability, thus check the cy… bio-pr…

Nc… ds to in… y and cell shrinkage. The estimation of cell siz… then all… n dead and living cells. Moreover, because de… cent ce… proven before detecting the fluorescence int… with a flu…

A typical flow cytometry result is a two-parameter diagram (Figure V. 4), displaying on the Y-axis – the fluorescence intensity, and on the X-axis – the cell size parameter.

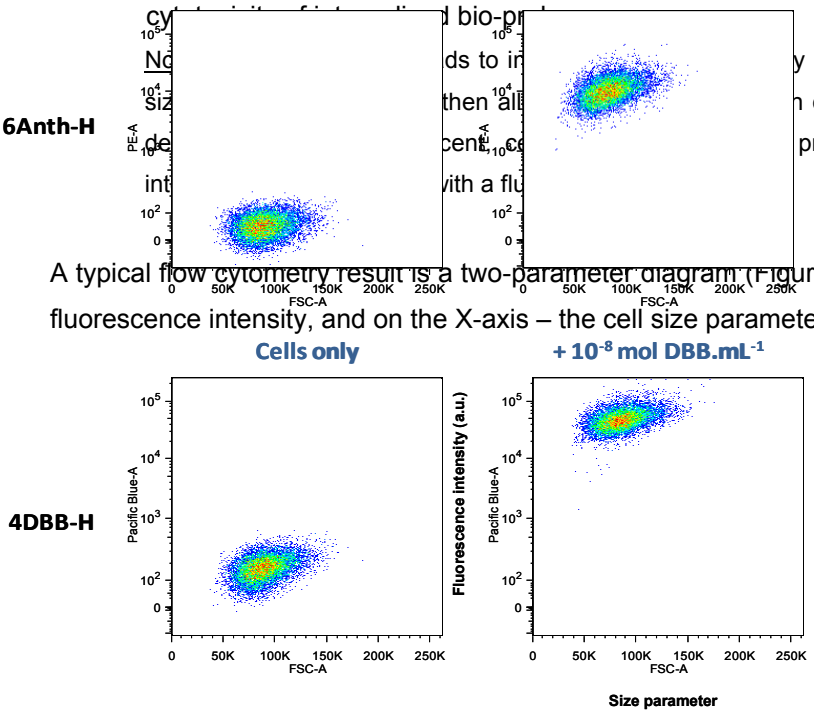

Figure V. 4: Example of two-parameter diagram recovered by flow cytometry analysis of cells labeled with fluorescent bio-probes.

It should be pointed out, that the main drawback of this analysis is that it cannot discriminate between surface bound and internalized fluorescent probes, yet, for all experiments, the uptake has been confirmed by confocal microscopy (Section V.4).

Procedure

In order to assess the uptake, cells were incubated, for various lengths of time, with TP-conjugates. Their fluorescence was then recorded by flow cytometry as a function of the incubation time (V.6. Experimental section). An important parameter of the experimental design was the concentration *per* chromophore used in these tests, fixed at 10^{-5} mol.L^{-1} for each experiment.

To quantify the toxicity induced in the presence of conjugates, cell mortality was determined using two different methods:

1) By flow cytometry, without prior treatment, using a Forward Scatter (FSC)/Side Scatter (SSC) gate to discriminate between live and dead cells *via* differences in their size and granulometry (*cf.* Note above).

2) By staining labelled cells with propidium iodide, PI (fluorescent probe), and analyzing them by flow cytometry. In this case, the plasma membrane of dead cells is permeable to PI; then the amount of dead cells can be calculated by monitoring the PI fluorescence inside dead cells.

Cell lines

Cell uptake and cytotoxicity tests have been carried out using two different cell lines.

- Baf-3 cell line was used as it is very sensitive to a wide spectrum of cell death inducing treatments.[18]
- B16-F10 metastatic melanoma cell line, often used to investigate the therapeutic value of various agents,[19] has also been tested here to prove the therapeutic efficiency of DBB-derivatives used as PS.

V.3.2. Results and discussion

Cell uptake kinetics could be monitored by plotting the fluorescence intensity of conjugates *per* cell (flow cytometry) as a function of incubation time, for both sets of water soluble TP conjugates (Ant and DBB). Preliminary results with grafted AuNP have also been reported, using AuNP with different diameters (synthesized by J. Navarro) grafted with DBB32KDa(B) block conjugate.

V.3.2.1. TP chromophore-polymer conjugates

Cell Uptake

Increase of fluorescence intensity *per* cell over time was indicative of a continuous uptake of TP-polymer conjugates into cells. Results corresponding to DBB-polymer conjugates are illustrated in Figure V. 5.

Compared to the free water-insoluble DBB chromophore (dissolved in DMSO, one of the most used water-miscible polar solvent in biology), a very high cell uptake is noted for all DBB conjugates (dissolved in water) (Figure V. 5, left graph)).

Moreover, while free DBB chromophore exhibited a linear cell uptake kinetics during 24 h incubation (Figure V. 5, right graph), more than 80% of the maximum amount of conjugates is internalized after only 3 h incubation (fluorescence signal reaching a plateau), indicative of a saturation cell uptake kinetics in the case of chromophore-polymer conjugates.

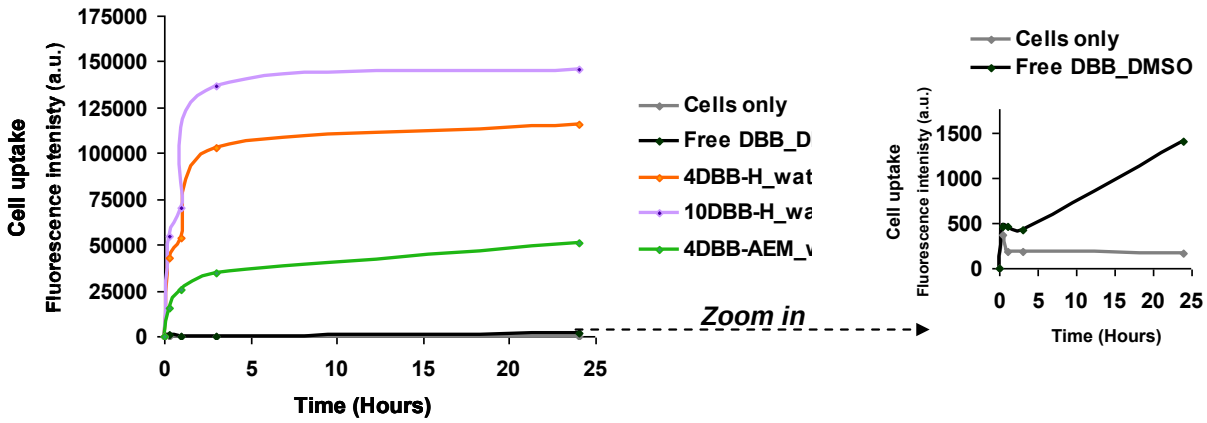

Figure V. 5: (Left graph) Kinetics of uptake for aqueous solutions of DBB conjugates *vs.* free DBB chromophore dissolved in DMSO. Baf-3 cells were incubated without (black line) with DBB conjugates (10^{-5} mol.L^{-1} DBB) for the indicated period of time. Uptake was measured by flow cytometry. Results are expressed as the average of the mean fluorescence intensity. (Right graph) Zoom on the kinetics of uptake for free DBB chromophore dissolved in DMSO, compared to cells only.

Although it seems difficult to compare these results with other polymeric systems, as cell uptake of polymers depends on multiple parameters (charge, amphiphilic character, size, conformation in biological media…), saturation cell uptake kinetics has been previously reported using molecular photosensitizers – phthalocyanine and hematoporphyrin derivatives – which accumulated into cells in a dose dependent manner, yet reaching a plateau after more than 12 h incubation time.[20] (However, neither the cell lines used in the later study, nor the experimental procedure correspond to those used in our case).

This type of kinetics could result indeed from a saturation level of bio-probes inside cells, but it could also be indicative of a dynamic equilibrium reached between the amount of probes taken up inside cells with respect to the amount present in the cellular medium. In order to discriminate between these two possibilities, we could consider testing the retention capacity of nano-probes inside cells.[20]

The fluorescence signal recovered by flow cytometry, depends not only on the chromophore concentration (which is the same for all tested samples), but on their respective extinction coefficients (ε) and fluorescent quantum yields (ϕ) in biological medium (Chapter IV). This consideration makes it difficult to compare the uptake of various conjugates between themselves.

Cytotoxicity

Results of toxicity on cells (in absence of light irradiation) with DBB-polymer conjugates (in water) and DBB free chromophore (in DMSO) are summarized in Figure V. 6, after 1h, 5h and 24h of incubation.

It can be observed that after 24h of incubation, free DBB chromophore (in DMSO) induces a high mortality of cells (~60%). This was caused by the known cytotoxicity of DMSO, used at higher concentration than the concentration tolerated by cells ($c > 5.10^{-3}$ mol.L^{-1}).*

* Due to the poor solubility of DBB free chromophore in polar solvents, a larger amount of DMSO was required to completely dissolve the molecule.

On the contrary, for all DBB-polymer conjugates, cytotoxicity levels are similar to the control experiments on cells only (without any nano-probes) even after 24h of incubation, confirming their safe use for further *in cellulo* studies at the chosen concentration of DBB (10^{-5} mol.L^{-1}).

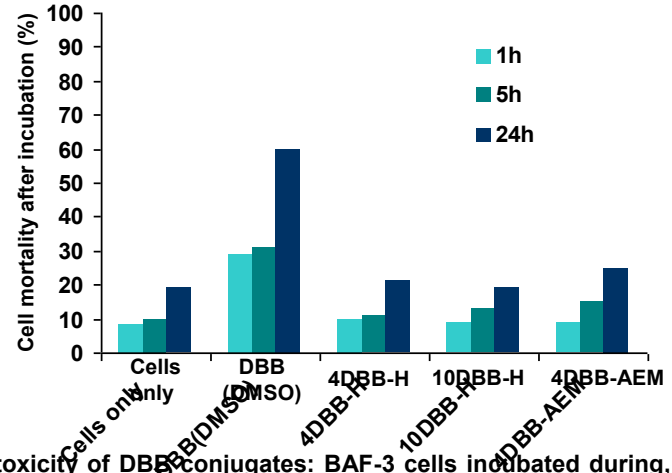

Figure V. 6: Cytotoxicity of DBB conjugates: BAF-3 cells incubated during, 1h, 5h and 24h with various DBB conjugates (in water) and free DBB chromophore in DMSO (at ~10^{-5} mol.L^{-1} DBB) (detection by flow cytometry after staining with propidium iodide).

In comparison to DBB-polymer conjugates, the uptake of Ant-polymer conjugates was also time-dependent and exhibited saturation kinetics (Appendix V.1), without any toxic effects.

V.3.2.2. AuNP grafted with DBB32KDa(B)

Preliminary tests have been carried out recently on aqueous solution of AuNP grafted with DBB32KDa(B) conjugate (synthesized by J. Navarro), after 24h incubation of melanoma B16-F10 cells. Three different diameters of grafted AuNP have been tested: ~40 nm, 65 nm, and ~80 nm.

Cell Uptake

As before, the uptake has been confirmed by confocal microscopy (Section V.4), and quantified by flow cytometry.

AuNP grafted with DBB32KDa(B) conjugate, containing approximately ~10^{-8} mol.L^{-1} DBB chromophore, exhibited similar levels of fluorescence intensity (Figure V. 7, flow cytometry results) compared to free DBB32KDa(B) conjugate (at similar concentration), proving their cell uptake capacity.

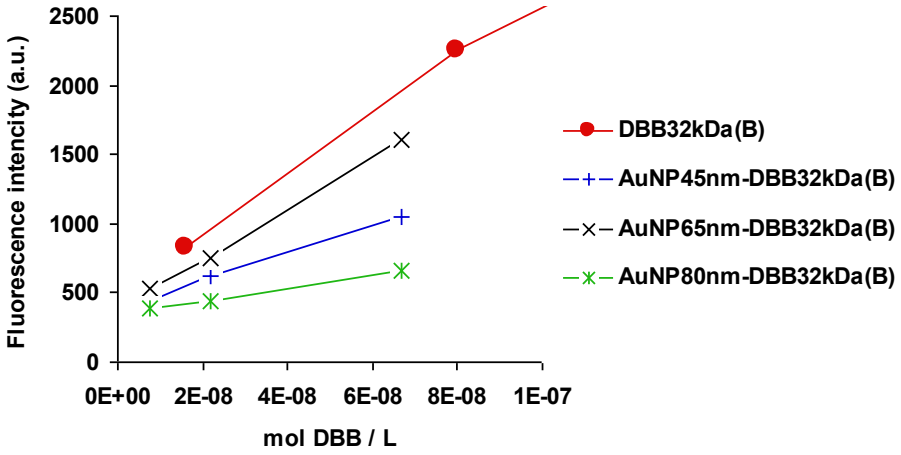

Figure V. 7: Cell uptake of AuNP grafted with DBB32KDa(B) conjugates *vs.* free DBB32KDa(B) conjugate in water, incubated during 24h in B16-F10 cells: Y-axis – fluorescence intensity detected by flow cytometry, X-axis – concentration of DBB chromophore in each sample (mol.L^{-1}).

It should be taken into account that fluorescence properties of conjugates can be either enhanced or quenched after grafting onto AuNP (Chapter IV) and that these changes depend also on the AuNP size.[21]

Cytotoxicity

Previous toxicity studies on AuNP have shown that spherical AuNP with diameters larger than 15 nm should have limited toxicity on cells.[22]

In our case, the toxicity would certainly depend on the behaviour of the entire hybrid system (AuNP and TP conjugates, the latter proven non-toxic above). No significant cytotoxicity has been recorded for AuNP (45 nm, 65 nm or 80 nm) grafted with DBB32KDa(B) conjugate.

In this section, we demonstrated that TP bio-probes, carrying Ant or DBB chromophores could be internalized in less than 5h inside cells, and were non-toxic for cells at the chosen concentration (10^{-5} mol.L^{-1} of chromophore).

Moreover, compared to free TP chromophore (in DMSO), coupling TP chromophores on hydrophilic polymer chains highly increased their uptake by cells.

In conclusion, these results highlight the potential of TP conjugates, and their corresponding grafted AuNP, for further testing in bioimaging and PDT applications.

V.4. One- and two-photon bioimaging

The goal was to answer one of the questions raised in the introduction of this chapter:

iii) Can TP-conjugate (and grafted AuNP) be used as probes for fluorescence microscopy under one- and two-photon excitation?

V.4.1. Fluorescence microscopy assays

One-photon bioimaging by confocal microscopy was performed with 6Ant-H and 4DBB-H conjugates, and with AuNP grafted with DBB32KDa(B) conjugate.
For this purpose, B16-F10 melanoma cells (adherent cells, easily examined by microscopy) were cultured during 24h in the presence of the probes details (Experimental Section V.7).

V.4.2. Results and discussion

V.4.2.1. TP chromophore-polymer conjugates

The fluorescence signal of TP-polymer conjugates (6Ant-H and 4DBB-H) could be successfully visualized upon one- and two-photon excitation inside the cells (Figure V. 8 a) and b)).

Qualitative examination of images below show that TP conjugates are located in the cytoplasm, slightly concentrated in the perinuclear region, but not in the nucleus, (Figure V. 8 a) and b), top panels).

Due to the lack of a sufficiently fluorescence signal during early stages of incubation (1h, 3h), it was not possible to monitor by microscopy and access information about intracellular localization of probes, able to give some clues about the mechanisms involved in their cell uptake. In the future, immunolabeling studies may provide more insight on this matter (*e.g.* by detecting their localization in early or late endosomes).

Fluorescence bioimaging of cells incubated with 6Ant-H and 4DBB-H conjugates

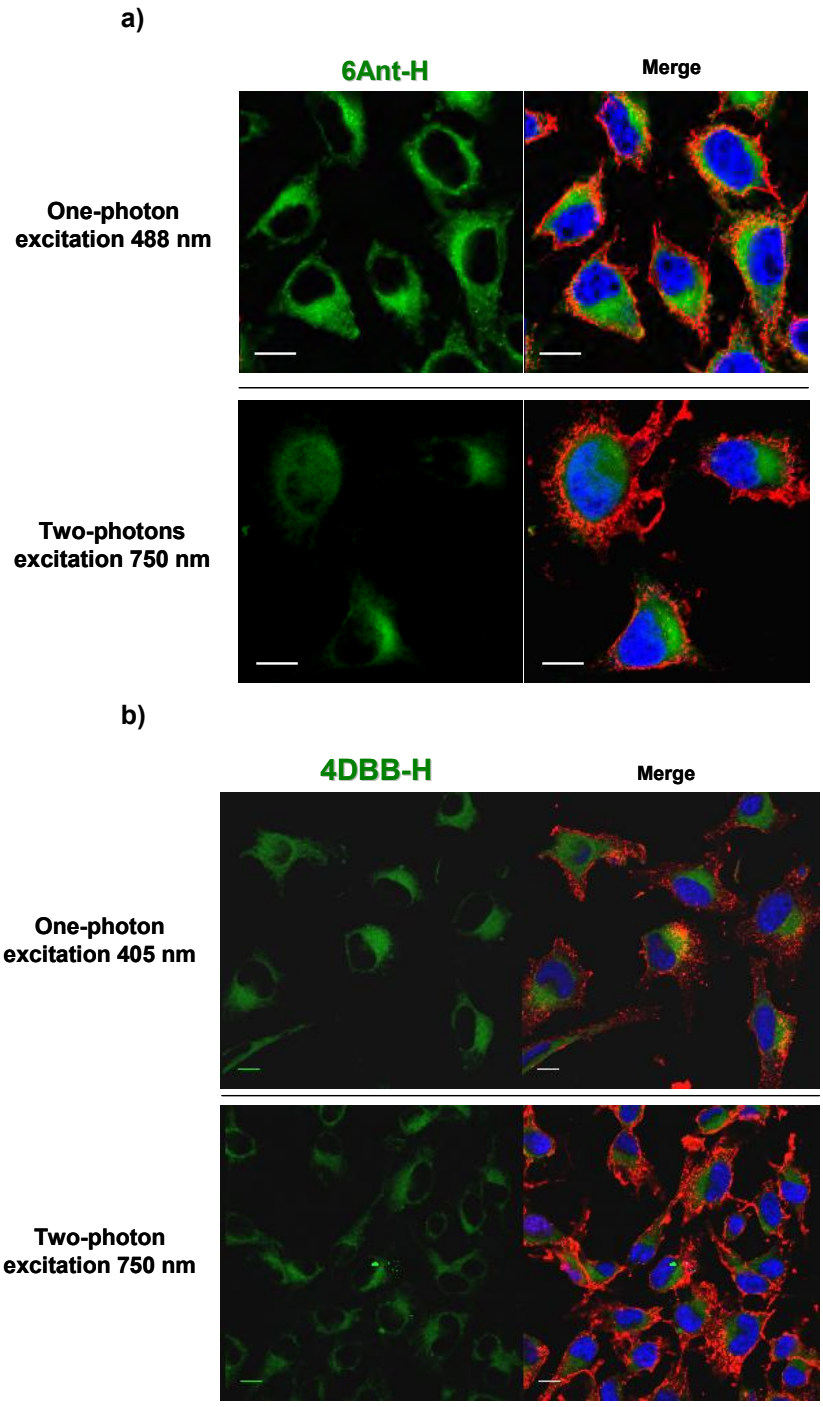

Figure V. 8: One-photon (top panels) and two-photon (bottom panels) fluorescence images of TP-polymer conjugates: a) 6Ant-H(aq.); b) 4DBB-H(aq.).
Adherent B16-F10 melanoma cells were cultured for 24 h in the presence of conjugates (10^{-5} mol.L^{-1} chromophore). Plasma membrane (red) and nuclei (blue) were visualized in all cases after one-photon excitation using anti-CD44 antibody (405 nm for Ant conjugate and 488 nm for DBB conjugate) and DRAQ5 DNA dye (633 nm), respectively. The conjugate (green) was detected using one-photon (488 nm for 6Ant-H and 405 for 4DBB-H) or two-photon excitation (750 nm). Scale bar is 10 µm.

Fluorescence emission spectra of the conjugates inside the cells

In Chapter IV, important solvatochromism was observed with Ant- and DBB-polymer conjugates. In order to investigate more thoroughly the photophysical behavior of conjugates inside cells, the fluorescence emission spectra *in cellulo* was compared with the spectra recorded in pure water and in dioxane for both 6Ant-H (Figure V. 9 a)) and 4DBB-H (Figure V. 9 b)) conjugates, respectively.

Fluorescence emission spectra *in cellulo* exhibited a maximum close to 550-560 nm for 6Ant-H and to 440 nm for 4DBB-H, with a very good signal-to-noise ratio (*in cellulo* spectra carefully corrected for noise).

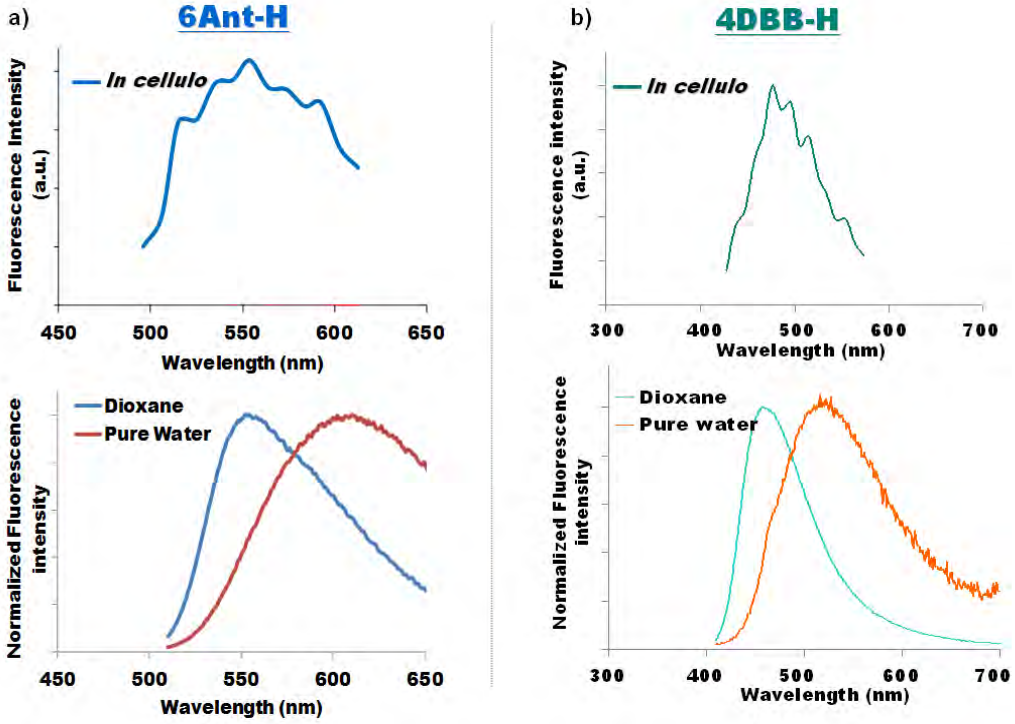

Figure V. 9: (Top graphs) Fluorescence emission spectra measured *in cellulo* after two-photon excitation at 750 nm in the presence of: a) 6Ant-H conjugate; b) 4DBB-H conjugate. (Bottom graphs) Spectra of the same conjugates in dioxane and pure water (measured by fluorescence spectroscopy).

Emission spectra collected *in cellulo* differed from those in pure water (maximum wavelength significantly blue-shifted compared to water). We can therefore suppose that inside cells, where ionic strength, pH and polarity can vary from one micro-environment to another, the fluorescence of water-soluble TP conjugates might be different compared to that in pure water, confirming that TP conjugates experienced a different environment. Conversely, the observed *in cellulo* emission profiles exhibited a maximum closer to that of conjugates in dioxane solution, reflecting that they were mainly in interaction with low polar regions of the cells (*e.g.* lipid membranes, proteins).

The higher fluorescence quantum yields of the conjugates in lower polarity environment compared to water (Chapter IV), probably explain the very good quality of the images recorded upon one- and two-photon excitation.

V.4.2.2. AuNP grafted with DBB32KDa(B)

Fluorescence bioimaging with 45 nm and 65 nm AuNP- DBB32KDa(B), upon one-photon excitation, has been carried out.

Preliminary results show that AuNP grafted with TP-polymer conjugates can be visualized inside cells (Figure V. 10), confirming their efficient cell uptake and that they can be tracked by fluorescence microscopy.

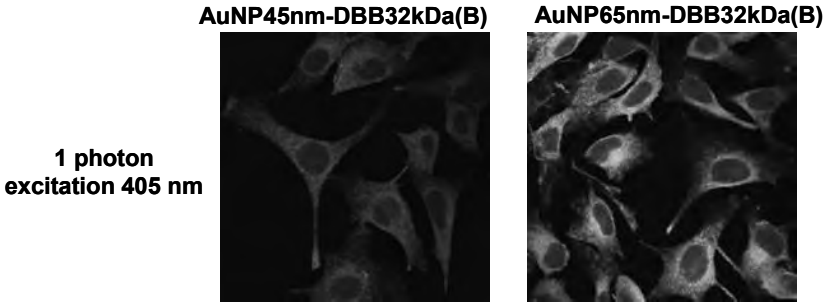

Figure V. 10: One-photon fluorescence images of 45 nm and 65 nm AuNP grafted with DBB32kDa conjugate (carried out with adherent B16-F10 melanoma cells, after 24h incubation with AuNP, ~10^{-8} mol.L^{-1} DBB).

We suppose that the cell uptake mechanism of these (relatively large) AuNP may be mainly endocytic, with perinuclear localization, as it is perhaps the most common result reported for a wide size-range of AuNP.[23]

We demonstrated that TP bio-probes (conjugates and AuNP) were efficiently taken up by cells, at 10^{-5} mol.L^{-1} chromophore (for polymer conjugates) and ~10^{-8} mol.L^{-1} chromophore (for grafted AuNP). Thanks to the coupling with hydrophilic copolymers, the cell uptake of polymer conjugates was highly improved without generating any toxic effects, compared to the free chromophore.

Despite their weak fluorescence properties determined in water (Chapter IV), the results obtained by fluorescence microscopy clearly demonstrate: 1) the potential of Ant-polymer conjugates to be used as fluorescent bio-probes; 2) and the capacity of DBB-polymer conjugates and grafted AuNP to be tracked by fluorescence microscopy, which can actually help to monitor the photoactivation of PS inside cells by observing its photobleaching after irradiation.

V.5. Photodynamic therapy (PDT) application

DBB molecular derivatives were previously used to induce cell death upon photoactivation.[24] In this section, the potential of DBB-derived compounds to be used as photosensitizers for PDT will be investigated.

Subsequently, the question addressed here was:

iv) Can DBB-polymer conjugates (and DBB grafted AuNP) induce death of cells upon photoactivation?

V.5.1. Photoactivation assays

Photoactivation was carried out on Baf-3 or B16-F10 cells after 24h incubation with DBB-derivatives (at the indicated concentration). Cells were then exposed or not to irradiation at 365 nm, with 8 $J.cm^{-2}$ fluence rate for Baf-3 cells, or 16 $J.cm^{-2}$ for more resistant B16-F10 melanoma cells. The percentage of cell mortality was assessed after irradiation (1h to 5h) by propidium iodide staining and followed by flow cytometry.

V.5.2. Results and discussion

One-photon activation effect on cell mortality has been investigated for DBB-polymer conjugates and grafted AuNP-DBB32KDa(B).

V.5.2.1. DBB-polymer conjugates

Photoactivation tests were first performed on various water-soluble DBB-polymer conjugates, with a similar chain length, but carrying different amounts of DBB *per* chain (4 or 10), and being post-treated by AEM capping (AEM) or hydrolysis (H)).

First results were very encouraging as all DBB conjugates induced cell death at 10^{-5} $mol.L^{-1}$ DBB after irradiation.

The highest efficiency was found with 4DBB-H conjugate, which caused more than 80% cell death even at a 10 times lower concentration (10^{-6} mol. L^{-1} DBB) (Figure V. 11). Consequently, 4DBB-H conjugate was chosen to perform an extensive study of photoactivation (Figure V. 12).

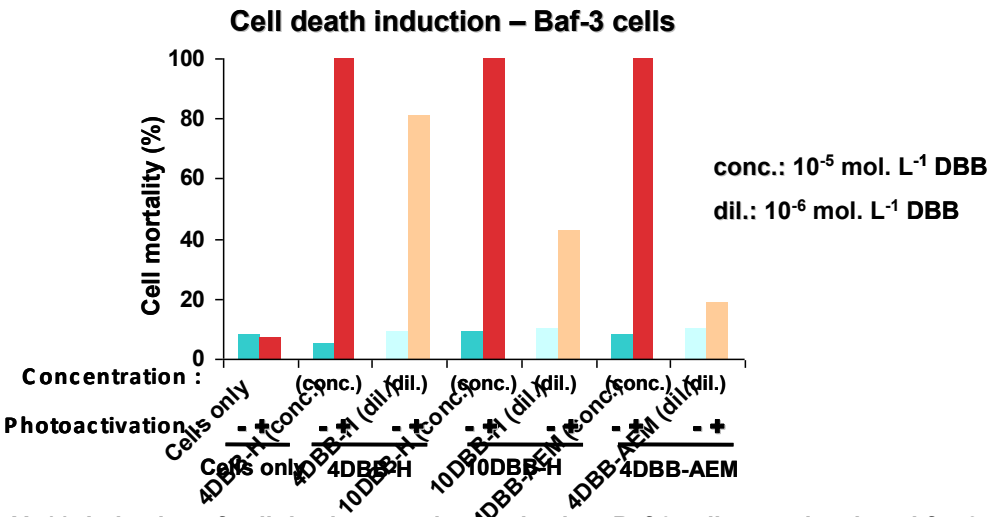

Figure V. 11: Induction of cell death upon photoactivation. Baf-3 cells were incubated for 24 h without or with increasing amount of conjugates (10^{-6} and 10^{-5} mol.L^{-1} DBB). Then, cells were submitted (+) or not (-) to irradiation (365 nm, 8 J.cm^{-2}). The percentage of cell mortality was assessed 1 h after irradiation by flow cytometry after propidium iodide staining.

The goal was to compare the phototoxic effect of 4DBB-H conjugate with the free DBB chromophore in DMSO, and study the effect of the 4DBB-H conjugate concentration on the extent of cell death induction (Figure V. 12).

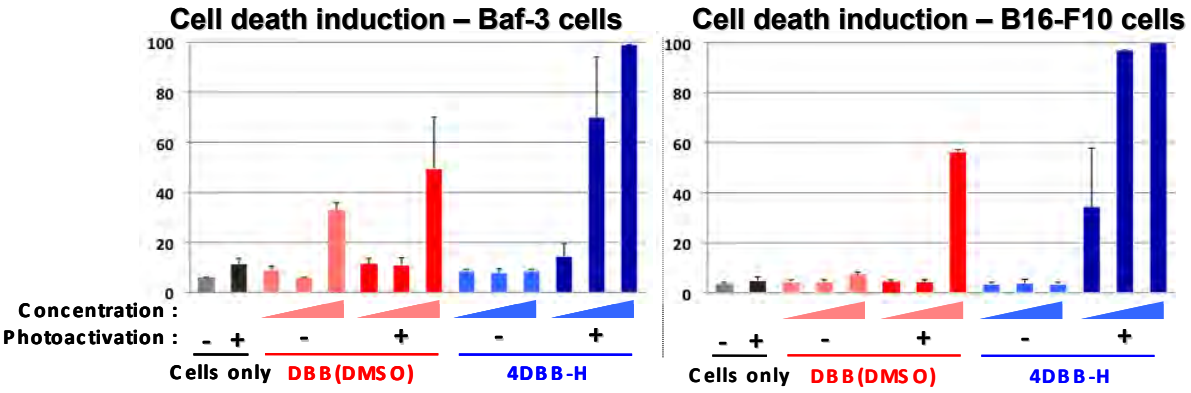

Figure V. 12: Induction of cell death upon photoactivation. Baf-3 cells and B16-F10 melanoma cells were incubated for 24 h without any PS (black) or with increasing amount of the free DBB in DMSO (red) or 4DBB-H conjugate (blue). Tested concentrations: 4.10^{-7}, 2.10^{-6} and 10^{-5} mol.L^{-1} DBB. Then, cells were submitted (+) or not (-) to irradiation (365 nm, 8/16 J.cm^{-2}). The percentage of cell mortality was assessed 5 h after irradiation by flow cytometry after propidium iodide staining. Results show the mean mortality ± SD of 2 to 4 independent experiments.

As shown in Section V.3, Baf-3 or B16-F10 cells did not show signs of increased mortality when incubated with 4DBB-H for 24 h (Figure V. 12). On the contrary, after irradiation of cells, 4DBB-H rapidly induced cell death in a dose-dependent manner. Induction of cell death upon photoactivation was very efficient for concentration as low as 2.10^{-6} mol.L^{-1} DBB, especially in the case of B16-F10 melanoma cells.

These results demonstrate that the copolymer chain strongly enhances the photosensitizer ability to induce cell death, likely due to increased uptake (Section V.3).

V.5.2.2. AuNP grafted with DBB32KDa(B)

In Chapter IV, we have studied the influence of 20 nm AuNP grafted with DBB-polymer conjugates on the fluorescence properties of conjugates. We have shown that fluorescence emission recovery of conjugates, after grafting onto 20 nm AuNP, increased for longer block copolymer conjugates. However, the interaction between AuNP and the triplet state of DBB-polymer conjugates could not be evidenced by spectroscopic measurements.

The goal here was to study the phototoxicity of grafted AuNP in cells, and compare it with free conjugates, in order to find whether in biological medium, the surface the effect of plasmon resonance (SPR) of AuNP on the phototoxicity of DBB compounds.

In this context, the cell phototoxicity of AuNP with different diameters (45 nm, 65 nm and 80 nm), functionalized with DBB32KDa(B) block copolymer (by J. Navarro), has been evaluated and compared to that of free DBB32KDa(B) conjugate (Figure V. 13).

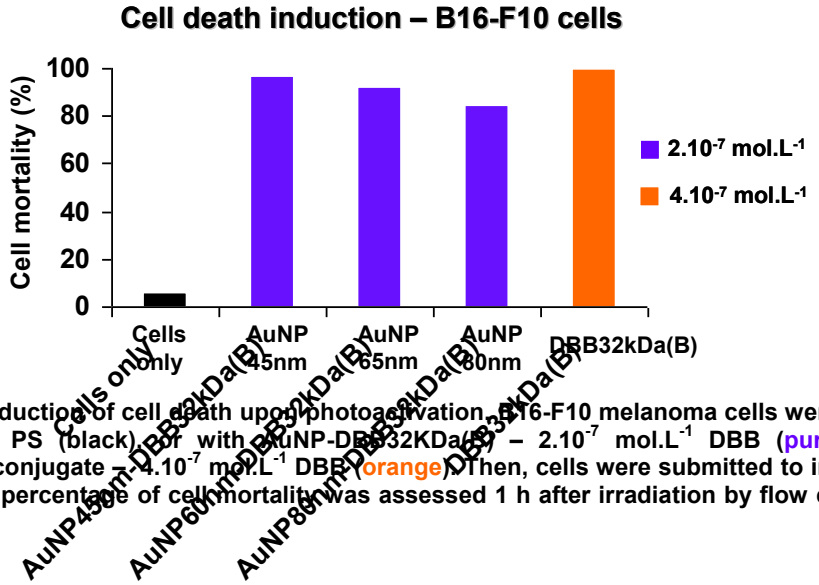

Figure V. 13: Induction of cell death upon photoactivation. B16-F10 melanoma cells were incubated for 24 h without any PS (black), or with AuNP-DBB32KDa(B) – 2.10^{-7} mol.L^{-1} DBB (purple), or with free DBB32KDa(B) conjugate – 4.10^{-7} mol.L^{-1} DBB (orange). Then, cells were submitted to irradiation (365 nm, 16 J.cm^{-2}). The percentage of cell mortality was assessed 1 h after irradiation by flow cytometry using PI staining.

Preliminary results of cell death induction using AuNP are encouraging (Figure V. 13), as, similarly to free conjugates, grafted AuNP display a high percentage of cell death after 24h incubation. No enhancement effect due to the presence of AuNP could be detected with these systems. These studies need to be repeated and confirmed, using this time the same concentration of chromophore for all samples.

It should be accounted that AuNP alone may also induce cell death by photothermal therapy (under one- or two-photon excitation).[25] [26] Yet, for our systems of grafted AuNP this effect was ruled out: since AuNP-PNAM samples (exhibiting the same size, but no chromophores) incubated into cells (24 h) showed no cell toxicity after irradiation.

Nonetheless, the occurrence of a photothermal effect should be checked every time, especially when using Au nanorods.

In cancer therapy, the combination of PDT and photothermal therapy in a single probe can be considered a huge advantage, allowing to increase the treatment efficacy and enabling to use less irradiation in order to induce cell death.

V.5.2.3. Mechanisms of photo-activated cell death

In Section V.2, two types of mechanisms were distinguished for cell death induction after PS photoactivation: type I reactions – cell death induced by reaction with oxygen radical and radical ions; type II reaction – cell death induced by reaction with singlet oxygen ($^1O_2$).

In Chapter IV, the ability of DBB-derivatives to produce singlet oxygen has been demonstrated by quantifying the quantum yield of $^1O_2$ production in $CHCl_3$. Even if the detection of $^1O_2$ in aqueous medium was not possible (due to quenching) (Chapter IV), we may suppose that $^1O_2$ could be produced in cellular medium containing DBB-derivatives, leading to cell death via type II reactions.
On the other hand, a technique allowing to evidence the type I reactions consists in using radical scavengers, capturing oxygen radicals and radical ions produced after photoactivation, thus limiting their toxic activity and decreasing the photoinduced death.[27] Indeed, preliminary studies with our probes (tests carried out with 4DBB-H conjugate) have demonstrated that type I reactions may also be involved in the phototoxic effect of DBB derivatives.
During PDT, cell death is induced by either apoptosis (programmed cell death) and/or necrosis (rapid and premature death of cells in living tissues, triggered by an external factor).[28]
In the case of 4DBB-H conjugate, the investigation of cell death triggering phenomena has been started during this work. Preliminary results evidenced the occurrence of apoptosis, by recording decreased cell mortality after inhibiting the expression of proapoptotic factors (caspases[29]) in cells incubated with the 4DBB-H conjugate.

PDT effect of DBB derivatives was successfully demonstrated under one-photon excitation. DBB-polymer conjugates alone and grafted onto AuNP efficiently induce cell death after irradiation, possibly due to the occurrence of both type I and II reactions with the triplet excited state of DBB chromophores.
However, the influence of the AuNP was yet not determined in preliminary tests, but is an important issue still under ongoing investigation (by our collaborators J. Navarro and E. ben Daoud).

Two-photon induced death of cells incubated with DBB-derivatives could not be evaluated up until now. The complicated experimental set-up, needed to irradiate cells under two-photon excitation, require a thorough optimization of multiple parameters. One particularly difficult to control under the TFEF microscopy is the fluence rate received by the irradiated sample. This study represents a short-term perspective of this work and is in progress.

V.6. Conclusion of Chapter V

Biological results discussed in this chapter demonstrate that water-soluble TP-polymer conjugates (and grafted AuNP) could provide valuable imaging probes for one- and two-photon excitation fluorescence microscopy as well as novel photosensitizers with significantly improved efficiency for photoactivated cancer cell death.

All tested samples resulted to be non-toxic for cells at 10^{-5} mol.L^{-1} chromophore concentration in the case of polymer conjugates (more than 90% of viable cells after 5h incubation), and were internalized more efficiently into cells compared to free chromophore.

DBB-polymer conjugate, 4DBB-H, induced ~10 times more cell mortality compared to free DBB (in DMSO), and 4 times more than 4DBB-AEM conjugate. Additionally, Ant- and DBB-derivatives could be detected by two-photon microscopy (after 24h incubation in cells).

At this stage, the TP bio-probes have only been submitted to basic biological tests which served as proof of concept. More extensive analyses are however required to thoroughly investigate their behaviour in biological media and their potential for future *in vivo* applications. In this context, finding answers related to their biodistribution (quick accumulation in the perinuclear region?) and mechanisms of their uptake (type of endocytosis), will undoubtably improve the understanding of their structure-property relationships in bio-relevant media (*e.g.* elucidate the impact of the conjugates structure, charge, chromophore density, and of AuNP size and shape etc.) and bring them closer to clinical trials.

V.7. Experimental section

Cell cultures
Murine IL-3 dependent Baf-3 cells and B16-F10 melanoma cells were cultivated in DMEM medium (Invitrogen Life Technologies) supplemented with 6% heat-inactivated Fetal Bovin Serum (Lonza, Belgium) and 10 mg.L-1 gentamicin (Invitrogen). Baf-3 cells are non-adherent cells and were grown in suspension with 5% WEHI 3B cell-conditioned medium as a source of IL-3. B16-F10 cells are adherent cells and were grown as sub-confluent monolayer. Cells were cultured at 37°C and 7% CO_2 in a humidified atmosphere.

Flow cytometry
To measure chromophore uptake, 2×10^5 Baf-3 cells.mL^{-1} were incubated at 37 °C with fluorescent probes, or free PS in DMSO (10^{-5} mol.L^{-1} chromophore) for the indicated period of time. Cells were analyzed using a LSR or a Canto II flow cytometer (Becton Dickinson Bioscience) with a 488 nm laser and a 525 nm emission filter or a 405 nm laser and a 450 nm emission filter to detect incorporation of Ant and DBB derivatives respectively. At least 5 000 cells per condition were recorded and dot plots were analyzed using FlowJo Software (Tree Star, Inc., USA).
To measure cell mortality, cells were collected and incubated with propidium iodide (PI, Sigma, 2 mg.L^{-1}) a standard flow cytometry viability probe and at least 5 000 cells were analyzed immediately by flow cytometry. This allows to distinguish between viable cells with intact plasma membrane that exclude PI and non-viable cells that are permeable to PI. Baf-3 cells are non-adherent and were collected by pipetting. Adherent cells loosen their attachment or detach from the substratum during apoptosis. Therefore cell mortality among B16-F10 cells was analyzed by pelleting floating cells and adherent cells harvested by trypsinization. Cells were then stained with PI and analyzed by flow cytometry.

Phototoxicity
To assay the phototoxicity of DBB derivatives in cell culture systems, 2×10^5 Baf-3 cells.mL^{-1} were seeded into 96-well plates and cultured for 24 h in the presence of PS agent in DMSO at the indicated concentration. B16-F10 were seeded at 6×10^4 cells.mL^{-1} into 24-well plates, grown over-night and incubated for 24 h with the PS. Cells were irradiated at 8 J.cm^{-2} (Baf-3 cells) or 16 J.cm^{-2} (B16-F10 cells) at 365 nm (Bio-Sun, Vilber Loumart, Marne la vallée, France). Cells viability was assessed 1 h later by flow cytometry.

Cell fluorescence imaging
B16-F10 cells were plated on glass coverslips (2×10^4 cells/coverslip) and allowed to adhere overnight. Cells were then incubated for 24 h with the probe (10^{-5} mol.L^{-1} chromophore). DRAQ5 (10 µM, Alexis Biochemicals) was added for the last 3 minutes of culture to stain the nuclei. Cells were washed with PBS and fixed with 4% paraformaldehyde (Sigma-Aldrich). The cell surface was stained using anti-CD44-eFluor450 (at 405 nm) in the case of Ant conjugates, and anti-CD44-FITC (at 488 nm) in the case of DBB conjugates (2 µg.mL^{-1}, Ebiosciences) in PBS for 2 h at room temperature. Specimens were mounted (Antifade Kit, Molecular Probes) and examined using an inverted LSM 710 Zeiss confocal microscope (Carl Zeiss, Germany) with 63X/1.4 objective. Zeiss 710 uses variable spectral detection system. 405 nm / 488 nm and 633 nm lasers were used for anti-CD44 and DRAQ5 excitation respectively. Imaging of conjugates was performed using one-photon excitation (488 nm for Ant and 405 for DBB) or two-photon excitation (750 nm) with the tunable infrared laser Ti:Sapphire Chameleon Ultra II (690 nm-1040 nm). Images were processed with ImageJ software, a public domain image processing and analysis program.

References

[1] **Two-Photon Fluorescence Microscopy: Basic Principles, Advantages and Risks,** S. J. Mulligan, B. A. MacVicar, *Modern Research and Educational Topics in Microscopy* **2007**, 881-889.

[2] **Two-photon laser scanning fluorescence microscopy,** W. Denk, J. H. Strickler W. W. Webb, *Science* **1990**, *248*, 73-76.

[3] **Two-photon Fluorescence Light Microscopy,** P. T. C. So, *Encyclopedia of life sciences* **2002**, Macmillan Publishers Ltd, Nature Publishing Group, www.els.net

[4] **Principles of two-photon excitation fluorescence microscopy and other nonlinear imaging approaches,** M. Oheim, D. J. Michael, M. Geisbauer, D. Madsen, R. H. Chow, *Adv. Drug Deliv. Rev.* **2006**, *58*, 788-808.

[5] **Going deeper than microscopy: the optical imaging frontier in biology,** V. Ntziachristos, *Nature Methods* **2010**, *7(8)*, 603-614.

[6] a) **Two-Photon Absorption and the Design of Two-Photon Dyes,** M. Pawlicki, H. A. Collins, R.G. Denning, H. L. Anderson, *Angew. Chem. Int. Ed.* **2009**, *48*, 3244-3266.

b) **Two-Photon Fluorescent Probes for Bioimaging,** S. Yao, K. D. Belfield, *Eur. J. Org. Chem.* **2012**, 3199-3217.

[7] **Chapter 3: Sensitizers in photodynamic therapy,** N. Rousset. L. Bourré, S. Thibaud, *Photodynamic Therapy*, **2003**, Ed. T. Patrice, series Ed. D.-P. Härder G. Jori, RSC, Cambrige.

[8] **Imaging and Photodynamic Therapy: Mechanisms, Monitoring, and Optimization,** J. P. Celli, B. Q. Spring, I. Rizvi, C. L. Evans, K. S. Samkoe, S. Verma, B. W. Pogue, T. Hasan, *Chem Rev.* **2010**, *110(5)*, 2795-838.

[9] **A Light in Muitidrug Resistance: Photodynamic Treatment of Muitidrug-Resistant Tumors,** M. Marques Capella, L. Sabbatini Capella, *J. Biomed. Sci.* **2003**, *10*, 361-366.

[10] **Photophysical and photobiological processes in the photodynamic therapy of tumours,** M. Ochsner, *J. Photochem. Photobiol. B: Biology* **1997**, *39*, 1-18.

[11] **Action and Diseases Caused by Light,** M.F. Blum, *Photodynamic* **1941**, New York, Reinhold.

[12] **Local treatment of viral disease using photodynamic therapy,** M. Wainwright, *Int. J. Antimicrob.Ag.* **2003**, *21*, 510-520.

[13] **Photodynamic Therapy in Oncology,** M. Triesscheijn, P. Baas, J. H. M. Schellens, F. A. Stewart, *The Oncologist* **2006**, *11*, 1034-1044.

[14] **Photodynamic therapy: novel third-generation photosensitizers one step closer?,** L. B. Josefsen, R. W. Boyle, *Br. J. Pharmacol.* **2008**, *154*, 1-3.

[15] **Novel Two-Photon Activated Photodynamic Therapy Agents: Design, Synthesis, and Preclinical Studies on Subcutaneous Cancerous Tumors,** A. Gong, F. Meng, J. R. Starkey, B. L. Moss, A. Rebane, M. Drobizhev, C. W. Spangler, *Polymers for Biomedical Applications* **2008** Chapter 13, 225-237.

[16] **Nanoparticles for Two-Photon Photodynamic Therapy in Living Cells,** D. Gao, R. R. Agayan, H. Xu, M.A. Philbert, R. Kopelman, *Nano Lett.* **2006**, *6(11)*, 2383-2386.

[17] **Simultaneous Two-photon Excitation of Photofrin in Relation to Photodynamic Therapy,** A. Karotki, M. Khurana, J. R. Lepock, B. C. Wilson, *Photochem. Photobiol. Sci.* **2006**, *82(2)*, 443-452.

[18] **Bcl-X is the major pleiotropic anti-apoptotic gene activated by retroviral insertion mutagenesis in an IL-3 dependent bone marrow derived cell line,** J. Thomas, Y. Leverrier, J. Marvel, *Oncogene* **1998**, *16*, 1399-1408.

[19] **RNA interference of metastasisassociated gene 1 inhibits metastasis of B16F10 melanoma cells in a C57BL/6 mouse model,** H. Qian, J. Yu, Y. Li, H. Wang, C. Song, X. Zhang, X. Liang, M. Fu, C. Lin, *Biol. Cell* **2007**, *99*, 573-581.

[20] **Cell uptake, distribution and response to aluminium chloro sulphonated phthalocyanine, a potential anti-tumour photosensitizer,** W. S. Chan, R. Svensen, D. Phillips, I. R. Hart, *Br. J. Cancer* **1986**, *53(2)*, 255-263.

[21] **Cellular Uptake and Fate of PEGylated Gold Nanoparticles Is Dependent on Both Cell-Penetration Peptides and Particle Size,** E. Oh, J. B. Delehanty, K. E. Sapsford, K. Susumu, R. Goswami, J. B. Blanco-Canosa, P. E. Dawson, J. Granek, M. Shoff, Q. Zhang, Peter L. Goering, A. Huston, I. L. Medintz, *ACS Nano* **2011**, *2(8)*, 6434-6448.

[22] **Size-Dependent Cytotoxicity of Gold Nanoparticles,** Y. Pan, S. Neuss, A. Leifert, M. Fischler, F. Wen, U. Simon, G. Schmid, W. Brandau, W. Jahnen-Dechent, S*mall* **2007**, *3(11)*, 1941-1949.

[23] **Biodistribution and Toxicity of Engineered Gold Nanoparticles: A Review of in Vitro and in Vivo Studies,** N. Khlebtsov, L. Dykman, *Chem. Soc. Rev.* **2011**, *40*, 1647-1671.

[24] **Photodynamic therapy and two-photon bio-imaging applications of hydrophobic chromophores through amphiphilic polymers vectorisation, T.** Gallavardin, M. Maurin, S. Marotte, T. Simon, A.-M. Gabudean, Y. Bretonnière, M. Lindgren, F. Lerouge, P. L. Baldeck, O. Stéphan, Y. Leverrier, J. Marvel, S. Parola,, O. Maury, C. Andraud*, Photochem. Photobiol. Sci.* **2011**, *10*, 1216-1225.

[25] **Cancer Cell Imaging and Photothermal Therapy in the Near-Infrared Region by Using Gold Nanorods,** X. Huang, I. H. El-Sayed, W. Qian, M. A. El-Sayed, *J. Am. Chem. Soc.* **2006**, *128*, 2115-2120.

[26] **Surface plasmonic gold nanorods for enhanced two-photon microscopic imaging and apoptosis induction of cancer cells,** J.-L. Li, M. Gu, *Biomaterials* **2010**, *31*, 9492-9498.

[27] **In vivo NADH fluorescence monitoring as an assay for cellular damage in photodynamic therapy,** B. W. Pogue, J. D. Pitts, M. A. Mycek, R. D. Sloboda, C. M. Wilmot, J. F. Brandsema, J. A. O'Hara, *Photochem. Photobiol.* **2001**, *74*, 817-824.

[28] **Chapter 2: Mechanisms of photodynamic therapy,** A. C.E. Moor, B. Ortel, T. Hasan, *Photodynamic Therapy*, **2003**, Ed. T. Patrice, series Ed. D.-P. Härder, G. Jori, RSC, Cambridge.

[29] **Caspases: Enemies Within,** N. A. Thornberry, Y. Lazebnik, *Science* **1998**, *281(5381)*, 1312-1316.

Final Conclusions and Future Work

The work carried out during this PhD project focused on the elaboration of hybrid nano-probes composed of two-photon chromophore-polymer conjugates grafted onto gold nanoparticles (Figure 1), capable to have their performance enhanced, for bioimaging and photodynamic therapy applications.

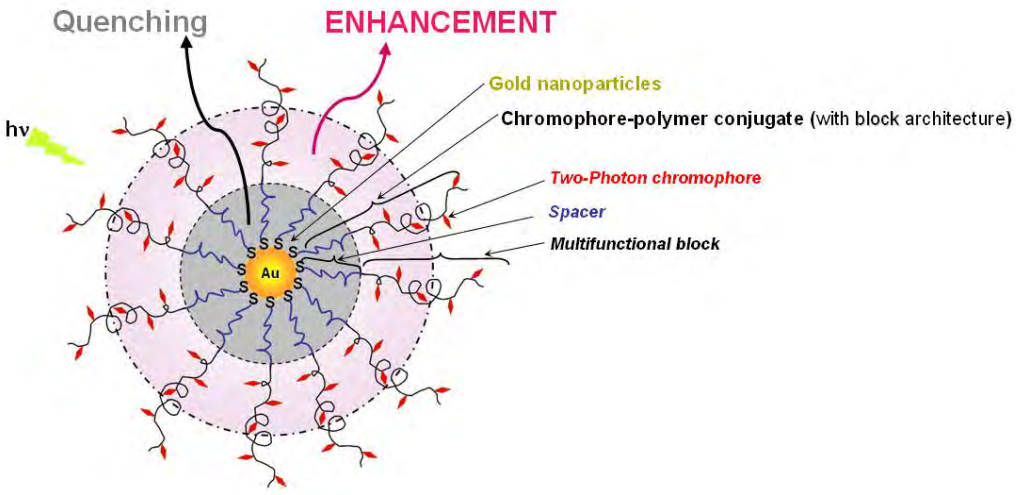

Figure 1: The hybrid nano-probes platform designed during the course of this work, composed of: gold nanoparticles, functionalized with Two-Photon chromophore-polymer conjugates. The Two-Photon chromophore-polymer conjugates have a block structure, displaying a 1st block (spacer) used to increase the distance between chromophores and AuNP surface.

Several aspects involved in the optimization of the structure and the composition of nano-probes have been addressed in this thesis. The main conclusions will be summarized below, followed by ideas on present and future outlooks.

In Chapter II, we evidenced the successful synthesis of well-defined chromophore-polymer conjugates using three different chromophores: LY (Lucifer Yellow) – a water-soluble commercial fluorophore used as a model; Ant (Anthracene-based) – hydrophobic TP fluorescent chromophore for bioimaging; and DBB (Dibromobenzene-based) – hydrophobic TP photosensitizer for PDT.

In the first par of the chapter, several water-soluble PNAM homopolymers, P(NAM-*co*-NAS) random copolymers and P[(NAM-*co*-NAS)-*b*-NAM] block copolymers with controlled MW (2 000 g.mol^{-1} < M_n < 80 000 g.mol^{-1}), low polydispersity (PDI<1.2), and good control over end-group functionality (dithioester end-groups: DT% > 85%), copolymer composition (no compositional drift in random copolymers) and architecture (block), were obtained.

In the 2nd part of the chapter, different chromophores have been bound to the copolymer chain (high yield > 75%), leading to conjugates with different lengths (2 700 g.mol^{-1} < M_n < 37 700 g.mol^{-1}) and a number of chromophores *per* chain (Nc) varying from 1 to 21. Three independent characterization techniques (SEC/UV, ^{1}H NMR, and UV-Vis absorption) have been used to accurately determine the precise number of covalently coupled chromophores along the chain.

We noted that although TP chromophores (Ant or DBB) were hydrophobic, chromophore-polymer conjugates were water-soluble. Their water-solubility was influenced by several factors:

- the chemical nature of the bound chromophore (DBB-conjugates seemed less water-soluble than Ant conjugates, compared to completely water-soluble LY-conjugates);

- the density of chromophores *per* chain (water-solubility of conjugates decreased with the increasing density: 10Ant-AEM was water-soluble *vs.* 21Ant-AEM, insoluble in water);
- the post treatment after chromophore coupling (negatively charged conjugates, post-treated by hydrolysis, were more water-soluble than conjugates capped with neutral aminoethyl morpholine, AEM).

In Chapter III, an oriented grafting of the chromophore-polymer conjugates onto ~20 nm AuNP has been achieved in aqueous media, leading to high grafting densities (~400 – 800 chains *per* AuNP), thus to an increased concentration of chromophores *per* AuNP (*e.g.* AuNP-LY37KDa with ~2 000 LY chromophores *per* AuNP).

First, two different approaches have been investigated using RAFT PNAM homopolymers: *in situ* approach, resulting in small ~2 nm AuNP and ligand exchange approach, resulting in larger ~20 nm AuNP. At this stage, AuNP-PNAM system was used to optimize the experimental conditions in order to reach high grafting densities, while using a minimum excess of polymer (initial Au concentration, Au/polymer molar ratio: ($[Au]_0/[PNAM]_0$=10), temperature ($T_{exchange}$=80°C), and polymer MW (when M_n increased from 14 100 to 47 300 g.mol^{-1}, the grafting density decreased form ~400 to ~300 chains *per* AuNP).Then, many efforts have been done to find an efficient purification technique (centrifugal ultrafiltration) and prove the purity of grafted AuNP (^{1}H DOSY NMR). Moreover polymer grafted AuNP exhibited high colloidal stability in aqueous medium for more than 12 months.

The optimized experimental conditions, established with AuNP-PNAM systems, were used afterwards for the grafting of the high added-value chromophore-polymer conjugates.

TEM imaging enabled to separately visualize the Au core and the grafted polymer corona. We demonstrated that the grafted polymer corona thickness increases with the polymer MW, suggesting that this parameter influences the chromophore-AuNP mean distance, thus the chromophore photophysical properties near AuNP.

In Chapter IV, photophysical properties of chromophore-polymer conjugates, before and after grafting onto 20 nm AuNP, have been investigated.

Generally, while the absorption properties of chromophores, under one- and two-photo excitation, did not change significantly after coupling along the polymer chain, their fluorescence quantum yields decreased with the increasing number of chromophores *per* chain, due to quenching *via* chromophore-chromophore interactions (Homo-FRET).

The photophysical properties of TP chromophore-polymer conjugate could be measured in water. Even if weak fluorescence quantum yields have been recorded in water (ϕ_{water}(Ant conjugates)<5%), due to increased quenching phenomena in aqueous medium, the overall brightness of TP chromophore-polymer conjugates reached values higher than 1 000 cm^{-1}.M^{-1} in water.

Two-photon absorption properties of conjugates could also be determined in water, with σ_{TPA} values reaching almost 2 000 GM.

Additionally, it has been evidenced that DBB-polymer conjugates could generate singlet oxygen ($^1O_2$) in organic media ($\Phi_{\Delta=}$=0.47 in chloroform), the $^1O_2$ yield being not affected by the density of chromophores on the chain.

After grafting Ant conjugates onto 20 nm AuNP, the fluorescence emission properties of these conjugates were completely quenched, whereas with LY and DBB grafted conjugates, fluorescence emission was partly preserved, possibly due to a lower extent of quenching by energy (or electron) transfer to Au.
AuNP grafted with LY-polymer conjugates with different lengths and architectures displayed an increased fluorescence emission with the increasing length of the polymer chain (distance-dependant fluorescence of LY chromophores near AuNP, *e.g.* 90% fluorescence recovery with LY37KDa conjugate *vs.* 10% with LY2KDa conjugate). Compared to LY-polymer conjugates, TP-polymer conjugates seemed more prone to quenching.

In the final Chapter V, *in cellulo* biological tests have shown that water-soluble TP polymer conjugates and grafted AuNP could be efficiently internalized into cells, with no toxic effects.
Two-Photon microscopy demonstrated the potential of Ant- and DBB-polymer conjugates as promising two-photon bioimaging probes.
Moreover, photoactivation of DBB conjugates and grafted AuNP in cells induced significant cell death (> 90% at 2.10^{-6} mol.L^{-1} DBB), highlighting their capacity to produce cytotoxic species and be further used for PDT.

At this stage, an ongoing work on grafted AuNP systems (post-doc of J. Navarro) is focused on producing AuNP with different sizes and shapes grafted with chromophore-polymer conjugates. More advantageous structures are therefore under investigation: Au nano-stars, nano-rods, nano-bipyramids), potentially triggering the enhancement of photophysical properties near AuNP.
In order to further improve the properties of such hybrid nano-object, we suggest designing block copolymers with one spacing block other than PNAM, parameter which should potentially influence not only the chromophores-AuNP mean distance, responsible for the photophysical properties of conjugates grafted onto AuNP, but also the hydrophilic/hydrophobic balance of the structure. Therefore, using a hydrophobic block (polystyrene (PS) or poly(buthylacrylate) (PBuA)) would possibly limit the access of chromophores to the AuNP surface, or a pH responsive negatively charged (poly(acrylic acid) (PAA)) – to increase the chromophore-AuNP mean distance.

The water-solubility of grafted AuNP in aqueous media, essential for bio-related applications, can also be improved, especially with TP chromophore-polymer conjugates, by increasing the surface functionalization *via* complementary grafting either with small water-soluble molecules (thioctic acids) or with water-soluble thiol-terminated polymers (*e.g.* PEG or PNAM exhibiting stealth properties).

TP chromophore-polymer conjugates before and after grafting onto AuNP were not completely characterized in terms of their photophysical properties. In this context, an efficient quantitative method to measure the extent of fluorescence / quenching with TP conjugates grafted onto AuNP still needs to be implemented.

Moreover, in order to better understand their structure-property relationships in connection with their activity in bio-relevant media, a couple of unanswered questions remain to be investigated with these systems:

- resistance to photobleaching;
- TPA cross section after grafting onto AuNP (by Z-scan method);
- singlet oxygen production in aqueous media (by using fluorescent singlet oxygen sensors).

Undoubtably, some biological studies are still needed before carrying out some investigation *in vivo*. Here, a comparison with commercially available photosensitizers in the same biological conditions, could give insights on the potential of these systems. In order to improve the specificity of action, targeting moieties could also be integrated in the structure of the nano-probe, either attached to the polymer chain, or directly grafted to the AuNP surface.

Finally, besides the fact that the multifunctional tunable nano-system designed here displays promising potential for bioimaging and PDT applications, from a fundamental point of view, it is an ideal model to finely study the interaction between the SPR of AuNP and chromophores.

Articles published and in preparation based on the work carried out in this thesis:

1) **Biocompatible well-defined chromophore–polymer conjugates for photodynamic therapy and two-photon imaging,** C. Cepraga, T. Gallavardin, S. Marotte , P.-H. Lanoë , J.-C. Mulatier, F. Lerouge, S. Parola , M. Lindgren, P. L. Baldeck, J. Marvel, O. Maury, C. Monnereau, A. Favier, C. Andraud, Y. Leverrier and M.-T. Charreyre, *Polym. Chem.* **2013**, *in press*.

2) **Gold nanoparticles and functional polymers as efficient nanoplatform towards luminescent probes**, J. R. G. Navarro, F. Lerouge, C. Cepraga, G. Micouin, D. Chateau, A. Favier, M.-T. Charreyre, P.-H. Lanoë, C. Monnereau, N. P. Blanchard, J. Lermé, F. Chaputa, A.-M. Gabudean, K. Kamada, C. Andraud, P. L. Baldecka S. Parola, in preparation.

3) **Two-photon absorption chromophore-polymer conjugates: synthesis, spectroscopic studies and fluorescence bio-imaging,** C. Cepraga *et al.*, article in preparation

4) **Two-photon absorption photosensitizer-polymer conjugates for both induction of melanoma cell death and fluorescence imaging,** C. Cepraga *et al.*, article in preparation.

5) **Fluorescent gold nanoparticles resulting from size-controlled chromophore-polymer conjugates end-grafted onto the gold surface,** C. Cepraga *et al.*, article in preparation.

6) **Polymer-gold hybrid nanoparticles: synthesis, full characterization of the polymer corona and preliminary confocal fluorescence microscopy images,** C. Cepraga *et al.*, article in preparation.

Appendixes

Appendix II.1: RAFT polymerization

Mechanism of RAFT polymerization

RAFT is a degenerative process involving a reversible transfer of the propagating radicals. The mechanism[1] or RAFT is similar to that of free radical polymerization in terms of initiation, propagation and termination steps, but differs from it by the use of CTA involved in an exchange step competing with propagation (below).

Mechanism of RAFT polymerization

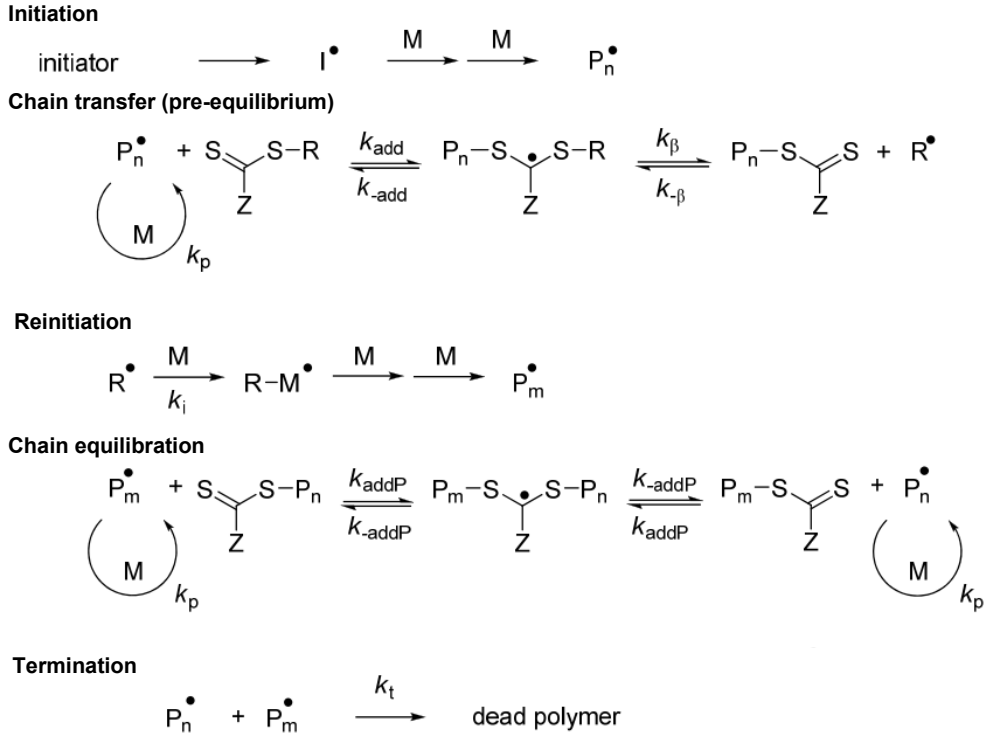

After initiation, primary radicals react with the CTA (pre-equilibrium), leading to the formation of "dormant species" corresponding to macro-CTAs and to the release of R• primary radicals capable to re-initiate polymer chains (see mechanism). "Dormant species" can further undergo chain equilibration (addition-fragmentation equilibrium) with active radicals in the medium. This step results in an equal probability for all chains to grow, thus in the formation of polymers with narrow MW distributions. Besides being involved in addition-fragmentation process, active radicals can also propagate and be terminated like in free radical polymerization. However, in RAFT polymerization due to the limited amount of initiator *vs.* CTA, the number of active species is very low, minimizing the occurrence of termination reactions.

In RAFT polymerization, termination is considerably reduced and all chains grow at a similar rate in the presence of the CTA. CTA is then able to reversibly deactivate propagating radicals such that the majority of living chains are maintained under a "dormant" form.

Because the concentration of the initiator is much lower than in free radical polymerization, and the majority of active radical are involved in addition-fragmentation equilibrium, the total number of polymer chains produced by RAFT can be approximated with the initial number of CTA molecules.

CTA in RAFT polymerization

There are four groups of RAFT agents according to the nature of the Z group: dithioesters (Z = – R); trithiocarbonates (Z = –SR); xanthates (Z = –OR); and dithiocarbamates (Z = $–NR_2$).[2]

The structure of CTA impacts the polymerization reaction kinetics and, most importantly, the degree of structural control. It is worth mentioning here that the proper choice of CTA, appropriate for a particular monomer and reaction conditions (solvent, temperature), determines the success of a well-controlled RAFT polymerization.

Control over polymer architecture *via* RAFT polymerization

Another advantage of RAFT polymerization is that it allows to prepare well-defined polymers with predetermined MW, low polydispersities, and also controlled architectures (below).

Polymers with controlled architecture, composition, and functionality, possible to be synthesized by RAFT.[3]

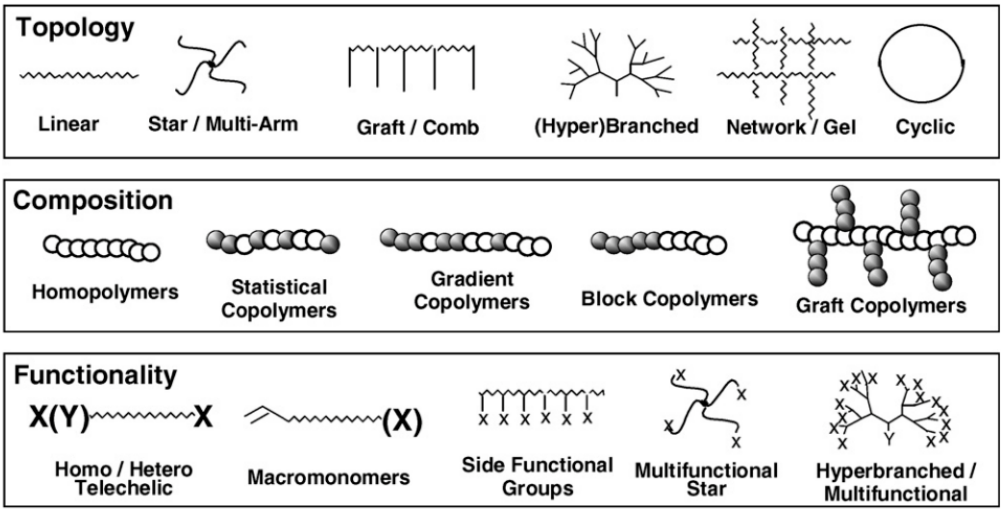

Control over M_n

If the initiator-derived chains are entirely neglected, then M_n(calc) molecular weights can be predicted and calculated from formula below, indicating a linear dependence between MW and monomer conversion.

$$M_n(\text{calc}) = \frac{[monomer]_0 \times conversion}{[CTA]_0} + M_{CTA}$$

$[CTA]_0$ and M_{CTA} are respectively the initial molar concentration and the molecular weight of the CTA.

In reality, the ratio between CTA and initiator determines the amount of the initiator-derived chains (which is never zero) *vs.* CTA-derived chains. If the number of initiator-derived chains is taken into account, then $\underline{M_n(\text{theo})}$ is obtained from the following formula:

$$M_n(\text{theo}) = \frac{[monomer]_0 \times conversion}{[CTA]_0 + 2f[initiator]_0(1-e^{-k_d t})(1+ f_c/2)} + M_{CTA}$$

k_d and f are respectively the initial molar concentration, the decomposition rate constant and the efficiency factor of the initiator. 't' is the polymerization duration and f_c is the proportion of coupling reactions relatively to the overall termination reactions.

Appendix II.2: Polymer conjugates in biology – synthesis strategies

Synthetic strategies used to obtain polymer conjugates

In order to achieve covalent conjugation between polymers and bio-active species, three different strategies have been developed.

They have been extensively described for the particular case of polymer-protein conjugates as:[4 5]

- "Grafting to" – coupling with a pre-formed polymer.
- "Grafting from" – conjugation to an initiator of polymerization.
- "Grafting through" – conjugation to the monomer.

Their characteristics, advantages and disadvantages are summarized below.

Strategies used in bio-conjugation between polymers and bio-active species.

Strategy	**Description**
"*Grafting-to*" or coupling approach 1. End-group functionalization 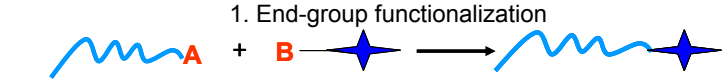 1. Pendant-group functionalization 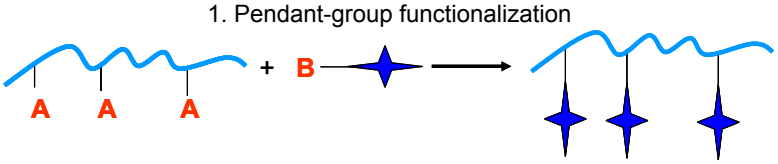	Involves the reaction between functional groups A and B of a preformed polymer and a bio-molecule, respectively. (+) Well-characterized structure of the preformed polymer; possibility to control the number of functions/chain. (-) Needs very efficient coupling chemistry to ensure a high functionalization yield.
"*Grafting-from*" or macro-initiator (or CTA) approach 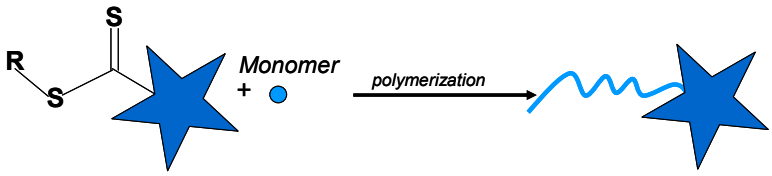	Polymer chain grows from a macro-initiator or macro-CTA carrying the bio-molecule. (+) High functionalization yield. (-) Using a macro-CTA instead of a molecular CTA may interfere with the polymerization process (kinetics, control of Mn, etc.). Bio-active molecule should not be degradable nor interfere with polymerization.
"*Grafting-through*" or macro-monomer approach 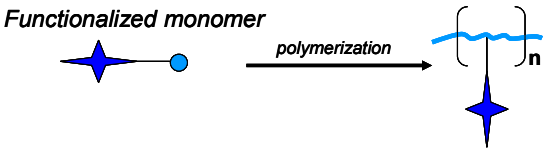	Involves the polymerization of functionalized monomers prior to polymerization. (+) High degree of functionalization. (-) Using a macro-monomer can complicate the polymerization process (kinetics, control of Mn, etc.). Bio-active molecule should not be degradable nor interfere with polymerization

(+) Advantages

(-) Limitations

Coupling chemistry

It is important to note that both bio-active molecules and polymers are generally not reactive by themselves and may need a preliminary step of functionalization before conjugation. Because many

bio-active molecules already carry functional groups, most of the time polymer moieties have to be transformed into reactive functions (before or after polymerization).

In this context, a very large variety of chemical reactions can be used to synthesize polymer conjugates.[6] The main functional groups leading to the formation of polymer conjugates are listed below: hydroxyl, amine, carboxyl, thiol groups involved in numerous coupling chemistry reactions.

Functional groups enabling the coupling between the polymer and the bio-active molecule.

Reactive group	**Description**
Hydroxyl (-OH)	Can be transformed into many activated functions suitable for coupling as mesylates and tosylates but also as succinimido- or imidazolyl-carbonates, and p-nitrophenylformates; all of them capable to readily react with primary amines.
Primary amine ($-NH_2$)	Are generally coupled to carboxyl-containing species.
Carboxyl ($-COO^-$)	Most commonly activated using N-hydroxysuccinimide (NHS), giving N-hydroxysuccinimidyl esters, suitable for coupling with primary amines and, less frequently, with hydroxyl functions.
Thiols (-SH)	Have a very good selective reactivity with double bonds (thiol-ene reaction) and have been largely developed especially in the framework of RAFT polymerization mediated bioconjugation. [7]

Besides coupling chemistry, several other approaches can be used for conjugation[4] (*e.g.* native chemical ligation, Staudinger ligation, “click” chemistry reactions).

Incorporation of a linker

Ideally, macromolecular conjugates should be stable and pharmacologically inactive in bio-relevant media, but be able to release the drug from the polymeric conjugate after uptake at the desired site of action. That is why in polymer conjugation, the active molecule (drug) may be conjugated to the polymer through a degradable linker. Peptidyl and ester degradable linkers have been widely employed (e.g. pH-sensitive cis-aconityl, hydrazone and acetal linkers).[8]

Often the drug release from polymer backbone is warranted through controlled hydrolysis of the linker which can be designed to respond to the passive hydrolysis, acid catalytic hydrolysis, and/or enzymatic hydrolysis.[9]

Position on the chain

Regarding the position of conjugation on a polymer chain, two main types of polymer conjugates can be identified: [10]

a) End-group conjugation

PEG is usually used as a linear polymer that can be functionalized at either one end or at both ends of the polymer chain. PEG conjugation has been developed with protein-drugs, peptides, oligonucleotides, antibodies. Many PEGylated drugs are in the stage of clinical trials; many of them being already approved and commercialized.[11]

Besides PEG conjugation, a very easy strategy to obtain end-group polymer bio-conjugate systems has emerged with the development of CRP techniques.[12] These new techniques allow obtaining a broad variety of well-defined and functionalized polymers by modifying the low molecular weight initiators or CTA with bio-active molecules before polymerization.

End-group conjugation is usually relatively easy to implement, however it exhibits limited drug loading efficiency. In order to improve the loading capacity, multiple conjugation sites could be reached by designing pendant-group systems.

b) Pendant-group conjugation

The design of pendant-group conjugates is based on Ringsdorf's model mentioned above. They can be synthesized with a controlled number of pendant reactive sites along the polymer backbone ether by introducing a functional co(monomer) capable of bio-conjugation, or polymerizing an already bio-conjugated monomer.

Copolymers of *N*-(2-hydroxypropyl) methacrylamide (HPMA) are probably the most developed pendant-group systems for the preparation of anti-cancer agents.[13] A relevant example would be PK1, the first clinically investigated water-soluble polymer-drug conjugate for cancer therapy.[14] This agent is composed of the anticancer anthracycline antibiotic doxorubicin (DOX) attached to a P(HPMA) copolymer backbone *via* a degradable linker (structure below).[15]

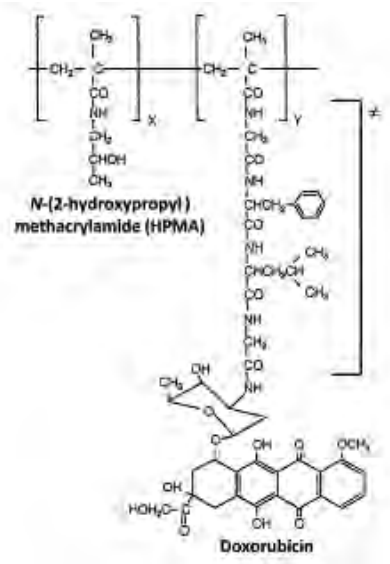

Structure of PK1 (FCE28068), a HPMA copolymer conjugate bearing the anticancer agent doxorubicin bound via the degradable linker (≠).[15]

To conclude, the design of polymer conjugates offers many opportunities in terms of synthesis strategies, coupling chemistry, position of bio-active species on the polymer chain etc., allowing to produce polymer conjugates with high degree of control over their structural and chemical properties (*e.g.* nature, biodegradability, chain composition and functionality, length, size, and architecture), thus finely tune them.

Appendix II.3: RAFT polymerization kinetics of NAM in Shlenk flask

a) Time-dependent monomer consumption during RAFT polymerization of NAM in Schlenk flask (left): $[M]_0$ – initial monomer concentration, [M] – monomer concentration at a known time "t"; b) Linear dependence of average number molecular weight with conversion: Mn(SEC/LS) – molecular weight determined by SEC/LS technique, M_n(calc) – calculated M_n.

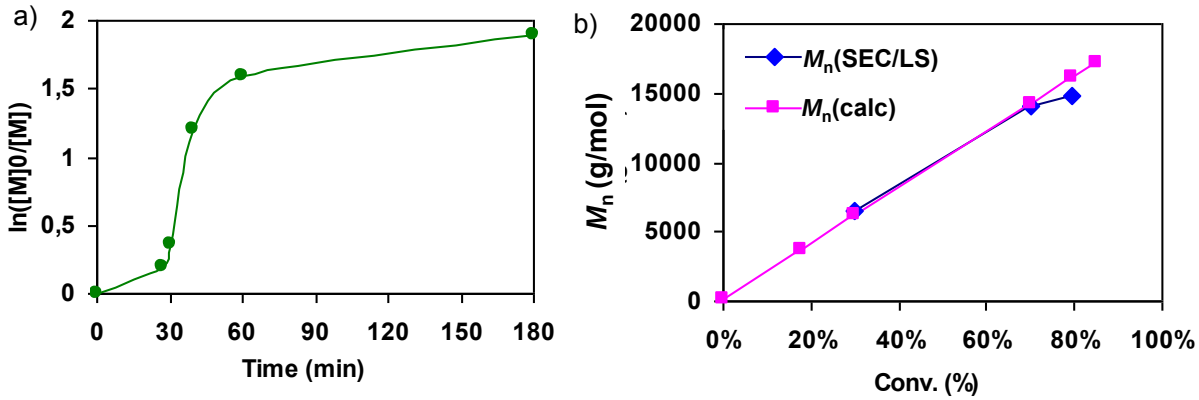

Appendix II.4: ^{1}H NMR of PNAM and P(NAM-*co*-NAS) (co)polymers obtained by RAFT in $CDCl_3$

^{1}H NMR spectrum of PNAM_1 from PNAM parallel reactor series.

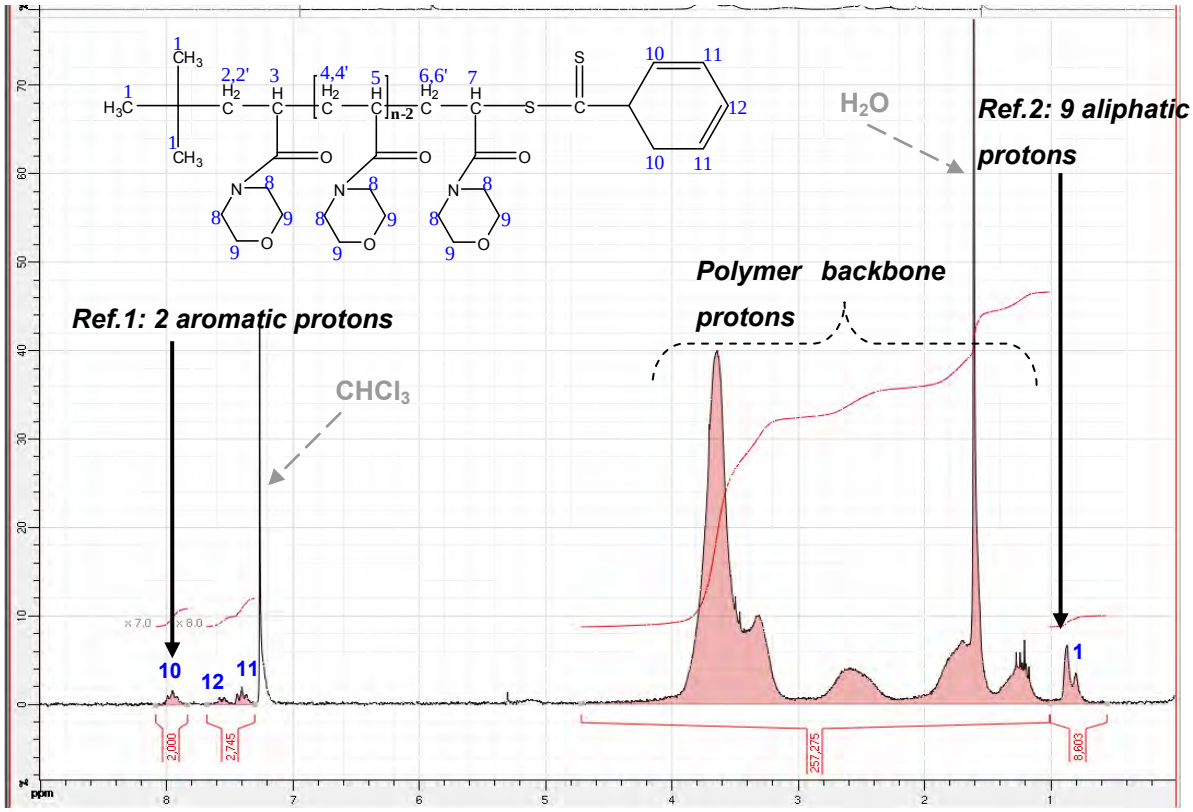

^{1}H NMR spectrum of COPO_1 from P(NAM-*co*-NAS) parallel reactor series.

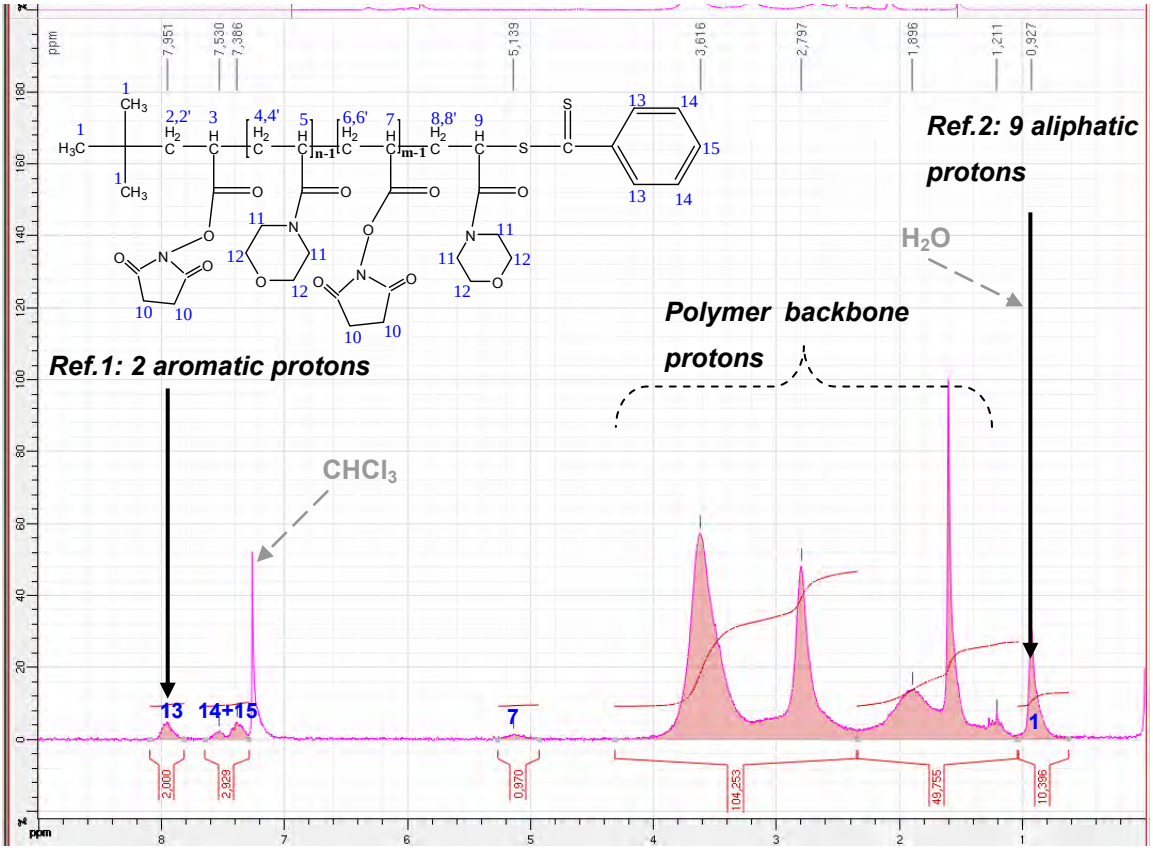

Appendix II.5: MALDI-TOF analysis of PNAM and P(NAM-co-NAS) (co)polymers obtained by RAFT

PNAM_1 from PNAM parallel reactor series,
MALDI-TOF – linear mode.

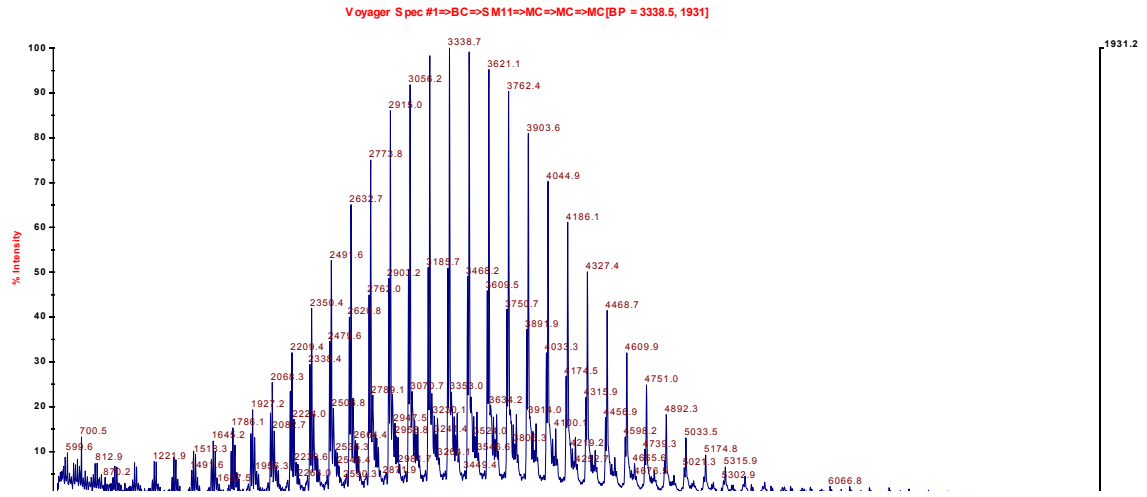

Zooming on a part of the spectrum

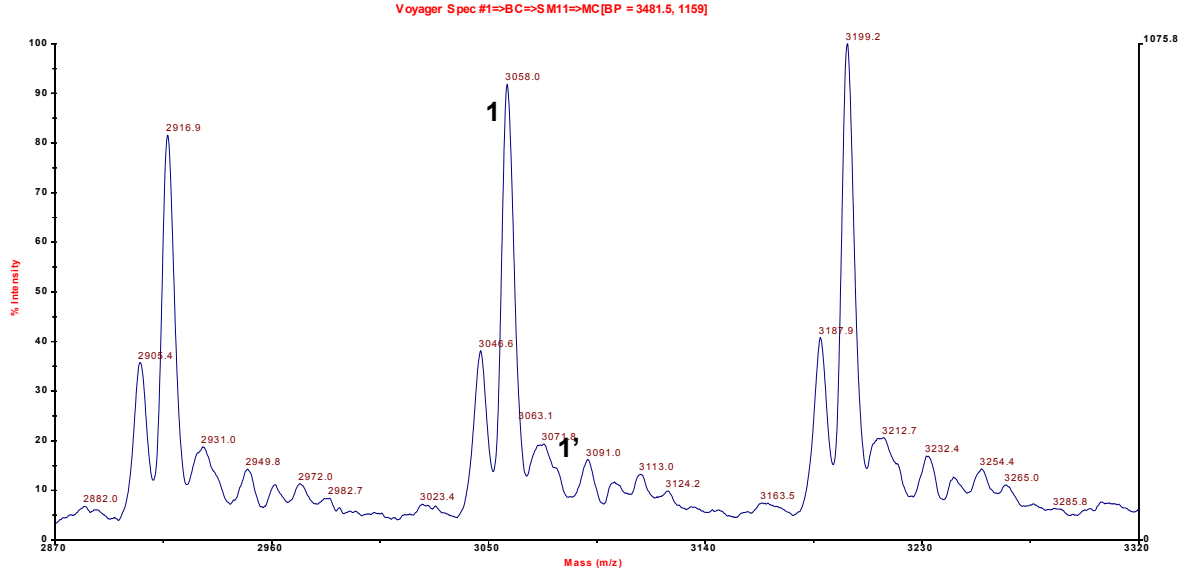

- Ionization of PNAM chains: Na^+ (1) and K^+ (1')
- Interval between 2 peaks: 141 m/z (corresponding to NAM unit)
- Raw formula of predominant species terminated with DT: $C_{151}H_{234}N_{20}O_{40}S_2Na_1$ (3056.7 m/z) / $C_{151}H_{234}N_{20}O_{40}S_2K_1$ (3072.8 m/z)

Range	M_n(MALDI-TOF)	PDI
770-5800	3 260	1.06

COPO_1 from P(NAM-co-NAS) parallel reactor series.

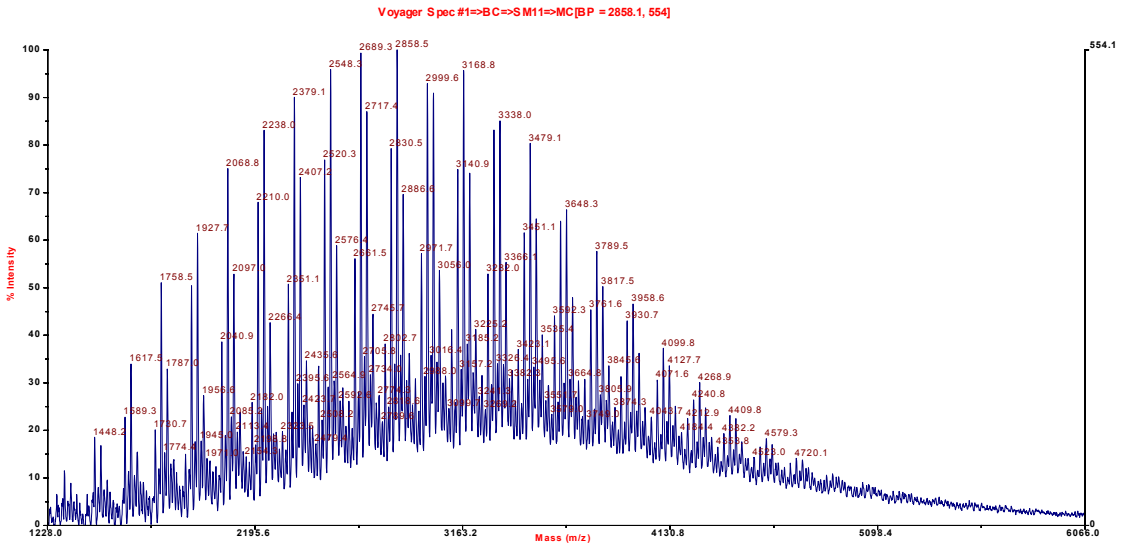

Zooming on a part of the spectrum

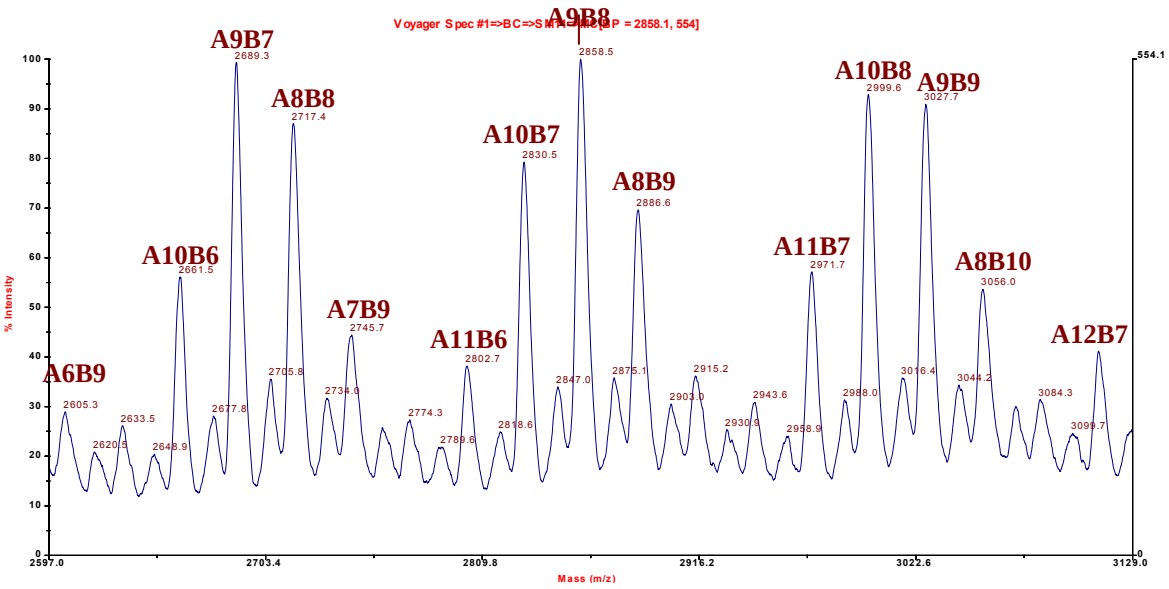

- A=NAM; B=NAS
- Ionization of chains : Na^+ (1) and K^+ (1')
- Interval between 2 peaks: 141 m/z (corresponding to NAM unit), 169 m/z (corresponding to NAS unit)
- Predominant species terminated with DT

Range	M_n(MALDI-TOF)	PDI
1100 – 6130	3 185	1.09

Appendix II.6: Determination of DT%

Molecular weights determined by SEC/LS

The total number of chains could be approximated from M_n(SEC/LS) and the number of DT-ended chains from M_n(calc) (Appendix II.1). A value of DT% could then be obtained from Eq. (3).

$$DT\% = \frac{Mn(calc)}{Mn(SEC/LS)} \times 100\% \quad (3)$$

This methodology may however be associated with a significant error since it is assumed that every CTA leads to one DT-ended chain. Moreover, the accuracy of this method can be influenced by the uncertainties in M_n(SEC/LS), especially for low M_n polymers, due to a weak LS signal.

UV absorption

Another potential method is based on the comparison between the specific absorption (Beer-Lambert's law (A=ε.l.c)) of amide groups of the polymer backbone (at 245 nm) (proportional to the total number of chains) with the specific absorption of DT chain-ends with a maximum at 305 nm[16] (proportional to the number of DT-terminated chains) (Eq. (4)). It has previously been employed to estimate the efficiency of RAFT polymerization.

$$DT\% = \frac{Nb.chains\_DT}{Nb.chains\_total} \times 100\% = \frac{conc.\_DT}{conc.\_copolymer} \times 100\% = \frac{\frac{A_{DT}}{\varepsilon_{DT}}}{\frac{A_{polymer}}{\varepsilon_{polymer}}} \times 100\% \quad (4)$$

'ε_{DT}' / '$\varepsilon_{polymer}$' are the molar extinction coefficients (at the maximum absorption wavelength) of the dithioester group and of the polymer backbone, respectively; and '*A*' – the absorbance values at the maximum absorption wavelength. However, since this method requires knowing both the extinction coefficients corresponding to DT chain-ends and that of the polymer backbone respectively, it was not applied in our case.

Appendix II.7: Nc determination from ^{1}H NMR spectrum of 4DBB-AEM conjugate in $CDCl_3$

^{1}H NMR spectrum was recorded on a Bruker 500 MHz spectrometer in $CDCl_3$.

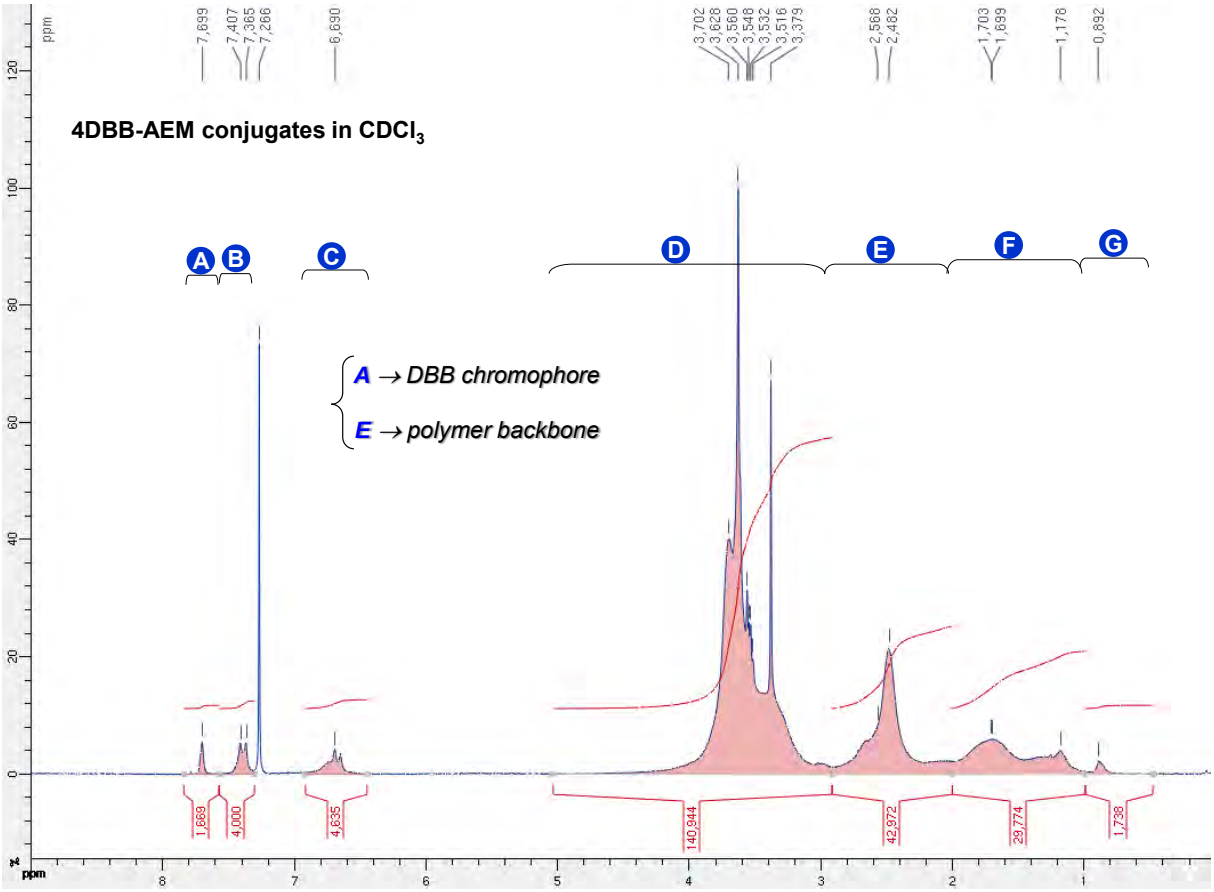

Calculations of the number of DBB/chain using NMR integrals A and E is given below

Integral system	Expression of Nc	Result of Nc
A & E	$Nc = \dfrac{(83.7 + 33.8 \times 4)}{2 \times \dfrac{E}{A} - 4}$	**4.6**

Appendix II.8: Nc determination by UV-Vis spectroscopy of 4DBB-H conjugate in DMF

UV-Vis absorption spectroscopy used to determine Nc – experimental steps followed to obtain Nc: compare at known concentrations the total integrated absorption oscillator strength (the ratio between integral of absorption curve and concentration) of DBB conjugate vs. DBB free chromophore.

For this method we suppose as known the values of ε for both samples (chromophore and conjugate) in order to calculate the respective concentrations from Beer-Lambert's law.

Results for 4DBB-H conjugate (M_n = 13 800 g/mol) using the absorption oscillator strength

Sample in DMF	ε at 400nm	Abs. integral (I)	Conc.	Ratio I/conc.	Nc = (2) (1)
DBB-NH_2	55 000	13.07	2.68×10^{-6}	$4.88 \times 10^{+6}$ (1)	-
4DBB-H	214 000	9.37	4.35×10^{-7}	$2.15 \times 10^{+7}$ (2)	**4.4**

Other methods providing proof of efficient coupling of chromophores along the polymer chain

Visual observations

P(NAM-*co*-NAS) copolymer is a light pink powder before coupling with the chromophore, due to the characteristic absorption of DT chain-ends at 305 nm (coloration which depends on the proportion of DT chain-end in the polymer, thus on polymer MW). Since the chromophores used in this study exhibit much stronger absorption properties in the visible region and are highly colored compounds (LY – bright yellow, Ant – red-orange, and DBB – yellow), their coupling onto the copolymers were then witnessed by the strong coloration of the final purified conjugates, that resembled to that of the chromophore.

Fluorescence spectroscopy

Fluorescence spectroscopy provided a qualitative proof of chromophore coupling. After reaction with the P(NAM-*co*-NAS) copolymer, which is initially not fluorescent, the resulting purified conjugates were fluorescent with an emission corresponding to the considered chromophore. However, using this method, it was not possible to quantify the coupling yield and Nc, since fluorescence quantum yield of the chromophore tend to decrease upon coupling onto the polymer chain. Photophysical properties of chromophore-polymer conjugates will be thoroughly presented and discussed in Chapter IV.

Appendix II.9: UV-Vis absorption of P(NAM-*co*-NAS) copolymers: i) after RAFT polymerization; ii) post-treated by hydrolysis; iii) post-treated by AEM capping

UV-Vis spectrum of P(NAM-*co*-NAS) copolymers in water:

- carrying a DT end-group;
- post-treated by hydrolysis;
- post-treated by AEM capping.

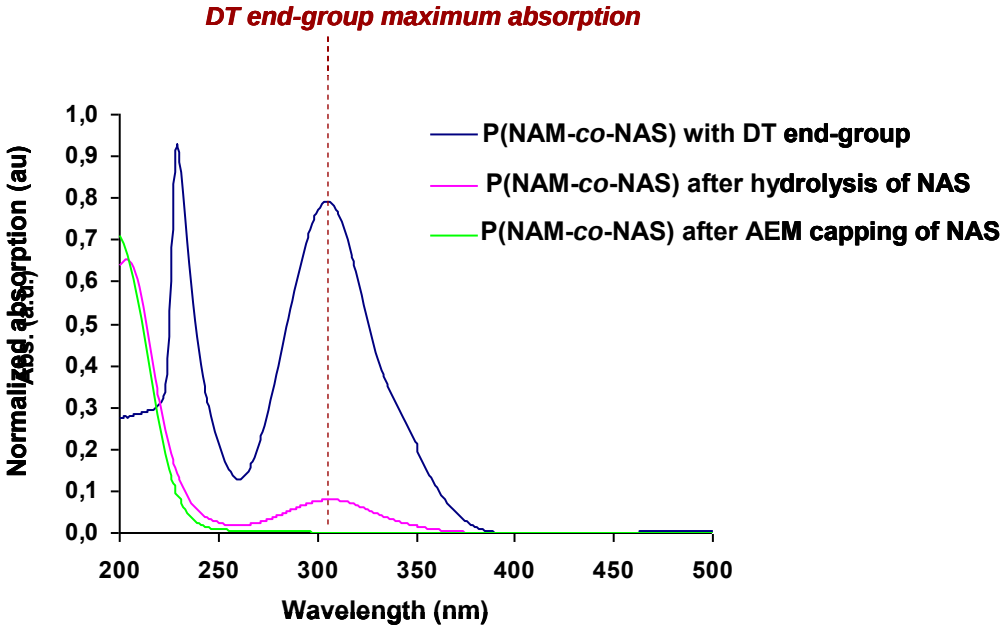

- After AEM capping, the absorption of DT end-groups (at ~310 nm) completely disappears.

- After hydrolysis, a residual absorption at ~310 nm indicated an incomplete transformation of DT into thiols.

Appendix III.1: Analytical techniques used to characterize polymer grafted AuNP

A list of analytical techniques often used to characterize grafted AuNP-polymer systems is summarized in the table below.

List of analytical techniques used to characterize polymer grafted AuNP

Analyses	Characterized parameter	Information	Ref.
TEM / SEM	AuNP size and grafted polymer corona	Structure: shape and size	[17]
AFM	Size before and after grafting	Proof of grafting	[18]
TGA*	Organic/inorganic weight ratio	Grafting density	[19]
DLS	Hydrodynamic diameter	Size in solution	[20]
Electrophoretic LS	Zeta potential	Surface charge	[21]
^{1}H NMR spectroscopy & PSGE NMR	Chemical characterization of a sample	Proof of grafting	[22]
UV-Vis spectroscopy	SPR band	- Proof of grafting (red-shifted SPR). - Stability - Study the effect of various parameters: pH, T, ionic force.	All articles
SERS	Imprint of adsorbed molecules	SERS enhancement factor	[22]
DSC	Heat capacity	Proof of grafting	[23]
Turbidity	Transmittance	Study the thermosensitive behavior	[24]
SEC	Relative molecular weight	Proof of grafting	[25]
EDAX **XPS**	Elemental analyses	Proof of grafting	[26] [27]

AFM = Atomic Force Microscopy

EDAX = Energy dispersive X-ray spectroscopy UV-Vis absorption

DLS = Diffusion Light Scattering

IR = Infra Red

LS = Light Scattering

NMR = Nuclear Magnetic Resonance

SEC = Size Exclusion Chromatography

SEM = Scanning Electron Microscopy

SERS =Surface Enhanced Raman Scattering

TEM = Transmission Electron Microscopy

TGA = Thermogravometric Analyses

XPS = X-ray Photoelectron Spectroscopy

Appendix III.2: Purification of grafted AuNP-PNAM systems

Purification methods applied to purify AuNP-PNAM system.

1) Dialysis

Dialysis is used to remove the molecules from a solution *via* osmosis. The mixture of grafted AuNP after synthesis was dialyzed against water using a regenerated cellulose porous membrane with a Molecular Weight Cut-Off MWCO=50kDa. MWCO is used to describe the retention capabilities of the membrane and refers to the molecular mass of a solute where the membranes have a rejection of greater than 90%.
Indeed, all species with a M_n << 50kDa are expected to be eliminated by dialysis, living inside the membrane only pure AuNP-PNAM.
Since the polymers molecular weight was always below 30kDa, the functionalized AuNP were expected to remain within the dialysis membrane and the unbound polymer eliminated.

2) Centrifugation

Centrifugation involves the use of the centrifugal force to sediment larger species in solution.
The mixture of grafted AuNP was centrifuged hoping that AuNP-PNAM sediment at the bottom of the tube and can be efficiently recovered.

3) Centrifugal ultrafiltration

Centrifugal ultrafiltration consists in filtrating a solution containing several species through a porous membrane by centrifugation. The principle of this technique is lustrated below. The device used for purification, Amicon, was fitted with a membrane with MWCO=50kDa of 100kDa (depending on the size of purified AuNP).
After centrifugation of AuNP mixture through the membrane, we expected to recover in the retentate pure AuNP-PNAM, while free polymer chains and other molecular species are recovered in the filtrate (figure below).

Principle of centrifugal ultrafiltration using Amicon type device: the top tube is fitted with a tangential porous membrane. After centrifugation, the filtrate (solvent + smaller species) is recovered in the bottom tube, while grafted AuNP remain in the retentate.

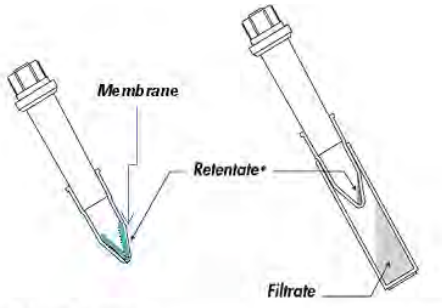

4) Size Exclusion Chromatography (SEC)

SEC involves the use of porous gels. It allows separating different species from a sample based on their size. Because species that have a larger size compared to the pore size of the gel have very little entrance into the pores, they are eluted quicker and can be collected first at the other end of the column.
This purification technique is applied for AuNP grafted with chromophore-polymer conjugates and thus detailed in Section III.4.

Appendix III.3: ^{1}H-DOSY NMR

^{1}H-DOSY NMR stands for Diffusion Ordered Spectroscopy (DOSY) NMR. The measurement of diffusion is carried out by observing the attenuation of the NMR spectra acquired as a function of the gradient filed strength (Pulsed-Field Gradient, PFG-NMR spectra).

Example of 1H-DOSY NMR: a) Pulsed-Filed Gradient-NMR spectra; b) 2D DOSY corresponding charts. *

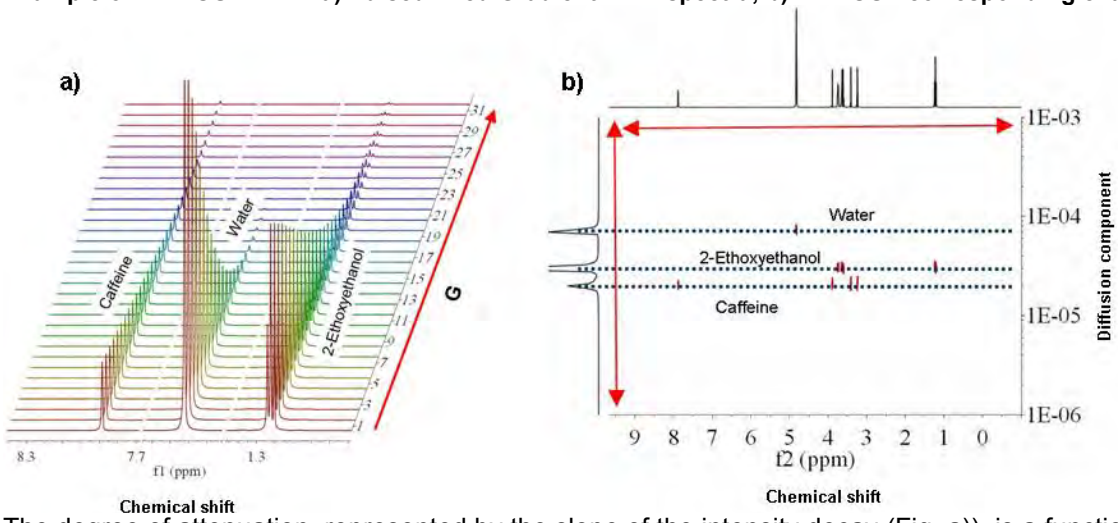

The degree of attenuation, represented by the slope of the intensity decay (Fig. a)), is a function of the magnetic gradient pulse amplitude and occurs at a rate proportional to the diffusion coefficient of the molecule. All signals corresponding to the same molecular species will then decay at the same rate, corresponding to the same diffusion coefficient.

Data processing of PFG-NMR spectra, called the DOSY transformation, will allow to obtain 2D charts (Fig. b)) containing a horizontal dimension, encoding the chemical shifts (classical ^{1}H NMR spectrum), and a vertical dimension, encoding the diffusion constants of each chemical species in the analyzed mixture.

* http://nmr-analysis.blogspot.fr/2008/07/dosy-nmr.html

Appendix III.4: Modification of DT end-groups of PNAM-DT polymer

Goal: Substitution of dithioester group (DT) on PNAM-**DT** by PNAM-**X**, with **X**= sulfur-free end-group.

Reaction: PNAM-**DT** + AIBN $\xrightarrow{\text{Dioxane, T=80°C}}$ PNAM-**X**

The purpose was to cleave the DT end-group in the presence of a large excess of initiator (AIBN, 10 eq., 2 hours under nitrogen), substituting it with the isobutyronitrile group (X=isobutyronitrile?).
M_n(PNAM-DT) = 3 300 g.mol^{-1}.

Results: Poof of dithioester (DT) end-group modification.

a) UV-Vis spectroscopy

After reaction (PNAM-**X**, black curve), the absence of a peak at 309 nm, characteristic of -C=S bond of DT group in PNAM-**DT** (purple curve), evidences the successful modification of the **DT** into **X**.
However, the chemical nature of **X** group could not be determined form this analysis.

UV-Vis spectroscopy of PNAM before and after reaction with AIBN.

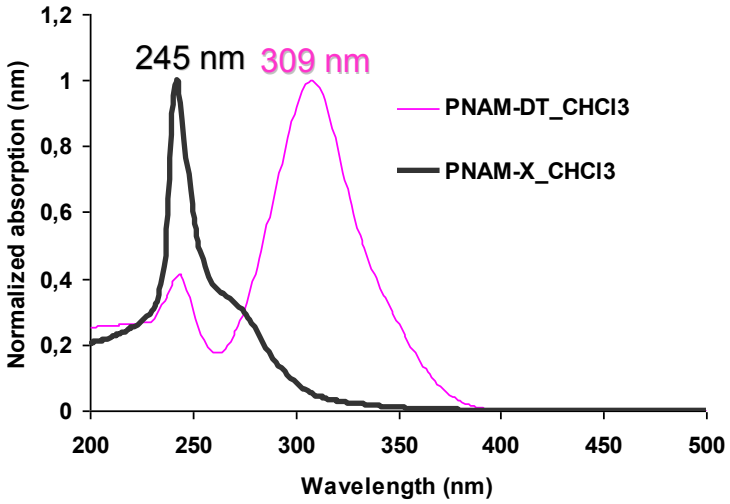

b) ^{1}H NMR spectroscopy in $CDCl_3$

The purpose was to determine what could be the nature of **X** group. If all **DT** end-group (containing aromatic protons) were completely cleaved, then no aromatic protons (~7-8 ppm) should appear on the spectrum.

^{1}H NMR spectrum of PNAM-DT before reaction in $CDCl_3$.

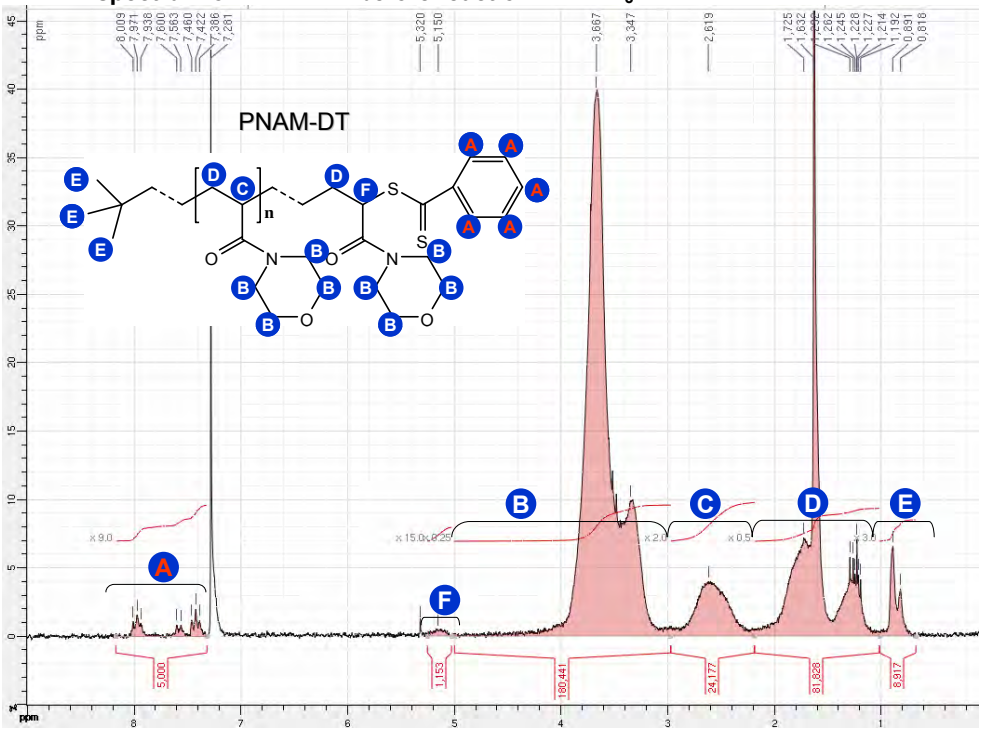

^{1}H NMR spectrum of PNAM-X after reaction in $CDCl_3$.

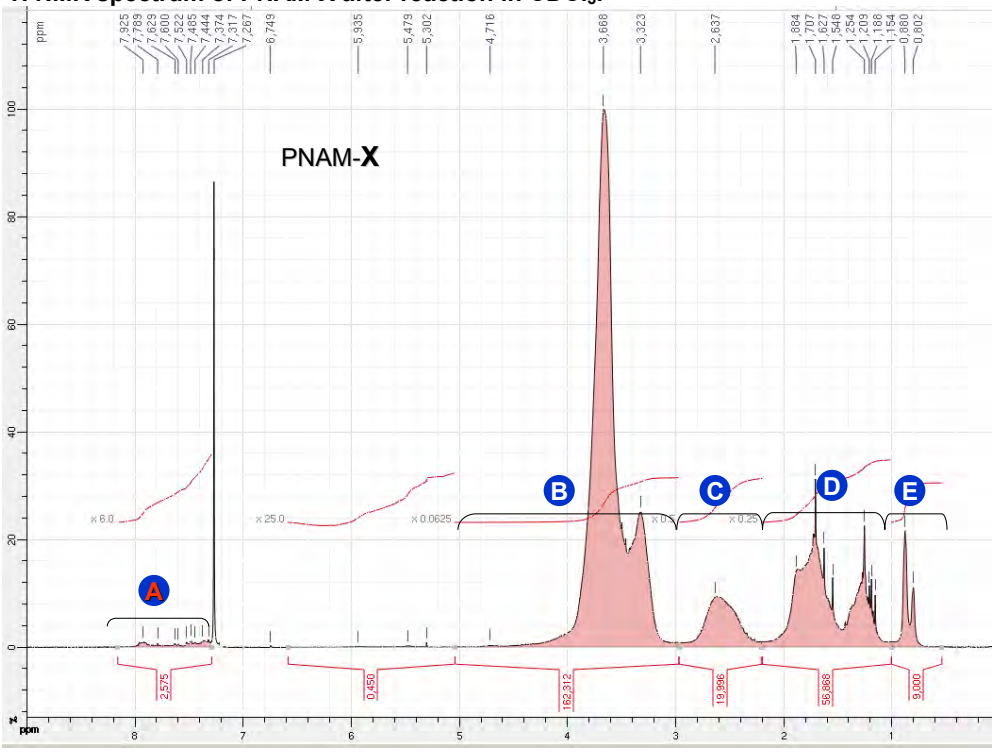

Conclusion: ^{1}H NMR spectroscopy showed that **DT** groups were partly cleaved; the absence of H linked to the carbon in a α position of relative to **DT** group (F) suggests the modification of **DT** end-groups. Nonetheless, the presence of residual aromatic protons (~7-8 ppm) on the spectrum of PNAM-**X** implies the possible addition or oxidation of DT group without the loss of phenyl moiety.

c) Maldi-TOF spectrometry

Maldi-TOF spectrometry was used to determine the chemical nature of **X** group after reaction with AIBN (results not shown here).

It seemed difficult to read out the Maldi-TOF peaks, due to the numerous species present in the sample, as well as to assign them and find possible structures of the X-group.

Nevertheless, Maldi-TOF chromatograms show that after reaction:

- PANM-**DT** species represent les than 10 % of the PNAM-**X** sample;
- Many other species contain 2 S atoms.

Conclusion: Maldi-TOF spectrometry shows that **X** may still contain sulfur atoms, but is possibly not a **DT**, nor a thiol.

General conclusion: PNAM-**DT** end-group modification was successful; the new PNAM-**X** reaction product still partly contained sulfur atoms, thus no **DT** or thiol end-groups were present.

Appendix III.5: DLS of AuNP-PNAM during the ligand exchange process – influence of the temperature

Goal: monitoring the changes in the hydrodynamic radius during the ligand exchange process between the citrate molecules and PNAM polymers anchoring the surface of AuNP.

DLS correlograms of AuNP-PNAM after 3 h ligand exchange at 25°C, 50°C, and 80°C.

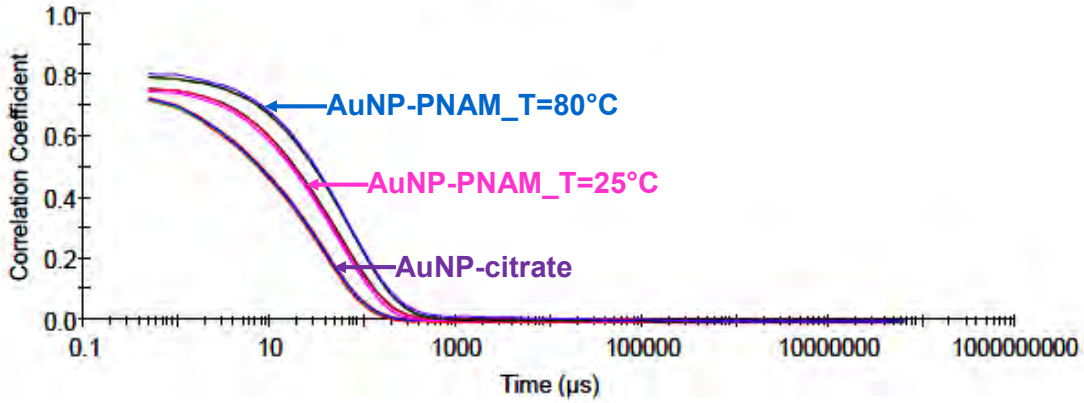

The DLS correlograms evidence that the higher the temperature, the larger is the hydrodynamic radius of AuNP, proving the increased rate of polymer grafting by ligand exchange.

Appendix III.6: Grafting density of AuNP-PNAM assemblies calculated from TEM and TGA analyses

a) Comparison between AuNP-PNAM synthesized by in situ and ligand exchange approaches.

Analyses	Results	In situ	Ligand exchange (T=880°C, Au/S=3)
ATG	Analyzed sample weight (mg)	11.59	3.322
	Polymer/Au weight ratio	1.98	0.21
TEM	AuNP mean diameter (nm)	2.6	17
	Polymer corona thickness (nm)	n.d.*	7 ± 1
Grafting density	Chains/AuNP	15	440
	Chains/nm²	0.73	0.49

*n.d.=not determined

b) Influence of Au/S ratio (Au/PNAM ratio) on the properties of AuNP-PNAM obtained by ligand exchange.

Analyses	Parameter	Au/S = 3/1	Au/S = 10/1	Au/S = 20/1
ATG	Analyzed sample weight (mg)	3.322	4.560	4.940
	Polymer/Au weight ratio	0.21	0.25	0.21
TEM	AuNP mean diameter (nm)	17	16	15.5
	Polymer corona thickness (nm)*	7 ± 1	8 ± 1	7 ± 1
Grafting density	Chains/AuNP	440	443	344
	Chains/nm²	0.49	0.55	0.46

c) Influence of temperature during the ligand exchange process on the properties of AuNP-PNAM.

Analyses	Parameter	T=25°C	T=50°C	T=80°C
ATG	Analyzed sample weight (mg)	3.932	1.114	3.332
	Polymer/Au weight ratio	0.15	0.18	0.21
TEM	AuNP mean diameter (nm)	17	17	17
	Polymer corona thickness (nm)	2 (PTA)*	5 (PTA*) / 6 (RuO_4)*	7 (RuO_4)*
Grafting density	Chains/AuNP	331	384	440
	Chains/nm²	0.36	0.42	0.49

d) Influence of polymer M_n on the properties of AuNP-PNAM obtained by ligand exchange.

Analyses	Parameter	M_n= 14 100g/mol	M_n= 26 400g/mol	M_n= 47 300g/mol
ATG	Analyzed sample weight (mg)	3.322	5.304	5.172
	Polymer/Au weight ratio	0.21	0.29	0.52
TEM	AuNP mean diameter (nm)	17 nm	16 nm	16 nm
	Polymer corona thickness (nm)	7 ± 1	12 ± 2	14 ± 2
Grafting density	Chains/AuNP	440	272	276
	Chains/nm²	0.49	0.33	0.34

Appendix III.7: Ligand exchange one-step process *vs.* ligand exchange two-step process

a) UV-Vis spectroscopy **results of AuNP-PNAM(aq.) obtained by ligand exchange one-step process (dashed blue line) vs. two-step process (straight purple line).**

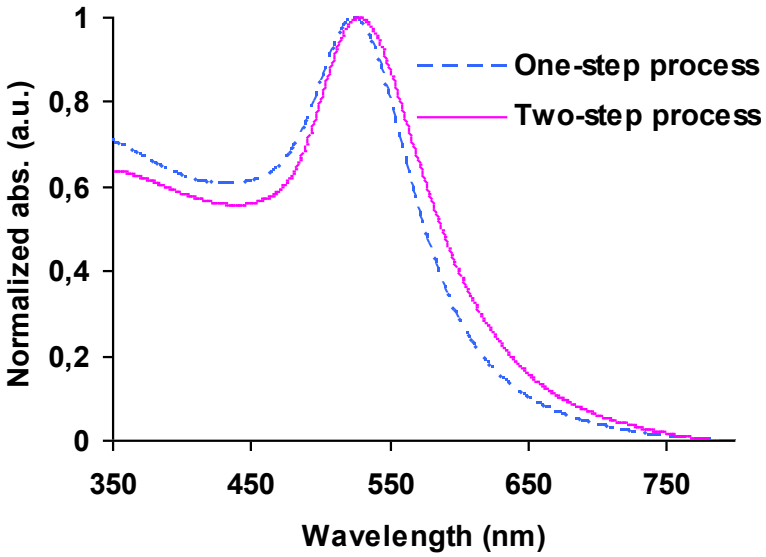

b) TEM imaging **of AuNP-PNAM obtained by ligand exchange one-step process (left) vs. two-step process (right) (under the same staining conditions: RuO_4, 15 min).**

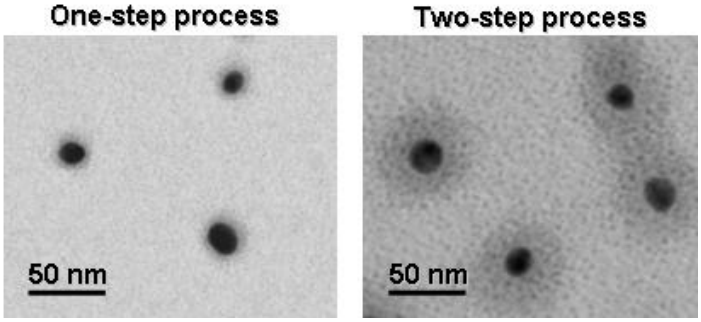

Appendix III.8: Purification of 20 nm AuNP grafted with chromophore-polymer conjugates

a) Purification by centrifugal ultrafiltration of AuNP-LY-conjugates.

Before centrifugation the reaction mixture (deep red) made of grafted AuNP and free LY conjugates. After centrifugation, grafted AuNP (purple) remain concentrated in the retentate (above the membrane), and ungrafted LY-conjugates (yellow), are recovered in the filtrate.

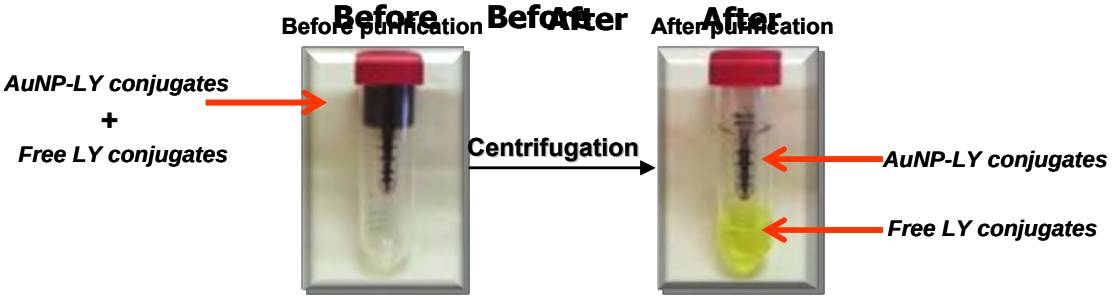

b) Purification of AuNP grafted with DBB- and Ant-conjugates by SEC column:

Schematic representation of SEC technique (a)) and the example of AuNP-10Ant-AEM conjugates purified by optimized SEC method (b)).

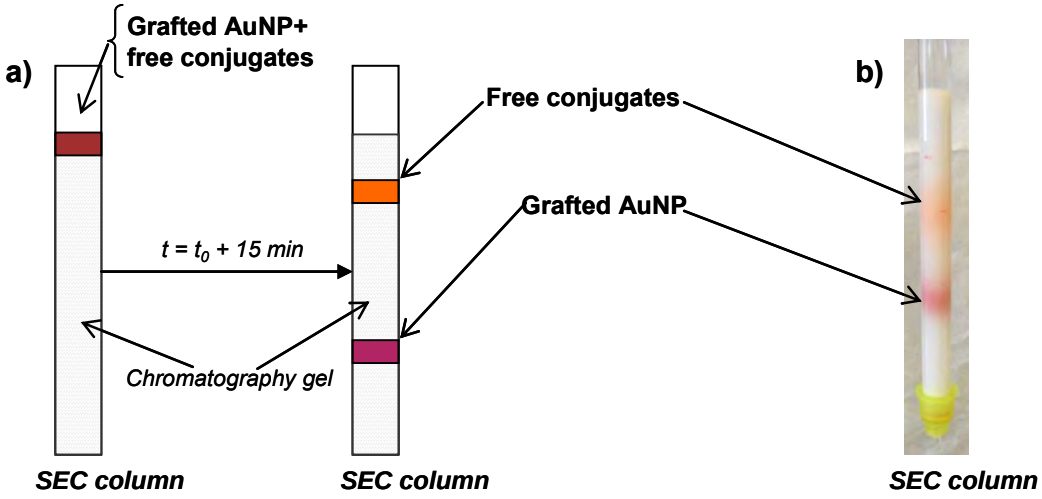

For an efficient separation (and avoid the adsorption of conjugates on the chromatography gel) we varied separately:

- the chemical nature of the chromatography gel (dextrane, allyl-dextran, polyamide, crosslinked cellulose);
- the type of bottom filter maintaining the gel (poly(ether sulphone), nylon, cotton, glass wool, sintered grass, sintered PTFE);
- the ionic force of the aqueous eluent (NaCl concentration: 0.1 % - 10 % wt.).

Optimum SEC purification conditions were found when using a glass SEC column fitted with PTFE porous filter and filled with crosslinked cellulose Cellufine GCL-2000 gel, running it with 0.25% wt. NaCl eluent.

Influence of SEC gel on the separation efficiency of the species in the sample.

Gel	Chemical structure	Elution flow	Eluent	Separation efficiency
Sephadex G-50 Fine DNA Grade	Dextran	Gravity	0.25% $NaCl_{(aq.)}$	No separation
Gel Sephacryl S200-HR	Crosslinked allyl dextran with N,N-bisacrylamide	Gravity	0.25% $NaCl_{(aq.)}$	A beginning of separation slightly visible
Bio-Gel P-100 Gel Medium	Polyamide	Gravity	0.25% $NaCl_{(aq.)}$	No separation
Cellufine GCL-2000	Crosslinked cellulose	Gravity	0.25% $NaCl_{(aq.)}$	Visible separation noticed by two different colors appearing on the gel during elution (Figure II. 3)

Appendix III.9: Grafting density of AuNP-conjugate assemblies calculated by UV-Vis spectroscopy and fluorescence spectroscopy

The grafting density in chains/AuNP was calculated as the ration between the concentrations of grafted conjugates ($c_{conjugates}$) on the concentration of AuNP (c_{AuNP}) (equation below).

$$Grafting\_density = \frac{c_{conjugates}}{c_{AuNP}}$$

***a) UV-Vis spectroscopy* method applied for AuNP-DBB conjugates**

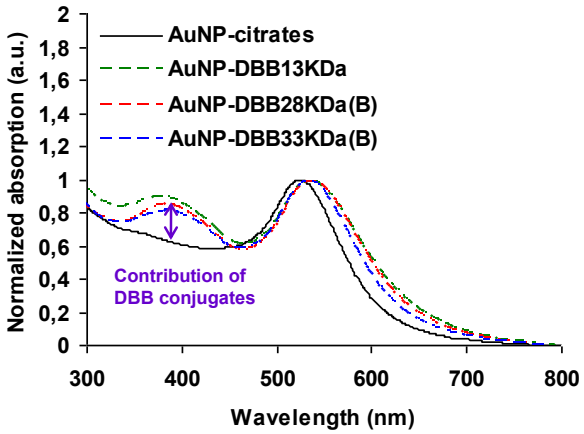

1) First the contribution of DBB conjugates to the absorption spectra of grafted AuNP has been calculated at 390nm, by subtracting the value of corresponding absorbance at this wavelength of only AuNP (corresponding to citrate-capped AuNP) Values are reported in the table above.

2) The concentrations of AuNP and of conjugates, were respectively calculated from Beer-Lambert's law ($A=\varepsilon lc$): with ε – the extinction coefficient of AuNP or conjugates, respectively; l=1 cm; and c – the concentration of AuNP / conjugates, respectively.

Grafted AuNP	**Relative Abs. of conjugates (max)***	**ε_{390nm} ($cm^{-1}.M^{-1}$)**	**c_{AuNP} (M)****	**$c_{conjugates}$ (M)**	**Grafting density (chains/AuNP // chains/nm²)**
AuNP-DBB13KDa @ 400 nm	0.27	176 000	1.66×10^{-9}	1.52×10^{-6}	913 // 1.01
AuNP-DBB27KDa(B) @ 400 nm	0.23	181 700	1.66×10^{-9}	1.25×10^{-6}	750 // 0.82
AuNP-DBB32KDa(B) @ 400 nm	0.19	157 400	1.66×10^{-9}	1.23×10^{-6}	740 // 0.92

* Relative to the maximum Abs. of 20 nm AuNP, fixed at 1.

** c_{AuNP} was calculated taken $\varepsilon_{528nm} = 6.01 \times 10^{+8}$ ($cm^{-1}.M^{-1}$), at the maximum SPR wavelength (525 nm, for 17 nm AuNP).

***b) Fluorescence spectroscopy* method applied for AuNP-LY conjugates**

1) The concentration of AuNP was calculated from UV-Vis spectra as described above.
UV-Vis spectra of ~20 nm AuNP grafted with DBB water-soluble conjugates:

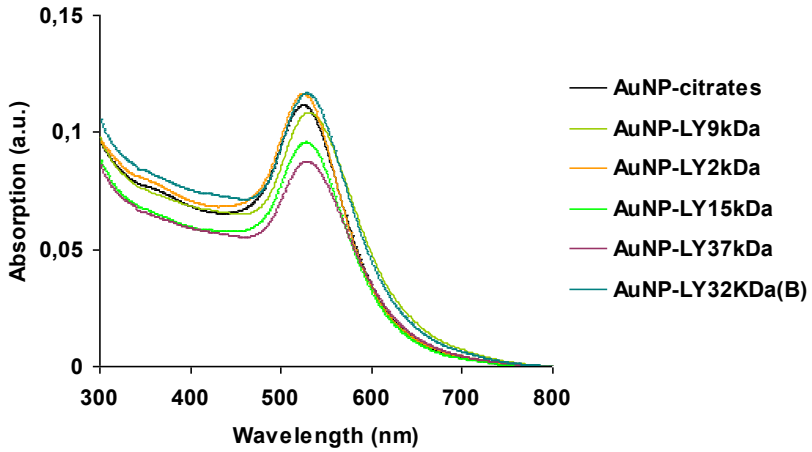

Sample	Abs Max	ε_{528nm} ($cm^{-1}.M^{-1}$)	c_{AuNP} (M)
AuNP-LY2KDa	0.089	$6.01 \times 10^{+8}$	1.48×10^{-10}
AuNP-LY9KDa	0.108	$6.01 \times 10^{+8}$	1.80×10^{-10}
AuNP-LY15KDa	0.096	$6.01 \times 10^{+8}$	1.60×10^{-10}
AuNP-LY37KDa	0.087	$6.01 \times 10^{+8}$	1.46×10^{-10}
AuNP-LY32KDa(B)	0.116	$6.01 \times 10^{+8}$	$1,94 \times 10^{-10}$

2) The concentration of conjugates ($c_{conjugates}$) was calculated, after Au core dissolution in the presence of cyanide (Chapter IV), by fluorescence spectroscopy.
Note: UV-Vis spectroscopy could not be used in this case as the concentration of grafted conjugates was very limited (under the detection limit of UV-Vis technique).

Fluorescence emission spectra of ~20 nm AuNP grafted with DBB water-soluble conjugates, before and after cyanide treatment (after cyanide treatment the entire fluorescence of free detached conjugates could be recovered):

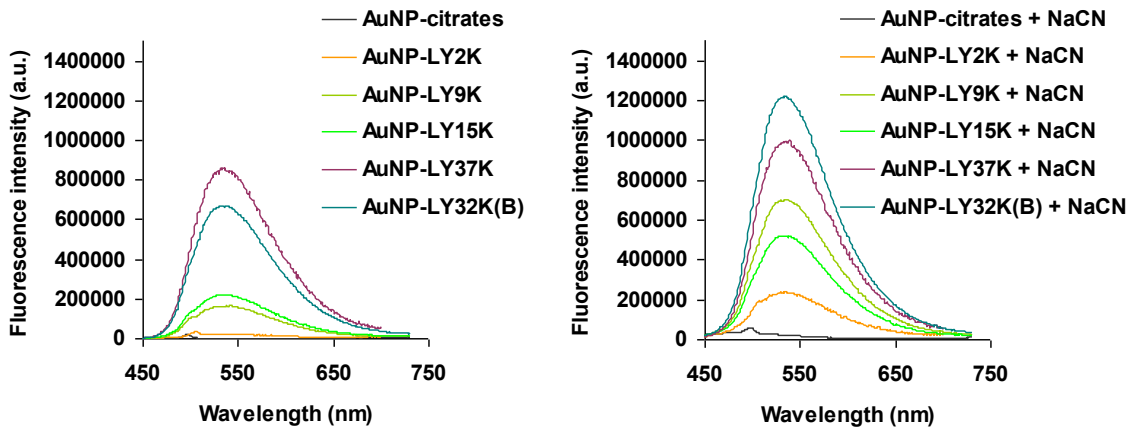

The detected fluorescence emission (area under the curve), was compared to the emission of a reference samples of conjugates with known concentrations, thus allowing to estimate the concentration of conjugates grafted onto AuNP.

Concentration and fluorescence emission of reference samples of free conjugates.

Reference Sample	ε_{430nm} ($cm^{-1}.M^{-1}$)	Concentration (M)	Fluorescence emission (area)
LY2KDa	11 600	4.05×10^{-6}	$1.50 \times 10^{+9}$
LY9KDa	29 900	2.41×10^{-7}	$1.99 \times 10^{+8}$
LY15KDa	42 600	2.48×10^{-7}	$2.74 \times 10^{+8}$
LY37KDa	46 500	8.57×10^{-7}	$1.28 \times 10^{+9}$
LY32KDa(B)	55 000	1.15×10^{-7}	$2.20 \times 10^{+8}$

Fluorescence emission and the concentration and of conjugates grafted onto AuNP after cyanide treatment.

Conjugates after Au core dissolution with cyanide	Fluorescence emission*	Concentration (M)
LY2KDa	$2.30 \times 10^{+7}$	6.22×10^{-8}
LY9KDa	$7.11 \times 10^{+7}$	8.61×10^{-8}
LY15KDa	$5.20 \times 10^{+7}$	4.72×10^{-8}
LY37KDa	$1.01 \times 10^{+8}$	6.75×10^{-8}
LY32KDa(B)	$1.24 \times 10^{+8}$	1.15×10^{-7}

*A blank with AuNP-citrate treated with cyanide was used to subtract the residual emission of Au(I) fluorescent complex formed in the presence of cyanide.

3) Knowing $\mathbf{c_{AuNP}}$ and $c_{conjugates}$, the grafting density could be calculated.

Results of grafting density.

Sample	$\mathbf{c_{AuNP}}$ (M)	$\mathbf{c_{conj.}}$ (M)	Grafting density (chains/AuNP // chains/nm²)
AuNP-LY2KDa	1.48×10^{-10}	6.22×10^{-8}	419 // 0.52
AuNP-LY9KDa	1.80×10^{-10}	8.61×10^{-8}	395 // 0.43
AuNP-LY15KDa	1.60×10^{-10}	4.72×10^{-8}	313 // 0.34
AuNP-LY37KDa	1.46×10^{-10}	6.75×10^{-8}	463 // 0.45
AuNP-LY32KDa(B)	$1,83 \times 10^{-10}$	1.15×10^{-7}	320 // 0.39

Appendix IV.1: Two-Photon Absorption Cross Section of free LY chromophore and LY32KDa(B) conjugate in water

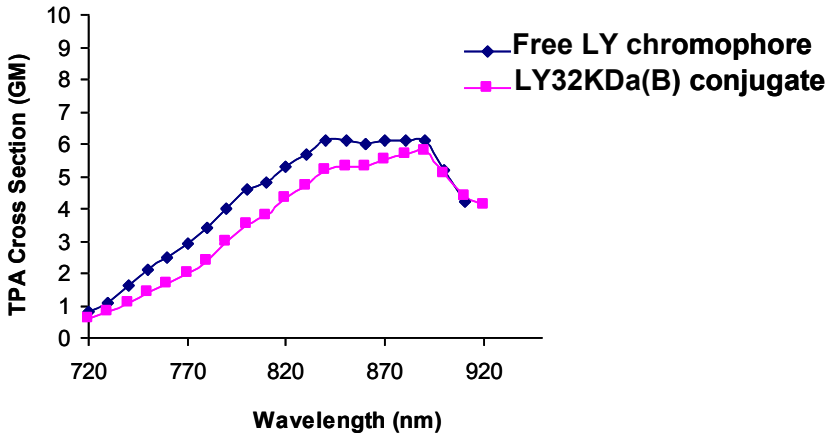

Appendix IV.2: Absorption / emission of 6Ant-AEM *vs.* 6Ant-H conjugate in water (λ_{ex}=470nm)

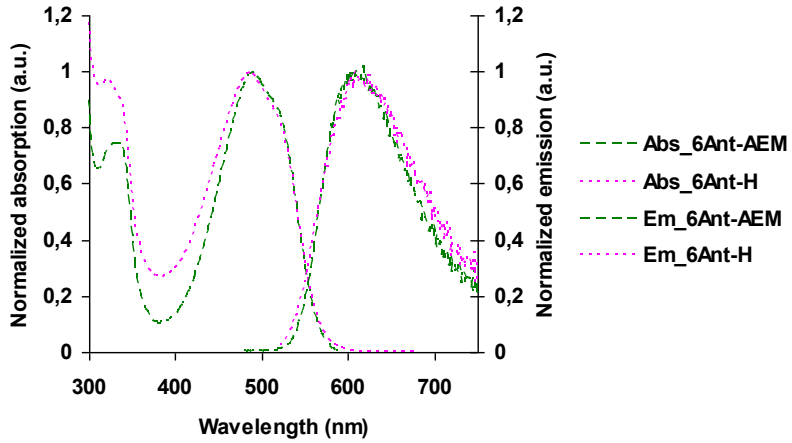

Appendix IV.3: Absorption / emission spectra of DBB13kDa conjugates in water and in dioxane (λ_{ex}=390 nm)

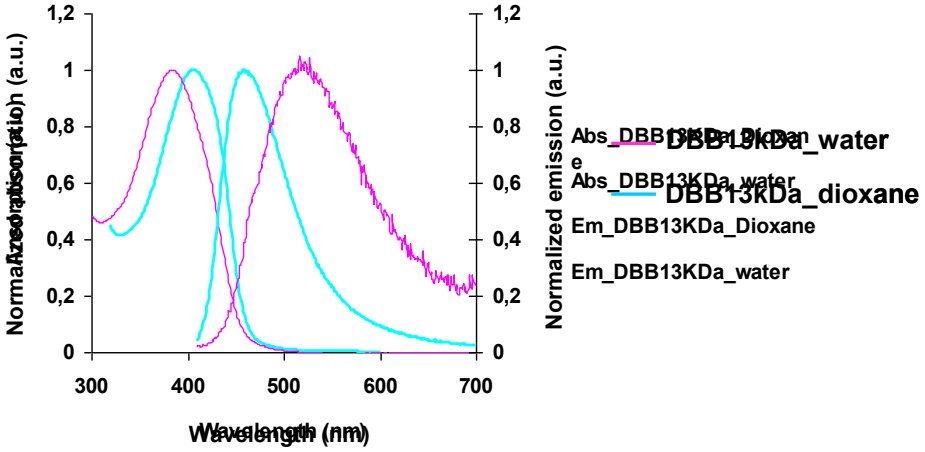

Appendix IV.4: Anisotropy parameters of Ant-polymer conjugates *vs.* free Ant chromophore in chloroform

For all Ant-derivatives (free chromophore and polymer conjugates) anisotropy decays were fitted with a bi-exponential model (Eq. (8)).

Characteristic anisotropy parameters determined from fitted time-resolved anisotropy decays.

Sample	r_0 – initial anisotropy	θ – rotational correlation time (ns)	r_∞ – residual anisotropy
Free Ant chromophore*	0.34	0.87*	-0.0156*
6Ant-AEM	0.25	1.14	0.0186
10 Ant-AEM	0.20	1.07	0.0065
21 Ant-AEM	0.15	1.06	0.00305

* The bi-exponential model was not appropriate to correctly fit the anisotropy decay of free Ant.

Appendix IV.5: Absorption and fluorescence emission recorded with AuNP-Ant systems in water or $CHCl_3$ (λ_{ex}=470 nm)

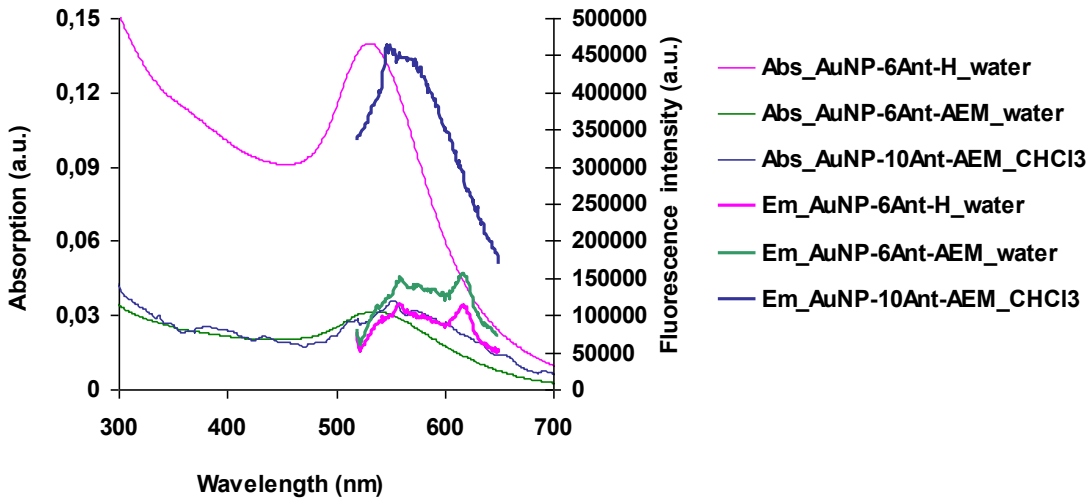

- Very weak maximum absorbance detected (highly diluted sample, due to limited amount of grafted AuNP recovered after reaction).
- Barely detected fluorescence, highly impacted by the background noise.

Appendix V.1: Cellular uptake of Ant-polymer conjugates

Baf-3 cells were incubated without (grey line) and with Ant conjugates (10^{-5} mol.L^{-1} Ant) for the indicated period of time. The cell uptake was measured by flow cytometry. Results are expressed as the average of the mean fluorescence intensity.

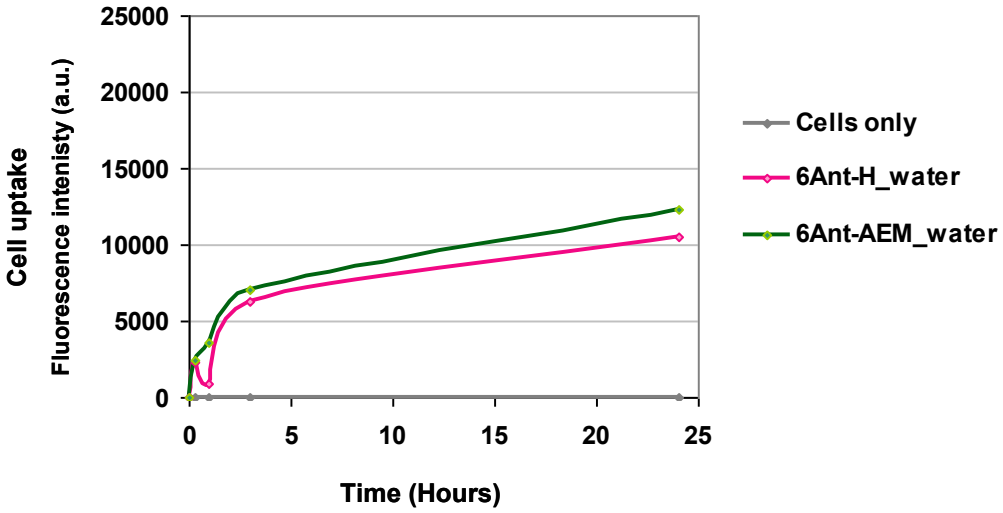

References

[1] **Chapter I: New Features of the Mechanism of RAFT Polymerization,** G. Moad, Y.K. Chong, R. Mulder, E. Rizzardo, S. H. Thang, *Progress in Controlled/Living Radical Polymerization: in RAFT, DT, NMP & OMRP*, K. Matyjaszewski, ACS Symposium Series; American Chemical Society: Washington, DC, **2009**.

[2] a) **Handbook of radical polymerization**, J. Chiefari, E. Rizzardo; Matyjaszewski, K., Davis, T.P., Ed.; Wiley-Interscience: Hoboken, **2002**.

b) **Living Radical Polymerization by the RAFT Process,** G.Moad, E.Rizzardo S.H. Thang, *Aust. J. Chem.* **2005**, *58*, 379-410.

[3] **The Persistent Radical Effect: A Principle for Selective Radical Reactions and Living Radical Polymerizations,** H. Fischer, *Chem. Rev.* **2001**, *101*, 3581-3610.

[4] **Strategies exploiting functions and self-assembly properties of bioconjugates for polymer and materials sciences,** H. G. Börner, *Prog. Polym. Sci.* **2009**, 34, 811-851.

[5] **Living Radical Polymerization as a Tool for the Synthesis of Polymer-Protein/Peptide Bioconjugates,** J. Nicolas, G. Mantovani, D. M. Haddleton, *Macromol. Rapid Commun.* **2007**, *28*, 1083-1111.

[6] a) **Bioconjugate Techniques,** G.T. Hermanson (Ed.), Academic Press, San Diego, **1996**.

b) **Methods in Enzymology, vol. XLIV (Immobilized Enzymes),** K. Mosbach (Ed.), Academic Press, San Diego, **1976**.

[7] **RAFT polymerization mediated bioconjugation strategies,** V. Bulmus, *Polym. Chem.* **2011**, *2*, 1463-1472.

[8] **Polymer-Drug Conjugates: Recent Achievements,** D. Gaikwad, S. Dhawale, J. Khandare, M. Patil, T. Khade, B. Gavitre, K. Bobe, V. Kulkarni, U. Gaikwad, *Res.J. Pharm. Biol. Chem. Sci.* **2011**, *2(2)*, 200-208.

[9] **Polymer-Based Therapeutics,** S. Liu, R. Maheshwari, K. L. Kiick, *Macromolecules* **2009**, *42(1)*, 3-13.

[10] **Covalent Polymer-Drug Conjugates,** C. Elvira, A. Gallardo, J. San Roman, A. Cifuentes, *Molecules* **2005**, *10*, 114-125.

[11] **PEGylated Protein Drugs: Basic Science and Clinical Applications,** F. M. Veronese, *Milestones in Drug Therapy* **2009**, Springer Science.

[12] **Dye-labelled polymer chains at specific sites: Synthesis by living/controlled polymerization,** M. Beija, M.-T. Charreyre, J. M.G. Martinho, *Progr. Polym. Sci.* **2011**, *36*, 568-602.

[13] **Drug-polymer conjugates: potential for improved chemotherapy,** R. Duncan, *Anti-Cancer Drugs* **1992**, *3*, 175-210.

[14] **Phase I clinical and pharmacokinetic study of PK1 [N-(2-hydroxypropyl)methacrylamide copolymer doxorubicin]: first member of a new class of chemotherapeutic agents-drug-polymer conjugates. Cancer Research Campaign Phase I/II Committee,** P. A. Vasey, S. B. Kaye, R. Morrison, C. Twelves, P. Wilson, R. Duncan, A. H. Thomson, L. S. Murray, T. E. Hilditch, T. Murray, S. Burtles, D. Fraier, E. Frigerio, J. Cassidy, *J. Clin. Cancer Res.* **1999**, *5(1)*, 83-94.

[15] **Polymeric Conjugates for Drug Delivery,** N. Larson, H. Ghandehari, *Chem. Mater.* **2012**, *24*, 840-853.

[16] **Modulation of the Surface Charge on Polymer-Stabilized Gold Nanoparticles by the Application of an External Stimulus,** C. Boyer, M. R. Whittaker, K. Chuah, J. Liu, T. P. Davis, *Langmuir* **2010**, *26(4)*, 2721-2730.

[17] **Thermoresponsive Nanohydrogels Cross-Linked by Gold Nanoparticles**, X. Lian, J. Jin, J. Tian, H. Zhao, *ACS Appl. Mater. Interfaces* **2010**, *2(8)*, 2261-2268.

[18] **Synthesis of Biotinylated α-D-Mannoside or N-Acetyl β-D-Glucosaminoside Decorated Gold Nanoparticles: Study of Their Biomolecular Recognition with Con A and WGA Lectins,** X. Jiang A. Housni, G. Gody P. Boullanger, M.-T. Charreyre, T. Delair, R. Narain, *Bioconjugate Chem.* **2010**, *21*, 521-530.

[19] **Salt Effect on the Heat-Induced Association Behavior of Gold Nanoparticles Coated with Poly(N-isopropylacrylamide) Prepared via Reversible Addition-Fragmentation Chain Transfer (RAFT) Radical**

Polymerization, S. Yusa, K. Fukuda, T. Yamamoto, Y. Iwasaki, A. Watanabe, K. Akiyoshi, Y. Morishima, *Langmuir* **2007**, *23*, 12842-12848.

[20] **Tuning the Structure of Thermosensitive Gold Nanoparticle Monolayers,** C. A. Rezende, J. Shan, L.-T. Lee, G. Zalczer, H. Tenhu, *J. Phys. Chem. B* **2009**, *113*, 9786–9794.

[21] **Synthesis of Gold Nanoparticles Coated with Polystyrene-block-poly(N-isopropylacrylamide) and Their Thermoresponsive Ultraviolet-Visible Absorbance,** Y. Liu, W. Tu, D. Cao, *Ind. Eng. Chem. Res.* **2010**, *49*, 2707-2715.

[22] **Self-Assembly and Encoding of Polymer-Stabilized Gold Nanoparticles with Surface-Enhanced Raman Reporter Molecules,** Z. Merican, T. L. Schiller, C. J. Hawker, P. M. Fredericks, I. Blakey, *Langmuir* **2007**, *23*, 10539-10545.

[23] **Thermoresponsive Properties of N-Isopropylacrylamide Oligomer Brushes Grafted to Gold Nanoparticles: Effects of Molar Mass and Gold Core Size,** J. Shan, Y. Zhao, N. Granqvist, H. Tenhu, *Macromolecules* **2009**, *42 (7)*, 2696-2701.

[24] **Gold Nanoparticles Protected with Thiol-Derivatized Amphiphilic Poly(E-caprolactone)-b-poly(acrylic acid),** I. Javakhishvili, S. Hvilsted, *Biomacromolecules* **2009,** *10,* 74-81.

[25] **Hydrophobic Nanocrystals Coated with an Amphiphilic Polymer Shell: A General Route to Water Soluble Nanocrystals,** T. Pellegrino, L. Manna, S. Kudera, T. Liedl, D. Koktysh, A. L. Rogach, S. Keller, J. Rädler, G. Natile, W. J. Parak, *Nano Lett.* **2004**, *4 (4)*, 703-707.

[26] **Controlled RAFT Synthesis of Polyacrylonitrile-b-poly(acrylic acid) Diblocks as Precursors of Carbon Nanocapsules with Assistance of Gold Nanoparticles,** A. Aqil, C. Detrembleur, B. Gilbert, R. Jérôme, C. Jérôme, *Chem. Mater.* **2007**, *19*, 2150-2154.

[27] **Synthesis of Hollow Polymer Nanocapsules Exploiting Gold Nanoparticles as Sacrificial Templates,** C. Boyer, M. R. Whittaker, C. Nouvel, T. P. Davis, *Macromolecules* **2010**, *43*, 1792-1799.

FOLIO ADMINISTRATIF

THESE SOUTENUE DEVANT L'INSTITUT NATIONAL DES SCIENCES APPLIQUEES DE LYON

NOM : CEPRAGA DATE de SOUTENANCE : 30 novembre 2012
(avec précision du nom de jeune fille, le cas échéant)

Prénom: Cristina

TITRE :
"Two-Photon Chromophore-Polymer Conjugates Grafted onto Gold Nanoparticles as Fluorescent Probes for Bioimaging and Photodynamic Therapy Applications"

NATURE : Doctorat Numéro d'ordre : 2012 ISAL 0125

Ecole doctorale : Ecole Doctorale Matériaux de Lyon (ED34)

Spécialité : Matériaux Polymères

RESUME :
La photothérapie dynamique (PTD) est un traitement alternatif du cancer qui nécessite l'utilisation de chromophores (photosensibilisateurs) capables d'induire la mort cellulaire après une irradiation lumineuse. Les nanoparticles d'or (AuNP), grâce à leur phénomène de résonance plasmon localisée, peuvent exalter les propriétés photophysiques des chromophores localisés à leur surface. De plus, l'excitation biphotonique, dans le proche infrarouge, peut être utilisée pour améliorer l'action thérapeutique (PTD) ou diagnostique (imagerie de fluorescence) des chromophores en augmentant la profondeur de pénétration dans les tissus et la résolution tridimensionnelle de la zone excitée.
Lors de ce travail, l'élaboration de nouvelles nanoparticules hybrides est proposée, présentant des applications potentielles en bioimagerie (sondes brillantes) et comme photosensibilisateurs pour la PTD. Ces nanoparticules sont composées d'un cœur d'or sur lequel sont greffés des conjugués polymère-chromophores biphotoniques. La stratégie de synthèse des nano-objets a consisté en : i) la synthèse des conjugués polymère-chromophores biphotoniques solubles dans l'eau ; ii) leur greffage, via une extrémité de chaine, à la surface des AuNP.
Les conjugués polymère-chromophores hydrosolubles ont été synthétisés via le couplage efficace de chromophores hydrophobes en position latérale des copolymères P(NAM-co-NAS) obtenus par la technique RAFT de polymérisation radicalaire contrôlée. Cette stratégie permet le contrôle à la fois de la longueur des chaînes polymère formées (2 000 g.mol-1 < Mn < 37 000 g.mol-1) et du nombre de chromophores couplés par chaîne (de 1 à 21). Le greffage via l'extrémité thiol de chaines de conjugués à la surface des AuNP a été mis en évidence (par MET, ATG et spectroscopie UV-Visible) avec des densités de greffage de ~0.5 chaîne/nm².
Un des rôles de la chaîne polymère était de contrôler la distance entre les chromophores et la surface des AuNP. La dépendance de la distance chromophores-AuNP avec la longueur, donc la masse moléculaire des conjugués a été illustrée en enregistrant une augmentation de la couronne greffée sur les AuNP (par MET), et une augmentation de l'émission de fluorescence des conjugués greffés quand la longueur de chaine augmentait.
Enfin, les propriétés biologiques des conjugués avant et après greffage sur les AuNP ont été évaluées in cellulo, mettant en valeur leur potentiel pour des applications thérapeutiques et diagnostiques.

MOTS-CLES :
Photothérapie dynamique, microscopie biphotonique, chromophore biphotonique, nanoparticles d'or, résonance plasmon de surface, quenching et exaltation de fluorescence, polymérisation RAFT, conjugués polymère-chromophore.

Laboratoire (s) de recherche :
Ingénierie de Matériaux Polymères (UMR CNRS 5223) –IMP@INSA
Laboratoire Joliot-Curie (CNRS USR 3010) - ENS de Lyon
Laboratoire de Chimie – ENS de Lyon

Directeur de thèse:
CHARREYRE Marie-Thérèse – Directeur de Recherche CNRS, INSA de Lyon
Co-Directeur de thèse:
PAROLA Stéphane – Professeur, UCBL Lyon

Président de jury :
DUCHET Jannick – Professeur, INSA de Lyon

Composition du jury :
ASTILEAN Simion – Professeur, Université Babes-Bolyai Cluj (Roumanie)
FARINHA José Paulo Sequeira – Professeur, Instituto Superior Técnico Lisebone (Portugal)
VAN DER SANDEN Boudewijn – Chargé de Recherche Institut des Neurosciences Grenoble
DUCHET Jannick – Professeur, INSA de Lyon
CHARREYRE Marie-Thérèse – Directeur de Recherche CNRS, INSA de Lyon
PAROLA Stéphane – Professeur, UCBL Lyon
FAVIER Arnaud – Chargé de Recherche CNRS, INSA de Lyon
LEROUGE Frédéric – Maitre de Conférence, UCBL Lyon